Neuronal Microtubule Organization

The role of microtubule associated proteins during neuronal development

Yujie Cao

Neuronal Microtubule Organization

The role of microtubule associated proteins during neuronal development

Neuronal Microtubule Organization
The role of microtubule associated proteins during neuronal development

Microtubuli organisatie in zenuwcellen

De rol van microtubuli-geassocieerde eiwitten tijdens zenuwcel ontwikkeling

(met een samenvatting in het Nederlands)

Proefschrift

ter verkrijging van de graad van doctor aan de
Universiteit Utrecht
op gezag van de
rector magnificus, prof.dr. H.R.B.M. Kummeling,
ingevolge het besluit van het college voor promoties
in het openbaar te verdedigen op

woensdag 17 februari 2021 des middags te 4.15 uur

door

Yujie Cao

geboren op 12 november 1988
te Shandong, China

Promotor:

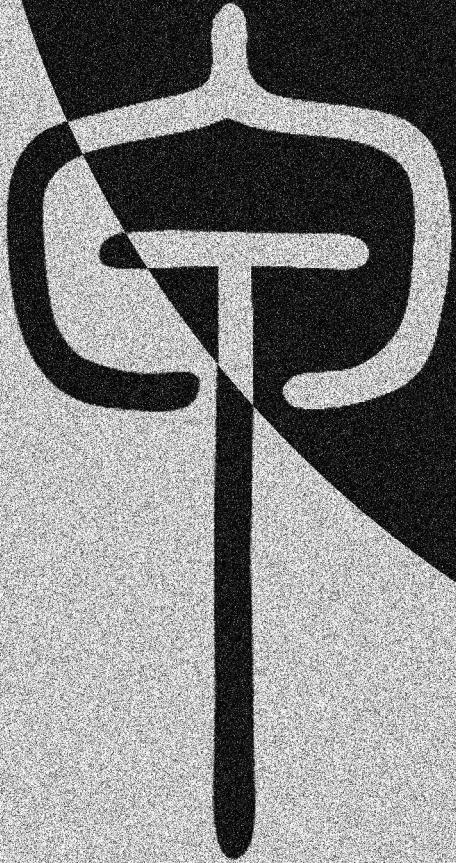Prof. dr. C.C. Hoogenraad

Copromotor:

Dr. M. Harterink

TABLE OF CONTENTS

Chapter 1
General Introduction

Yujie Cao[1]

[1]Cell Biology, Department of Biology, Faculty of Science, Utrecht University, 3584 CH Utrecht, The Netherlands

1

The brain is an incredibly complex organ that is central to the nervous system in all vertebrates and most invertebrate animals. It processes the information from the sensory organs, stores this to form memories and controls motor functions. Neurons are the fundamental units of the brain. These highly specialized cells are connected via synapses to form a gigantic network to pass on and store information. There are around 100 billion neurons in the human brain (Azevedo et al., 2009) each having 1000 synapses on average, illustrating the enormous complexity of this organ.

Neurons have specialized regions to receive or send information called dendrites and axons, respectively. Neurons typically possess several dendrites and a single long and thin axon (Figure 1). Signals from other neurons are received by the synapses in the dendrites and subsequently transferred to the soma and then to the axon. There is a specialized region at the proximal axon, called axon initial segment (AIS), that contains a high density of ion channels (Huang and Rasband, 2018). Here, a neuron can generate an action potential that travels along the axon to propagate signaling to the distal axon. An action potential enables the release of neurotransmitters at synapses, which in turn activates postsynaptic receptors.

Neurons critically rely on their cytoskeletal filaments to acquire and maintain their specialized morphology and for proper neuronal functioning. Microtubules are the major cytoskeletal components of neurons, which serve as tracks for long distance transport, support neuronal morphology, and control local signaling events (Kapitein and Hoogenraad, 2015). Recent studies show that microtubule associated proteins (MAPs) participate in the establishment and maintenance of the neuronal microtubule architecture and mutations in these proteins are associated with various neurodevelopmental and neurodegenerative diseases (Tortosa et al., 2016). To date, our knowledge on MAPs and their function in neuronal microtubule organization is still limited. This thesis aims to investigate the function of several MAPs on the microtubule organization during neuronal development. For this we used primary cultured rat hippocampal neurons, which have been extensively used as a model to study neuronal microtubule organization and polarized transport, and mouse organotypic slice cultures to study neuronal migration. Advanced fluorescent imaging techniques have been used to study cytoskeleton dynamics in neurons. For example, spinning disk confocal microscopy was used to visualize live neurons and stimulated emission depletion microscopy (STED) to image fixed samples (in detail). The application of these imaging techniques in MAPs study will be discussed in more detail in the subsequent chapters.
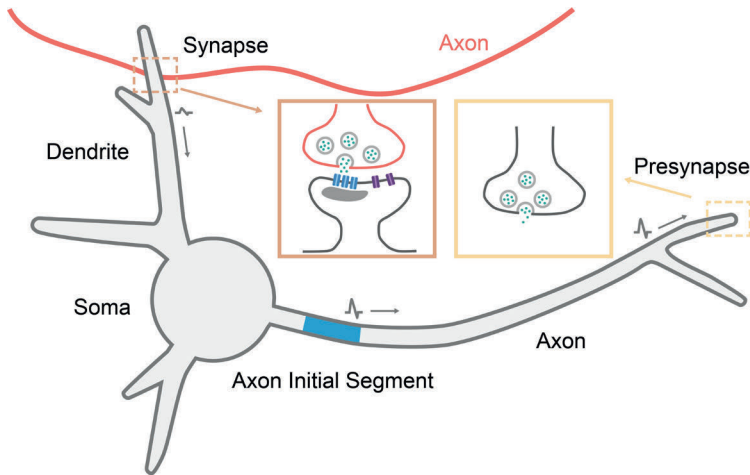
Figure 1. Schematic representation of a typical neuron.
Neurotransmitters (green dots) from a neighboring neuron activate the postsynaptic receptors (blue and purple proteins on the membrane) at the postsynapse and initiate an electrical response (brown box). The electrical signals generated at the postsynapses in the dendrite are transferred to the soma and axon. At the AIS an action potential is initiated and propagated towards the distal axon, which triggers the release of neurotransmitters at the presynapse (yellow box). The released neurotransmitters will activate the postsynaptic receptors of the next cell.

THE NEURONAL CYTOSKELETON

The cytoskeleton is a complex and dynamic network composed of three main components: the actin, microtubule, and intermediate filaments (Wickstead and Gull, 2011). The major function of the cytoskeleton is to maintain the cell shape, provide mechanical resistance to deformation and ensure the stability of cells and tissues (Herrmann et al., 2007). It is also involved in many cellular activities, like migration, signaling pathways, cell division and intracellular transport. In neurons, the cytoskeleton is important for neuronal functioning (Kevenaar and Hoogenraad, 2015).

Microtubules

Microtubules are filaments assembled from α/β-tubulin heterodimers (Janke, 2014). They are relatively stable and participate in many processes during neuronal development, such as neurogenesis, migration and differentiation (Kapitein and Hoogenraad, 2015). At the structural level, α- and β-tubulin are very similar. Both consist of three parts, a GTP-binding N-terminal domain, a middle domain and a C-terminal domain (Manka and Moores, 2018a). During polymerization, α/β-tubulin dimers are added to the microtubule end, after which the GTP from the β-tubulin is hydrolyzed to GDP (Figure 2). Aligned dimers form protofilaments with a 'head to tail' association. Afterwards, the protofilaments are linked together via lateral connections (Manka and Moores, 2018b) and form a polarized, hollow cylindrical

microtubule, typically of 13 protofilaments (Akhmanova and Steinmetz, 2015). The end with β-tubulin exposed is the microtubule plus-end and the other end with α-tubulin exposed is the minus-end.

The microtubule ends are dynamic and both ends can grow and shrink (Tran et al., 1997). The property of microtubules to switch between growing and shrinking phases is known as 'dynamic instability' (Mitchison and Kirschner, 1984). The switching from microtubule growth to shrinkage is called 'catastrophe' and the opposite is called 'rescue' (Figure 2). Microtubule plus-ends are highly dynamic and undergo fast growth and frequent catastrophe *in vitro* and *in vivo* (Akhmanova and Steinmetz, 2015). Unlike the plus-ends, microtubule minus-ends are relatively stable, grow slower and undergo catastrophe less frequently, especially *in vivo* (Feng et al., 2019; Jiang et al., 2014). The dynamic instability of microtubules is partly caused by the different characteristics of GTP- and GDP-bound β-tubulin. The hydrolysis of GTP to GDP leads to a conformational change of the tubulin dimer (Yajima et al., 2012). Growing microtubule plus-ends are capped by GTP-tubulin and exhibit a slightly curved flattened structure, as discovered by cryogenic electron microscopy studies. It is thought that the loss of this more stable GTP-tubulin cap, leaving the GDP-tubulin exposed, leads to microtubule depolymerization with strongly curved and peeling protofilaments (Akhmanova and Steinmetz, 2010).

Microtubules are subject to a remarkable number of post-translational modifications (PTMs) (Song and Brady, 2015). Most PTMs target the outer surface of the microtubule, where the C-terminal tail of tubulin is exposed, and those PTMs do not change the intrinsic properties of microtubules. A wide range of PTMs, such as detyrosination, glutamylation, glycylation, Δ2-tubulin and Δ3-tubulin, take place on the C-terminal tail of tubulins by adding side chains or removing amino acids (Song and Brady, 2015). There are also tubulin PTMs that occur in the lumen of microtubules, for example acetylation (Gadadhar et al., 2017). Microtubules tend to accumulate PTMs over time, which thus can be used to distinguish different subsets of microtubules, e.g. acetylation for long-lived, stable, microtubules (Portran et al., 2017) and microtubules with a C-terminal tyrosine on α-tubulin for dynamic microtubules (Peris et al., 2006).

Microtubules are critical for intracellular transport. There are two classes of molecular motors, Kinesins and Dynein, that walk along microtubules and directionally transport cargos, protein complexes and mRNAs (Hirokawa et al., 2009). There are 45 Kinesins in mammals, that can be further divided into 14 subfamilies. Most Kinesins walk and transport cargoes toward microtubule plus-ends, while dynein and Kinesin14 family proteins move towards the minus-ends. Compared to most other motors, Kinesin14 family proteins are poorly studied in neurons. There are 3 members in Kinesin14 family, KIFC1, KIFC2 and KIFC3. In this thesis we found that KIFC3 is involved in dendritic microtubule organization and details will be further discussed in Chapter 2. The microtubule binding and recognition of Kinesins can be further regulated by tubulin PTMs and MAPs. In Chapter 3, we describe MAP7D2 and its regulation on Kinesin1-driven transport in neurons.
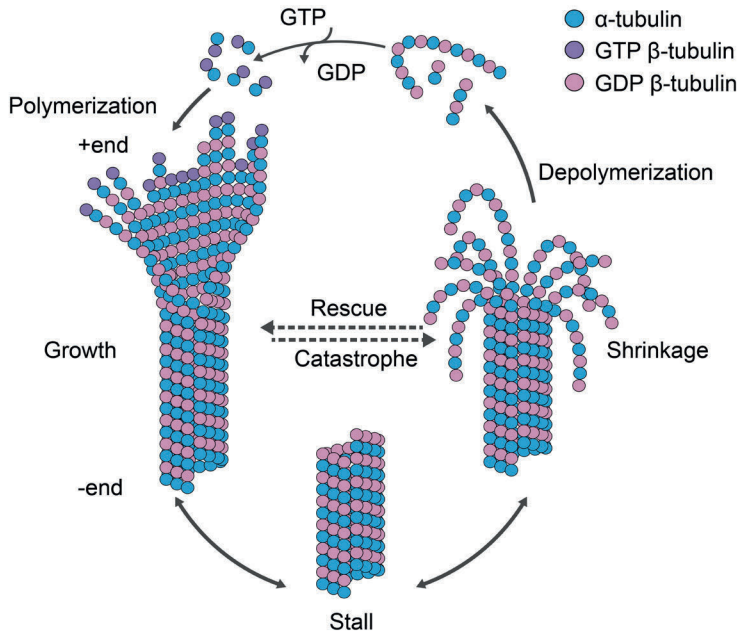
Figure 2. Microtubule assembly and disassembly.

During polymerization α/β-tubulin dimers assemble 'head to tail' to form protofilaments, after which the GTP from the β-tubulin is hydrolyzed into GDP. 10 to 15 protofilaments (usually 13 in mammalian cells) are linked together via lateral connections to form a hollow cylindrical microtubule. The end with β-tubulin exposed is the microtubule plus-end and the other end with α-tubulin exposed is the minus-end. During depolymerization α/β-tubulin dimers are dissociated from microtubule plus-ends. Catastrophe: The transition from shrinking phase to growing phase; Rescue: The transition from growing phase to shrinking phase; Stall: Paused microtubule exhibiting neither growth nor shrinkage. The figure is adapted from the following references (Akhmanova and Steinmetz, 2015).

Actin

Actin filaments are polymers of actin proteins. The actin cytoskeleton is important for cell shaping and cell morphology maintenance, and it is also involved in various cellular functions, including cell motility, cell division, cell signalling and intracellular transport (Pollard and Cooper, 2009). Actin undergoes fast growth and disassembly, which allows it to rapidly remodel itself in response to the environment or to the internal signals. In neurons, actin additionally contributes to spine remodelling (Figure 3), growth cone motility (Gomez and Letourneau, 2014) and neuronal plasticity. Apart from that, several new actin-based structures were recently discovered in neurons, such as actin patches, longitudinal actin fibres and actin rings. Actin patches are regions enriched with branched F-actin in dendrites (Willig et al., 2014), which is important for filopodia outgrowth (Konietzny et al., 2017) and dendritic spine morphogenesis (Korobova and Svitkina, 2010). Longitudinal actin fibres are long and loosely aligned F-actin bundles (Bar et al., 2016; D'Este et al., 2015). Their properties and functions are not clear yet. Actin rings are long-lasting
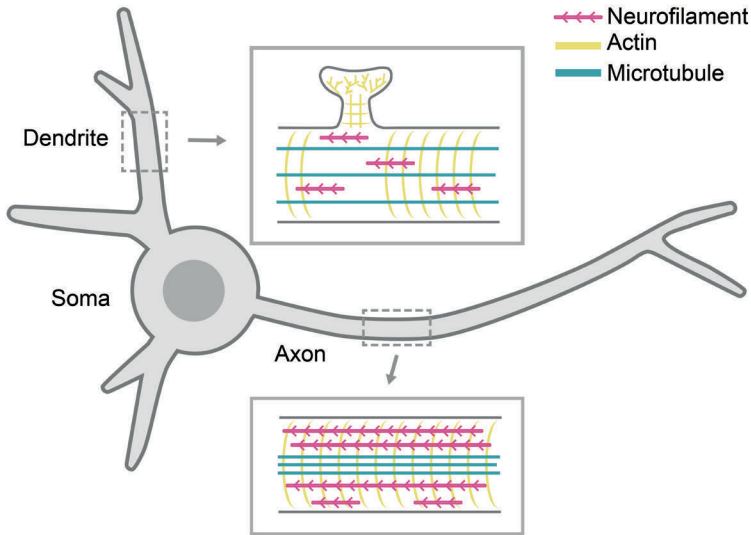
1

Figure 3. Schematic representation of the neuronal cytoskeleton.
Actin comes in various organizations in axons and dendrites. For simplicity, only the periodic actin and branched F-actin in spines are shown here, and longitudinal actin fibres and actin patches in dendrites are not indicated in the figure (Konietzny et al., 2017). Neurofilaments are more abundant in axon and less abundant in dendrite and are important for the maintenance of axon calibre.

periodic cytoskeletal structures (Figure 3) in both dendrites and the axons (Han et al., 2017; Xu et al., 2013), which are thought to be important for long-term axon and dendrite maintenance (Vassilopoulos et al., 2019), axonal microtubule regulation (Qu et al., 2017) and dendritic spine shaping (Bar et al., 2016).

Neurofilaments

Intermediate filaments (IFs) are important cytoskeletal structural components and include 6 different types that are expressed in different types of cell and tissues (Kurup et al., 2018). IFs, that are specifically expressed in the nervous system, are Neurofilaments, which belong to type IV intermediate filaments (Herrmann et al., 2007; Yuan et al., 2012). Neurofilaments are composed of Neurofilament protein L, Neurofilament protein M, Neurofilament protein H and Internexin. They are abundant in axons (Figure 3) and important for the maintenance of axon calibre (Friede and Samorajski, 1970; Kelemen, 2017). Neurofilaments are suggested to play a role in regeneration upon neuron injury, but further research to elucidate this function is needed (Wang et al., 2012).

MICROTUBULE-ASSOCIATED PROTEIN IN NEURON

MAPs are proteins that can associate with microtubules. Over the past decades, numerous functions of MAPs have been revealed. Based on their function, MAPs can be roughly divided into five groups: the structural/classical MAPs, microtubule

post-translation modification enzymes, motor proteins, microtubule plus-end binding proteins, and minus-end binding proteins. Structural MAPs can bind the microtubules lattice, and they can also couple microtubules to actin, neurofilaments or the membrane. Post-translation modification enzymes can target specific sites on microtubules and regulate microtubule modifications. Motor proteins regulate intracellular transport of cargoes, such as organelles, protein complexes and mRNAs. Microtubule plus-end and minus-end binding proteins are important for microtubule assembly and dynamic instability (Akhmanova and Steinmetz, 2010, 2019). The MAPs that are within the scope of this thesis are discussed below: structural MAPs, plus-end binding proteins, and minus-end binding proteins.

Structural MAPs

Structural MAPs were isolated from mammalian brains by co-purification with microtubules more than 20 years ago (Schoenfeld and Obar, 1994). They can bind along the microtubule lattice and regulate microtubule polymerization, stabilization (Al-Bassam et al., 2002; Kawachi et al., 2003), determine microtubule spacing and couple microtubules with other cytoskeleton components and organelles (Chen et al., 1992). The binding of specific MAPs can also alter kinesin-binding affinity towards microtubules, and thus affect cargo transport in neurons. There are 7 structural MAP families, MAP1, MAP2, MAP3/4, MAP6, MAP7, MAP9 and Tau/MAPT (Bodakuntla et al., 2019; Schoenfeld and Obar, 1994; Tortosa et al., 2016). Though some of these MAPs are widely expressed in tissues, the structural MAPs are mainly studied in the nervous system, because they have proven to be of importance for neuronal development. Depletion of structural MAPs leads to neuron and brain function defects and some of these MAPs are also involved in neurodegenerative disorders, such as Alzheimer's disease (Bodakuntla et al., 2019; Tortosa et al., 2016).

The expression of MAPs during neuron development is under tight regulation. In general, MAPs that are important for axon formation appear during early stages of neuronal development, for example, MAP1B. MAPs that are important for dendritogenesis are usually expressed later, such as MAP1A, which regulates dendrite elongation (Tortosa et al., 2016). Most structural MAPs show a specific subcellular distribution, although this can vary in different types of neurons during development. For example, MAP1A (Liu et al., 2015; Szebenyi et al., 2005) and MAP6-E (Tortosa et al., 2017) are enriched in the AIS and the distal axon. Tau (Black et al., 1996; Kempf et al., 1996; Mandell and Banker, 1996) is also enriched in the axon, but it is excluded from the AIS. There are also MAPs that are present in all compartments, such as MAP2C (Albala et al., 1995; Meichsner et al., 1993), MAP6-N (Baratier et al., 2006), MAP9 (Gumy et al., 2017; Venoux et al., 2008) and MAP1B (Gordon-Weeks and Fischer, 2000; Tortosa et al., 2011). Currently, much remains unknown about other MAPs, such as MAP4 (Tokuraku et al., 2010). There are also new MAPs found to have properties of "structural MAPs" that were not identified in the initial co-purification assays, such as TRIM46 (Tripartite Motif Containing 46), which localizes to the AIS (van Beuningen et al., 2015). In this thesis, we have analyzed the various MAP7 family members and found their specific localization in neurons. MAP7 family proteins can promote transport, through the interaction with Kinesin1 family proteins (Hooikaas et al., 2019). The details of

1

1

MAP7D2 (MAP7 Domain Containing 2) function on Kinesin1 mediated cargo transport in neurons will be further discussed in Chapter 3.

The microtubule binding properties of structural MAPs are often regulated by phosphorylation (Ramkumar et al., 2018). In most cases, phosphorylation will reduce the microtubule binding of structural MAPs. For example, phosphorylation reduces the binding of MAP2 to microtubules (Murthy and Flavin, 1983; Tsuyama et al., 1987). Phosphorylation of Tau results in loss of its microtubule binding as well (Busciglio et al., 1995). Moreover, phosphorylated MAP6 cannot stabilize microtubules against cold treatment (Bosc et al., 2003; Job et al., 1983) and the phosphorylation of MAP6 promotes its translocation from microtubules to actin in synapses (Baratier et al., 2006). Studies show that structural MAPs can have a preference for different subsets of microtubules, but the exact mechanisms are still unclear, as reviewed in (Bodakuntla et al., 2019). The specialized microtubule-binding domain of structural MAPs might explain this preference, and also local regulation of binding (e.g. phosphorylation) (Tymanskyj et al., 2018). MAP1S (Tegha-Dunghu et al., 2014), MAP7 (Tymanskyj and Ma, 2019) and MAP6 (Tortosa et al., 2017) are reported to bind to stable microtubules. MAP4 prefers dynamic microtubules, and may be important to maintain a dynamic microtubule pool (Tokuraku et al., 2010). For many years, it was believed that Tau prefers stable microtubules, but recent research found that Tau co-localizes with both stable and dynamic microtubules (Baas and Qiang, 2019; Biswas and Kalil, 2018; Qiang et al., 2018). One difficulty is that the regulation of microtubule dynamics by MAPs is concentration-dependent and MAP overexpression, which is used in most studies, can induce unnatural microtubule stabilization. The potential artificial effect of Tau overexpression should be taken into account when concluding about the specific role of Tau on microtubule stabilization.

Apart from microtubules, structural MAPs can also bind to other cytoskeleton components or to membranes. For example, MAP1 (Kawakami et al., 2003; Orban-Nemeth et al., 2005; Szebenyi et al., 2005), MAP2 (Caceres et al., 1983) and MAP6 (Baratier et al., 2006) were shown to bind to actin, and to be important for the morphology of spines and neuronal plasticity. MAP2 might also bind neurofilaments, thus crosslinking microtubules and neurofilaments (Hirokawa et al., 1988). MAP6, in addition to microtubules, also associates with the *Golgi* apparatus and secretory vesicles and therefore might be involved in cargo trafficking (Tortosa et al., 2017).

Microtubule plus-end binding proteins
The microtubule plus-end exhibits dynamic instability (Akhmanova and Steinmetz, 2015) and microtubule plus-end binding proteins are defined by their ability to concentrate at growing microtubule plus-ends. They are involved in the regulation of microtubule plus-end dynamics and microtubule plus-end interaction with other structures such as the cell cortex, the endoplasmic reticulum (ER) or the actin cytoskeleton. End Binding family proteins (EBs) are the best studied plus-end binding proteins. EBs can autonomously track growing microtubule plus-ends and they are considered to be the core components of the microtubule plus-end network (Akhmanova and Steinmetz, 2010). Many other microtubule plus-end binding

proteins track the microtubule plus-end through the interaction with EBs. EBs have a calponin homology (CH) domain, a coiled-coil (CC) domain, an EB homology (EBH) motif and an EEY/F motif. The CH domain is important for microtubule binding, the CC domain is responsible for dimerization and the EBH and EEY/F motifs interact with other microtubule plus-end binding proteins. There is a large group of microtubule plus-end proteins that can bind to the EBH domain of EBs using an SxIP motifs.

In neurons, microtubule plus-end binding proteins are important for the establishment in the microtubule cytoskeleton during development. As EBs and their binding proteins also label growing microtubule plus-ends in neurons, GFP-tagged EB or GFP-tagged peptides binding to EBs (GFP-MT+Tip) are commonly used as marker to study microtubule orientation and dynamics (Yau et al., 2014). In Chapter 2 and 3, live imaging of EBs is used to investigate microtubule polarity in neurons. In addition to plus-end binding, EBs were also found to be enriched in the AIS (Freal et al., 2019; Leterrier, 2018), which suggests that additional functions for microtubule plus-end binding proteins should be considered.

Microtubule minus-end binding proteins

Microtubule minus-ends undergo growth and disassembly at a slower rate than the plus-ends (Feng et al., 2019; Jiang et al., 2014). Various microtubule minus-end binding proteins were found to be involved in microtubule nucleation and stabilization, but only very few of them, including γ-tubulin, ASPM (Assembly Factor For Spindle Microtubules), KANSL (KAT8 Regulatory NSL Complex) and CAMSAP/Patronin, could bind microtubule minus-ends directly (Akhmanova and Steinmetz, 2019). The mechanism of minus-end recognition of other autonomous minus-end binding proteins is still largely unknown. The most studied microtubule minus-end binding protein is γ-tubulin, which is predominantly found at centrosomes and spindle pole bodies and is important for microtubule nucleation. Together with other proteins it forms a complex with a ring of γ-tubulin exposed, where tubulin dimers subsequently bind to and polymerize, is thought to function as a microtubule nucleation template and/or capping complex (Kollman et al., 2011). The CAMSAP proteins (Calmodulin-Regulated Spectrin-Associated Proteins) contain a CKK domain that recognizes and binds the microtubule lattice with the characteristic curvature of the microtubule minus-ends (Atherton et al., 2019). CAMSAP2 can promote microtubule stabilization and elongation through microtubule minus-end binding and CAMSAP3 is found to maintain a dynamic pool of microtubules in axons (Jiang et al., 2014; Pongrakhananon et al., 2018; Yau et al., 2014). Dendritic microtubule stabilization by CAMSAP2 will be further discussed in Chapter 2.

MICROTUBULE ORGANIZATION IN NEURONS

Neurons are highly polarized cells with asymmetric morphology and function. For a large part the development and maintenance of neuronal polarization depends on their specialized microtubule cytoskeleton architecture, which allows microtubule motor proteins to selectively transport cargo into axons or dendrites (Kapitein et al., 2010). During the past decade, significant progress has been made to identify

microtubule-related processes and signalling pathways that control the neuronal cytoskeleton. However, fundamental properties of the neuronal microtubule network and basic molecular mechanisms regulating microtubule organization in various neuronal model systems remain unclear.

In newborn neurons, microtubules are primarily organized by the centrosome (Cunha-Ferreira et al., 2018). During neuron maturation, the centrosome gradually loses its microtubule nucleation activity and the microtubule organization becomes non-centrosomal (Kapitein and Hoogenraad, 2015). Indeed, it was found that the HAUS/augmin complex regulates microtubule nucleation in the axon and dendrites through the interaction with the γ-tubulin ring complex in stage 3 neurons (Cunha-Ferreira et al., 2018; Sanchez-Huertas et al., 2016). New microtubules can also be generated by cutting pre-existing microtubules. Microtubule severing by Katanin and spastin is particularly important for the formation of axonal branches and dendritic development (Yu et al., 2008).

Microtubule stabilization is important for the maintenance of the microtubule complex. CAMSAP family proteins are known to stabilize microtubule minus-ends and numerous structural MAPs, for example MAP2 and MAP6, are known to stabilize the microtubule lattice. Apart from that, microtubule bundling and anchoring also play a role in the stabilization and organization of microtubule arrays. Several proteins have been revealed as microtubule crosslinker recently. Motor proteins, including dynein and KIFC1 are found to cluster and crosslink microtubules(Muralidharan and Baas, 2019). In addition, we found that CAMSAP2 can interact with KIFC3 to anchor microtubule minus-end to the existing minus-end out microtubules in dendrites. The details of the CAMSAP2-KIFC3 complex and its function in dendritic microtubule organization will be discussed in Chapter 2.

Neurons exhibit a highly specialized microtubule organization in axons and dendrites. In the axon, microtubules are organized in parallel with a plus-end out orientation. Around 90% of the growing microtubule plus-end tips are anterograde, moving towards distal axon. Most axonal microtubules are stable and acetylated (Tas et al., 2017). In dendrites, there are both plus-ends and minus-ends out microtubules. In mature neurons, around 70% of the growing microtubule plus-ends in dendrites move towards the distal dendrite, whereas 30% are retrograde, moving back to the soma (Yau et al., 2016). Recently it was found that microtubules with the same orientation in dendrites are preferentially bundled together (Tas et al., 2017). Most minus-ends out microtubules are stable and acetylated, while most plus-ends out microtubules are dynamic and tyrosinated. The mechanism of dendritic microtubule establishment is still unknown, but it likely depends on neuronal MAPs and microtubule-organizing motors that spatially separate different microtubule populations. The spatial arrangement of microtubules is believed to be important for selective transport and neuronal polarization (Tas and Kapitein, 2018).

In general, the mechanisms that organize the microtubules in neurons are still for a large part unclear, but several hypothesises have arisen/occurred over the past years. One possibility is that pre-existing microtubules are transported into the correct

orientation by sliding. It was found that in axons, microtubule sorting is driven by dynein and is necessary for proper axonal microtubule organization (Rao and Baas, 2018; Zheng et al., 2008). However, it is still not clear how dynein recognizes different orientated microtubules and would transports them directionally (Craig et al., 2017). Another hypothesis is that microtubule orientation is regulated by specific crosslinking proteins. TRIM46 for example can form parallel microtubule bundles, and is required for neuronal polarity and axon specification *in vitro* and *in vivo* (van Beuningen et al., 2015). Paralogues of TRIM46, the E3 ligase TRIM family members MID1 (Midline 1) and MID2 (Midline 2) are also involved in neuronal microtubule organization, which will be further discussed in Chapter 4.

SCOPE OF THIS THESIS

Neuronal polarization and development largely depend on the proper organization of the microtubule cytoskeleton and polarized cargo transport. Although we know that numerous MAPs are involved in the regulation of neuronal microtubule organization, the establishment of the microtubule cytoskeleton in neurons is for a large part unclear. This thesis aims to broaden the knowledge of the microtubule cytoskeleton, MAPs and their contribution to neuronal development. Using advanced live imaging techniques, we elucidate the function of several MAPs in the regulation of microtubule dynamics, the stability of the neuronal microtubule cytoskeleton and cargo transport. CAMSAP2 is well known to stabilize microtubule minus-ends in cell lines and neurons (Jiang et al., 2014; Yau et al., 2014). In Chapter 2, we describe a novel mechanism that regulates the dendritic microtubule organization by CAMSAP2 and KIFC3. CAMSAP2-KIFC3 complex can anchor microtubule minus-ends to other microtubules, thus crosslinking microtubules in dendrites to stabilize the dendritic microtubule cytoskeleton. MAP7 family members contain a Kinesin1 binding domain, which could promote Kinesin1-related transport in neurons. However, MAP7 proteins have hardly been studied in neurons. In Chapter 3, we investigate all MAP7 proteins in primary cultured rat hippocampal neurons and focus on the only axon localized MAP7, MAP7D2, and its function in Kinesin1-mediated transport into the axon. We found that MAP7D2 localizes to the proximal axon and specifically interacts with Kinesin1 family proteins. Depletion of MAP7D2 in neurons leads to defects in axon development and neuronal migration due to reduced cargo entry into the axon. We propose a model that MAP7D2 locally promotes Kinesin1 mediated cargo transport into the axon. TRIM46 is important for microtubule stabilization in the AIS and it is associated with paraneoplastic neurological syndromes (van Beuningen et al., 2015; van Coevorden-Hameete et al., 2017). The TRIM46 paralogues, MID1 and MID2, are also associated with neurological disorders. In Chapter 4, we investigate MID1, MID2 and their function on neuronal development. Similar to TRIM46, MID1 and MID2 bind to microtubules in neurons and are both important for axonal development. Moreover, MID2 also plays a role in dendrite development and controls the dynamics and organization of dendritic microtubules. It was recently found that the interplay between the ER and microtubule cytoskeleton is critical for neuronal polarity and the alterations in ER function and microtubule organization could contribute to neurodegenerative diseases (Farias et al., 2019). The ER tubules present in the axon

are important for microtubule stabilization. Furthermore, the axonal ER tubules may provide a local source of lipid and/or control local calcium homeostasis. In Chapter 5, we describe an interaction between VAP (vesicle-associated membrane protein-associated protein) and SCRN1 (Secernin-1), which can mediate ER remodeling and presynaptic function. The VAP-SCRN1 complex is required for proper ER morphology, maintenance of ER continuity and dynamics, preservation of Ca^{2+} homeostasis and synaptic vesicle cycling at presynaptic sites.

1

Abbreviation	Definition
AIS	Axon Initial Segment
ASPM	Assembly Factor For Spindle Microtubules
Ca^{2+}	Calcium Ions
CAMSAP1/2/3	Calmodulin-Regulated Spectrin-Associated Protein 1/2/3
CC domain	Coiled-Coil Domain
CH domain	Calponin Homology Domain
C-terminus/terminal	Carboxyl Terminus/Terminal
EB(s)	End Binding Family Protein(s)
EBH motif	EB Homology Motif
ER	Endoplasmic Reticulum
F-actin	Filamentous Actin
GDP	Guanosine Diphosphate
GFP	Green Fluorescent Protein
GTP	Guanosine Triphosphate
IFs	Intermediate Filaments
KANSL	KAT8 Regulatory NSL Complex
KIFC1/2/3	Kinesin Family Member C1/C2/C3
MAP(s)	Microtubule Associated Protein(s)
MAP7D2	MAP7 Domain Containing 2
MID1	Midline 1
MID2	Midline 2
mRNA	Messenger Ribonucleic Acid
N-terminus/terminal	Amino Terminus/Terminal
PTM(s)	Post-translational Modification(s)
SCRN1	Secernin 1
STED	Stimulated Emission Depletion Microscopy
SxIP motif	Serine-Any Amino Acid-Isoleucine-Proline
TRIM	Tripartite Motif (RING, B-box and Coiled-coil)
TRIM46	Tripartite Motif Containing 46
VAP	Vesicle-associated Membrane Protein-associated Protein

1

REFERENCES

Akhmanova, A., and Steinmetz, M.O. (2010). Microtubule +TIPs at a glance. J Cell Sci 123, 3415-3419.

Akhmanova, A., and Steinmetz, M.O. (2015). Control of microtubule organization and dynamics: two ends in the limelight. Nat Rev Mol Cell Biol 16, 711-726.

Akhmanova, A., and Steinmetz, M.O. (2019). Microtubule minus-end regulation at a glance. J Cell Sci 132.

Al-Bassam, J., Ozer, R.S., Safer, D., Halpain, S., and Milligan, R.A. (2002). MAP2 and tau bind longitudinally along the outer ridges of microtubule protofilaments. J Cell Biol 157, 1187-1196.

Albala, J.S., Kress, Y., Liu, W.K., Weidenheim, K., Yen, S.H., and Shafit-Zagardo, B. (1995). Human microtubule-associated protein-2c localizes to dendrites and axons in fetal spinal motor neurons. J Neurochem 64, 2480-2490.

Atherton, J., Luo, Y., Xiang, S., Yang, C., Rai, A., Jiang, K., Stangier, M., Vemu, A., Cook, A.D., Wang, S., et al. (2019). Structural determinants of microtubule minus end preference in CAMSAP CKK domains. Nat Commun 10, 5236.

Azevedo, F.A., Carvalho, L.R., Grinberg, L.T., Farfel, J.M., Ferretti, R.E., Leite, R.E., Jacob Filho, W., Lent, R., and Herculano-Houzel, S. (2009). Equal numbers of neuronal and nonneuronal cells make the human brain an isometrically scaled-up primate brain. J Comp Neurol 513, 532-541.

Baas, P.W., and Qiang, L. (2019). Tau: It's Not What You Think. Trends Cell Biol 29, 452-461.

Bar, J., Kobler, O., van Bommel, B., and Mikhaylova, M. (2016). Periodic F-actin structures shape the neck of dendritic spines. Sci Rep 6, 37136.

Baratier, J., Peris, L., Brocard, J., Gory-Faure, S., Dufour, F., Bosc, C., Fourest-Lieuvin, A., Blanchoin, L., Salin, P., Job, D., et al. (2006). Phosphorylation of microtubule-associated protein STOP by calmodulin kinase II. J Biol Chem 281, 19561-19569.

Biswas, S., and Kalil, K. (2018). The Microtubule-Associated Protein Tau Mediates the Organization of Microtubules and Their Dynamic Exploration of Actin-Rich Lamellipodia and Filopodia of Cortical Growth Cones. J Neurosci 38, 291-307.

Black, M.M., Slaughter, T., Moshiach, S., Obrocka, M., and Fischer, I. (1996). Tau is enriched on dynamic microtubules in the distal region of growing axons. J Neurosci 16, 3601-3619.

Bodakuntla, S., Jijumon, A.S., Villablanca, C., Gonzalez-Billault, C., and Janke, C. (2019). Microtubule-Associated Proteins : Structuring the Cytoskeleton. Trends Cell Biol 29, 804-819.

Bosc, C., Andrieux, A., and Job, D. (2003). STOP proteins. Biochemistry 42, 12125-12132.

Busciglio, J., Lorenzo, A., Yeh, J., and Yankner, B.A. (1995). beta-amyloid fibrils induce tau phosphorylation and loss of microtubule binding. Neuron 14, 879-888.

Caceres, A., Payne, M.R., Binder, L.I., and Steward, O. (1983). Immunocytochemical localization of actin and microtubule-associated protein MAP2 in dendritic spines. Proc Natl Acad Sci U S A 80, 1738-1742.

Chen, J., Kanai, Y., Cowan, N.J., and Hirokawa, N. (1992). Projection domains of MAP2 and tau determine spacings between microtubules in dendrites and axons. Nature 360, 674-677.

Craig, E.M., Yeung, H.T., Rao, A.N., and Baas, P.W. (2017). Polarity sorting of axonal microtubules: a computational study. Mol Biol Cell 28, 3271-3285.

Cunha-Ferreira, I., Chazeau, A., Buijs, R.R., Stucchi, R., Will, L., Pan, X., Adolfs, Y., van der Meer, C., Wolthuis, J.C., Kahn, O.I., et al. (2018). The HAUS Complex Is a Key Regulator of Non-centrosomal Microtubule Organization during Neuronal Development. Cell Rep 24, 791-800.

D'Este, E., Kamin, D., Gottfert, F., El-Hady, A., and Hell, S.W. (2015). STED nanoscopy reveals the ubiquity of subcortical cytoskeleton periodicity in living neurons. Cell Rep 10, 1246-1251.

Farias, G.G., Freal, A., Tortosa, E., Stucchi, R., Pan, X., Portegies, S., Will, L., Altelaar, M., and Hoogenraad, C.C. (2019). Feedback-Driven Mechanisms between Microtubules and the Endoplasmic Reticulum Instruct Neuronal Polarity.

Neuron 102, 184-201 e188.

Feng, C., Thyagarajan, P., Shorey, M., Seebold, D.Y., Weiner, A.T., Albertson, R.M., Rao, K.S., Sagasti, A., Goetschius, D.J., and Rolls, M.M. (2019). Patronin-mediated minus end growth is required for dendritic microtubule polarity. J Cell Biol 218, 2309-2328.

Freal, A., Rai, D., Tas, R.P., Pan, X., Katrukha, E.A., van de Willige, D., Stucchi, R., Aher, A., Yang, C., Altelaar, A.F.M., et al. (2019). Feedback-Driven Assembly of the Axon Initial Segment. Neuron 104, 305-321 e308.

Friede, R.L., and Samorajski, T. (1970). Axon caliber related to neurofilaments and microtubules in sciatic nerve fibers of rats and mice. Anat Rec 167, 379-387.

Gadadhar, S., Bodakuntla, S., Natarajan, K., and Janke, C. (2017). The tubulin code at a glance. J Cell Sci 130, 1347-1353.

Gomez, T.M., and Letourneau, P.C. (2014). Actin dynamics in growth cone motility and navigation. J Neurochem 129, 221-234.

Gordon-Weeks, P.R., and Fischer, I. (2000). MAP1B expression and microtubule stability in growing and regenerating axons. Microsc Res Tech 48, 63-74.

Gumy, L.F., Katrukha, E.A., Grigoriev, I., Jaarsma, D., Kapitein, L.C., Akhmanova, A., and Hoogenraad, C.C. (2017). MAP2 Defines a Pre-axonal Filtering Zone to Regulate KIF1- versus KIF5-Dependent Cargo Transport in Sensory Neurons. Neuron 94, 347-362 e347.

Han, B., Zhou, R., Xia, C., and Zhuang, X. (2017). Structural organization of the actin-spectrin-based membrane skeleton in dendrites and soma of neurons. Proc Natl Acad Sci U S A 114,E6678-E6685.

Herrmann, H., Bar, H., Kreplak, L., Strelkov, S.V., and Aebi, U. (2007). Intermediate filaments: from cell architecture to nanomechanics. Nat Rev Mol Cell Biol 8, 562-573.

Hirokawa, N., Hisanaga, S., and Shiomura, Y. (1988). MAP2 is a component of crossbridges between microtubules and neurofilaments in the neuronal cytoskeleton: quick-freeze, deep-etch immunoelectron microscopy and reconstitution studies. J Neurosci 8, 2769-2779.

Hirokawa, N., Noda, Y., Tanaka, Y., and Niwa, S. (2009). Kinesin superfamily motor proteins and intracellular transport. Nat Rev Mol Cell Biol 10, 682-696.

Hooikaas, P.J., Martin, M., Muhlethaler, T., Kuijntjes, G.J., Peeters, C.A.E., Katrukha, E.A., Ferrari, L., Stucchi, R., Verhagen, D.G.F., van Riel, W.E., et al. (2019). MAP7 family proteins regulate kinesin-1 recruitment and activation. J Cell Biol 218, 1298-1318.

Huang, C.Y., and Rasband, M.N. (2018). Axon initial segments: structure, function, and disease. Ann N Y Acad Sci 1420, 46-61.

Janke, C. (2014). The tubulin code: molecular components, readout mechanisms, and functions. J Cell Biol 206, 461-472.

Jiang, K., Hua, S., Mohan, R., Grigoriev, I., Yau, K.W., Liu, Q., Katrukha, E.A., Altelaar, A.F., Heck, A.J., Hoogenraad, C.C., et al. (2014). Microtubule minus-end stabilization by polymerization-driven CAMSAP deposition. Dev Cell 28, 295-309.

Job, D., Rauch, C.T., Fischer, E.H., and Margolis, R.L. (1983). Regulation of microtubule cold stability by calmodulin-dependent and -independent phosphorylation. Proc Natl Acad Sci U S A 80, 3894-3898.

Kapitein, L.C., and Hoogenraad, C.C. (2015). Building the Neuronal Microtubule Cytoskeleton. Neuron 87, 492-506.

Kapitein, L.C., Schlager, M.A., Kuijpers, M., Wulf, P.S., van Spronsen, M., MacKintosh, F.C., and Hoogenraad, C.C. (2010). Mixed microtubules steer dynein-driven cargo transport into dendrites. Curr Biol 20, 290-299.

Kawachi, A., Ichihara, K., Hisanaga, S., Iida, J., Toyota, H., Hotani, H., and Itoh, T.J. (2003). Different protofilament-dependence of the microtubule binding between MAP2 and MAP4. Biochem Biophys Res Commun 305, 72-78.

Kawakami, S., Muramoto, K., Ichikawa, M., and Kuroda, Y. (2003). Localization of microtubule-associated protein (MAP) 1B in the postsynaptic densities of the rat cerebral cortex. Cell Mol Neurobiol 23, 887-894.

Kelemen, G.H. (2017). Intermediate Filaments Supporting Cell Shape and Growth in Bacteria. Subcell Biochem 84, 161-211.

Kempf, M., Clement, A., Faissner, A., Lee, G., and Brandt, R. (1996). Tau binds to the distal axon early in development of polarity in a microtubule- and microfilament-dependent manner. J Neurosci 16, 5583-5592.

1

1

Kevenaar, J.T., and Hoogenraad, C.C. (2015). The axonal cytoskeleton: from organization to function. Front Mol Neurosci 8, 44.

Kollman, J.M., Merdes, A., Mourey, L., and Agard, D.A. (2011). Microtubule nucleation by gamma-tubulin complexes. Nat Rev Mol Cell Biol 12, 709-721.

Konietzny, A., Bar, J., and Mikhaylova, M. (2017). Dendritic Actin Cytoskeleton: Structure, Functions, and Regulations. Front Cell Neurosci 11, 147.

Korobova, F., and Svitkina, T. (2010). Molecular architecture of synaptic actin cytoskeleton in hippocampal neurons reveals a mechanism of dendritic spine morphogenesis. Mol Biol Cell 21, 165-176.

Kurup, N., Li, Y., Goncharov, A., and Jin, Y. (2018). Intermediate filament accumulation can stabilize microtubules in Caenorhabditis elegans motor neurons. Proc Natl Acad Sci U S A 115, 3114-3119.

Leterrier, C. (2018). The Axon Initial Segment: An Updated Viewpoint. J Neurosci 38, 2135-2145.

Liu, Y., Lee, J.W., and Ackerman, S.L. (2015). Mutations in the microtubule-associated protein 1A (Map1a) gene cause Purkinje cell degeneration. J Neurosci 35, 4587-4598.

Mandell, J.W., and Banker, G.A. (1996). A spatial gradient of tau protein phosphorylation in nascent axons. J Neurosci 16, 5727-5740.

Manka, S.W., and Moores, C.A. (2018a). Microtubule structure by cryo-EM: snapshots of dynamic instability. Essays Biochem 62, 737-751.

Manka, S.W., and Moores, C.A. (2018b). The role of tubulin-tubulin lattice contacts in the mechanism of microtubule dynamic instability. Nat Struct Mol Biol 25, 607-615.

Meichsner, M., Doll, T., Reddy, D., Weisshaar, B., and Matus, A. (1993). The low molecular weight form of microtubule-associated protein 2 is transported into both axons and dendrites. Neuroscience 54, 873-880.

Mitchison, T., and Kirschner, M. (1984). Dynamic instability of microtubule growth. Nature 312, 237-242.

Muralidharan, H., and Baas, P.W. (2019). Mitotic Motor KIFC1 Is an Organizer of Microtubules in the Axon. J Neurosci 39, 3792-3811.

Murthy, A.S., and Flavin, M. (1983). Microtubule assembly using the microtubule-associated protein MAP-2 prepared in defined states of phosphorylation with protein kinase and phosphatase. Eur J Biochem 137, 37-46.

Orban-Nemeth, Z., Simader, H., Badurek, S., Trancikova, A., and Propst, F. (2005). Microtubule-associated protein 1S, a short and ubiquitously expressed member of the microtubule-associated protein 1 family. J Biol Chem 280, 2257-2265.

Peris, L., Thery, M., Faure, J., Saoudi, Y., Lafanechere, L., Chilton, J.K., Gordon-Weeks, P., Galjart, N., Bornens, M., Wordeman, L., et al. (2006). Tubulin tyrosination is a major factor affecting the recruitment of CAP-Gly proteins at microtubule plus ends. J Cell Biol 174, 839-849.

Pollard, T.D., and Cooper, J.A. (2009). Actin, a central player in cell shape and movement. Science 326, 1208-1212.

Pongrakhananon, V., Saito, H., Hiver, S., Abe, T., Shioi, G., Meng, W., and Takeichi, M. (2018). CAMSAP3 maintains neuronal polarity through regulation of microtubule stability. Proc Natl Acad Sci U S A 115, 9750-9755.

Portran, D., Schaedel, L., Xu, Z., Thery, M., and Nachury, M.V. (2017). Tubulin acetylation protects long-lived microtubules against mechanical ageing. Nat Cell Biol 19, 391-398.

Qiang, L., Sun, X., Austin, T.O., Muralidharan, H., Jean, D.C., Liu, M., Yu, W., and Baas, P.W. (2018). Tau Does Not Stabilize Axonal Microtubules but Rather Enables Them to Have Long Labile Domains. Curr Biol 28, 2181-2189 e2184.

Qu, Y., Hahn, I., Webb, S.E., Pearce, S.P., and Prokop, A. (2017). Periodic actin structures in neuronal axons are required to maintain microtubules. Mol Biol Cell 28, 296-308.

Ramkumar, A., Jong, B.Y., and Ori-McKenney, K.M. (2018). ReMAPping the microtubule landscape: How phosphorylation dictates the activities of microtubule-associated proteins. Dev Dyn 247, 138-155.

Rao, A.N., and Baas, P.W. (2018). Polarity Sorting of Microtubules in the Axon. Trends Neurosci 41, 77-88.

Sanchez-Huertas, C., Freixo, F., Viais, R., Lacasa, C., Soriano, E., and Luders, J. (2016). Non-centrosomal nucleation mediated

by augmin organizes microtubules in post-mitotic neurons and controls axonal microtubule polarity. Nat Commun 7, 12187.

Schoenfeld, T.A., and Obar, R.A. (1994). Diverse distribution and function of fibrous microtubule-associated proteins in the nervous system. Int Rev Cytol 151, 67-137.

Song, Y., and Brady, S.T. (2015). Post-translational modifications of tubulin:pathways to functional diversity of microtubules. Trends Cell Biol 25, 125-136.

Szebenyi, G., Bollati, F., Bisbal, M., Sheridan, S., Faas, L., Wray, R., Haferkamp, S., Nguyen, S., Caceres, A., and Brady, S.T. (2005). Activity-driven dendritic remodeling requires microtubule-associated protein 1A. Curr Biol 15, 1820-1826.

Tas, R.P., Chazeau, A., Cloin, B.M.C., Lambers, M.L.A., Hoogenraad, C.C., and Kapitein, L.C. (2017). Differentiation between Oppositely Oriented Microtubules Controls Polarized Neuronal Transport. Neuron 96, 1264-1271 e1265.

Tas, R.P., and Kapitein, L.C. (2018). Exploring cytoskeletal diversity in neurons. Science 361, 231-232.

Tegha-Dunghu, J., Bausch, E., Neumann, B., Wuensche, A., Walter, T., Ellenberg, J., and Gruss, O.J. (2014). MAP1S controls microtubule stability throughout the cell cycle in human cells. J Cell Sci 127, 5007-5013.

Tokuraku, K., Okuyama, S., Matsushima, K., Ikezu, T., and Kotani, S. (2010). Distinct neuronal localization of microtubule-associated protein 4 in the mammalian brain. Neurosci Lett 484, 143-147.

Tortosa, E., Adolfs, Y., Fukata, M., Pasterkamp, R.J., Kapitein, L.C., and Hoogenraad, C.C. (2017). Dynamic Palmitoylation Targets MAP6 to the Axon to Promote Microtubule Stabilization during Neuronal Polarization. Neuron 94, 809-825 e807.

Tortosa, E., Kapitein, L.C., and Hoogenraad, C.C. (2016). Microtubule Organization and Microtubule-Associated Proteins (MAPs). In Dendrites:Development and Disease, K. Emoto, R. Wong, E. Huang, and C. Hoogenraad, eds. (Tokyo: Springer Japan), pp. 31-75.

Tortosa, E., Montenegro-Venegas, C., Benoist, M., Hartel, S., Gonzalez-Billault, C., Esteban, J.A., and Avila, J. (2011). Microtubule-associated protein 1B (MAP1B) is required for dendritic spine development and synaptic maturation. J Biol Chem 286, 40638-40648.

Tran, P.T., Walker, R.A., and Salmon, E.D. (1997). A metastable intermediate state of microtubule dynamic instability that differs significantly between plus and minus ends. J Cell Biol 138, 105-117.

Tsuyama, S., Terayama, Y., and Matsuyama, S. (1987). Numerous phosphates of microtubule-associated protein 2 in living rat brain. J Biol Chem 262, 10886-10892.

Tymanskyj, S.R., and Ma, L. (2019). MAP7 Prevents Axonal Branch Retraction by Creating a Stable Microtubule Boundary to Rescue Polymerization. J Neurosci 39, 7118-7131.

Tymanskyj, S.R., Yang, B.H., Verhey, K.J., and Ma, L. (2018). MAP7 regulates axon morphogenesis by recruiting kinesin-1 to microtubules and modulating organelle transport. Elife 7.

van Beuningen, S.F.B., Will, L., Harterink, M., Chazeau, A., van Battum, E.Y., Frias, C.P., Franker, M.A.M., Katrukha, E.A., Stucchi, R., Vocking, K., et al. (2015). TRIM46 Controls Neuronal Polarityand Axon Specification by Driving the Formation of Parallel Microtubule Arrays. Neuron 88, 1208-1226.

van Coevorden-Hameete, M.H., van Beuningen, S.F.B., Perrenoud, M., Will, L.M., Hulsenboom, E., Demonet, J.F., Sabater, L., Kros, J.M., Verschuuren, J., Titulaer, M.J., et al. (2017). Antibodies to TRIM46 are associated with paraneoplastic neurological syndromes. Ann Clin Transl Neurol 4, 680-686.

Vassilopoulos, S., Gibaud, S., Jimenez, A., Caillol, G., and Leterrier, C. (2019). Ultrastructure of the axonal periodic scaffold reveals a braid-like organization of actin rings. Nat Commun 10, 5803.

Venoux, M., Delmouly, K., Milhavet, O., Vidal-Eychenie, S., Giorgi, D., and Rouquier, S. (2008). Gene organization, evolution and expression of the microtubule-associated protein ASAP (MAP9). BMC Genomics 9, 406.

Wang, H., Wu, M., Zhan, C., Ma, E., Yang, M., Yang, X., and Li, Y. (2012). Neurofilament proteins in axonal regeneration and neurodegenerative

diseases. Neural Regen Res 7, 620-626.

Wickstead, B., and Gull, K. (2011). The evolution of the cytoskeleton. J Cell Biol 194, 513-525.

Willig, K.I., Steffens, H., Gregor, C., Herholt, A., Rossner, M.J., and Hell, S.W. (2014). Nanoscopy of filamentous actin in cortical dendrites of a living mouse. Biophys J 106, L01-03.

Xu, K., Zhong, G., and Zhuang, X. (2013). Actin, spectrin, and associated proteins form a periodic cytoskeletal structure in axons. Science 339, 452-456.

Yajima, H., Ogura, T., Nitta, R., Okada, Y., Sato, C., and Hirokawa, N. (2012). Conformational changes in tubulin in GMPCPP and GDP-taxol microtubules observed by cryoelectron microscopy. J Cell Biol 198, 315-322.

Yau, K.W., Schatzle, P., Tortosa, E., Pages, S., Holtmaat, A., Kapitein, L.C., and Hoogenraad, C.C. (2016). Dendrites In Vitro and In Vivo Contain Microtubules of Opposite Polarity andAxon Formation Correlates with Uniform Plus-End-Out Microtubule Orientation. J Neurosci 36, 1071-1085.

Yau, K.W., van Beuningen, S.F., Cunha-Ferreira, I., Cloin, B.M., van Battum, E.Y., Will, L., Schatzle, P., Tas, R.P., van Krugten, J., Katrukha, E.A., et al. (2014). Microtubule minus-end binding protein CAMSAP2 controls axon specification and dendrite development. Neuron 82, 1058-1073.

Yuan, A., Rao, M.V., Veeranna, and Nixon, R.A. (2012). Neurofilaments at a glance. J Cell Sci 125, 3257-3263.

Zheng, Y., Wildonger, J., Ye, B., Zhang, Y., Kita, A., Younger, S.H., Zimmerman, S., Jan, L.Y., and Jan, Y.N. (2008). Dynein is required for polarized dendritic transport and uniform microtubule orientation in axons. Nat Cell Biol 10, 1172-1180.

Chapter 2

Microtubule Minus-End Binding Protein CAMSAP2 and Kinesin-14 Motor KIFC3 Control Dendritic Microtubule Organization

Yujie Cao[1], Joanna Lipka[1], Riccardo Stucchi[1,2], Mithila Burute[1], Xingxiu Pan[1], Sybren Portegies[1], Roderick Tas[1], Jelmer Willems[1], Lena Will[1], Harold MacGillavry[1], Maarten Altelaar[2], Lukas C. Kapitein[1], Martin Harterink[1], and Casper C. Hoogenraad[1,3,4,*]

[1]Cell Biology, Neurobiology and Biophysics, Department of Biology, Faculty of Science, Utrecht University, 3584 Utrecht, the Netherlands

[2]Biomolecular Mass Spectrometry and Proteomics, Bijvoet Center for Biomolecular Research and Utrecht Institute for Pharmaceutical Sciences, Utrecht University, 3584 Utrecht, the Netherlands

[3]Department of Neuroscience, Genentech, Inc., South San Francisco, CA 94080, USA

[4]Lead Contact

[*]Correspondence: c.hoogenraad@uu.nl

SUMMARY

Neuronal dendrites are characterized by an anti-parallel microtubule organization. The mixed oriented microtubules promote dendrite development and facilitate polarized cargo trafficking, however the mechanism that regulates dendritic microtubule organization is still unclear. Here, we found that the kinesin-14 motor KIFC3 is important for organizing dendritic microtubules and to control dendrite development. The kinesin-14 motor proteins (*Drosophila melanogaster* Ncd, *Saccharomyces cerevisiae* Kar3, *Saccharomyces pombe* Pkl1, *Xenopus laevis* XCTK2) are characterized by a C-terminal motor domain and are well described to organize the spindle microtubule during mitosis using an additional microtubule binding site in the N-terminus (Braun et al., 2009; Fink et al., 2009; Hirokawa, 1998; Peterman and Scholey, 2009). In mammals there are three kinesin-14 members, KIFC1, KIFC2 and KIFC3. It was recently shown that KIFC1 is important for organizing axonal microtubules in neurons, a process that depends on the two microtubule interacting domains (Muralidharan and Baas, 2019). Unlike KIFC1, KIFC2 and KIFC3 lack the N-terminal microtubule binding domain and only have one microtubule interacting domain, the motor domain (Norris et al., 2018; Zhang and Sperry, 2004). Thus, in order to regulate microtubule-microtubule cross-linking or sliding, KIFC2 and KIFC3 need to interact with additional microtubule binding proteins to connect two microtubules. We found that KIFC3 has a dendrite specific distribution and interacts with microtubule minus-end binding protein CAMSAP2. Depletion of KIFC3 or CAMSAP2 results in increased microtubule dynamics during dendritic development. We propose a model in which CAMSAP2 anchors KIFC3 at microtubule-minus ends and immobilizes microtubule arrays in dendrites.
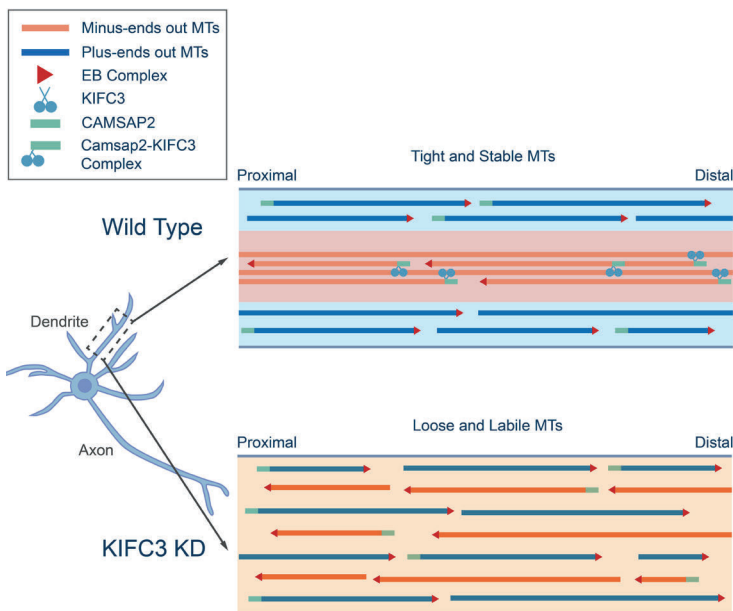
RESULTS

KIFC3 localizes to the soma and dendrites and controls dendritic branching

In order to determine the role of KIFC3 during neuronal development, we depleted endogenous KIFC3 protein from cultured hippocampal neurons at stage 3 with short hairpin RNAs (shRNA). The efficiency of our shRNAs was quantified by Western blot (Figure S1A and S1B). KIFC3 shRNA1, shRNA2 and shRNA4 efficiently reduced KIFC3 protein levels and were subsequently used for the experiments in this study. Depletion of KIFC3 during stage 3 led to simplified dendritic arbors as determined by Sholl analysis (Figure 1A, 1B and S1C) and shorter total dendrite length (Figure 1C). KIFC3 depletion did not result in significant changes in the number of total dendritic arbors or the average dendrites length (Figure 1D and 1E). We next performed ex vivo electroporation experiments to study KIFC3 function in the mouse cortex (Figure S1D and S1E). We found that KIFC3-depleted neurons can still migrate through the cortex but showed abnormal dendrite development (Figure 1F). We defined the cortical neurons into four different categories according to their morphology (Figure 1G). Consistent with the morphology phenotype in primary cultured neurons, the KIFC3 depletion in cortical slices leads to simplified dendritic arbors. The branching defect is rescued by shRNA resistant KIFC3 expression (Figure 1G). Together these data suggest that KIFC3 is required for the proper dendrite morphology but not for neuronal migration.

We next determined the cellular localization of KIFC3. We found that full length mCherry-tagged KIFC3 decorates microtubule stretches in dendrites and that it is excluded from the axon (Figure 2A and 2D). KIFC3 preferentially colocalizes with stable microtubule bundles, marked by acetylated microtubule arrays, and less with more labile tyrosinated microtubules (Figure 2A-C). Recent super-resolution data showed that stable and acetylated microtubules are mostly oriented minus-end out (Tas et al., 2017). Therefore, our data suggest that KIFC3 associates with bundles of mostly minus end out oriented stable microtubules. KIFC3 consists of three N-terminal coiled-coil domains and a C-terminal motor domain (Figure 2G). Since kinesin-14 family members are minus-end directed motors, the axon exclusion of full length KIFC3 could be the result of retrograde motor activity in the axon towards the cell body. To test this, we generated five truncation mutants that lack the motor domain, from KIFC3-N1 to KIFC3-N5 (Figure 2G). KIFC3-FL (Figure 2D) and KIFC3-N1 (Figure 2E), but not the shorter KIFC3-N2 (Figure 2F) and -N5 (results not shown), localized specifically to the somatodendritic compartment (Figure 2H). These data suggest that the axonal exclusion of KIFC3 is not due to its motor domain. Unfortunately, the anti-KIFC3 antibodies that worked on Western blot did not give specific endogenous KIFC3 staining in neuronal cultures. In the next section we applied the HITI CRISPR knock-in system to integrate a tag into the endogenous KIFC3 gene (Suzuki et al., 2016).

KIFC3 interacts with minus-end binding protein CAMSAP2

To investigate the role of KIFC3 in dendrite development we performed KIFC3 pull-down experiments from brain lysates followed by mass spectrometry to identify binding partners. GFP-tagged KIFC3 full length, KIFC3-N1 and KIFC3-N3 with a

Figure 1. KIFC3 is important for dendrite branching.

(A-B) DIV11 hippocampal neurons expressing GFP and pSuper-scrambled shRNA as a Control or KIFC3 shRNAs. ShRNA efficiency was indicated in Figure S1A and S1B. (A) Representative images of the neurons with the dendrites marked in red. Scale bar = 25μm. (B) Sholl analysis of the dendritic branching upon Control and KIFC3 depletion. Control: N=7, n=46; KIFC3 shRNA2: N=7, n=57; KIFC3 shRNA4: N=5, n=36. Error bars represent SEM. Significant difference was shown in Figure S1C.

(C-E) Quantification of the neurons described in (A, B). Total dendrite length (C), average dendrite length (D) and total number of dendrite branches (E) were quantified. Error bars represent SEM. *p < 0.05; **p < 0.01; *** p < 0.001 (Unpaired T-test).

(F) Representative images of mouse cortical plate. Same images with larger view were used to quantify migration defects (Figure S1D and S1E). Neurons were transfected with MARCKS-GFP and KIFC3 shRNAs or pSuper-scrambled shRNA. A shRNAs resistant mCherry-KIFC3 was used for rescue. Scale bars=50μm. Control: N=10, n=175; KIFC3 shRNAs: N=8, n=184; KIFC3 shRNAs+KIFC3: N=9, n=264.

(G) Quantifications of the neuronal morphology of transfected cells in the cortical plate (CP), defined as 80-100% of the radial axis from ventricular surface to the pial surface corresponding to (F). Error bars represent SEM. *p < 0.05; **p < 0.01; *** p < 0.001 (Unpaired T-test). Schematic diagram was used to show the typical morphology of different type neurons.

BirA recognition site together with the biotin ligase BirA were expressed in HEK293 cells and were used as bait for a pull down from brain extracts. GFP protein was used as negative control. Several potential KIFC3 associated proteins were identified by mass spectrometry, including several cytoskeleton proteins such as the microtubule minus-end binding protein CAMSAP2 (Table S1). CAMSAP2 is known to protect and stabilize free microtubule minus-ends and is required for neuronal polarity and development (Yau et al., 2014). To further validate the interaction between KIFC3 and CAMSAP2, we performed additional pull-down experiments. KIFC3 full length was used as bait and pulled down endogenous CAMSAP2 from HEK293T (Figure 2I). The interaction was not specific to CAMSAP2 since we found that KIFC3 can also pull down the other two CAMSAPs family members (Figure 2J). Expression of full length GFP-tagged KIFC3 in COS7 cells (Figure S2A) or cultured neurons (Figure S2C) and co-staining for endogenous CAMSAP2 revealed strong overlap between both proteins. The localization of endogenously tagged KIFC3 is very similar to the full-length mCherry-KIFC3 (Figure 2A and 2D) and reveals specific microtubule staining in dendrites (Figure S2D). Endogenous KIFC3 and endogenous CAMSAP2 coincide along microtubule stretches in cultured neurons. Similar result was observed in live neurons co-expressed with mCherry-tagged KIFC3 and 3GFP-tagged CAMSAP2 (Video S1). To identify the minimal domains required for the KIFC3-CAMSAP2 interaction, we performed pull down experiments using truncated KIFC3 constructs (Figure 2G). Specifically, the second coiled-coil domain of KIFC3 (mCherry-KIFC3-N4) pulls down full length CAMSAP2 (Figure 2K). Consistently, mCherry-KIFC3-N4 and GFP-CAMSAP2 markedly coincide in COS7 cells (Figure S2E-F). On the CAMSAP2 side, the second and third coiled-coil domain (GFP-CAMSAP2-N2 and -N3) colocalized with KIFC3 but not the C-terminus or other N-terminal fragments (Figure S2B and S2G-J). Altogether, these
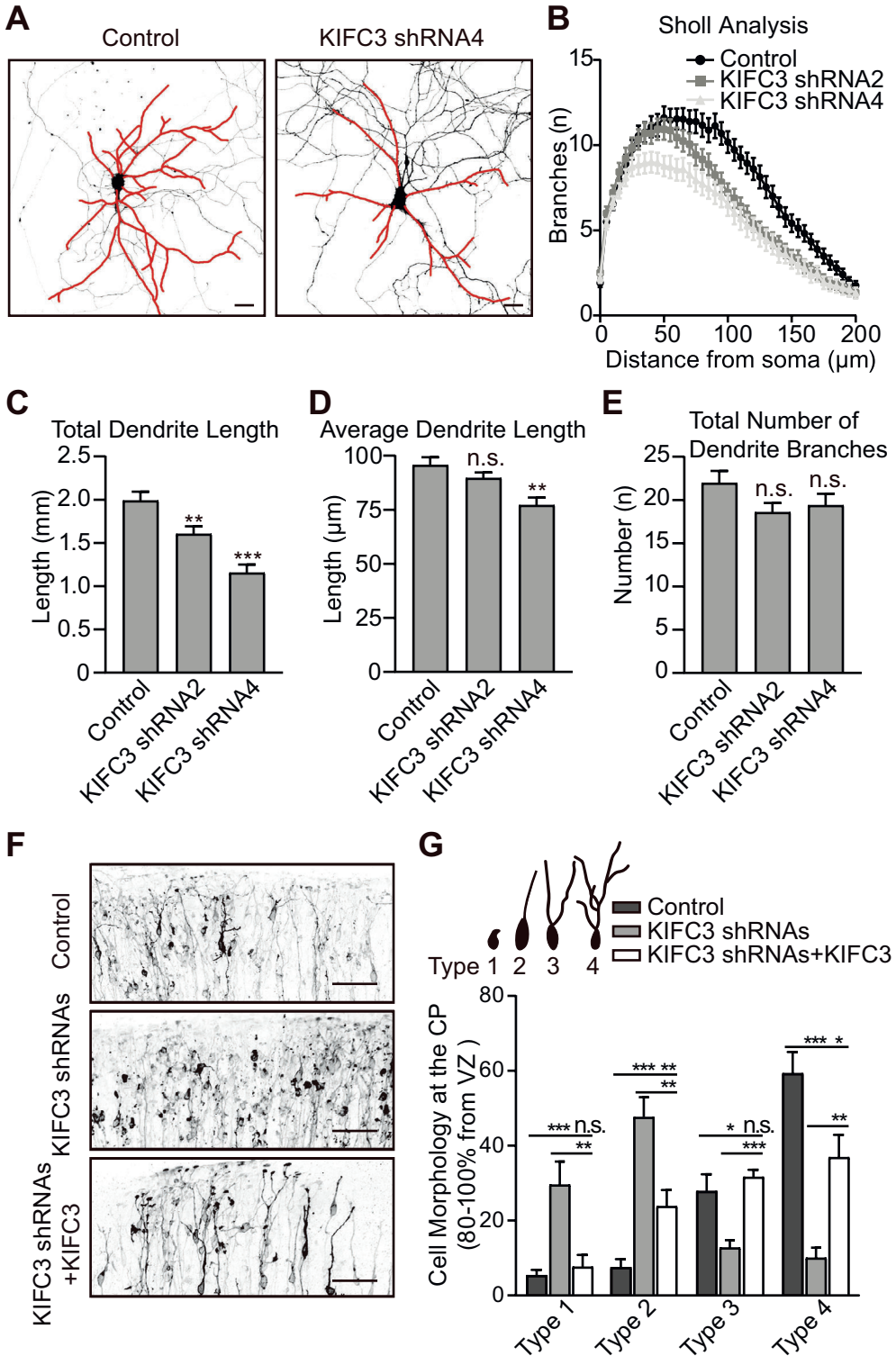
Figure 2. KIFC3 localizes to dendrites and interacts with CAMSAP2.

(A-B) Representative images of DIV11 hippocampal neurons transfected with mCherry-KIFC3-FL and co-stained with acetylated tubulin and tyrosinated tubulin antibody. (A) Selected axonal (marked with a blue box) and dendritic (marked with an orange box) regions are enlarged below. Scale bar=10μm and 5μm in enlargements. (B) Further enlargement of a dendrite region is shown. Scale bar=2μm.

(C) Intensity profile of the indicated region in (B).

(D-F) Representative images of DIV10 hippocampal neurons transfected with GFP fill and mCherry-KIFC3-FL, mCherry-KIFC3-N1 or mCherry-KIFC3-N2 and stained for TRIM46 to visualize the Axon Initial Segment (AIS). Selected axonal (marked with a blue box) and dendritic (marked with an orange box) regions are enlarged below. Scale bar=10μm.

(G) Schematic representation of the KIFC3 secondary structure and truncation constructs used. CC: coiled-coiled domain, MD: motor domain.

(H) Polarity index analysis from KIFC3-FL and truncations corresponding to (D-F). Positive values indicate axon enrichment, and negative values indicate dendrite enrichment.

(I) Biotin pull-downs from extracts of HEK293T cells transfected with BirA recognition site conjugated mCherry-KIFC3-FL and probed for mCherry and CAMSAP2. For all pull-down experiments the input is 25% of the biotin pull-down. CAMSAP2 was found from KIFC3 pull-downs with brain extracts (Table S1). The interaction is also proved by co-localization experiment in neurons and COS7 cells (Figure S2 and Video S1).

(J) Biotin pull-downs from extracts of HEK293T cells transfected with BirA recognition site conjugated mCherry-KIFC3-FL together with GFP tagged CAMSAP1, 2 or 3 and probed for mCherry and GFP.

(K) Biotin pull-downs from extracts of HEK293T cells transfected with BirA recognition site conjugated KIFC3 truncation constructs together with GFP tagged CAMSAP2 and probed for mCherry and GFP.

(L) Representative images of COS7, transfected with 3GFP-CAMSAP2 and mCherry-KIFC3 (Video S2). SIR-tubulin was applied to visualize microtubules. Microtubule photoablation was indicated by red stars. Minus end was indicated by white and black arrows. 3GFP-CAMSAP2 was shown in Green, mCherry-KIFC3 in Red and SIR-tubulin in Cyan. Scale bar=2μm.

(M) The quantification of CAMSAP2 and KIFC3 puncta intensity corresponding to (H).

---

results suggest that KIFC3 uses its second coiled-coil domain to bind to the second and third coiled-coil domain of CAMSAP2.

KIFC3 and CAMSAP2 regulate microtubule density and dynamics in dendrites

We next tested the role of KIFC3 and CAMSAP2 in dendritic microtubule organization. Depletion of KIFC3 or CAMSAP2 causes a marked reduction in total microtubules, stable and dynamic microtubules, as marked by α-tubulin, acetylated and tyrosinated tubulin, in dendrites of DIV11 neurons (Figure 3A-C), suggesting that both KIFC3 and CAMSAP2 control microtubule density in dendrites. KIFC3 expression also reduced the intensity of tyrosinated tubulin in dendrite, but hardly affects the acetylated-tubulin staining (Figure S3A). Next, we determined the dynamics and orientation of dendritic microtubules using the microtubule plus-end marker, GFP-MACF18 (Figure 3D). KIFC3 depletion, using two independent shRNAs, strongly increased the number of retrograde MT+TIP comets tagged by GFP compared to control neurons (Figure 3E and 3F).
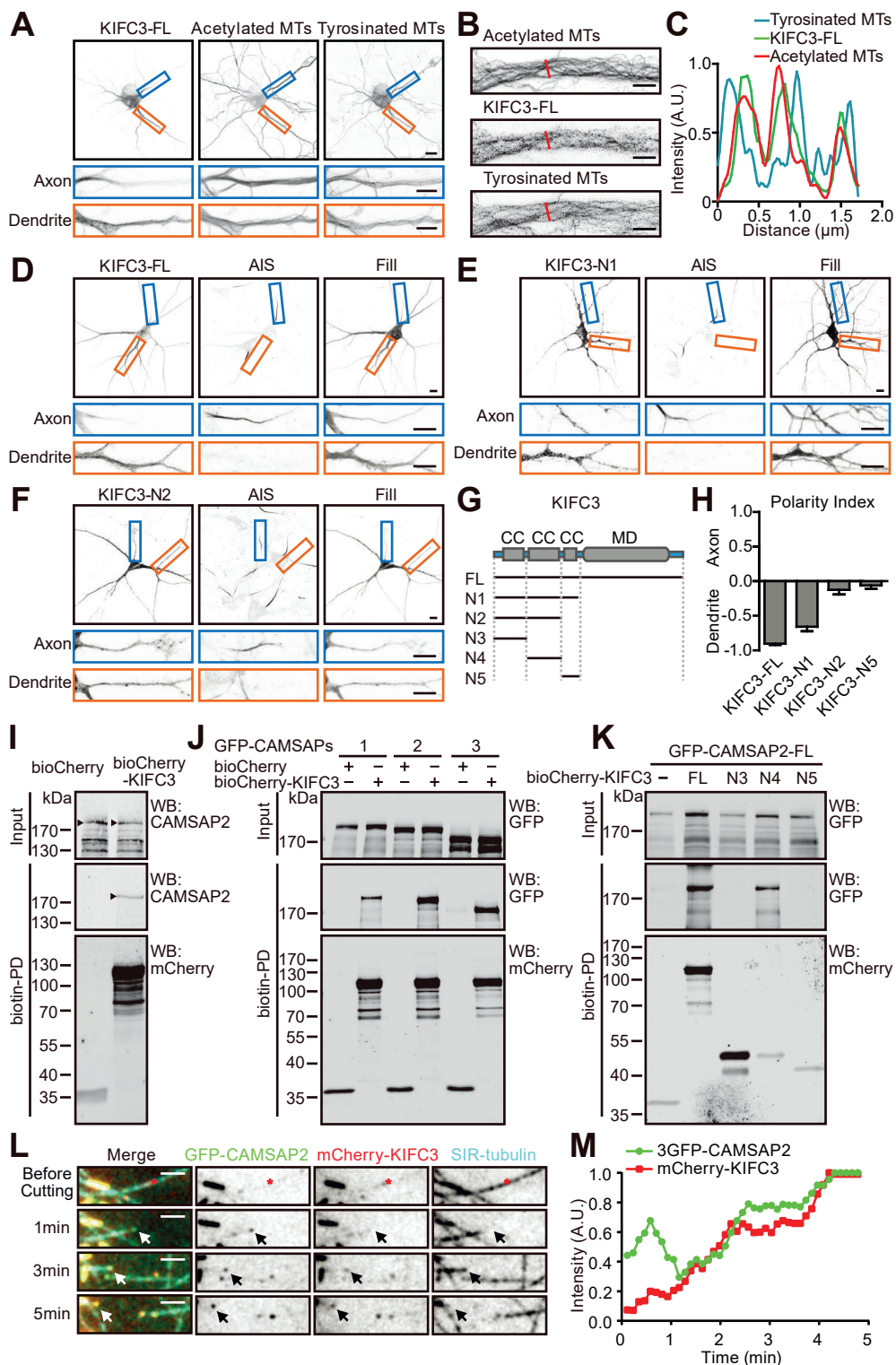
Figure 3. CAMSAP2 and KIFC3 stabilize minus-end out microtubules.

(A-C) Quantification of α-tubulin, acetylated tubulin and tyrosinated tubulin levels in DIV11 neurons transfected with pSuper scrambled or CAMSAP2 shRNA or KIFC3 shRNA2 or KIFC3 over-expression (Figure S3A). Control: N=7, n=58; CAMSAP2 shRNA: N=7, n=25; KIFC3 shRNA2: N=7, n=34. Error bars represent SEM. Unpaired-T-test was performed, and columns were compared with corresponding Control. *p < 0.05; **p < 0.01; *** p < 0.001.

(D) Original and illustrated kymographs of GFP-MACF18 traced with life-cell microscopy from Control, KIFC3 shRNA2 and CAMSAP2 shRNA transfected neurons. GFP-MACF18 was used to visualize microtubule plus-end tips. Anterograde comets are marked in green and retrograde comets are marked in red. Scale bar=3μm.

(E) Quantification of the number of comets moving retrogradely and anterogradely in dendrites of neurons described in (C). N=2, Control: n=26, KIFC3 shRNA1: n=20, KIFC3 shRNA2 n=19, CAMSAP2 shRNA: n=20. Error bars represent SEM. *p < 0.05; **p < 0.01; *** p < 0.001 (Unpaired T-test).

(F) Quantification of the ratio of retrograde/total comets in dendrites of cells described in (D) with (black bars) and without (white bars) laser severing. No laser severing: N=2, Control: n=26, KIFC3 shRNA1: n=20, KIFC3 shRNA2 n=19, CAMSAP2 shRNA: n=20. Conditions with laser severing: Control N=1, n=4, KIFC3 shRNA1 N=1, n=3, KIFC3 shRNA2 N=1, n=3, CAMSAP2 shRNA N=2, n=3. Error bars represent SEM. *p < 0.05; **p < 0.01; *** p < 0.001 (Unpaired T-test).

(G) Schematic representation of the KIFC3, CAMSAP2 and CAMSAP2-KIFC3 chimeric protein. CC: coiled-coiled domain, MD: motor domain, CH: Calponin-homology domain, MBD: microtubule binding domain, CKK: CKK domain. The domains present in the chimeric protein are marked by blue rectangles. Green lines mark amino acids from CAMSAP2; orange lines mark amino acids from KIFC3. Microtubules with their orientations are marked in gray.

(H-J) Quantification of retrograde/total comets ratio in dendrites of neurons transfected with pSuper-scrambled as Control or KIFC3 shRNA2 together with different KIFC3 rescue constructs. KIFC3-rigor was validated by Peroxisome Distribution Assay (Figure S3B and S3C). Control: N=12, n=78; KIFC3 shRNA2: N=13, n=85; Control+KIFC3-FL: N=3, n=13; KIFC3 shRNA2+KIFC3-FL: N=3, n=21; KIFC3 shRNA2+Chimera: N=3, n=18; KIFC3 shRNA2+KIFC3-CC-MD: N=3, n=22; KIFC3 shRNA2+CAMSAP2-MBD-CKK: N=4, n=37; KIFC3 shRNA2+EMTB-MBD-CKK: N=3, n=15; KIFC3 shRNA2+KIFC3-rigor: N=4, n=32. Error bars represent SEM. Columns were compared with Control or KIFC3 shRNA2 respectively. *p < 0.05; **p < 0.01; *** p < 0.001 (Unpaired T-test).

This effect was rescued by full length KIFC3, but not KIFC3-CC-MD lacking the CAMSAP2 interacting N-terminal region (Figure 3H and 3I). We next tested whether the KIFC3 motor activity is required for this effect and generated, based on the KIF5B rigor mutation (Nakata and Hirokawa, 1995), a KIFC3(396T-N) rigor mutant, which cannot walk but still binds to microtubules (Figure 3B and S3C). The KIFC3 rigor mutant did not rescue the KIFC3 knockdown phenotype (Figure 3J), suggesting that the KIFC3 motor activity is required for regulating dendritic microtubule dynamics. The number of retrograde comets was also increased upon CAMSAP2 depletion, however, in contrast to KIFC3 shRNAs, the number of anterograde comets was reduced (Figure 3E), suggesting that CAMSAP2 has additional function in dendrites. To assess total microtubule polarity (dynamic and stable) we quantified minus- and plus-end out microtubules after laser photoablation
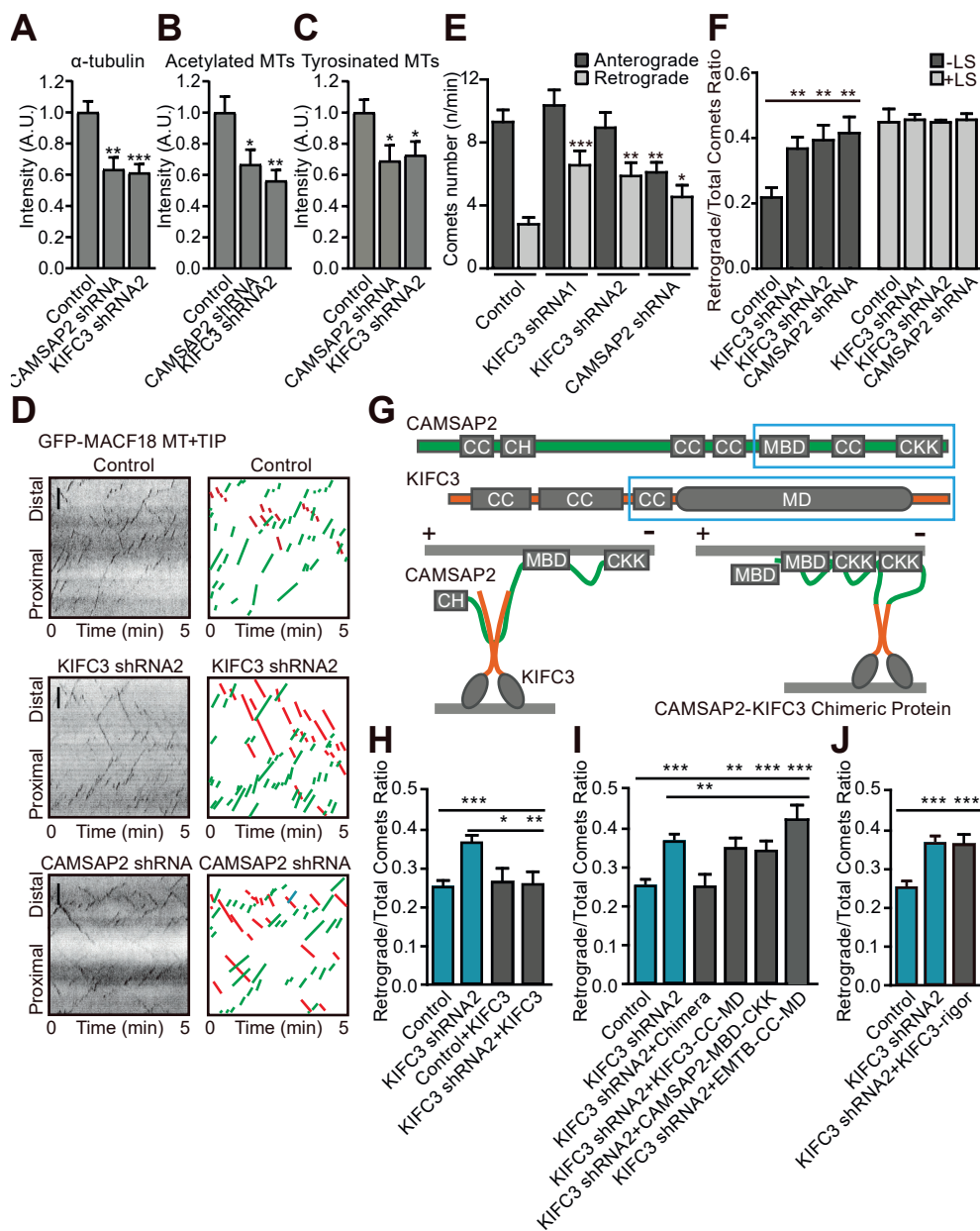
to generate new plus-ends (Yau et al., 2014). This showed no difference in microtubule orientation between Control, KIFC3 and CAMSAP2 depleted neurons (Figure 3F). To determine whether the KIFC3-CAMSAP2 interaction is important to regulate microtubules dynamics, we generated a CAMSAP2-KIFC3 chimeric construct, which is a direct fusion between the CAMSAP2 minus-end binding domain (CAMSAP-MD-CKK) and the KIFC3 the third coiled-coil and motor domain and (KIFC3-CC-MD) (Figure 3G). While the individual KIFC3-CC-MD and CAMSAP2-MD-CKK constructs were not able to rescue the knockdown phenotype, the chimera fully rescued the microtubules dynamics alterations after KIFC3 depletion (Figure 3I). These results suggest that the KIFC3-CAMSAP2 interaction is required for proper microtubule dynamics in dendrites.

KIFC3 prevents microtubule mobility in dendrites

We next tested whether KIFC3 and CAMSAP2 control the stability of microtubule bundles in dendrites. Neurons were transfected with photoactivatable GFP-α-tubulin, mCherry-α-tubulin and either Control, KIFC3 or CAMSAP2 shRNA. Segments of 15 µm in the middle of the dendrites were photoactivated and imaged over 3 hours (Figure 4A, 4C and Video S3). In wild-type neurons, retrograde displacement of the photoconverted region was observed, only ~25% of the neurons displayed microtubule bundle elongation (longer than 0.8µm elongation) of the photoconverted region (Figure 4B). However, upon KIFC3 or CAMSAP2 knockdown the dendritic microtubule bundles became dynamic; in ~80% of the neurons the photoactivated region elongated and moved towards the soma (Figure 4A-C and Figure S3D-J). The microtubule displacement can be rescued by KIFC3 or KIFC3-CAMSAP2 chimera expression (Figure 4D). These data suggest that the interaction between KIFC3 and CAMSAP2 immobilizes microtubule arrays in dendrites (Figure 4E). We next tested the KIFC3-rigor mutant and microtubule stabilization agent Taxol treatment in these experiments. Interestingly, both conditions could rescue the displacement phenotype (Figure 4D), suggesting KIFC3 motor activity is not required for microtubule crosslinking and bundling. All together, these results suggest KIFC3 and CAMSAP2 are important for microtubule stabilization and immobilization in dendrites.
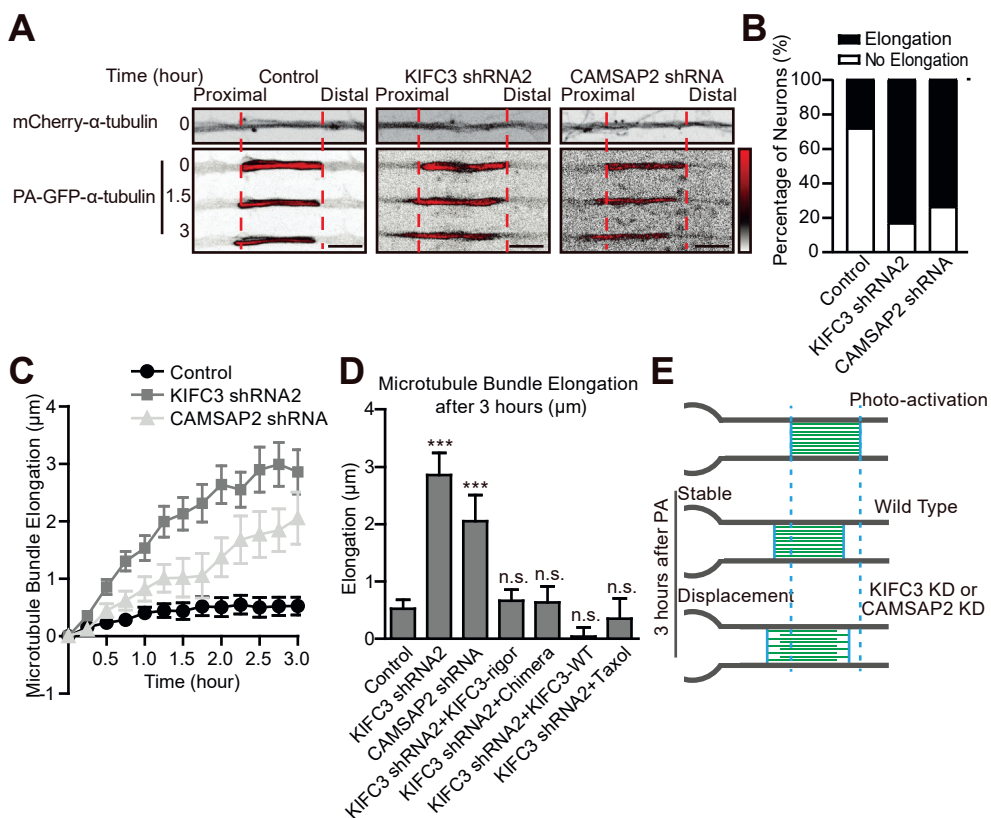
Figure 4. Dendritic microtubules become more dynamic with KIFC3 or CAMSAP2 depletion.

(A) Representative images of dendrites of hippocampal neurons DIV12 transfected with mCherry-α-tubulin, photoactivated GFP-α-tubulin together with pSuper-scrambled Control or KIFC3 shRNA2 or CAMSAP2 shRNA (Video S3). Time is indicated at the left of each image. PA-GFP channel was indicated in Black and Red, and LUT was shown from the right. Red dash lines indicate the photoactivated microtubule region. Scale bar=5μm.

(B) Quantification of the percentage of the neurons described in (A) in which the photoconverted region elongated.

(C) Quantification of microtubule bundle elongation. Other measurements were shown in Figure S3D-J. Control: N=5, n=36; KIFC3 shRNA2: N=4, n=35; CAMSAP2 shRNA: N=2, n=15. Error bars represent SEM.

(D) Quantification of microtubule bundle elongation 3 hours after photo-conversion corresponding to (A) and (C). KIFC3 shRNA2+KIFC3-rigor: N=2, n=20; KIFC3 shRNA2+KIFC3-Chimera: N=3, n=10; KIFC3 shRNA2+KIFC3-WT: N=3, n=12; KIFC3 shRNA2+Taxol: N=3, n=8. Error bars represent SEM. Columns were compared with Control. *p < 0.05; **p < 0.01; *** p < 0.001 (Unpaired T-test).

(E) Schematic graph of microtubule displacement in (A).

DISCUSSION

In epithelial cells, KIFC3 was found to localize to the zonula adherens (ZA), a specialized cadherin-based structure found at the contacts between cells (Meng et al., 2008). The localization of KIFC3 depends upon pleckstrin homology domain-containing family A member 7 (PLEKHA7), CAMSAP3 and microtubules. Depletion of any of these factors resulted in disorganized ZA, suggest that KIFC3 may provide a structural link between microtubules and the ZA at epithelial cell-cell junctions (Meng et al., 2008). Alternatively, KIFC3 may play a role in cargo transport required for ZA formation. Consistent with a role in trafficking in epithelial cells, KIFC3 has also been described to transport annexin XIIIb to the apical membranes and the ubiquitin-specific protease 47 (USP47) to the adherens junction (Noda et al., 2001; Sako-Kubota et al., 2014). Moreover, KIFC3 has been postulated to participate in positioning of the Golgi apparatus under cholesterol depleted conditions (Xu et al., 2002). Here we found that KIFC3 in neurons has a more structural role by working together with minus-end binding protein CAMSAP2 to organize dendritic microtubules.

The CAMSAP / Patronin / Nezha family has been characterized previously and found to specifically recognize microtubule minus-ends and stabilize microtubules against depolymerization (Akhmanova and Hoogenraad, 2015). In Drosophila, the CAMSAP family member, named Patronin, associates with free microtubule minus-ends and inhibits their disassembly by the action of the kinesin-13 microtubule depolymerase (Goodwin and Vale, 2010). In mammals, all three CAMSAP family members recognize growing microtubule minus-ends and CAMSAP2 and CAMSAP3 form stretches that are stably deposited on the MT lattice generated by minus-end polymerization (Hendershott and Vale, 2014; Jiang et al., 2014). In worms, loss of the CAMSAP homolog PTRN-1 caused alterations in neuronal morphology and synaptic vesicle localization (Borgen et al., 2019; Marcette et al., 2014; Richardson et al., 2014) and also affected the axonal regeneration after injury (Chuang et al., 2014). In mammalian neurons, CAMSAP may stabilize short microtubule stretches to serve as seeds for microtubule re-growth (Yau et al., 2014). We propose a model in which CAMSAP2 anchors KIFC3 at microtubule-minus ends and immobilizes microtubule arrays in dendrites.

KIFC1 has been found to slide microtubule during cell division (She and Yang, 2017). In vitro, KIFC1 could form bundles and aster shape microtubules by joining microtubule minus-ends together and create higher order microtubule organization the axonal microtubule (Norris et al., 2018). In neurons KIFC1 was found to organize axonal microtubules using a second microtubule binding domain (Muralidharan and Baas, 2019). Unlike KIFC1, KIFC3 does not have the second microtubule-binding domain required for crosslinking microtubules. The KIFC3 association with CAMSAP2 may provide the additional microtubule-binding site to form microtubule bundles. Recently it was suggested that KIFC3 may form a tetrameric kinesin through its tail interactions in vitro (Hata et al., 2019). The potential interaction between tertameric KIFC3 and CAMSAP2 is not inconsistent with our model. The KIFC3-rigor mutation was not able

to rescue the KIFC3 knock down phenotype, suggesting that KIFC3 motor activity is important for dendritic microtubule organization. The force generated by the KIFC3 motor domain may facilitate bundle formation and crosslink microtubules together. Microtubule bundling and crosslinking by the KIFC3-CAMSAP2 interaction could prevent microtubule sliding driven by other motor proteins. This model is consistent with the observation that microtubule mobility and sliding was increased in KIFC3 and CAMSAP2 depleted neuron.

Recent super-resolution experiments suggest that microtubule with the same orientation are bundled in dendrites (Tas et al., 2017). Stable and acetylated microtubules are mostly oriented minus-end out, while dynamic and tyrosinated microtubules are oriented oppositely. We found that KIFC3 prefers acetylated microtubules in dendrites, which suggests KIFC3 may recognize minus-end out microtubules. It is tempting to speculate that the KIFC3-CAMSAP2 interaction may preferentially stabilize minus-end out microtubules in dendrite. Consistently, in KIFC3 depleted neurons, microtubule acetylation was decreased and minus-end out microtubules showed increased dynamics. Some kinesins are reported to be directly sensitive for microtubule modifications, which may influence their activity in neurons (Ikegami et al., 2007; Sirajuddin et al., 2014). However, building a coherent model of how microtubule modifications influence KIFC3 function and microtubule organization will require additional work.

Together our data provide new insights in dendritic microtubule organization. We propose a model in which CAMSAP2 anchors KIFC3 at microtubule-minus ends to immobilize microtubule arrays in dendrites. Parallel mechanisms could play additional roles in organizing microtubule dynamics. For example, recently APC2, the brain-specific homolog of tumor-suppressor protein adenomatous polyposis coli (APC), has been shown to promote minus-end out microtubule dynamics in dendrites (Kahn et al., 2018). Recent developments in super-resolution and single-molecule imaging techniques could be applied to further investigate neuronal microtubule structure.

2

ACKNOWLEDGEMENTS

AUTHOR CONTRIBUTIONS

Y.C. designed and performed the experiments, analyzed results and wrote the manuscript; J.L. initiated the project and designed KIFC3 shRNAs; R.S. performed the mass spectrometry experiment; R.T. helped with super-resolution imaging; M.B. helped with the microtubule severing experiment in COS7 and PEX imaging and quantification; L.W. and S.P. performed ex vivo electroporation and organotypic slice cultures; X.P. performed immunohistochemistry staining, imaging and quantification for ex vivo experiments; J.W. helped with the CRISPR KI plasmid cloning; H.M., M.A. and L.K. gave valuable advise; M.H. and C.C.H. designed the experiments, supervised the research, and wrote the manuscript.

DECLARATION OF INTERESTS

Casper Hoogenraad is an employee of Genentech, Inc., a member of the Roche group. The authors declare that they have no additional conflict of interest.

LEAD CONTACT AND MATERIALS AVAILABILITY

Plasmids generated in this study are available on request. Further information and requests for resources and reagents should be directed to and will be fulfilled by the Lead Contact, Casper Hoogenraad (c.hoogenraad@uu.nl).

EXPERIMENTAL MODEL AND SUBJECT DETAILS

Animals

All animal experiments were performed in compliance with the guidelines for the welfare of experimental animals issued by the Federal Government of the Netherlands, and were approved by the Animal Ethical Review Committee (DEC) of Utrecht University (permit number 2014.I.03.020 and AVD1080020173404).

Cell line culture and transfection

HEK 293T were used for biochemistry experiments and cultured in DMEM/Ham's F10 (50:50) supplemented with 10% FCS and 1% penicillin/streptomycin at 37 °C and 5% CO2. HEK cells were transfected with PEI (Polyethylenimine HCl MAX Linear MW 40000 (PolySciences, 24765–2)). Cells were spitted 24hour before transfection with 1:3 dilutions. The next day, PEI (1 µg/µL): DNA (1 µg/µL) (3:1) were mixed in Ham's F10 and incubated for 5 minutes at room temperature. The mixture was added to cells and incubated overnight. Cells were harvest after 24 hours for the pull-down experiments.

COS7 cells were used for localization studies and cultured in DMEM supplemented with 10% FCS and 1% penicillin/streptomycin at 37 °C and 5% CO2. For immunocytochemistry experiments, COS7 cells were transfected with FuGENE6. Cells were spitted 24hour before transfection with 1:5 dilutions. The next day, Fugene6: DNA (1 µg/µL) (3:1 vol) were mixed in DMEM and incubated for 5 minutes at room temperature. The mixture was added to cells with DMEM empty medium and incubated for 30mins. Then, the empty medium was replaced by the full culture medium. Cells were fixed after 24 hours for staining and imaging. All cell lines were routinely tested negative for mycoplasma.

Primary neuron culture and transfection

Primary hippocampal neurons were prepared from embryonic 18 rat brain, dissociated with Trypsin at 37 degree and plated on coverslips pre-coated with Poly-L-lysine (37.5 µg/ml, Sigma) and Laminin (1.25µg/ml, Sigma). Neurons were cultured in Neurobasal medium (Invitrogen) containing 2% B27 (Invitrogen), 0.5 mM glutamine (Invitogen), 15.6 µM glutamate (Sigma) and 1% penicillin/streptomycin (Invitrogen) at a density of 100,000/coverslip.

All neurons were transfected with Lipofectamine 2000 (ThermoFisher, 11668019) mixed with proper DNA. For knock-down experiments, neurons were transfected 3 days before fixation with 1.5 µg shRNA constructs and 0.5 µg pβactin-GFP construct as fill or 0.25µg GFP-MT+TIP to visualize microtubule plus-end tips per well. And for normal over expression experiments, neurons were transfected 24 hours before fixation with 1µg in total specified constructs. First, neurons were incubated with the mixture in NB with 15.6µM glutamate at 37 °C in 5% CO2 for 45 minutes. Washed once with NB and then neurons were transferred to their original medium.

Neuron transfected with CRISPR knock-in construct at DIV4 and fixed at DIV11. GFP was knocked in rat genomic DNA after KIFC3 coding sequence. GFP antibody

was used to enhance signal and Trim46 were stained to visualize AIS.

Ex vivo electroporation and organotypic brain slice cultures

Pregnant C57Bl/6 mice at E14.5 were sacrificed by cervical dislocation. Embryonic mice brains were electroporated with 1.5μl DNA mixture containing a MARCKS-GFP together with pSuper-scrambled, KIFC3 shRNAs, or KIFC3 shRNA in the presence of KIFC3 as rescue. The DNA mix was dissolved in MQ with 0.05% FastGreen FCF Dye (Sigma) and injected in the lateral ventricles of the embryonic brains by using borosilicate glass micro-pipettes (World Precision Instruments) and a PLI-100A Picoliter Microinjector (Warner Instruments). The electroporation was conducted using platinum plated electrodes (Nepagene) with an ECM 830 Electro Square Porator (Harvard Apparatus) which was set to 3 unipolar pulses of 100ms at 30V with 100ms intervals. Embryonic brains were then isolated and collected in ice-cold cHBSS, embedded in 3% SeaPlaque GTG Agarose (Lonza) in cHBSS and sectioned coronally into 300μm thick slices using a VT1000 S Vibratome (Leica). Slices were collected on Poly-L-lysine and Laminin-coated culture membrane inserts (Falcon), placed on top of slice culture medium (70% v/v Basal Eagle Medium, 26% v/v cHBSS, 20mM D-glucose, 1mM L-glutamine, 0.1 mg/mL penicillin/streptomycin) and cultured 4 days prior to fixation.

METHOD DETAILS

DNA and shRNA constructs

CAMSAP2 shRNA has been previously described (Yau et al., 2014). All KIFC3 shRNAs target sequences and CRISPR KI target sequences were shown in Table S2.

Bio-mCherry (Wu et al., 2016) and Bio-GFP-N1 (Jiang et al., 2012) vectors are gifts from Dr. Anna Akhmanova (Utrecht University). The following plasmids have been described: pβactin-GFP, pGW1-GFP (Kapitein et al., 2010a), pSuper vector (Brummelkamp et al., 2002), pβactin-GFP-FRB, pGW1-PEX-RFP-FKBP (Kapitein et al., 2010b), protein-biotin ligase BirA (Lansbergen et al., 2006), GFP-MT+TIP, mCherry-α-tubulin, GFP-CAMSAP1, GFP-CAMSAP2, GFP-CAMSAP3, GFP-CAMSAP2-CC-CKK and 3GFP-CAMSAP2 has been described (Yau et al., 2014).

For the dox-inducible PA-GFP-α-tubulin construct, Transactivator (rtTA2-M2) is taken from pSIN-TRE-S (Schatzle et al., 2016) and it is inserted after CMV promoter. α-Tubulin with photoactivatable GFP tag is sub-cloned from PA-GFP-α-tubulin construct described before (Kuijpers et al., 2016).

CAMSAP2 truncations and KIFC3-CAMSAP2 chimera construct was cloned by a PCR-base strategy into pGW1-GFP vector. All KIFC3 constructs were generated from Mouse KIFC3 (NM_001145832) (IMAGE:6810893) and cloned by a PCR-base strategy into a Bio-mCherry vector or Bio-GFP-N1 vector.

EMTB-CC-MD chimera construct was cloned by a PCR-base strategy into Bio-mCherry vector. EMTB domain was taken from EMTB-3GFP (Addgene plasmid #26741)(Miller and Bement, 2009). The motor domain was taken from Mouse

KIFC3 full length (NM_001145832) (IMAGE:6810893).

Coiled coil regions were identified in the protein structure of kinesins using COILS prediction software (www.ch.embnet.org/software/COILS_form.html). Gibson assembly system was applied to produce KIFC3-rigor (396T>N) construct. KIFC3-CC-MD-WT and KIFC3-CC-MD-rigor was cloned by PCR into pβactin-GFP-FRB vector.

PCR-base strategy was used and the KIFC3 fragment carrying mutations was cloned into Bio-mCherry vector. The mutations for cloning mouse shRNA resistant KIFC3 didn't lead to amino acid change. The primers were shown in Table S2.

Antibody and reagents
The following antibodies were used for the immunofluorescence staining: mouse anti-α-tubulin (1:800, Sigma-Aldrich, T-5168), mouse anti-acetylated-tubulin (1:400, Sigma-Aldrich, T7451), rat anti-tyrosinated-tubulin (1:400, Abcam, ab6160), chicken anti-MAP2 (1:1,000, Abcam, ab5392), chicken anti-GFP (1:1000, Aves Labs, GFP-1020), rabbit anti-CAMSAP2 (1:200, Proteintech, 17880-1-AP), rabbit anti-KIFC3 (1:400 Santa Cruz, sc-134681), rabbit anti-TRIM46 (van Beuningen et al., 2015); mouse anti-MAP2 (1:600, Sigma-Aldrich, M9942) and rabbit anti-mCherry/RFP (1:1,000, Rockland, 600-401-379).

Secondary antibodies were used at 1:1,000 concentrations as follows: Alexa Fluor 405-, Alexa Fluor 488-, Alexa Fluor 568-, Alexa Fluor 647-conjugated secondary antibodies (Life Technologies).

The following antibodies were used for Western blot: mouse anti-mCherry (1:1,000 Clonetech, 632543); rabbit anti-GFP (1:2,500 Abcam, ab290); IRDye 680LT-(1:20,000) and IRDye 800CW-conjugated (1:15,000) secondary antibodies (LI-COR Biosciences).

Other reagents used in this study include: Doxycyclin (0.5µg/ml, Sigma-Aldrich), Lipofectamine2000 (Thermofiser, 11668019), PEI (PolySciences, 24765–2), FuGENE 6 (Roche, Cat#11836145001), Vectashield mounting medium (Vectorlabs, H-1000) and Mowiol mounting medium (10% Mowiol 4-88, 25% Glycerol, 0.1M Tris-Cl (0.2M, pH8.5) and 2.5% DABCO).

Biotin-streptavidin pull-down and western blot
Streptavidin pull-down assays were performed by using Dynabeads M-280 streptavidin beads (Invitrogen). For normal pull down, HEK293 cells were transfected with overexpression constructs indicated in figure legend together with BirA. After 24 hours expression, cells were harvested in ice-cold PBS and lysed with lysis buffer (150 mM Tris-HCl pH 7.5, 150 mM NaCl, 1% Triton X-100 and 1x protease inhibitor cocktail). 80% of the total cell lysates were centrifuged at 13,000 rpm for 5 minutes and the supernatants were transferred and incubated with streptavidin beads which were already blocked by 0.2% Chicken Egg Albumine (Sigma). The left cell lysates were denatured with SDS/DTT sample buffer and used

as input. After 40 minutes incubation at 4 degree, beads was washed 5 times with normal washing buffer (100mM Tris pH7.5, 150 mM NaCl, 0.5% Triton X-100 and 0.5x protease inhibitor cocktail). Samples were eluted with SDS/DTT sample buffer and boiled for 5 minutes at 95 degree.

For the western blot assays, samples were loaded into 10% SDS-PAGE gels and transferred to nitrocellulose membrane. Membranes were blocked with 2% BSA (bovine serum albumin) in PBS/0.05% Tween 20. Primary antibodies were diluted in blocking buffer and incubated with the membranes overnight at 4°C, washed 3 times with PBS/0.05% Tween 20 and incubated with secondary IRDye 680LT or IRDye 800LT antibodies for 45 minutes at room temperature. Membranes were then washed 3 times with PBS/0.05% Tween 20 and scanned on Odyssey Infrared Imaging system (LI-COR Biosciences).

Biotin-streptavidin pull-down and Mass spectrometry

The first part of the Biotin-streptavidin pull-down for mass spectrometry is the same as the pull-down for protein interaction validation. But instead of 5 times normal wash buffer, 2 times high salt washing buffer (20 mM Tris pH 8.0, 500 mM KCl, 0.1% Triton X-100)   , 2 times low salt washing buffer (20 mM Tris pH 8.0, 100 mM KCl and 0.1% Triton X-100)   and 2 times high salt washing buffer again were used to wash the bead. Brains were obtained from female adult rats and homogenized in tissue lysis buffer (50 mM Tris HCl, 150 mM NaCl, 0.1% SDS, 0.2% NP-40, and protease inhibitors). Brain lysates were centrifuged at $16,000 \times g$ for 15 minutes at 4°C, and the supernatant was then incubated for 1 hour at 4°C with beads previously conjugated with the protein of interest. After second incubation of 1 hour at 4 degree, beads were washed 5 times with normal washing buffer.

For MS analysis, the beads were resuspended in 15 μl of Laemmli Sample buffer (Biorad), boiled at 99ºC for 10 minutes and supernatants were loaded on 4-12% Criterion XT Bis-Tris precast gel (Biorad). The gel was fixed with 40% methanol and 10% acetic acid and then stained for 1h using colloidal coomassie dye G-250 (Gel Code Blue Stain Reagent, Thermo Scientific). Each lane from the gel was cut in 3 slices, destained and digested using trypsin. In brief, each lane from the gel was cut into three pieces and placed in 0.5ml tubes. Gel pieces were then washed with 250 μl of water, followed by 15 minutes dehydration in acetonitrile. Proteins were reduced (10 mM dithiothreitol, 1h at 56°C), dehydrated and alkylated (55 mM iodoacetamide, 1h in the dark). After two rounds of dehydration, trypsin (Promega) was added to the samples (20 μl of 0.1 mg/ml trypsin in 50 mM Ammoniumbicarbonate) and incubated overnight at 37°C. Peptides were extracted with ACN, dried down and reconstituted in 10% formic acid prior MS analysis. (Cunha-Ferreira et al., 2018; Kevenaar et al., 2016).

Immunofluorescence fixation and staining

Extraction, fixation and immunocytochemistry were performed as previously described (Chazeau et al., 2016). For COS7 without staining, cells were fixed in 4% paraformaldehyde, washed 3 times in PBS. For COS7, which need to be stained, cells were further permeabilized with 0.25% Triton X-100, blocked with 2% w/v

bovine serum albumin (BSA) in PBS and incubated with primary antibodies in PBS with 2% BSA overnight at 4 degree.

For neurons, cells were fixed with 4% PFA (paraformaldehyde) for 10-15 minutes, washed 3 times with PBS (phosphate buffer saline), and incubated with primary antibodies in GDB buffer (0.2% BSA, 0.8 M NaCl, 0.5% Triton X-100, 30 mM phosphate buffer) overnight at 4 degree. For super-resolution imaging, cells were incubated for 90 s in an extraction buffer preheated at 37°C (80 mM pipes, 2 mM MgCl2, 1 mM EGTA, 0.3% Triton X100 and 0.25% glutaraldehyde, pH 6.9), followed by incubation with 4% PFA preheated at 37°C for 10 minutes. Neurons were further permeabilized with 0.25% Triton X100 and blocking was performed with 2% w/v bovine serum albumin (BSA), in PBS, pH 7.4. Primary antibodies were incubated overnight at 4 degree in blocking buffer.

For neurons and COS7, secondary antibodies were incubated 1 hour at room temperature. Mowiol or Vectashield mounting medium was used for mounting.

Slice immunofluorescence and imaging

Organotypic slices were fixed with 4% paraformaldehyde in PBS. Fixed slices were then permeabilized and blocked in 10% normal goat serum/0.2% Triton X-100/PBS. GFP signal was amplified by incubating with anti-GFP antibody overnight, followed by secondary Alexa 488 antibody and DAPI incubation overnight. Slices were washed 4 times for 15 min in PBS. Slices were mounted using Vectashield mounting medium (Vector Laboratories) with DAPI. Z-stack acquisitions were taken along dorsal telencephalon covering the transfected area using a LSM700 (Zeiss) confocal microscope equipped with a Plan-Apochromat 20x NA 0.8 objective with a 0.5x magnification.

Laser Scanning Confocal and STED microscopy

After immunofluorescence staining, neurons and COS7 cells were imaged using Zeiss LSM700 confocal laser scanning microscope with 63x NA 1.4 oil objective. Gated STED imaging was performed with Leica TCS SP8 STED 3×microscope using HC PL APO ×100/1.4 oil STED WHITE objective.

Live cell imaging

All the live imaging was performed on a Nikon Eclipse TE2000E inverted microscope equipped with Evolve 512 EMCCD camera (Roper Scientific), spinning disk confocal (Roper Scientific), incubate chamber (Tokai Hit) and MetaMorph 7.7.5 software (Molecular Device) was used for all the live imaging experiments.

GFP-MT+TIP tracking

GFP-MT+TIP construct was co-transfected with proper shRNA in DIV9 neurons and imaged at DIV12. Around 20 μm region was selected from middle proximal dendrites and imaged with 1frame/second for 5 minutes. ImageJ plugin KymographWideSlice was used to analyse microtubule comets movement.

Photo-ablation experiments in neurons

A Teem Photonics 355 nm Q-switched pulsed laser was used for photo-ablation on the described spinning disk microscope. For microtubule orientation experiments, microtubules were photo-ablated in proximal dendrites and the 10μm region before and after was imaged with 1 frame/second for 5 minutes.

Microtubule photo ablation in COS7

COS7 cells were transfected with 3GFP-CAMSAP2 and mCherry-KIFC3. 100nM of SIR-tubulin (Spirochrome) was added to the medium and incubated overnight to visualize microtubules. Cells were imaged using Eclipse 80i(Nikon) microscope equipped with an Apo 100x 1.49 N.A. Oil objective Photometrics Evolve 512 EMCCD camera (Roper scientific) and perfect focus system and iLas2 laser illumination system (Roper Scientific France).

The 532nm Q-switched pulsed laser (Teem Photonics) was used for photoablation. Microtubules were severed using 532 nm laser and then imaged with 7 sec intervals for total 5 min to track CAMSAP2 and KIFC3 localization at microtubule minus end.

Photoactivation experiments

The Dox-inducible PA-GFP-α-Tubulin with proper shRNAs was co-transfected in DIV9 neurons and Doxycycline was added the next day. Neurons were imaged at DIV12. Photoactivation of PA-GFP-α-Tubulin was performed on the FRAP setup and 405 nm laser was used for activation. Around 15μm regions were selected from middle dendrite and it was imaged every 15minutes for 3 hours. The elongation of the selected region during imaging is regarded as microtubule sliding.

QUANTIFICATION AND STATISTICAL ANALYSIS

All statistical details including the definitions of n, numbers of n and statistical tests performed can be found in each Figures and Figure legends. GraphPad were used for graphs and statistics. T-test (column graph) or 2-way Anova (line graph) test was performed for statistics and $p<0.05$ was considered significant (*$p < 0.05$; **$p < 0.01$; *** $p < 0.001$.). Image processing and analysis were performed by using ImageJ. Secondary structure of KIFC3 was defined by using SMART (Simple Modular Architecture Research Tool; at EMBL) and COILS (Prediction of coiled coil regions in proteins, Lupas's method, at EMBnet-CH).

Sholl analysis

ImageJ plug-in, Sholl analysis and NeuronJ(Meijering et al., 2004), was used for neuron morphology analysis. The distance is measured from outer edge of soma. The interval is 5μm and 4 data points were averaged for line graph.

Quantification of ex vivo neuronal migration and morphology.

The relative positions of the cell bodies of GFP-positive neurons along the radial axis starting from 30% above ventricular to pial surface were measured by Image J

plugin (Analyze Particle). The relative position of neurons in the regions of interest was recorded in terms of distance between the ventricular and the pial surface. The positional information of all transfected neurons, together with the top (pial surface) and bottom (ventricular surface) boundaries were exported to Excel. Based on the relative position of each neuron and the total numbers of neurons counted, the radial cell distribution along the radial axis was obtained by further data processing using an Excel macro and presented as percentage of migration.

Regions representing 20% of the cortical width below the pial were cropped for morphology analysis. Neurons were classified into 4 types: type 1 with no leading process, type 2 with 1 leading process, type 3 with secondary branches, type 4 with branches over 2. Counting was performed using Image J plugin (Analyze Particle).

Mass spectrometry analysis

All samples were analyzed with an Agilent 1290 Infinity LC (Agilent Technologies), operating in reverse-phase (C18) mode, coupled to a TripleTOF 5600 (Ab Sciex). Peptides were loaded onto a trap column (Reprosil pur C18, Dr. Maisch, 100 µm x 2 cm, 3 µm; constructed in-house) with solvent A (0.1% formic acid in water) at a maximum pressure of 800 bar and chromatographically separated over the analytical column (Poroshell 120 EC C18, Agilent Technologies, 50 µm x 50 cm, 2.7 µm) using 90 minutes linear gradient from 7-30% solvent B (0.1% formic acid in acetonitrile) at a flow rate of 150 nL/min. MS spectra (350-1250 m/z) were acquired in high-resolution mode (R > 30,000), whereas MS2 was in high-sensitivity mode (R > 15,000). For data analysis, raw files were processed using Proteome Discoverer 1.4 (version 1.4.1.14, Thermo Scientific). Database search was performed using the Uniprot rat database and Mascot (version 2.5.1, Matrix Science, UK) as the search engine. Carbamidomethylation of cysteines was set as a fixed modification and oxidation of methionine was set as a variable modification. Trypsin was set as cleavage specificity, allowing a maximum of 2 missed cleavages. Data filtering was performed using a percolator, resulting in 1% false discovery rate (FDR). Additional filters were search engine rank 1 and mascot ion score >20.

Analysis of polarity index

KIFC3 and truncations were expressed in DIV10 neurons, fixed at DIV11, stained for TRIM46 as axon marker. Average intensity of 15 µm in the proximal axon or dendrite was measured. At least 2 dendrites were included, and background was subtracted. Polarity index was calculated with the formula: $PI = (Ia-Id)/(Id+Ia)$. Id corresponds to mean dendrite intensity, while Ia is the mean proximal axon intensity. $PI > 0$ indicates the polarization is biased toward axon and $PI < 0$ to the dendrite.

Microtubule ablation in COS7

Images were processed using FIJI software. Background intensity was subtracted from each frame of the time-lapse movies. Gaussian Blur filter of 2 pixels was applied. After microtubule severing, ROI of 10x10 pixels was selected at the end of the microtubule minus end to measure the intensity of CAMSAP2 and KIFC3 in each frame. Intensity was normalized to the maximum value of the time-

lapse acquisition. For plotting (Figure 2M) moving time average of 5 frames was calculated.

PEX quantification

At least, six cells were analyzed per condition. Images were processed for background subtraction. Cell contour was manually traced using the motor channel and cell center was determined. Peroxisome distribution was measured by radial intensity analysis. The radius of the circle containing up to 90% peroxisome intensity was determined and was normalized by radius of the circle containing the entire cell. The normalized radius was used as the parameter for peroxisome distribution in Figure S3C.

DATA AND CODE AVAILABILITY

The published article includes all datasets generated or analyzed during this study. Additional requests should be sent to the Lead Contact, Casper Hoogenraad

REFERENCES

Akhmanova, A., and Hoogenraad, C.C. (2015). Microtubule minus-end-targeting proteins. Curr Biol 25, R162-171.

Borgen, M.A., Giles, A.C., Wang, D., and Grill, B. (2019). Synapse maintenance is impacted by ATAT-2 tubulin acetyltransferase activity and the RPM-1 signaling hub. Elife 8.

Braun, M., Drummond, D.R., Cross, R.A., and McAinsh, A.D. (2009). The kinesin-14 Klp2 organizes microtubules into parallel bundles by an ATP-dependent sorting mechanism. Nat Cell Biol 11, 724-730.

Brummelkamp, T.R., Bernards, R., and Agami, R. (2002). A system for stable expression of short interfering RNAs in mammalian cells. Science 296, 550-553.

Chazeau, A., Katrukha, E.A., Hoogenraad, C.C., and Kapitein, L.C. (2016). Studying neuronal microtubule organization and microtubule-associated proteins using single molecule localization microscopy. Methods Cell Biol 131, 127-149.

Chuang, M., Goncharov, A., Wang, S., Oegema, K., Jin, Y., and Chisholm, A.D. (2014). The microtubule minus-end-binding protein patronin/PTRN-1 is required for axon regeneration in C. elegans. Cell Rep 9, 874-883.

Cunha-Ferreira, I., Chazeau, A., Buijs, R.R., Stucchi, R., Will, L., Pan, X., Adolfs, Y., van der Meer, C., Wolthuis, J.C., Kahn, O.I., et al. (2018). The HAUS Complex Is a Key Regulator of Non-centrosomal Microtubule Organization during Neuronal Development. Cell Rep 24, 791-800.

Fink, G., Hajdo, L., Skowronek, K.J., Reuther, C., Kasprzak, A.A., and Diez, S. (2009). The mitotic kinesin-14 Ncd drives directional microtubule-microtubule sliding. Nat Cell Biol 11, 717-723.

Goodwin, S.S., and Vale, R.D. (2010). Patronin regulates the microtubule network by protecting microtubule minus ends. Cell 143, 263-274.

Hata, S., Pastor Peidro, A., Panic, M., Liu, P., Atorino, E., Funaya, C., Jakle, U., Pereira, G., and Schiebel, E. (2019). The balance between KIFC3 and EG5 tetrameric kinesins controls the onset of mitotic spindle assembly. Nat Cell Biol 21, 1138-1151.

Hendershott, M.C., and Vale, R.D. (2014). Regulation of microtubule minus-end dynamics by CAMSAPs and Patronin. Proc Natl Acad Sci U S A 111, 5860-5865.

Hirokawa, N. (1998). Kinesin and dynein superfamily proteins and the mechanism of organelle transport. Science 279, 519-526.

Ikegami, K., Heier, R.L., Taruishi, M., Takagi, H., Mukai, M., Shimma, S., Taira, S., Hatanaka, K., Morone, N., Yao, I., et al. (2007). Loss of alpha-tubulin polyglutamylation in ROSA22 mice is associated with abnormal targeting of KIF1A and modulated synaptic function. Proc Natl Acad Sci U S A 104, 3213-3218.

Jiang, K., Hua, S., Mohan, R., Grigoriev, I., Yau, K.W., Liu, Q., Katrukha, E.A., Altelaar, A.F., Heck, A.J., Hoogenraad, C.C., et al. (2014). Microtubule minus-end stabilization by polymerization-driven CAMSAP deposition. Dev Cell 28, 295-309.

Jiang, K., Toedt, G., Montenegro Gouveia, S., Davey, N.E., Hua, S., van der Vaart, B., Grigoriev, I., Larsen, J., Pedersen, L.B., Bezstarosti, K., et al. (2012). A Proteome-wide screen for mammalian SxIP motif-containing microtubule plus-end tracking proteins. Curr Biol 22, 1800-1807.

Kahn, O.I., Schatzle, P., van de Willige, D., Tas, R.P., Lindhout, F.W., Portegies, S., Kapitein, L.C., and Hoogenraad, C.C. (2018). APC2 controls dendrite development by promoting microtubule dynamics. Nat Commun 9, 2773.

Kapitein, L.C., Schlager, M.A., Kuijpers, M., Wulf, P.S., van Spronsen, M., MacKintosh, F.C., and Hoogenraad, C.C. (2010a). Mixed microtubules steer dynein-driven cargo transport into dendrites. Curr Biol 20, 290-299.

Kapitein, L.C., Schlager, M.A., van der Zwan, W.A., Wulf, P.S., Keijzer, N., and Hoogenraad, C.C. (2010b). Probing intracellular motor protein activity using an inducible cargo trafficking assay. Biophys J 99, 2143-2152.

Kevenaar, J.T., Bianchi, S., van Spronsen, M., Olieric, N., Lipka, J., Frias, C.P., Mikhaylova, M., Harterink, M., Keijzer,

2

N., Wulf, P.S., et al. (2016). Kinesin-Binding Protein Controls Microtubule Dynamics and Cargo Trafficking by Regulating Kinesin Motor Activity. Curr Biol 26, 849-861.

Kuijpers, M., van de Willige, D., Freal, A., Chazeau, A., Franker, M.A., Hofenk, J., Rodrigues, R.J., Kapitein, L.C., Akhmanova, A., Jaarsma, D., et al. (2016). Dynein Regulator NDEL1 Controls Polarized Cargo Transport at the Axon Initial Segment. Neuron 89, 461-471.

Lansbergen, G., Grigoriev, I., Mimori-Kiyosue, Y., Ohtsuka, T., Higa, S., Kitajima, I., Demmers, J., Galjart, N., Houtsmuller, A.B., Grosveld, F., et al. (2006). CLASPs attach microtubule plus ends to the cell cortex through a complex with LL5beta. Dev Cell 11, 21-32.

Marcette, J.D., Chen, J.J., and Nonet, M.L. (2014). The Caenorhabditis elegans microtubule minus-end binding homolog PTRN-1 stabilizes synapses and neurites. Elife 3, e01637.

Meijering, E., Jacob, M., Sarria, J.C., Steiner, P., Hirling, H., and Unser, M. (2004). Design and validation of a tool for neurite tracing and analysis in fluorescence microscopy images. Cytometry A 58, 167-176.

Meng, W., Mushika, Y., Ichii, T., and Takeichi, M. (2008). Anchorage of microtubule minus ends to adherens junctions regulates epithelial cell-cell contacts. Cell 135, 948-959.

Miller, A.L., and Bement, W.M. (2009). Regulation of cytokinesis by Rho GTPase flux. Nat Cell Biol 11, 71-77.

Muralidharan, H., and Baas, P.W. (2019). Mitotic Motor KIFC1 Is an Organizer of Microtubules in the Axon. J Neurosci 39, 3792-3811.

Nakata, T., and Hirokawa, N. (1995). Point Mutation of Adenosine Triphosphate-Binding Motif Generated Rigor Kinesin That Selectively Blocks Anterograde Lysosome Membrane-Transport. J Cell Biol 131, 1039-1053.

Noda, Y., Okada, Y., Saito, N., Setou, M., Xu, Y., Zhang, Z., and Hirokawa, N. (2001). KIFC3, a microtubule minus end-directed motor for the apical transport of annexin XIIIb-associated Triton-insoluble membranes. J Cell Biol 155, 77-88.

Norris, S.R., Jung, S., Singh, P., Strothman, C.E., Erwin, A.L., Ohi, M.D., Zanic, M., and Ohi, R. (2018). Microtubule minus-end aster organization is driven by processive HSET-tubulin clusters. Nat Commun 9, 2659.

Peterman, E.J., and Scholey, J.M. (2009). Mitotic microtubule crosslinkers: insights from mechanistic studies. Curr Biol 19, R1089-1094.

Richardson, C.E., Spilker, K.A., Cueva, J.G., Perrino, J., Goodman, M.B., and Shen, K. (2014). PTRN-1, a microtubule minus end-binding CAMSAP homolog, promotes microtubule function in Caenorhabditis elegans neurons. Elife 3, e01498.

Sako-Kubota, K., Tanaka, N., Nagae, S., Meng, W., and Takeichi, M. (2014). Minus end-directed motor KIFC3 suppresses E-cadherin degradation by recruiting USP47 to adherens junctions. Mol Biol Cell 25, 3851-3860.

Schatzle, P., Kapitein, L.C., and Hoogenraad, C.C. (2016). Live imaging of microtubule dynamics in organotypic hippocampal slice cultures. Methods Cell Biol 131, 107-126.

She, Z.Y., and Yang, W.X. (2017). Molecular mechanisms of kinesin-14 motors in spindle assembly and chromosome segregation. J Cell Sci 130, 2097-2110.

Sirajuddin, M., Rice, L.M., and Vale, R.D. (2014). Regulation of microtubule motors by tubulin isotypes and post-translational modifications. Nat Cell Biol 16, 335-344.

Suzuki, K., Tsunekawa, Y., Hernandez-Benitez, R., Wu, J., Zhu, J., Kim, E.J., Hatanaka, F., Yamamoto, M., Araoka, T., Li, Z., et al. (2016). In vivo genome editing via CRISPR/Cas9 mediated homology-independent targeted integration. Nature 540, 144-149.

Tas, R.P., Chazeau, A., Cloin, B.M.C., Lambers, M.L.A., Hoogenraad, C.C., and Kapitein, L.C. (2017). Differentiation between Oppositely Oriented Microtubules Controls Polarized Neuronal Transport. Neuron 96, 1264-1271 e1265.

van Beuningen, S.F.B., Will, L., Harterink, M., Chazeau, A., van Battum, E.Y., Frias, C.P., Franker, M.A.M., Katrukha, E.A., Stucchi, R., Vocking, K., et al. (2015). TRIM46 Controls Neuronal Polarity and Axon Specification by Driving the Formation of Parallel Microtubule Arrays. Neuron 88, 1208-1226.

Wu, J.C., de Heus, C., Liu, Q.Y., Bouchet, B.P.,

Noordstra, I., Jiang, K., Hua, S.S., Martin, M., Yang, C., Grigoriev, I., et al. (2016). Molecular Pathway of Microtubule Organization at the Golgi Apparatus. Developmental Cell 39, 44-60.

Xu, Y., Takeda, S., Nakata, T., Noda, Y., Tanaka, Y., and Hirokawa, N. (2002). Role of KIFC3 motor protein in Golgi positioning and integration. J Cell Biol 158, 293-303.

Yau, K.W., van Beuningen, S.F., Cunha-Ferreira, I., Cloin, B.M., van Battum, E.Y., Will, L., Schatzle, P., Tas, R.P., van Krugten, J., Katrukha, E.A., et al. (2014). Microtubule minus-end binding protein CAMSAP2 controls axon specification and dendrite development. Neuron 82, 1058-1073.

Zhang, Y., and Sperry, A.O. (2004). Comparative analysis of two C-terminal kinesin motor proteins: KIFC1 and KIFC5A. Cell Motil Cytoskeleton 58, 213-230.

2

SUPPLEMENTAL INFORMATION INVENTORY

Supplemental Figures S1-S3

Figure S1, related to Figure 1

Figure S2, related to Figure 3

Figure S3, related to Figure 4 and Figure 5

Video S1, related to Figure 3

Video S2, related to Figure 3
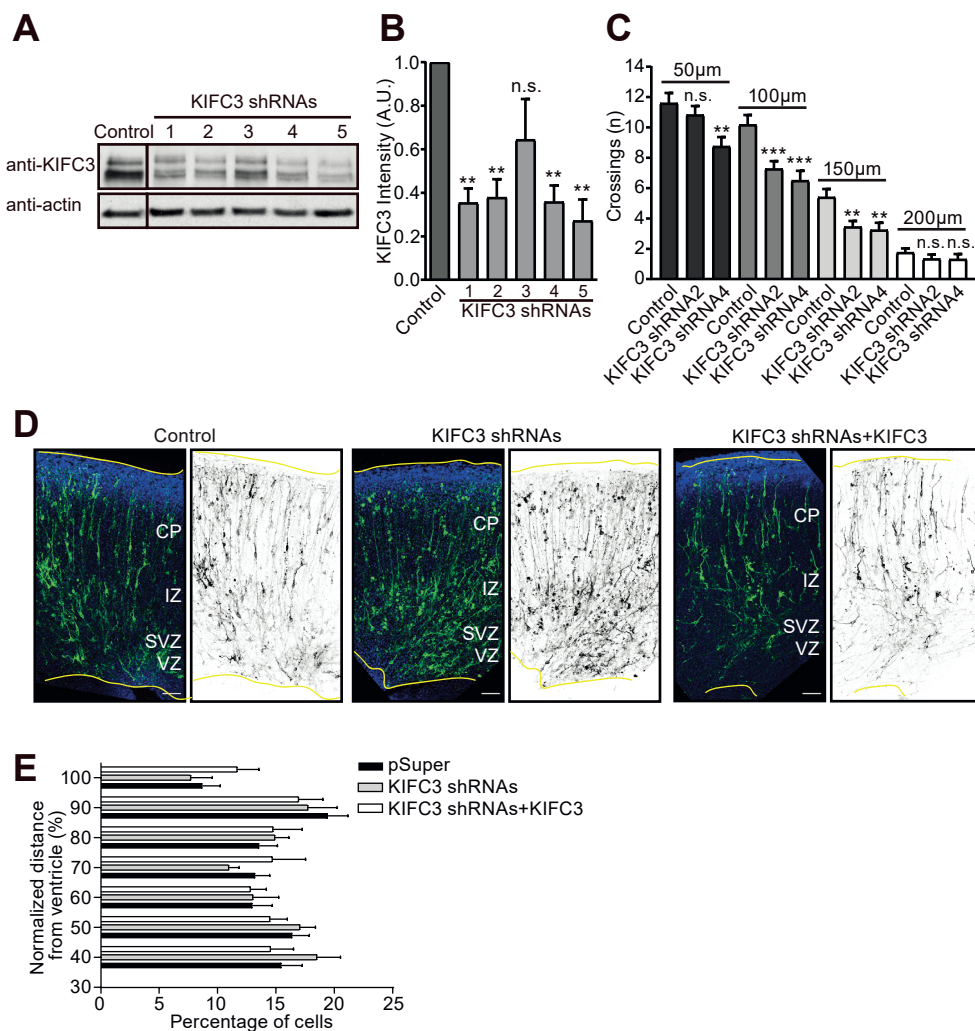
Video S3, related to Figure 5

2

Figure S1. KIFC3 is important for dendrite branching. Related to Figure 1.

(A) Example of a western blot of protein extracts of DIV 7 hippocampal neurons electroporated at DIV 0 with pSuper-scrambled as Control or KIFC3-shRNA1, 2 , 3, 4 and 5. Levels of actin were used as loading Control.

(B) Quantification of protein levels of KIFC3 of samples represented in (A) (N=3). Error bars represent SEM. *p < 0.05; **p < 0.01; *** p < 0.001 (Unpared T-test).

(C) Quantification of crossings from the sholl analysis in Figure 1B at 50µm, 100µm, 150µm and 200µm positions. Error bars represent SEM. Unpared T-test was performed and columns were compared with corresponding Control. *p < 0.05; **p < 0.01; *** p < 0.001.

(D-E) Representative images of mouse cortex after 4 days of ex vivo electroporated with GFP and pSuper-scrambled, KIFC3 shRNAs or KIFC3 shRNAs with KIFC3 as rescue. Left panels represent GFP and DAPI channels. DAPI is in blue and GFP is in Green. Pail surface at the top and ventricle at the bottom are outlined in yellow. CP, cortical plate; IZ, intermediate zone;SVZ, subventricular zone; VZ, ventricular zone. Right panels represent GFP only channel and GFP is in gray. Scale bars=50µm. Error bars represent SEM.

Figure S2. KIFC3 interacts with CAMSAP2. Related to Figure 2.

(A) Representative images of a COS7 cell transfected with KIFC3-GFP and stained with CAMSAP2 antibody. Scale bar=10μm.

(B) Schematic representation of CAMSAP2 truncation constructs used. CC: coiled-coiled domain, MD: motor domain, CH: Calponin-homology domain, MBD: microtubule binding domain, CKK: CKK domain.

(C) Representative images of a DIV7 neuron transfected with KIFC3-GFP and stained with CAMSAP2 antibody. Scale bar=5μm.

(D) Representative images of a DIV11 neuron transfected with the HITI CRISPR GFP knock-in construct and probed for CAMSAP2 and GFP (to enhance the signal in transfected cells). Scale bar=5μm.

(E-F) Representative images of COS7 cells transfected with GFP-CAMSAP2-FL or GFP and co-transfected with mCherry-KIFC3-N4 or mCherry-KIFC3-N5. Scale bar=10μm.

(G-J) Representative images of COS7 cells transfected with either mCherry or mCherry-KIFC3 together with GFP tagged CAMSAP2 truncations. Scale bar=10μm.
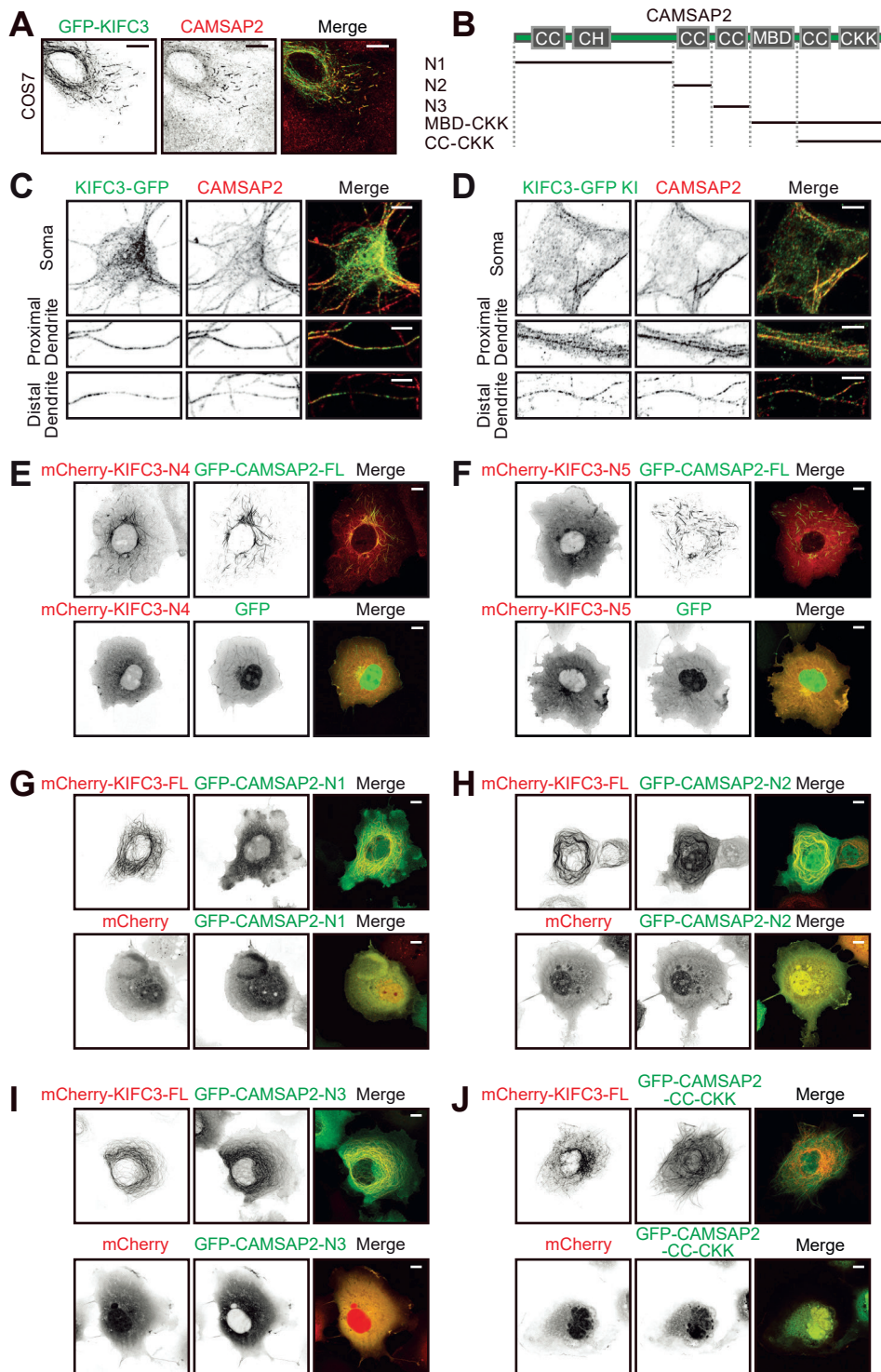
2

Figure S3. KIFC3-N1 shows dominant negative effect, KIFC3-rigor mutation validation and microtubule mobility rescue and quantification. Related to Figure 3 and Figure 4.

(A) Quantification of acetylated tubulin, tyrosinated tubulin levels in DIV11 neurons transfected with mCherry-KIFC3. Neighboring non-transfected neurons were used as Control. N=2. Control: n=22; mCherry-KIFC3: n=20. Error bars represent SEM. Unpared-T-test was performed and columns were compared with corresponding Control. *$p < 0.05$; **$p < 0.01$; *** $p < 0.001$.

(B) Representative images of COS7 cells transfected with either PEX-RFP-FKBP and KIFC3-CC-MD-GFP-FRB or PEX-RFP-FKBP and KIFC3-CC-MD Rigor (396T-N)-GFP-FRB. PEX-RFP-FKBP was used to visualize peroxisomes in cells. Scale bar=10 μm.

(C) Quantification of peroxisome redistribution in cells described in (B). KIFC3-MD-Rigor: N=1, n=7; KIFC3-MD-Rigor+Rapalog: N=1, n=6, KIFC3-MD-WT: N=1, n=6; KIFC3-MD-WT+Rapalog: N=1, n=12. Error bars represent SEM. *$p < 0.05$; **$p < 0.01$; *** $p < 0.001$ (Unpaired T-test).

(D) Quantification of microtubule elongation corresponding to Figure 4A, 4C and 4D. Control: N=5, n=36; KIFC3 shRNA2: N=4, n=35; KIFC3 shRNA2+KIFC3-rigor: N=2, n=20; KIFC3 shRNA2+KIFC3-Chimera: N=3, n=10; KIFC3 shRNA2+KIFC3-WT: N=3, n=12; KIFC3 shRNA2+Taxol: N=3, n=8. Error bars represent SEM.

(E-J) Quantification of microtubule movement of the left edge, right edge and middle position of the photo-converted region corresponding to Figure 4A, 4C and 4D. Error bars represent SEM.
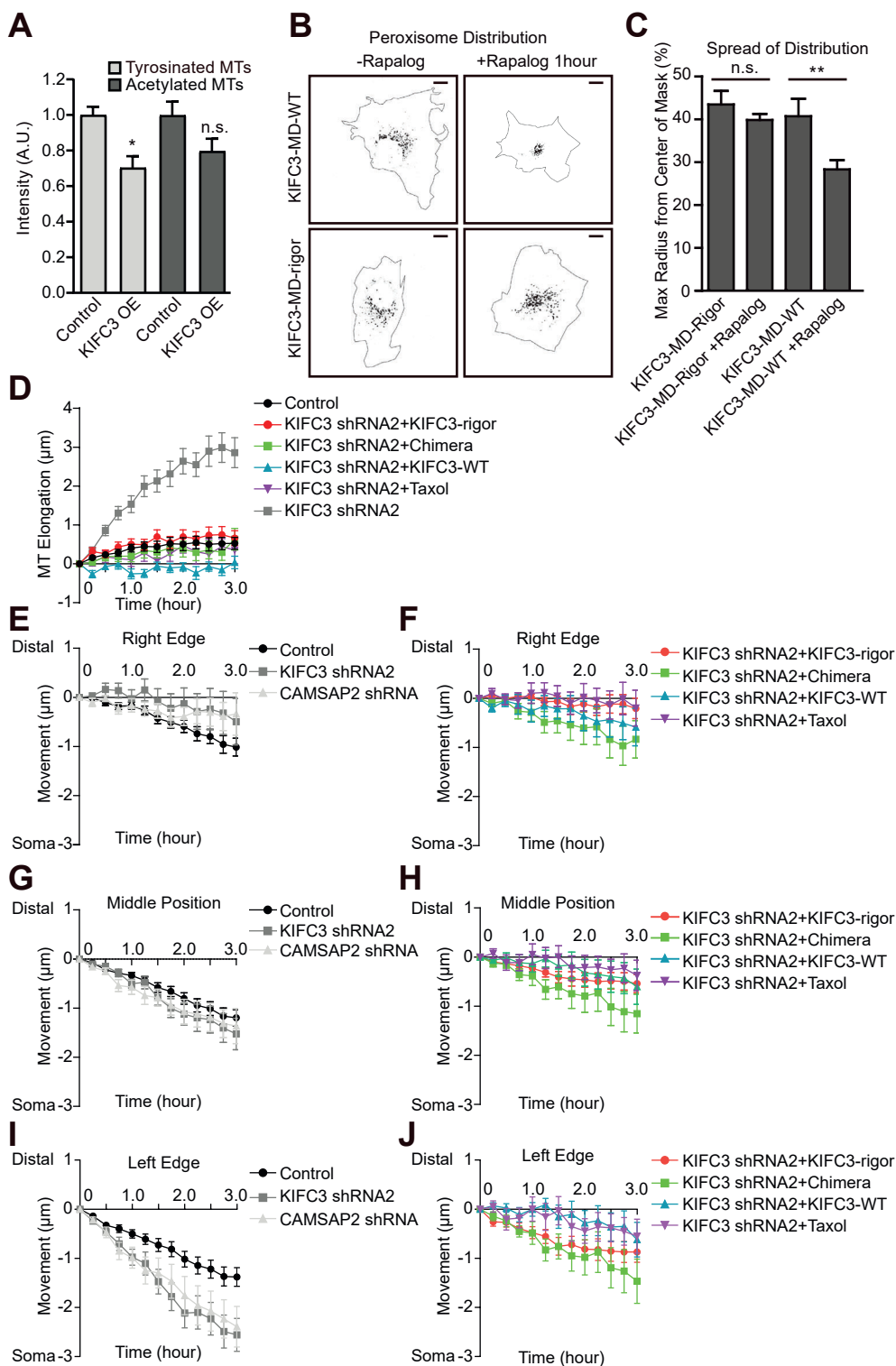
		Control		KIFC3-FL		KIFC3-N1		KIFC3-N3		
PROTID	Name	Peptides	PSM	Peptides	PSM	Peptides	PSM	Peptides	PSM	
Q4KLH6	CEP162	0	0	9	17	10	21	9	17	MT/Centrosome
Q63560	Map6	0	0	9	12	0	0	0	0	MT
D4AEC2	Camsap2	0	0	7	7	4	4	0	0	MT
Q63170	Dnah7	0	0	17	27	14	20	0	0	Dynein-ralated
E9PSL8	Kif6	0	0	6	37	1	32	5	48	Kinesin
G3V6L4	Kif5c	1	1	4	5	4	4	4	5	Kinesin
D3Z9C7	Piccolo	0	0	14	18	24	30	12	21	presynapse
F1M8A4	Liprinα	0	0	14	20	7	10	5	7	presynapse
Q9JIR4	Rims1	0	0	10	11	11	12	6	7	presynapse
F1M3B4	UNC13b/MUNC13	0	0	7	8	8	8	0	0	presynapse
R9PY00	Vamp2	0	0	5	5	4	4	0	0	presynapse
P21707	Synaptotagmin1	0	0	4	8	4	6	0	0	presynapse
B5DEH2	Erlin2	1	1	8	9	2	3	0	0	ER
D4ABS2	Dnml1	0	0	9	10	11	14	2	3	Membrane-related
O08679	Mark2	0	0	19	23	0	0	0	0	kinase
P63086	Mapk1	0	0	8	9	2	2	0	0	kinase
B5DFK6	Ap3d1	0	0	10	16	5	7	0	0	AP-3 complex
P62944	Ap2b1	0	0	15	18	6	9	3	3	AP-2 complex

Table S1. Mass Spectrometry Analysis of KIFC3 Interacting Proteins. Related to Figure 2.

Data from affinity purification mass spectrometry analyses (AP-MS) of KIFC3 and truncations in rat brain extracts. PROTID: Uniprot accession code; Name: corresponding gene name; Peptides: peptide matches; PSM: peptide spectrum matches.

Oligonucleotides	Source	Identifier
KIFC3 shRNAs and CRISPR KI target sequences		
pSuper-rat KIFC3 shRNA#1 targeting sequence: cgagaacccaggcattaat	This paper	N/A
pSuper-rat KIFC3 shRNA#2 targeting sequence: cagctccgggacaggttat	This paper	N/A
pSuper-rat KIFC3 shRNA#3 targeting sequence: ccacctgttaagtatgtca	This paper	N/A
pSuper-rat KIFC3 shRNA#4 targeting sequence: ctccctaaatcctatttaa	This paper	N/A
pSuper-rat KIFC3 shRNA#5 targeting sequence: cgcatcagctgacaataca	This paper	N/A
pSuper-mouse KIFC3 shRNA#1 targeting sequence: cagctccgtgacaagctgt	This paper	N/A
pSuper-mouse KIFC3 shRNA#2 targeting sequence: ggcttcaatgtctgtatct	This paper	N/A
pSuper-mouse KIFC3 shRNA#3 targeting sequence: ttccaaactcacctacctg	This paper	N/A
CRISPR KI rat KIFC3 targeting sequence: cggctgcagtttccttcgga	This paper	N/A
Primers for mouse shRNA resistant KIFC3		
P1-fw: tcgcggccgcctcgagctcaagcttatggtggaga	This paper	N/A
P1-rev: acagcttgtccctcaattggctgctctcctggctg	This paper	N/A
P2-fw: ccaattgagggacaagctgtcccagctgc	This paper	N/A
P2-rev: ggaacacgtcctgttggcttgcccacggggagaagacc	This paper	N/A
P3-fw: aagccaacaggacgtgttccaggaggtgcaggccctcattacctcctgcatcgatggatttaac	This paper	N/A
P3-rev: gttaaatccatcgatgcaggaggtaatgagggcctgcacctcctggaacacgtcctgttggctt	This paper	N/A
P4-fw: cctgcatcgatggatttaacgtctgtatctttgcttacggc	This paper	N/A
P4-rev: tcagcttgctattgcggaagggcacatg	This paper	N/A
P5-fw: cttccgcaatagcaagctgacctacctgctgcaggac	This paper	N/A
P5-rev: atcccgggcccgcggtaccgtcgactcaggctgacggctgcag	This paper	N/A

Table S2. Oligonucleotides. Related to Oligonucleotides section of the Key Resources Table of the STAR Methods.
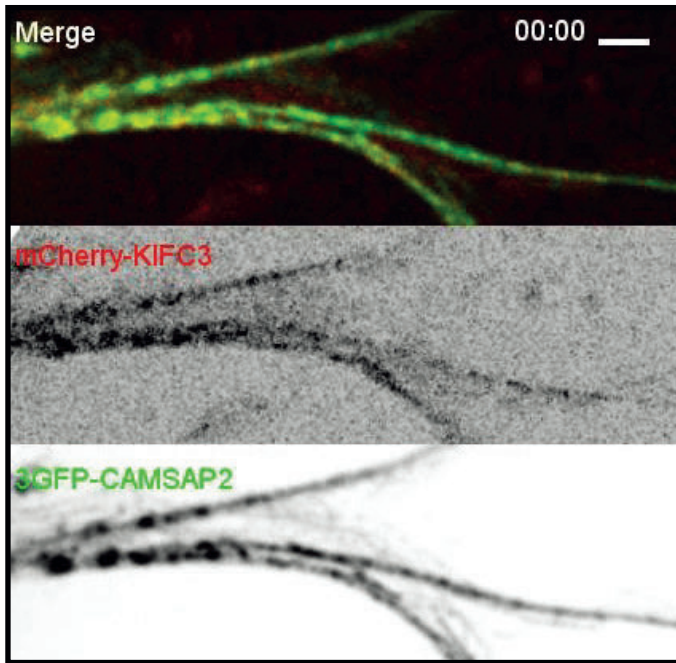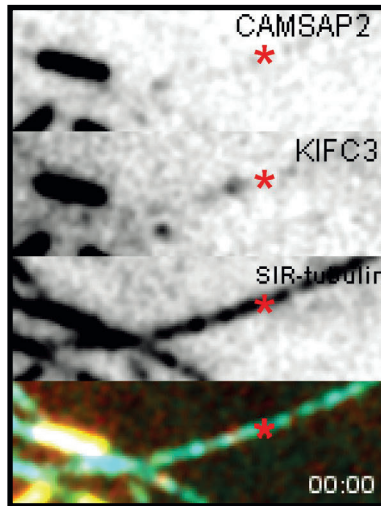
Video S1. Localization of KIFC3 in neurons, Related to Figure 2.

Representative movie of DIV12 neuron transfected with mCherry-KIFC3 and 3GFP-CAMSAP2. Total time is 5 minutes. 1 frame per second. Displayed at 24 frames per second. Scale bar=2 μm.

Video S1 can be accessed via the folloing QR code:

Video S2. KIFC3 Co-localizes with CAMSAP2 at Microtubule Minus Ends, Related to Figure 2.

Representative images of COS7, transfected with 3GFP-CAMSAP2 and mCherry-KIFC3. SIR-tubulin was applied to visualize microtubules. Microtubule photoablation was indicated by red stars. Minus end was indicated by white and black arrows. GFP-CAMSAP2 was shown in Green, mCherry-KIFC3 in Red and SIR-tubulin in Cyan. Total time is 5 minutes and 7 s per frame. Displayed at 15 frames per second.

Video S2 can be accessed via the folloing QR code:
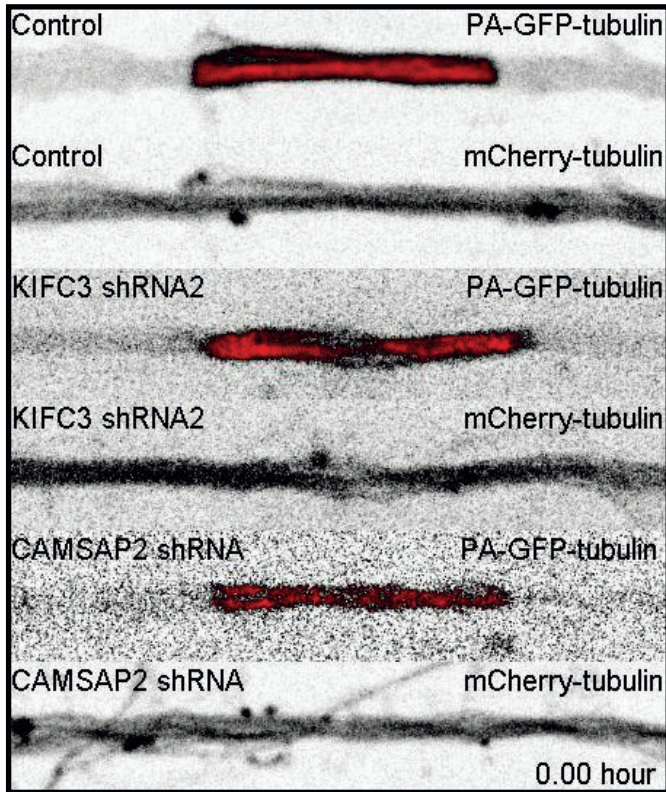
Video S3. Dendritic Microtubules Become More Dynamic with KIFC3 or CAMSAP2 Depletion, Related to Figure 4.

Representative images of dendrites of hippocampal neurons DIV12 transfected with mCherry-α-tubulin, photoactivated GFP-α-tubulin together with pSuper-scrambled Control or KIFC3 shRNA2 or CAMSAP2 shRNA. Images are acquired from a time series with 15min per frame for in total 3 hours. Around 15 μm region are photo-activated before imaging. Displayed at 15 frames per second.

Video S3 can be accessed via the folloing QR code:

Chapter 3

MAP7D2 Localizes to the Proximal Axon and Locally Promotes Kinesin-1-Mediated Cargo Transport into the Axon

Xingxiu Pan[1], **Yujie Cao[1]**, Riccardo Stucchi[1], Peter Jan Hooikaas[1], Sybren Portegies[1], Lena Will[1], Maud Martin[1], Anna Akhmanova[1], Martin Harterink[1,*], and Casper C. Hoogenraad[1,2,*]

[1]Cell Biology, Department of Biology, Faculty of Science, Utrecht University, 3584 Utrecht, the Netherlands

[2]Lead Contact

[*]Correspondence: c.hoogenraad@uu.nl

SUMMARY

The motor protein kinesin-1 plays an important role in polarized sorting of transport vesicles to the axon. However, the mechanism by which the axonal entry of kinesin-1 dependent cargo transport is regulated remains unclear. Microtubule associated protein Ensconsin/MAP7 is an essential kinesin-1 cofactor and promotes kinesin-1 recruitment to microtubules. Here, we found that MAP7 family member MAP7D2 concentrates at the proximal axon, where it overlaps with the axon initial segment and interacts with kinesin-1. Depletion of MAP7D2 results in reduced axonal cargo entry and defects in axon development and neuronal migration. We propose a model in which MAP7D2 in the proximal axon locally promotes kinesin-1 mediated cargo entry into the axon.

3

INTRODUCTION

The microtubule cytoskeleton and proper coordination over intracellular organelle transport are critically important for the development and function of neurons. Microtubules serve as tracks for long-distance cargo trafficking and have an intrinsic polarity that is recognized by molecular motors to transport cargo in a directional manner. Plus-end directed kinesin-1 motors selectively drive transport vesicles into axons and are required for polarized cargo sorting at the axon initial segment (AIS) (Farías et al., 2015; Kapitein et al., 2010). However, the mechanism by which the axonal entry of kinesin-1 dependent cargo transport is regulated remains unclear.

Several regulatory mechanisms have been proposed to contribute to polarized cargo trafficking. For instance, the preference of kinesin-1 for stable microtubules may contribute to sorting and trafficking of axonal cargo (Farías et al., 2015). By using optical nanoscopy, it was recently shown that within the mixed dendritic microtubule arrays stable microtubules are mostly oriented plus-end inwards and guide kinesin-1 motors out of dendrites (Tas et al., 2017). This particular microtubule organization favors kinesin-1 transport towards the axon, however additional sorting mechanisms may play a role at the proximal axon.

The microtubule associated protein ensconsin/MAP7 was described as an essential kinesin-1 cofactor by promoting kinesin-1 recruitment to microtubules (Barlan et al., 2013; Sung et al., 2008). Ensconsin/MAP7 is required for all known kinesin-1 dependent processes in polarized Drosophila oocytes (Metivier et al., 2018; Sung et al., 2008) and essential for kinesin-1 mediated myonuclear positioning in mammalian myotubes (Metzger et al., 2012). Moreover, ensconsin/MAP7 cooperates with kinesin-1 to transport cargo (Barlan et al., 2013) and triggers centrosome separation during interphase (Gallaud et al., 2014). The mammalian MAP7 family members include MAP7 (ensconsin, E-MAP-115), MAP7D1, MAP7D2 and MAP7D3. All family members share a highly conserved N-terminal coiled-coil motif, which interacts with microtubules and a conserved C-terminal MAP7 coiled-coil domain that is presumed to binds to kinesin-1. MAP7 and MAP7D1 are broadly expressed and have been described to play a role in neuronal developmental processes, including in axonal development in cultured neurons (Koizumi et al., 2017; Tymanskyj et al., 2017). MAP7D2 on the other hand is predominantly expressed in brain tissues (Niida and Yachie, 2011), however little is known about its localization and function in neuronal cells.

In this study, we show that MAP7D2 interacts with all three kinesin-1 family members and accumulates in proximal axon. We found that MAP7D2 localizes to the proximal axon through its N-terminal microtubule-binding domain. Depletion of MAP7D2 results in reduced axonal cargo entry and defects in axon formation and outgrowth during early stages of neuronal development. These data indicate that MAP7D2 is a local kinesin-1 regulator that promotes cargo entry into the axon.

3

RESULTS

MAP7D2 localizes to the proximal axon

To study the subcellular distributions of MAP7 family members in neurons, we first expressed mCherry tagged MAP7, MAP7D1, MAP7D2 and MAP7D3 in primary cultured hippocampal neurons (Figure 1A). Whereas MAP7 and MAP7D1 are mainly present in the somatodendritic compartment, MAP7D2 and MAP7D3 localize to the proximal axon overlapping with the axon initial segment (AIS) markers TRIM46 and AnkyrinG (AnkG) (Figure 1B). MAP7D2 is not abundant in other parts of the axon, evident by the lack of Tau colocalization (Figure 1C). Moreover, by labelling neurons with an antibody against MAP7 confirmed its the dendrite localization (Figure S1A), evident by the intensity of MAP7 decreasing in the TRIM46 positive axon and the polarity index being biased to dendrites (Figure S1B,C). These data suggest that MAP7 family members have a distinct distribution in neurons.

Since MAP7D3 is only expressed in non-brain tissues and MAP7D2 is specifically present in brain tissues (Niida and Yachie, 2011; Uhlén et al., 2015; Zhang et al., 2014), we decided to further investigate the neuronal function of MAP7D2. To study the localization of endogenous MAP7D2, we performed immunofluorescence labelling of cultured neurons. In agreement with the exogenous mCherry-MAP7D2 distribution, antibodies against endogenous MAP7D2 labelled the proximal axon overlapping with AnkG (Figure 1D) but also extends into the axon. The MAP7D2 antibody is highly specific, as it cannot recognize the overexpression of the other MAP7 proteins (Figure S1D). We did not detect any endogenous MAP7D3 in the proximal axon by labelling neurons with a MAP7D3 specific antibody (Figure S1E), and MAP7D3 is only present at microtubules in WT Hela cells but not in MAP7D3 KO Hela cells, while MAP7D2 is both absent in WT or MAP7D3 KO Hela cells (Figure S1F,G), again suggesting that MAP7D3 is only expressed in non-brain tissues where MAP7D2 is not expressed. Taken together, these data indicate that MAP7D2 is exclusively expressed in the proximal axon of hippocampal neuron.

Figure 1. MAP7D2 is enriched in proximal axon

(A) Schematic domain structure of human MAP7 family members. Numbers represent amino acids.

(B) DIV15 neurons expressing mCherry tagged MAP7 proteins and co-stained for AnkG (green), TRIM46 (blue). Bar graph shows the polarity index of MAP7 proteins together with AnkG and TRIM46 (n > 10 neurons in each group). Bottom panels are zooms of the proximal axons and line scans for the normalized intensity of each channel from soma to axon.

(C) DIV3 neurons expressing mCherry-MAP7D2 and stained for TAU (green). Line graphs of each channel are shown.

(D) DIV14 neurons stained with endogenous MAP7D2 (green) and AnkG (red). Line graph shows that MAP7D2 fluorescence aligns with AnkG maximum intensity (n=21).

(E, F) DIV1 neurons stained for endogenous MAP7D2 (green) and TAU (red). Line scans for stage 2, 3 show the normalized fluorescent intensity from soma to axon.

Scale bars: 20 µm (B, D), 50 µm (C, E).
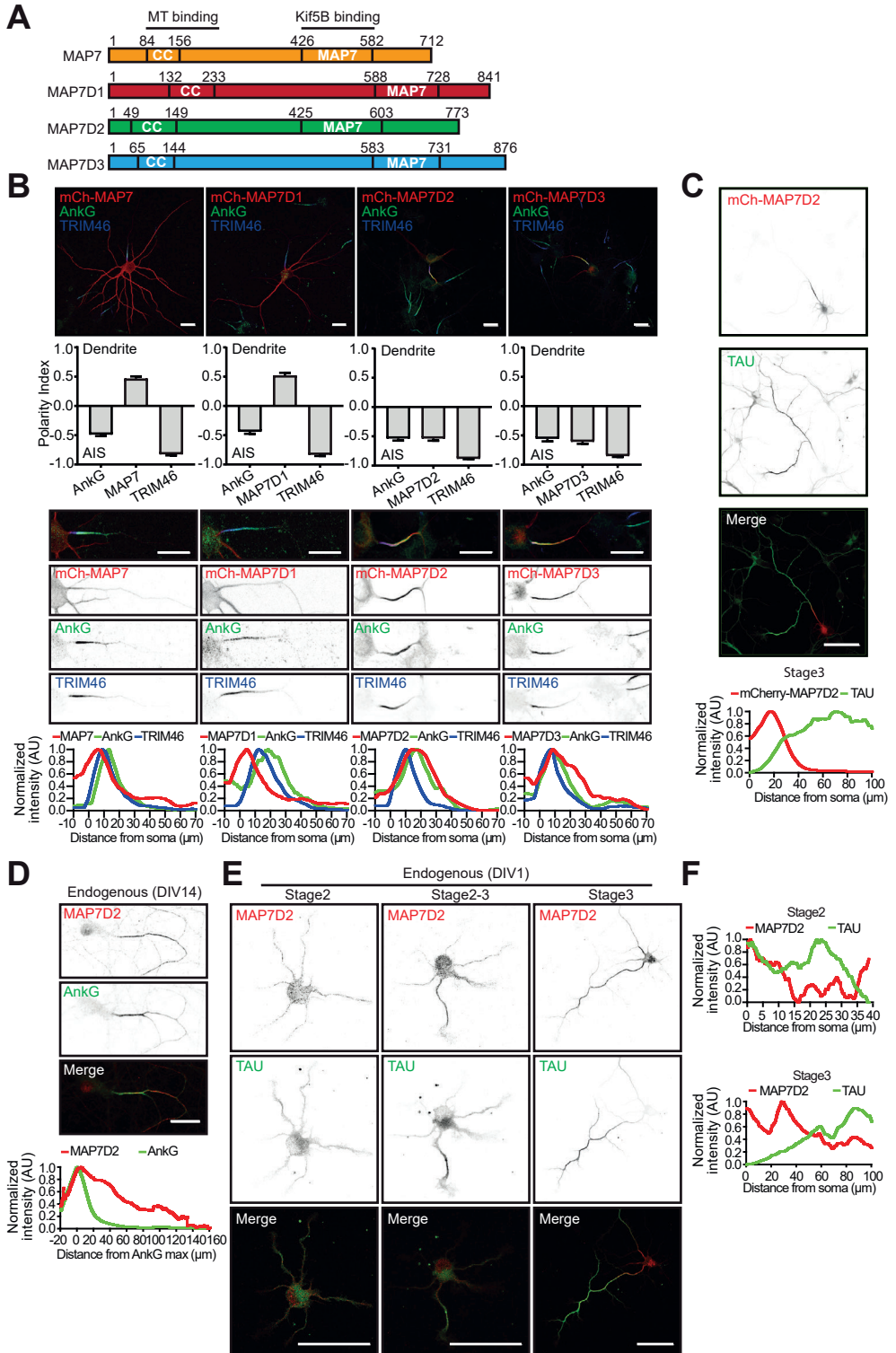
Figure 2. MAP7D2 stably localizes to proximal axon through its domain aa 151-387

(A) Overview of MAP7D1 and MAP7D2 truncations and chimeras.

(B) DIV9 neurons expressing mCherry tagged MAP7D1 and MAP7D2 respectively, and co-stained for TRIM46 (green).

(C-F) DIV4 or DIV9 neurons expressing with GFP tagged N-MAP7D1, N-MAP7D2, indicated chimeras in A, or MAP7D2 aa 151-387, and co-stained for TRIM46 (red).

(G and H) FRAP images and quantifications of mCherry-MAP7D2, GFP-N-MAP7D2 and GFP-C-MAP7D2 fluorescence recovery in the axons of DIV9 neurons. n=4-7 neurons. Error bars represents SEM.

Scale bars: 20 µm (D); 50 µm (B, C, E, F)

We next determined the localization in DIV1 (1 day in vitro) neurons cultures, which contains both stage 2 (unpolarized) and stage 3 (polarized) cells. MAP7D2 is found in the cell body and throughout the neurites in unpolarized stage 2 cells, but strongly accumulates at the proximal axon in polarized stage 3 neurons (Figure 1E,F). These data indicate that MAP7D2 localizes to the proximal axon directly after neuronal polarization.

MAP7D2 localizes to proximal axon through its microtubule-binding domain

To determine which domain is required for the proximal axon localization, we generated MAP7D1 and MAP7D2 truncation constructs (Figure 2A). The C-terminal domains of both MAP7D1 (MAP7D1-C) as well as MAP7D2 (MAP7D2-C) are diffusely localized throughout the neuron and accumulate at axon tips (Figure S2A). In contrast the N-terminal microtubule-binding region of MAP7D2 (MAP7D2-N) accumulates at the proximal axon and the N-terminal domain of MAP7D1 (MAP7D1-N) localizes to dendrites similar to the full length proteins (Figure 2B,C). To map the minimal regions required for the axon specific localization, we generated chimeric proteins by swapping domains of the N-terminal parts of MAP7D1 and MAP7D2 (Figure 2A). All N-terminal containing truncations and chimeras of MAP7D1 and MAP7D2 showed microtubule binding (Figure S2B-E). Chimeras containing the MAP7D2 region downstream of the coiled coil motif (chimeras 1 and 2) localized to the proximal axon, while constructs containing the similar region of MAP7D1 (chimeras 3 and 4) were enriched in the dendrites (Figure 2E). GFP and HA-tagged constructs containing the 151-387 region of MAP7D2 strongly associated with microtubules in COS7 cells and showed proximal axon localization in neurons (Figure 2F and S2F).

To determine the dynamics of MAP7D2 in cells, we performed fluorescence recovery after photobleaching (FRAP) experiments in the proximal axon using N-terminal, C-terminal or full length MAP7D2. The MAP7D2 C-terminus quickly and completely recovers, while full length and N-terminal MAP7D2 only showed ~20% recovery after 3 minutes (Figure 2G,H). In dendrites, MAP7 and MAP7D1 show very similar recovery profiles (~20-30% recovery after 3 minutes) (Figure S2G,H). Together these data indicate that MAP7D2 stably localizes to the proximal axon through its N-terminal microtubule-binding domain.
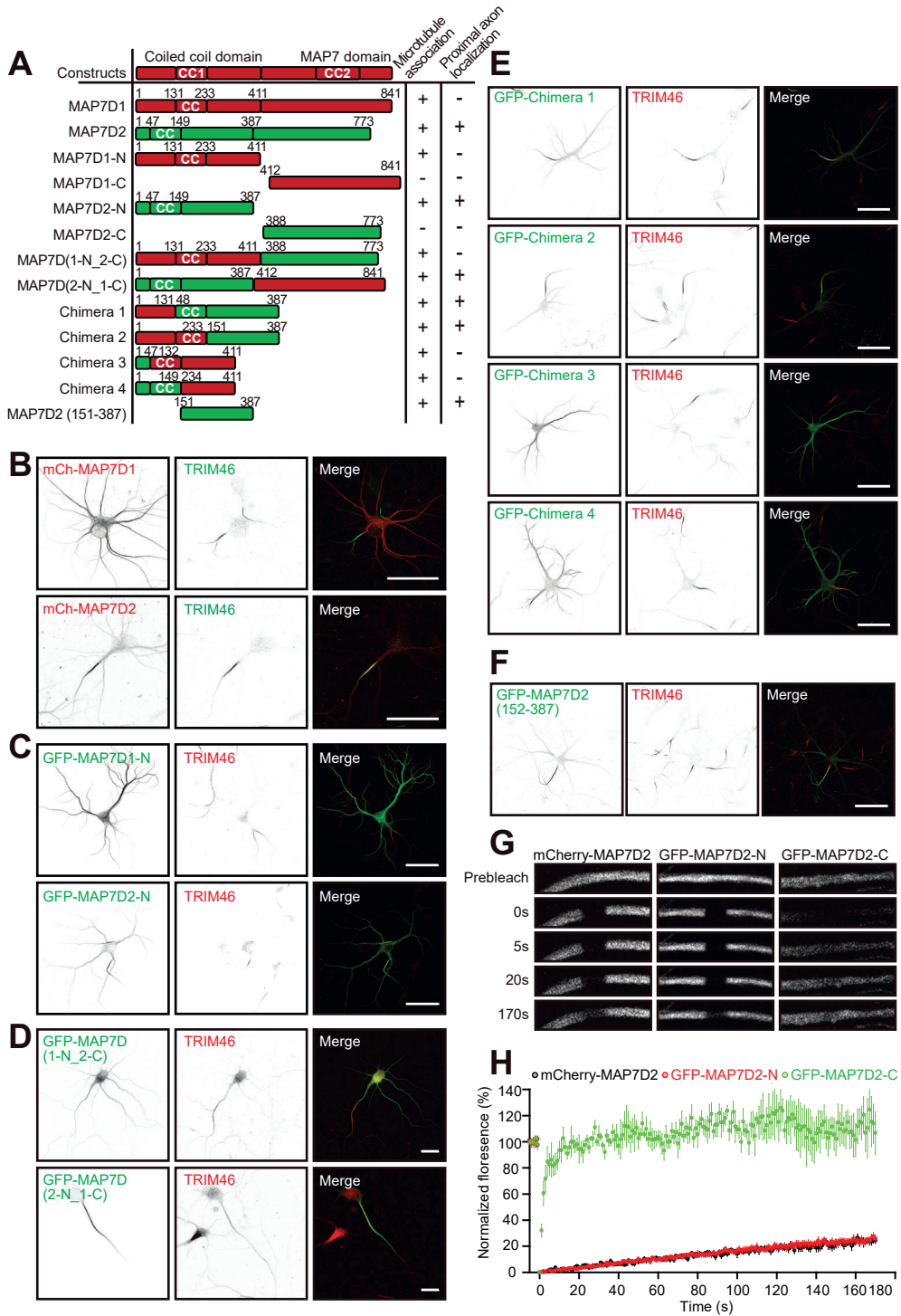
Figure 3. MAP7D2 is important for axon development

(A) DIV14 control, TRIM46 depleted or AnkG depleted neurons co-transfected with "β"-gal (red), and stained for MAP2 (blue), MAP7D2 (green). Arrowheads point to the proximal axon.

(B) Bar graph shows the average intensity of MAP7D2 in each condition. n= 9-10 neurons.

(C) DIV14 control or MAP7D2 depleted neurons co-transfected with "β" fill, and stained for AnkG (blue), MAP7D2 (green).

(D) Bar graph shows the average intensity in the specified condition. n=15-20 neurons

(E and F) Representative images of DIV4 neurons of indicated conditions, together with GFP (E) or mCherry fill (F).

(G, H, and I) Quantifications of the numbers of axon branches of indicated conditions. n=19-123 neurons.

P<0.05 *; P<0.01 **; P<0.001 ***. Unpaired t-test. Error bars represents SEM.

Statistics in (G) was made by control, in (H, I) was made by MAP7D2 sh1.

Scale bars: 20 μm (A, C); 50 μm (E, F)

TRIM46 is required for proximal axon localization of MAP7D2

Since MAP7D2 localizes to the proximal axon, we next determined the underlying mechanism of this specific localization. Previously several proteins were shown to localize to the AIS and to be important for this structure, including the microtubule binding protein TRIM46 and AIS scaffolding protein Ankyrin G (AnkG). TRIM46 forms parallel microtubule bundles in the proximal axon and plays key role in axon specification (van Beuningen et al., 2015). AnkG is the major AIS scaffold protein required for AIS assembly, which forms a barrier between axonal and somatodendritic compartment for neuronal polarity maintenance (Winckler et al., 1999). We first depleted TRIM46 or AnkG with short hairpin RNAs (shRNAs) and determined the MAP7D2 localization at the proximal axon. MAP7D2 staining was still present in AnkG knockdown neurons but largely decreased from the proximal axon in TRIM46 depleted cells (Figure 3A,B), suggesting that MAP7D2's localization to the proximal axon depends on TRIM46 but not AnkG. To address whether MAP7D2 interacts with TRIM46, we co-expressed them in COS7 cells where they co-localize on microtubule bundles. However when we expressed a truncated TRIM46 protein lacking the microtubule binding domain (TRIM46 ΔCOS) (van Beuningen et al., 2015) together with MAP7D2, the colocalization is lost (Figure S3A). This suggests that MAP7D2 does not directly interact with TRIM46.

To test the effect of MAP7D2 depletion on TRIM46 and AnkG localization, we generated several independent shRNAs to deplete MAP7D2 expression and validated the knockdown efficiency by staining transfected neurons with MAP7D2 antibody. Compared to control cells, the MAP7D2 staining was reduced by ~85% in neurons transfected with either shRNA1 or shRNA3 (Figure 3C,D). However the MAP7D2 knockdown only slightly reduced the levels of both TRIM46 as well as AnkG (Figure S3B-D), which may be caused by the reduced diameter of the AIS segment upon MAP7D2 depletion (Figure S3E,F). MAP7D3 could not be detected upon MAP7D2 depletion and neither did we find changes in MAP7 localization,arguing against a potential compensatory mechanism by other MAP7 proteins (Figure S4).
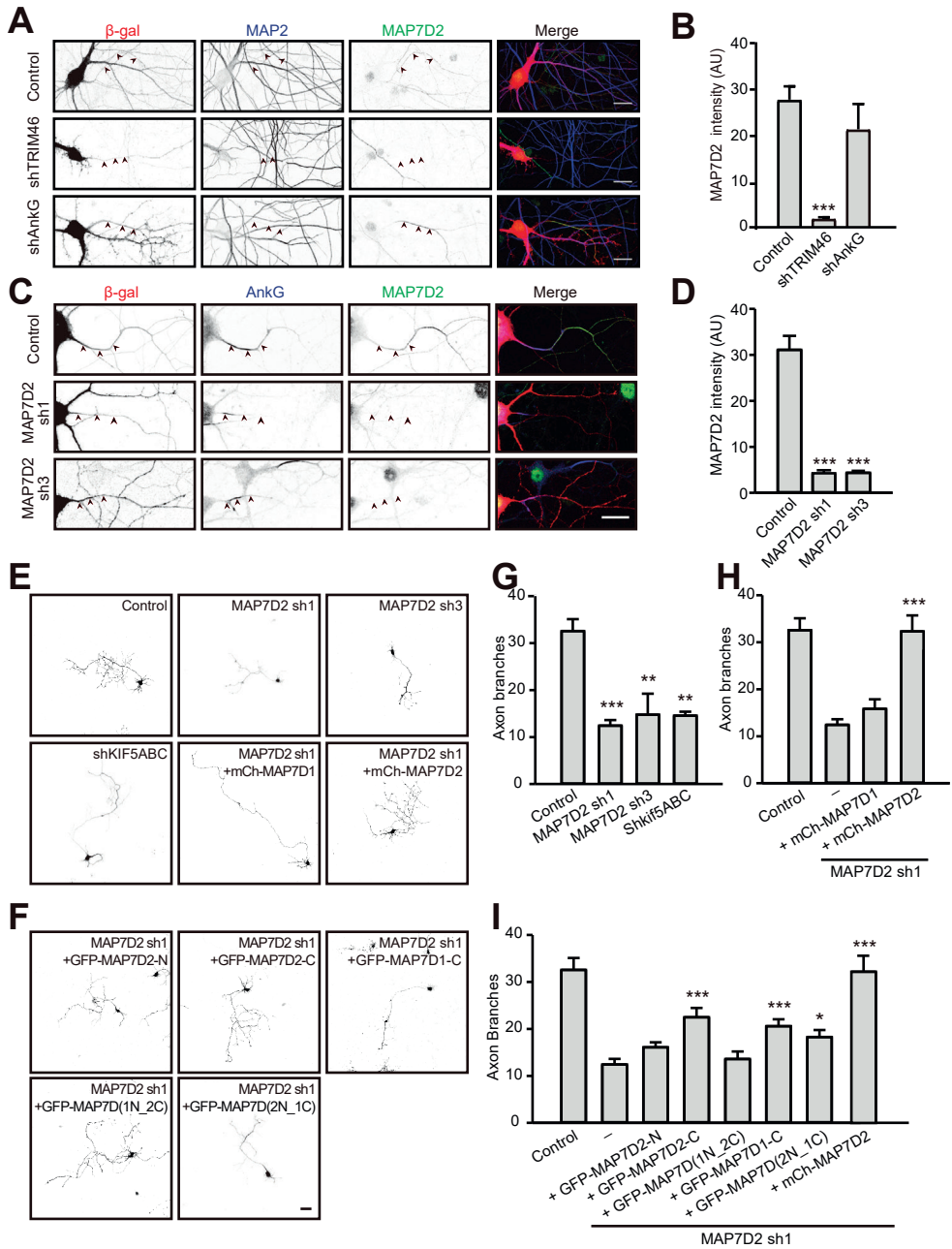
MAP7D2 is important for neuronal migrations and axon development

Since MAP7D2 localizes to the proximal axon, we tested whether MAP7D2 is important for axon development. We found that developing DIV4 neurons depleted of MAP7D2 show reduced axon branching compared to control neurons (Figure 3E,G). The axonal phenotype is rescued by re-expression of MAP7D2 but not MAP7D1 (Figure 3E,H), potentially due to their difference in cellular localization. In addition to axon branching, we tested whether MAP7D2 is important for axon formation. Low concentration of the microtubule stabilizing drug taxol has been shown to induce the formation of multiple axons, somewhat mimicking the process of axon initiation (Witte et al., 2008). Indeed, after taxol treatment, control neurons form 5 axons on average. Neurons depleted of MAP7D2 do not form multiple axons after taxol addition, indicating that MAP7D2 is important for taxol-induced axon formation (Figure S5A,B). To confirm these results, we electroporated hippocampal neurons with shRNAs targeting MAP7D2 or control before plating and analyzed axon formation in non-taxol treated neurons at DIV3 by using Tau and TRIM46 antibodies to mark the axon (Figure S5C). Compared to control cells, there was a small but significantly reduction in the number of Tau or TRIM46 positive neurons after MAP7D2 knockdown. Conversely the overexpression of MAP7D2 leads to a slight increased number of axons (Figure S5D,E). Therefore, MAP7D2 is important for axon branching and potentially also for axon formation.

Neurons in the developing neocortex migrate from the ventricular zone to the different layers in the cortical plate. To test whether MAP7D2 is involved in this process, we performed ex vivo electroporation on mouse E14.5 embryos and cultured brain slices for 3 days to allow GFP labelled cells in ventricular zone to migrate. Whereas control neurons efficiently migrated to the upper layers of the cortical plate, upon MAP7D2 knockdown neurons accumulated in the ventricular zone. Importantly, this migration defect could be rescued by re-expressing MAP7D2, showing that MAP7D2 is important for neuronal migration (Figure S5 F-H).

MAP7D2 activity requires proximal axon localization and kinesin binding

To address the functional differences between MAP7D1 and MAP7D2, we expressed truncation as well as chimeric constructs (Figure 2A-D and S2A), as it was recently shown in Drosophila that ensconsin/MAP7 C-terminal kinesin-binding domain was sufficient to rescue several of the mutant phenotype (Metivier et al., 2018). Interestingly, we also observed a partial rescue by overexpressing of MAP7D2-C, however MAP7D1-C could not reverse the knockdown phenotype. Moreover, even when we fused MAP7D1-C to the AIS targeting MAP7D2-N (chimera MAP7D(2N_1C)), it only partially rescues the MAP7D2 knockdown phenotype (Figure 3F,I), suggesting that MAP7D2 C-terminus plays a specific role in axonal branching. We next tested whether the axonal branching phenotype of MAP7D2 can be phenocopied by knocking down kinesin-1. To address this, we depleted allthree kinesin-1/KIF5 family members (KIF5A,B,C) and observed a similar axonal branching phenotype as for MAP7D2 (Figure 3E,G). Taken together, these data suggest that both the proximal axon localization as well as specific features of the MAP7D2 C-terminus are important determinants for axonal branching.

All three kinesin-1 family members interact with MAP7D2

Previous studies have reported the association between the first coil-coil of kinesin-1 and ensconsin/MAP7 (Metzger et al., 2012). To study the interaction in an unbiased manner we performed pull-down experiments coupled to mass spectrometry. Here GFP-tagged motor domain and coiled-coil region (MDC) of KIF5A-MDC (1-566) and KIF5B-MDC (1-807) were expressed in HEK293 cells, isolated with beads coupled with GFP antibodies, incubated with rat brain extracts, and isolated proteins were analyzed by mass spectrometry. In these pull down experiments we used GFP, KIF1A-MDC (1-500) as well as the KIF5C-MD (1-401) lacking the first coil-coil as controls. Both KIF5A-MDC and KIF5B-MDC pulled down MAP7 family members from HEK cells and brain extracts (Figure 4A). More MAP7D1 was pulled down from brain lysates, which can be explained by that dendritic enriched MAP7D1 in neurons is much more abundant than axonal MAP7D2. The differences in MAP7 protein pull down between brain tissue lysates versus HEK293 cell lysates again indicates that MAP7D2 is exclusively expressed in brain tissues, while MAP7D3 is only expressed in non-brain tissues. These mass spectrometry results were confirmed by more direct pull down experiments in HEK cells coexpressing MAP7D2 and kinesin-1 constructs (Figure 4B), indicating that all three kinesin-1 family members interact with MAP7D2.

MAP7D2 regulates kinesin-1 activity

Ensconsin/MAP7 has been shown to stimulate kinesin-1 activity by promoting microtubule landing and activity (Sung et al., 2008). To determine whether MAP7D2 affects kinesin-1 activity, we co-expressed a truncated constitutively active KIF5 (KIF5C-MDC) together with a full length MAP7D2 or MAP7D2-N that lack of kinesin-1 association domain in COS7 cells. KIF5C-MDC was strongly recruited to microtubules in the presence of MAP7D2 but not MAP7D2-N (Figure S6A). The lack of overlap between the proteins probably reflects that kinesin-1 is recruited to the microtubules by MAP7D2 and then walks away. The microtubule binding but non-walking KIF5A(G235A) (Rigor-KIF5A) was found to preferentially bind to proximal axonal microtubules (Farías et al., 2015). To investigate if the recruitment of Rigor-KIF5A is affected by MAP7D2, we expressed it in control or MAP7D2 depleted neuron. We observed a significant decrease of the Rigor-KIF5A in the proximal axon in MAP7D2 depleted neuron (Figure S6B,C), suggesting that MAP7D2 is important for kinesin-1 recruitment to microtubules in the proximal axon.

To further address MAP7D2's role on kinesin-1, we analyzed endogenous KIF5C upon MAP7D2 depletion in DIV3 neurons. In control neurons KIF5C is largely absent from the proximal axon where endogenous MAP7D2 is localized (Figure 4C-E). Upon MAP7D2 depletion however there is a significant increase in the proximal axon localized kinesin-1, which could be rescued by re-expression of the full length MAP7D2 and only partially by MAP7D(2N_1C) (Figure 4D,E). In addition, overexpression of MAP7D2 leads to a significant reduction in proximal localized kinesin-1 whereas MAP7D(2N_1C) did not (Figure 4F-G). Together this suggests that MAP7D2 stimulates kinesin-1 activity in the proximal axon.

3

Figure 4. MAP7D2 interacts with kinesin-1 family and affects kinesin-1 distribution in the proximal axon

(A) Indicated baits incubated with rat brain and HEK293 cell extracts identified proteins by mass spectrometry.

(B) Western blot analysis of biotinylated (bio) pull down from extracts of HEK 293 cells transfected with indicated constructs, probed for GFP and mCherry.

(C) Representative images of neurons with control, MAP7D2 sh1 or sh3 and fixed at DIV3, stained for KIF5C and the axonal marker Tau. Arrowheads point to the proximal axon.

(D and E) Quantifications of KIF5C intensity or ratio at the beginning and the end of axon in indicated conditions. n=15-32 neurons.

(F and G) Quantifications of KIF5C intensity or ratio at the beginning and the end of axon in specified conditions. n=19-27 neurons.

$P<0.05$ *; $P<0.01$ **; $P<0.001$ ***. Unpaired t-test. Error bars represents SEM.

Scale bars: 20 μm (C)

MAP7D2 is required for kinesin-1 based cargo transport

The axonal transport of mitochondria, endoplasmic reticulum (ER) and lysosomes strongly depend on kinesin-1 activity (Farías et al., 2017; van Spronsen et al., 2013; Woźniak et al., 2009). To investigate whether kinesin-1 mediated cargo trafficking is affected by MAP7D2 we performed live cell imaging experiments using the cargos indicated above. We observed a marked decrease in the number of mitochondria entering the axon in MAP7D2 depleted neurons (Figure 5A,G). Also the transport events in the distal axon were reduced (Figure S6D,E), which may well be due to reduced activation of kinesin-1 in the axon (Figure 4C-E). Similar results were found for the axon entry of lysosomes and the ER (Figure 5B-D,H,I). Imaging of Rab3 vesicles, which are mainly transported by kinesin-3 family members (Kevenaar et al., 2016), did not reveal differences between control and MAP7D2 knock-down cells (Figure 5E,F,J). Finally we were able to fully rescue the axonal entry of mitochondria upon MAP7D2 depletion by re-expression of the full length protein, but not the MAP7D(2N_1C) (Figure 5K-M). Together these data indicate that MAP7D2 is required for kinesin-1 mediated cargo transport to enter the axon.

DISCUSSION

In this study we analyzed the proteins of the MAP7 family in rat hippocampus neurons. Mammals have 4 MAP7 family members, of which MAP7, MAP7D1 and MAP7D2 are expressed in neuronal tissues. We found that these proteins have very specific localization patterns; whereas MAP7 and MAP7D1 localize to the somatodendritic compartment, MAP7D2 specifically accumulates to the proximal axon, largely overlapping with the AIS, and also extends some into the axon. This is markedly different to sensory DRG neurons, which do not possess dendrites nor a classic AIS, where MAP7 was shown to localize to axon branch points (Tymanskyj et al., 2017, 2018). We found that MAP7D2 is tightly associated with proximal axon via an N-terminal microtubule binding fragment, which we mapped to a 235 amino acid domain. The proximal axon localization of MAP7D2 depends on TRIM46, which bundles microtubules in the AIS in a parallel fashion (van Beuningen et al., 2015). We speculate that MAP7D2 may recognize a modification and/or a change

A

PD-MS

IP Bait	Brain lysates	Unique peptides			
Identified	GFP	KIF1A	KIF5A	KIF5B	KIF5C
MAP7	0	0	0	1	0
MAP7D1	0	1	13	20	2
MAP7D2	0	0	1	2	0

IP Bait	HEK293 lysates	Unique peptides			
Identified	GFP	KIF1A	KIF5A	KIF5B	KIF5C
MAP7	0	0	0	2	0
MAP7D1	0	0	1	1	0
MAP7D3	0	0	0	2	0

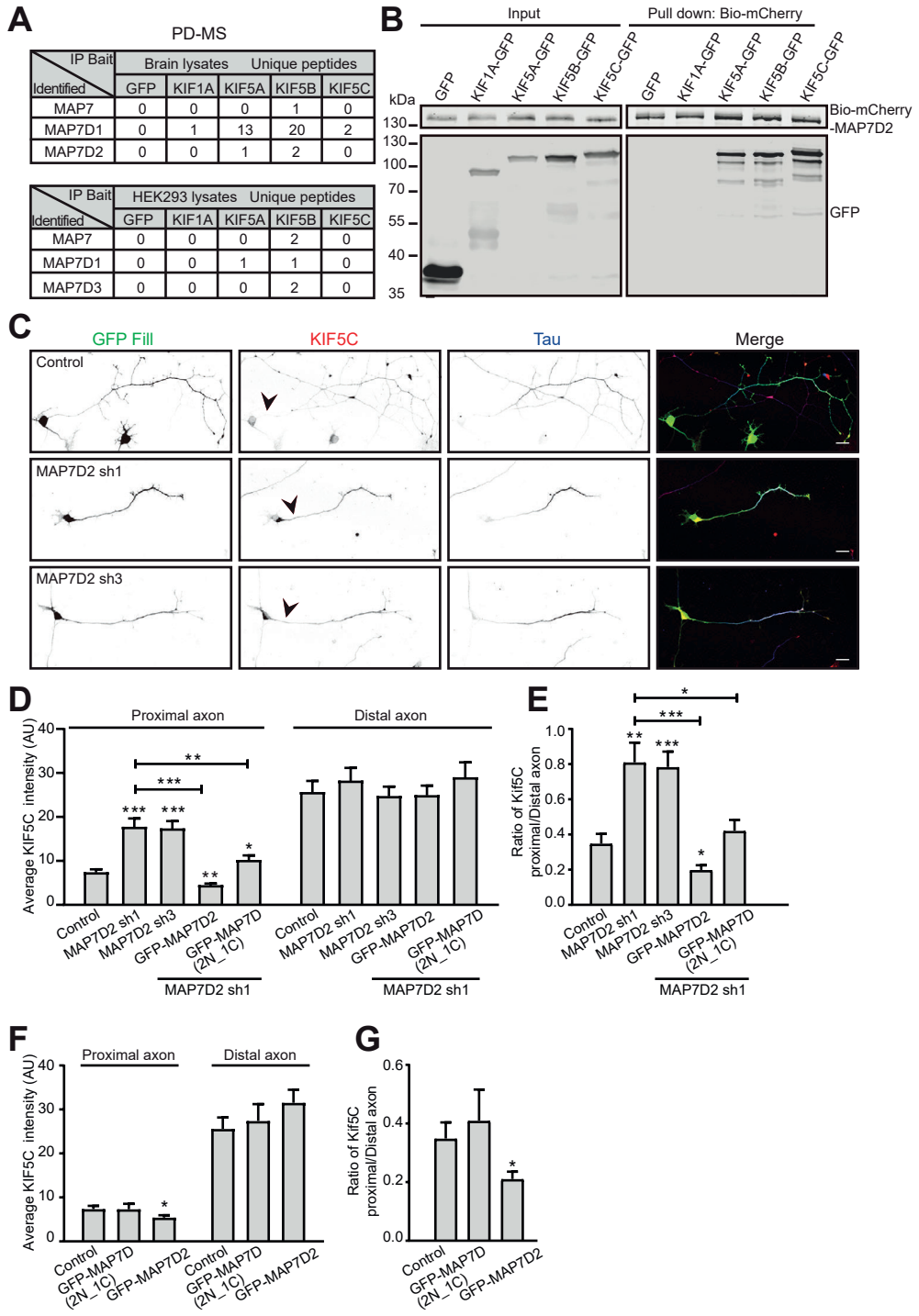## B

C

D

E

F

G

3

Figure 5. MAP7D2 promotes kinesin-1 based cargo transport

(A-C) Kymographs showing live cell imaging of mitochondria, lysosome or ER (after FRAP) in control or MAP7D2 depleted neurons co-transfected with mito-DsRed (A), LAMP1-GFP (B) or Rtn4A-GFP (C).

(D) Drawing of the anterograde ER movements along the proximal axon in C.

(E) Kymographs showing live cell imaging of Rab3 vesicles in control or MAP7D2 depleted neurons.

(F) Drawing of the anterograde Rab3 vesicles movement along the proximal axon in D.

(G-J) Quantifications of mitochondria, lysosome, ER or Rab3 vesicles entry into axon as described for A-F. n=12-44 neurons.

(K-M) Stills and kymographs for live cell imaging of mitochondria in neurons co-transfected with mito-DsRed and indicated constructs (K,L). Quantifications for mitochondria entry into axon within 5 minutes upon specified conditions (M). n=12-21 neurons. Unpaired t-test. Scale bars: 10 μm.

P<0.05 *; P<0.01 **; P<0.001 ***. Mann-Whitney Rank Sum Test. Error bars represents SEM.

---

in the microtubule lattice induced by TRIM46 at the AIS. Additionally as MAP7 microtubule binding and subcellular localization was shown to be influenced by phosphorylation (Ramkumar et al., 2018), this might also play a role in targeting MAP7D2 to the proximal axon.

Like for other MAP7 proteins, we show that MAP7D2 can interact with all three KIF5/kinesin-1 isoforms but not with KIF1A/Kinesin-3. Accordingly, depletion of MAP7D2 leads to a reduction of kinesin-1 dependent cargo to enter the axon, whereas kinesin-3 dependent RAB3 vesicles were unaffected. Moreover, we observed a decreased recruitment of rigor KIF5A to the proximal axon whereas endogenous KIF5C is increased in the proximal axon, suggesting that the MAP7D2 is important for both kinesin-1 recruitment and processivity in the proximal axon. These data leads to a model where the kinesin-1 activator MAP7D2 is localized to the proximal axon to stimulate kinesin-1 dependent cargo entry into the axon. We also observed reduced mitochondria transport in the distal axon upon MAP7D2 depletion, which may well be caused by the reduced activation of axonal kinesin-1, although we cannot exclude that there are low remaining levels of MAP7D2 in the distal segment promoting kinesin-1 transport.

A recent study addressed the functioning of the MAP7 family in both cultured cells as well as with purified proteins in vitro and found that there is a high degree of redundancy (Hooikaas et al., 2018). In neurons we find that the expression of both MAP7D1 as well as MAP7D2 C-terminus end up at the tips of the axon branches, suggesting that they bind to kinesin-1 and are co-transported. The MAP7D2 C-terminus can partially rescue the axonal branching phenotype. When the MAP7D1 C-terminus is attached to the AIS binding domain of MAP7D2 it hardly rescues the axon branching phenotype. Similarly, full length MAP7D2 was able to rescue the MAP7D2 knockdown induced kinesin-1 accumulation at the proximal axon and the reduced axonal entries of mitochondria, whereas the chimera construct could not or only partially rescue the defects. This suggests that MAP7D2 has a unique function in regulating kinesin-1 activity in the proximal axon to regulate branching.
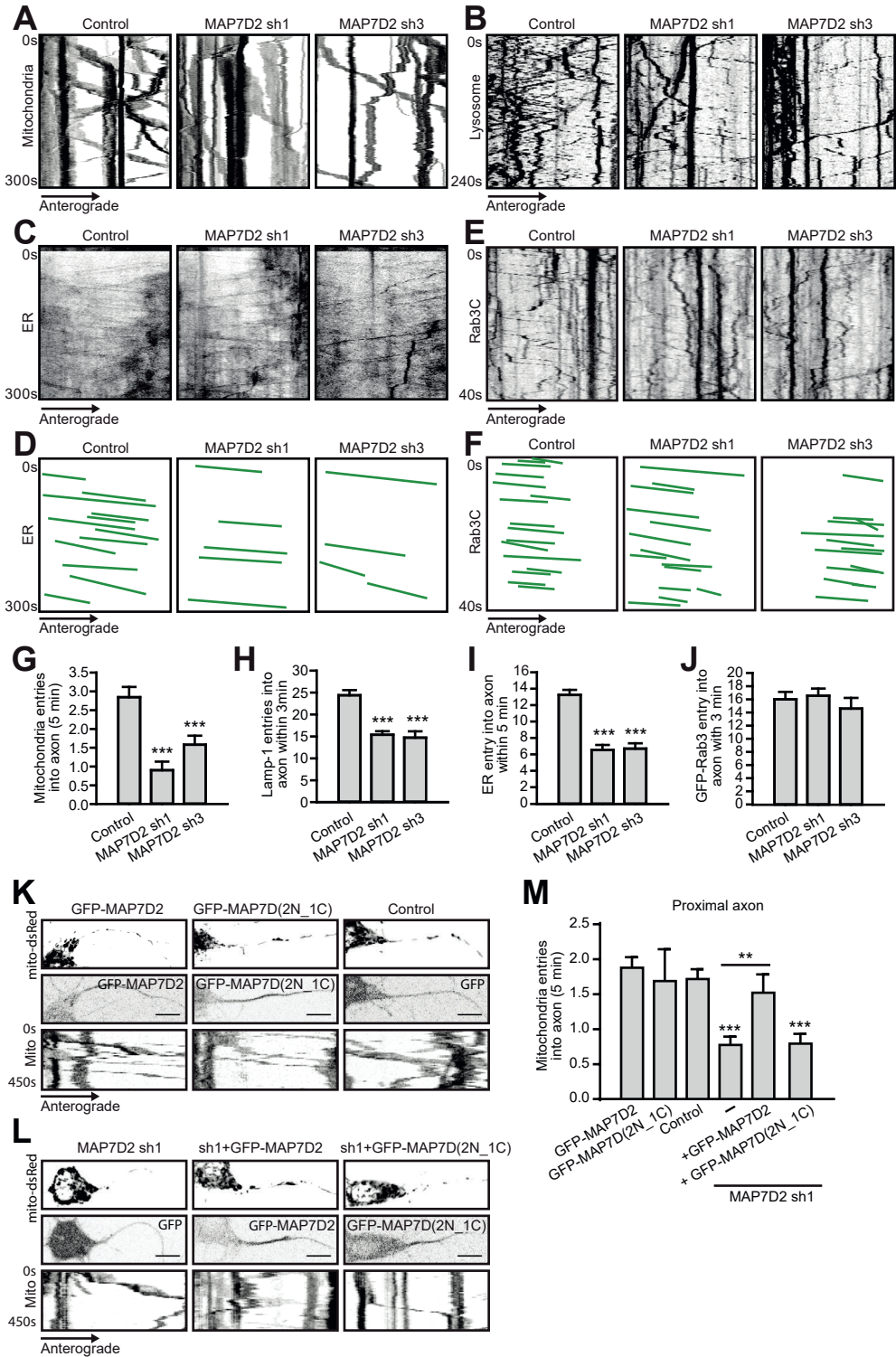
The idea that spatially confined microtubule-associated proteins form a 'MAP code' that locally controls microtubule motor activities is an emerging concept. In neurons for example, doublecortin stimulates kinesin-3 to target dendrites (Lipka et al., 2016), whereas MAP2 and SEPT9 were found to prevents kinesin-1 cargo to enter the dendrite (Gumy et al., 2017; Karasmanis et al., 2018). For axons the protein Tau is suggested to prevent kinesin-1 landing/activity on axonal microtubules (Seitz et al., 2002; Vershinin et al., 2007). In this study we found that MAP7D2 promotes kinesin-1 transport into the axon of hippocampal neurons. It was shown that MAP7 and Tau compete for microtubule binding in vitro (Monroy et al., 2018). Whether the same applies for Tau and MAP7D2 remains to be seen, although we did not observe clear proximal relocalization of Tau upon MAP7D2 depletion. Since mutations in kinesin-1 family member KIF5A are associated with several neurological diseases (Crimella et al., 2012; Nicolas et al., 2018), in the future it will be interesting to address the functions of MAP7 family members in these diseases.

ACKNOWLEDGEMENTS

AUTHOR CONTRIBUTIONS

X.P. designed and performed the experiments, analyzed results and wrote the manuscript; Y.C. performed pull-down and Rigor KIF5A experiments; R.S. performed the mass spectrometry experiment; L.W. and S.P. performed ex vivo electroporation and organotypic slice cultures; P.J.H., M.M. and L.W. provided critical reagents; A.A. gave advise and edited the manuscript; M.H. and C.C.H. designed experiments, supervised the research and correct the manuscript.

DECLARATION OF INTERESTS

The authors declare no competing interests.

STAR METHODS

CONTACT FOR REAGENT AND RESOURCE SHARING

Further information and requests for resources and reagents should be directed to and will be fulfilled by the Lead Contact Casper Hoogenraad (c.hoogenraad@uu.nl).

EXPERIMENTAL MODEL AND SUBJECT DETAILS

Animals

All animal experiments were performed in compliance with the guidelines for the welfare of experimental animals issued by the Federal Government of the Netherlands, and were approved by the Animal Ethical Review Committee (DEC) of Utrecht University.

Heterologous cell and Hippocampal neuron cultures

HEK293 cells, Hela cells and African Green Monkey SV40-transformed kidney fibroblast (COS7) cells were cultured in a 10 cm plate with 10 ml 50% DMEM/ 50% Ham's F10 medium containing 10% FBS (Gibco) and 1% Penicillin/streptomycin in incubator with 37°Cand 5% CO2. WT and MAP7D3 knockout Hela cells lines were already described (Hooikaas et al., 2018).

Hippocampus were dissected out from embryonic 18 Janvier WISTAR rat brain and dissociated with Trypsin in 37°C water bath. 100K/well neurons were plated in glass coverslips pre-coated with Poly-L-lysine (37.5 μg/ml, Sigma) and Laminin (1.25μg/ml, Sigma). Neurobasal medium (Invitrogen) containing 2% B27 (Invitrogen), 0.5 mM glutamine (Invitogen), 15.6 μM glutamate (Sigam) and 1% penicillin/streptomycin (Invitrogen) were used for neuron culture.

Ex vivo electroporation and organotypic brain slice cultures

Pregnant C57Bl/6JRj mice were sacrificed by cervical dislocation, and brains from E14.5 embryos were electroporated with 1.5μl DNA mixture containing a MARCKS-GFP together with shRNA target to MAP7D2 or pSuper empty vector (control), which was dissolved in MQ with 0.05% FastGreen FCF Dye (Sigma). The DNA mix was injected in the lateral ventricles of the embryonic brains using borosilicate glass micro-pipettes (World Precision Instruments) and a PLI-100A Picoliter Microinjector (Warner Instruments). Embryonic brains (region in the motor cortex) were electroporated using platinum plated electrodes (Nepagene) with an ECM 830 Electro Square Porator (Harvard Apparatus) set to 3 unipolar pulses of 100ms at 30V with 100ms intervals. Embryonic brains were then isolated and collected in ice-cold cHBSS, embedded in 3% SeaPlaque GTG Agarose (Lonza) in cHBSS and sectioned coronally into 300μm thick slices using a VT1000 S Vibratome (Leica). Slices were collected on Poly-L-lysine and Laminin-coated culture membrane inserts (Falcon), placed on top of slice culture medium (70% v/v Basal Eagle Medium, 26% v/v cHBSS, 20mM D-glucose, 1mM L-glutamine, 0.1 mg/mL penicillin/streptomycin) and cultured 4 days prior to fixation.

3

METHOD DETAILS

Antibody and reagents

The following antibodies were used for the immunofluorescence staining: mouse anti-AnkG (Neuromab, 75-146); rabbit anti-TRIM46 (van Beuningen et al., 2015); rabbit anti-MAP7D2 (Atlas Antibodies, HPA051508); mouse anti-Tau (Chemicon, MAB3420); rat anti-HA (Roche, 1-867-423); mouse anti-MAP7 (MaxPab, B01P); Alexa Fluor 405-, Alexa Fluor 488-, Alexa Fluor 568-, Alexa Fluor 647-conjugated secondary antibodies (Life Technologies). The following antibodies were used for Western blot: mouse anti-mCherry (Clonetech, 632543); rabbit anti-GFP (Abcam, ab290); IRDye 680LT- and IRDye 800CW-conjugated secondary antibodies (LI-COR Biosciences).

Other reagents used in this study include: Taxol (Sigma, T7402); Lipofectamine2000 (Thermofiser, 11668019), Vectashield mounting medium (Vectorlabs, H-1000).

DNA and shRNA constructs

All full-length MAP7 family protein constructs were cloned by a PCR-based strategy into a Bio-mCherry-C1 vector, except for MAP7D1 which has been cloned into a Bio-mCherry-C3 vector. MAP7 constructs were generated from Hela cDNA, MAP7D1 was cloned based on cDNA from IMAGE clone IRATp970A04109D (Source Bioscience), MAP7D2 was cloned based on cDNA of IMAGE clone IRAKp961B22199Q (Source Bioscience) and MAP7D3 was cloned based on cDNA of IMAGE clone IRAKp961K1163Q (Source Bioscience). All chimeras and truncation constructs of MAP7D1 and MAP7D2 were cloned into GW1 vector(Kapitein et al., 2010). MARCKS-GFP for ex vivo experiment was described before (De Paola et al., 2003). The kinesin constructs: pβactin-GFP-FRB, KIF1A (1-500)-GFP, KIF5A (1-566)-GFP, KIF5B (1-807)-GFP, KIF5B (1-560)-GFP and KIF5C (1-401)-GFP (Gumy et al., 2017; Kapitein et al., 2010; Kevenaar et al., 2016; Lipka et al., 2016). KIF5C (1-560) was generated by using full length rat KIF5C cDNA (NM_001107730.1) as PCR template and was cloned into pβactin-GFP-FRB vector. Plasmids for live imaging experiments: Mito-dsRed (van Spronsen et al., 2013), GFP-SBP-Rtn4A was cloned into GFP C1 vector from human RTN4A-GFP (ADDGENE #61807) by Dr. Ginny Farías, LAMP1-GFP was cloned into GFP N1 vector from Rat LAMP1-RFP (ADDGENE #1817) by Dr. Ginny Farías (Farías et al., 2017), GFP-Rab3C (Kevenaar et al., 2016). The following shRNAs were used for knockdown experiments: Rat MAP7D2 shRNA #1 (5'-ggaacctcctatgagtaaa-3'), MAP7D2 shRNA #3 (5'-ctgaagaagttcaatctat-3'), KIF5A shRNA (5'-gagacatcttcaaccacat-3'), KIF5B shRNA (5'-tggagggtaaacttcatga-3'), KIF5C shRNA (5'-tgagatctacttggacaaa-3'). Mouse MAP7D2 shRNA (5'-gagacaaagattagccaaa-3'). ShRNAs for TRIM46 and AnkG has been described previously (Kuijpers et al., 2016; van Beuningen et al., 2015).

Transfections and immunofluorescence

HEK293, Hela, or COS7 cells were diluted in a ratio 1:3 24 hours before transfection. MaxPEI or phusioere seud for HEK293 cell transfection based on

manufacture's protocol and incubated for 24 hours to 36 hours before pull-down experiments.

For the DIV0 hippocampus neuron transfection, the Amaxa Rat Neuron Nucleofector kit (Lonza) was used based on manufacture's protocol. Briefly, 120K/well neurons were transfected with 2 μg DNA and cultured in Neurobasal medium (Invitrogen) containing 2% B27 (Invitrogen), 0.5 mM glutamine (Invitrogen), 15.6 μM glutamate (Sigam) and 1% penicillin/streptomycin (Invitrogen), after 3 days' incubation, neurons were fixed for immunofluorescence and imaging.

For neurons older than DIV0, Lipofectamin 2000 (Invitrogen) was used for transfection via manufacture's protocol. Briefly, 1.8 μg DNA and 3.3 μl Lipofectamin 2000 reagent were mixed in 200μl Neurobasal medium for 30 minutes. The neuronal growth medium was transferred to a new 12 well plate, and the original plate was filled with fresh Neurobasal medium supplemented with 0.5 mM glutamine. The DNA mix was added into neurons for 45 minutes, washed the coverslips with pre-warmed Neurobasal medium and placed them to the new plate with growth medium. Neurons were imaged after 1 day (all the overexpression experiments) or 3 days (all knockdown experiments) transfection.

For immunofluorescence experiments, neurons were fixed with 4% PFA (paraformaldehyde) for 10-15 minutes, washed 3 times with PBS (phosphate buffer saline), and incubated with primary antibodies in GDB buffer (0.2% BSA, 0.8 M NaCl, 0.5% Triton X-100, 30 mM phosphate buffer) overnight at 4°C. Neurons were then washed with PBS for 3 times, incubated with secondary antibodies in GDB buffer for 45 minutes at room temperature, followed by washing 3 times with PBS and mounting with Vectashield mounting medium (Vector Laboratories).

Fixed cell Imaging

After immunofluorescence staining, neurons were imaged using a Nikon Eclipse 80i upright microscope or a Zeiss LSM700 confocal laser scanning microscope. A Plan Fluor 40x NA 1.30 oil objective was used for upright microscope. For the confocal microscope, a Plan Apochromat 20x NA 0.8 dry objective, 40x NA 1.3 oil and 63x NA 1.4 oil objectives were used.

Live cell imaging and Photo bleaching experiments

All the live imaging was performed on a Nikon Eclipse TE2000E inverted microscope equipped with Evolve 512 EMCCD camera (Roper Scientific), spinning disk confocal (Roper Scientific), incubate chamber (Tokai Hit) and MetaMorph 7.7.5 software (Molecular Device) was used for all the live imaging experiments. In order to visualize mitochondria, ER, lysosome and Rab3 vesicles, neurons were transfected with Mito-dsRed, Rtn4A-GFP, Lamp1-GFP and GFP-Rab3C respectively as described previously. Neurons were maintained in 37°C /5% CO2 and imaged with 1 frame/s for 5 minutes using a Plan Fluor 40x NA 1.3 oil objective for the mitochondria and ER transport, 1 frame/s for 3 minutes using a Plan Apo VC 60x NA 1.3 oil objective for the lysosome transport and 4 frames/s for 40 seconds by using a Plan Apo VC 100x NA 1.4 oil objective for the Rab3 vesicle transport.

For image acquisition of ER movement, fluorescence recovery after photobleaching (FRAP) experiment was performed at the beginning of axons by using the ILas2 system (Roper Scientific). For the mitochondria imaging upon MAP7D2 rescue and distal axon transport experiment, multi-position acquisition setting was used for imaging 3 neurons at the same time, in total for 15-30 minutes, and quantifications were normalized to 5 minutes. For FRAP experiments with all MAP7 family members both in COS7 cells and neurons, movies were taken for 3 minutes at 1 frame/s and indicated areas were bleached at 10 seconds.

GFP pull-down and mass spectrometry

GFP pull-down experiments were performed using GFP-trap magnetic beads (ChromoTek) against either HEK293 cell lysates or rat brain lysates. HEK293 cells were transfected with different kinesin constructs tagged with GFP at the C terminus or GFP-FRB empty construct as contrtol for 2 days and then lysed by incubating cells for 30 minutes on ice in lysis buffer (20 mM Tris-HCl pH8.0, 150 mM NaCl, 1% Triton X-100 and 1x protease inhibitor cocktail), cell lysates were centrifuged at 13,000 rpm for 10 minutes and the supernatants were incubated with beads for 40 minutes at 4°C. Rat brains were lysed with the same lysis buffer, centrifuged at 16,000 g for 20 minutes and the supernatants were incubated with the beads already bound to kinesins with GFP tagged constructs for 2 hours. After incubation, beads were washed 3 times with wash buffer (25 mM Tris-HCl pH8.0, 100 mM NaCl, 0.1% NP40). For protein elution, beads were boiled with NuPAGE LDS 4 sample buffer (Invitrogen), centrifuged, and supernatants were run on a 4-12% NuPAGE tris-acetate gel (Invitrogen). Gels were stained with Colloidal Blue kit (Invitrogen), and samples were cut from SDS-PAGE gel lanes for mass spectrometry as described before (Kevenaar et al., 2016).

Biotin-streptavidin pull-down and western blot

Streptavidin pull-down assays were performed by using Dynabeads M-280 streptavidin beads (Invitrogen). HEK293 cells were transfected with bio-mCherry-MAP7D2 and BirA together with GFP-FRB or GFP-FRB tagged KIF1A-MDC (1-500), KIF5A-MDC (1-566), KIF5B-MDC (1-560) or KIF5C-MDC (1-560) . After 24-48 hours, cells were harvested in ice-cold PBS and lysed with lysis buffer (100 mM Tris-HCl pH 7.5, 150 mM NaCl, 1% Triton X-100 and 1x protease inhibitor cocktail). Cell lysates were centrifuged at 13,000 rpm for 7 minutes and the supernatants were incubated with streptavidin beads which were already blocked by 0.2% Chicken Egg Albumine (Sigma). After incubating for 40 minutes at room teraperature, beads were washed 3-5 times with wash buffer (50mM Tris pH7.5, 150 mM NaCl, 0.5% Triton X-100 and 1x protease inhibitor cocktail). Samples were eluted with SDS/DTT sample buffer and boiled for subsequent western blot assay.

For the western blot assays, samples were loaded into 10% SDS-PAGE gels and transferred to nitrocellulose membrane. Membranes were blocked with 2% BSA (bovine serum albumin) in PBS/0.05% Tween 20. Primary antibodies were diluted in blocking buffer and incubated with the membranes overnight at 4°C, washed 3 times with PBS/0.05% Tween 20 and incubated with secondary IRDye 680LT or IRDye 800LT antibodies for 45 minutes at room temperature. Membranes were

then washed 3 times with PBS/0.05% Tween 20 and scanned on Odyssey Infrared Imaging system (LI-COR Biosciences).

Slice immunofluorescence and imaging

Mice brain slices from 4 days organotypic cultures were fixed with 4% paraformaldehyde in PBS. Fixed slices were then permeabilized and blocked in 10% Normal Goat Serum (NGS)/0.2% Triton X-100/PBS. The signal was increased by staining with an anti-GFP antibody overnight, followed by secondary Alexa 488 antibody staining. Slices were washed 4 times for 15 min in PBS in between. Slices were mounted using Vectashield mounting medium (Vector Laboratories) containing DAPI. Z-stack acquisitions were taken using a LSM700 (Zeiss) confocal microscope equipped with a Plan-Apochromat 20x NA 0.8 objective with a 0.5x magnification.

QUANTIFICATION AND STATISTICAL ANALYSIS

All statistical details including the definitions of n, numbers of n and statistical tests performed can be found in each Figures and Figure legends. Sigma Plot or GraphPad were used for graphs and statistics. T-test or Mann-Whitney U test was performed for statistics and $p<0.05$ was considered significant.

Image processing and analysis were performed using ImageJ, Matlab, and Adobe Photoshop. Phylogenetic analysis Conserved Coiled coil motif within MAP7 family proteins was defined by using Pfam and Coiled Coils Prediction (Prabi), while MAP7 domain was defined using Pfam. ClustalX and Mega5 were used for alignment and phylogenetic tree analysis based on conserved domains.

Protein localizations in neurons.

To study protein localization in neurons, images stained for different axonal markers were obtained by confocal microscope, tracings were made along axons by using segmented lines in ImageJ and average intensity profiles were normalized by MatLab program as previously described (van Beuningen et al., 2015). For the endogenous MAP7D2 and AnkG distributions, the relative alignment of intensity profiles was made according to the position of maximum intensity in the AnKG staining.

Analysis of polarity index.

MAP7 family members were expressed in DIV9 neurons, and fixed at DIV10, stained for AnkG and TRIM46. Average intensity of 20 µm in the AIS or dendrite were measured. Rigor-KIF5A-GFP was expressed in DIV1 neurons together with control or MAP7D2 shRNAs, and fixed at DIV4, stained for TRIM46 for marker of the axon, average intensity of 10 µm in the AIS or dendrite were measured, at least 2 dendrites were included and background was subtracted. Polarity index was calculated with the formula: $PI = (Id-Ia)/(Id+Ia)$. Id corresponds to mean dendrite intensity, while Ia is the mean AIS intensity. $PI > 0$ indicates the polarization is biased toward dendrite and $PI < 0$ to the AIS.

Analysis of Endogenous protein.

To validate both the efficiency of MAP7D2 shRNAs, neurons transfected with control or shRNAs were stained with MAP7D2 antibody. The staining intensity was calculated by measuring the average intensity of the proximal axons (50 µm) and subtracting the intensity of areas adjacent to the axons with the same length, leaving a final intensity value per axon. For TRIM46 and AnkG level analysis, the average intensity of 20 µm in the AIS in the transfected neuron was normalized to the same region of non-transfected neighbouring neuron. For the MAP7D2 shRNA specificity experiment, MAP7D3 (average intensity at the proximal axon of around 20 µm) and MAP7 (average soma intensity) were measured.

Analysis of FRAP experiments.

For the FRAP analysis, the mean intensities of bleached area were correct by subtracting background with the same ROI region frame by frame and calculated as $I(t)= I_{(bleached\ region)} (t) – I_{background} (t)$. The normalization of recovery $R_{norm} (t)$ was calculated according to the formula:

$$R_{norm} (t)=(I(t)-I(0))/(<I(\Delta t)>-I(0))$$

$I(0)$ corresponds to the mean intensity of regions directly after bleaching, $<I(\Delta t)>$-intensity averaged over 5 frames before bleaching. To correct bleaching due to imaging, the non-bleached region next to the bleached region was account and calculated:

$$R(t)= R_{norm} (t)\times(<I_{control} (\Delta t)-I_{background} (t)>)/(I_{control} (t)-I_{background} (t))$$

$I_{control}$ corresponds to the mean intensity of the non-bleached region and time interval Δt denotes 5 initial frames before bleaching. The curves were made by averaging each frame the recovery rate.

Quantification of ex vivo neuronal migration.

The degree of neuronal migration was quantified as described previously (Hand et al 2015). Briefly, the positions of the cell bodies of GFP-positive neurons within the cortex were measured by Image J plugin, the Analyze Particle. The relative position of neurons in the regions of interest was recorded in terms of distance between the ventricle and the pial surface. The position information, including neurons across the entire Z series in the electroporated neocortial region together with the top (pial surface) and bottom (ventricle) boundaries, were imported to Excel. Based on the relative position of each neuron and the total numbers of neurons counted, the radial cell distribution along the radial axis was obtained by further data processing using an Excel macro and expressed as percentage of migration.

Quantification of axon branching.

To quantify the axon branches of each neuron, an ImageJ plugin, NeuronJ (Meijering et al., 2004) was used for tracing the morphology of axon.

Quantification of axon formation by electroporation or Taxol inducement.

For the analysis of axon formation by electroporation, neurons were stained with either TAU or TRIM46 as markers for polarization. For the Taxol inducement of axon formation, DIV3 neurons were transfected with Psuperb, MAP7D2 shRNA together with GFP as described before, after 1 day, a concentration of 20 nM Taxol was added to neurons for maintaining 48 hours. Neurons were stained with TRIM46 as an axon marker, imaged on the confocal microscope, and images were analyzed using ImageJ software.

Quantifications of organelle and vesicle movement.

To quantify organelle dynamics, kymographs were made using Kymoreslicewide plugins in ImageJ on the proximal or distal axons. For the ER movement, FRAP was used to remove the background.

3

REFERENCES

Barlan, K., Lu, W., and Gelfand, V.I. (2013). The Microtubule-Binding Protein Ensconsin Is an Essential Cofactor of Kinesin-1. Curr. Biol. 23, 317–322.

Conde, C., and Cáceres, A. (2009). Microtubule assembly, organization and dynamics in axons and dendrites. Nat. Rev. Neurosci. 10, 319–332.

Crimella, C., Baschirotto, C., Arnoldi, A., Tonelli, A., Tenderini, E., Airoldi, G., Martinuzzi, A., Trabacca, A., Losito, L., Scarlato, M., et al. (2012). Mutations in the motor and stalk domains of KIF5A in spastic paraplegia type 10 and in axonal Charcot-Marie-Tooth type 2. Clin. Genet. 82, 157–164.

De Paola, V., Arber, S., and Caroni, P. (2003). AMPA receptors regulate dynamic equilibrium of presynaptic terminals in mature hippocampal networks. Nat. Neurosci. 6, 491–500.

Farías, G.G., Guardia, C.M., Britt, D.J., Guo, X., and Bonifacino, J.S. (2015). Sorting of Dendritic and Axonal Vesicles at the Pre-axonal Exclusion Zone. Cell Rep. 13, 1221–1232.

Farías, G.G., Guardia, C.M., De Pace, R., Britt, D.J., and Bonifacino, J.S. (2017). BORC/kinesin-1 ensemble drives polarized transport of lysosomes into the axon. Proc. Natl. Acad. Sci. U. S. A. 114, E2955–E2964.

Gallaud, E., Caous, R., Pascal, A., Bazile, F., Gagné, J.-P., Huet, S., Poirier, G.G., Chrétien, D., Richard-Parpaillon, L., and Giet, R. (2014). Ensconsin/Map7 promotes microtubule growth and centrosome separation in Drosophila neural stem cells. J Cell Biol 204, 1111–1121.

Gumy, L.F., and Hoogenraad, C.C. (2018). Local mechanisms regulating selective cargo entry and long-range trafficking in axons. Curr. Opin. Neurobiol. 51, 23–28.

Gumy, L.F., Katrukha, E.A., Grigoriev, I., Jaarsma, D., Kapitein, L.C., Akhmanova, A., and Hoogenraad, C.C. (2017). MAP2 Defines a Pre-axonal Filtering Zone to Regulate KIF1- versus KIF5-Dependent Cargo Transport in Sensory Neurons. Neuron 94, 347-362.e7.

Hoogenraad, C.C., Milstein, A.D., Ethell, I.M., Henkemeyer, M., and Sheng, M. (2005). GRIP1 controls dendrite morphogenesis by regulating EphB receptor trafficking. Nat. Neurosci. 8, 906–915.

Hooikaas, P.J., Martin, M., Kuijntjes, G.-J., Peeters, C.A.E., Katrukha, E.A., Ferrari, L., Stucchi, R., Verhagen, D.G.F., Riel, W.E. van, Altelaar, A.F.M., et al. (2018). MAP7 family proteins are microtubule-tethered allosteric activators of kinesin-1. BioRxiv 388512.

Kapitein, L.C., and Hoogenraad, C.C. (2015). Building the Neuronal Microtubule Cytoskeleton. Neuron 87, 492–506.

Kapitein, L.C., Schlager, M.A., Kuijpers, M., Wulf, P.S., van Spronsen, M., MacKintosh, F.C., and Hoogenraad, C.C. (2010). Mixed microtubules steer dynein-driven cargo transport into dendrites. Curr. Biol. CB 20, 290–299.

Karasmanis, E.P., Phan, C.-T., Angelis, D., Kesisova, I.A., Hoogenraad, C.C., McKenney, R.J., and Spiliotis, E.T. (2018). Polarity of Neuronal Membrane Traffic Requires Sorting of Kinesin Motor Cargo during Entry into Dendrites by a Microtubule-Associated Septin. Dev. Cell 46, 204-218.e7.

Kevenaar, J.T., Bianchi, S., van Spronsen, M., Olieric, N., Lipka, J., Frias, C.P., Mikhaylova, M., Harterink, M., Keijzer, N., Wulf, P.S., et al. (2016). Kinesin-Binding Protein Controls Microtubule Dynamics and Cargo Trafficking by Regulating Kinesin Motor Activity. Curr. Biol. 26, 849–861.

Kikuchi, K., Nakamura, A., Arata, M., Shi, D., Nakagawa, M., Tanaka, T., Uemura, T., Fujimori, T., Kikuchi, A., Uezu, A., et al. (2018). Map7/7D1 and Dvl form a feedback loop that facilitates microtubule remodeling and Wnt5a signaling. EMBO Rep. 19, e45471.

Koizumi, H., Fujioka, H., Togashi, K., Thompson, J., Yates, J.R., Gleeson, J.G., and Emoto, K. (2017). DCLK1 phosphorylates the microtubule-associated protein MAP7D1 to promote axon elongation in cortical neurons. Dev. Neurobiol. 77, 493–510.

Kuijpers, M., van de Willige, D., Freal, A., Chazeau, A., Franker, M.A., Hofenk, J., Rodrigues, R.J.C., Kapitein, L.C., Akhmanova, A., Jaarsma, D., et al. (2016). Dynein

3

Regulator NDEL1 Controls Polarized Cargo Transport at the Axon Initial Segment. Neuron 89, 461–471.

Lipka, J., Kapitein, L.C., Jaworski, J., and Hoogenraad, C.C. (2016). Microtubule-binding protein doublecortin-like kinase 1 (DCLK1) guides kinesin-3-mediated cargo transport to dendrites. EMBO J. e201592929.

Meijering, E., Jacob, M., Sarria, J.-C. f., Steiner, P., Hirling, H., and Unser, M. (2004). Design and validation of a tool for neurite tracing and analysis in fluorescence microscopy images. Cytometry A 58A, 167–176.

Metivier, M., Monroy, B., Gallaud, E., Caous, R., Pascal, A., Richard-Parpaillon, L., Guichet, A., Ori-McKenney, K., and Giet, R. (2018). The Kinesin-1 binding domain of Ensconsin/MAP7 promotes Kinesin-1 activation in vivo. BioRxiv 325035.

Metzger, T., Gache, V., Xu, M., Cadot, B., Folker, E.S., Richardson, B.E., Gomes, E.R., and Baylies, M.K. (2012). MAP and kinesin-dependent nuclear positioning is required for skeletal muscle function. Nature 484, 120–124.

Monroy, B.Y., Sawyer, D.L., Ackermann, B.E., Borden, M.M., Tan, T.C., and Ori-McKenney, K.M. (2018). Competition between microtubule-associated proteins directs motor transport. Nat. Commun. 9, 1487.

Nicolas, A., Kenna, K.P., Renton, A.E., Ticozzi, N., Faghri, F., Chia, R., Dominov, J.A., Kenna, B.J., Nalls, M.A., Keagle, P., et al. (2018). Genome-wide Analyses Identify KIF5A as a Novel ALS Gene. Neuron 97, 1268-1283.e6.

Niida, Y., and Yachie, A. (2011). MAP7D2 is a brain expressing X-linked maternal imprinted gene in humans. Nat. Preced. <http://hdl.handle.net/10101/npre.2011.6684.1>

Ramkumar, A., Jong, B.Y., and Ori-McKenney, K.M. (2018). ReMAPping the microtubule landscape: How phosphorylation dictates the activities of microtubule-associated proteins. Dev. Dyn. Off. Publ. Am. Assoc. Anat. 247, 138–155.

Seitz, A., Kojima, H., Oiwa, K., Mandelkow, E.-M., Song, Y.-H., and Mandelkow, E. (2002). Single-molecule investigation of the interference between kinesin, tau and MAP2c. EMBO J. 21, 4896–4905.

van Spronsen, M., Mikhaylova, M., Lipka, J., Schlager, M.A., van den Heuvel, D.J., Kuijpers, M., Wulf, P.S., Keijzer, N., Demmers, J., Kapitein, L.C., et al. (2013). TRAK/Milton motor-adaptor proteins steer mitochondrial trafficking to axons and dendrites. Neuron 77, 485–502.

Sung, H.-H., Telley, I.A., Papadaki, P., Ephrussi, A., Surrey, T., and Rørth, P. (2008). Drosophila ensconsin promotes productive recruitment of Kinesin-1 to microtubules. Dev. Cell 15, 866–876.

Tas, R.P., Chazeau, A., Cloin, B.M.C., Lambers, M.L.A., Hoogenraad, C.C., and Kapitein, L.C. (2017). Differentiation between Oppositely Oriented Microtubules Controls Polarized Neuronal Transport. Neuron 96, 1264-1271.e5.

Tymanskyj, S.R., Yang, B., Falnikar, A., Lepore, A.C., and Ma, L. (2017). MAP7 Regulates Axon Collateral Branch Development in Dorsal Root Ganglion Neurons. J. Neurosci. 37, 1648–1661.

Tymanskyj, S.R., Yang, B.H., Verhey, K.J., and Ma, L. (2018). MAP7 regulates axon morphogenesis by recruiting kinesin-1 to microtubules and modulating organelle transport. ELife 7, e36374

Uhlén, M., Fagerberg, L., Hallström, B.M., Lindskog, C., Oksvold, P., Mardinoglu, A., Sivertsson, Å., Kampf, C., Sjöstedt, E., Asplund, A., et al. (2015). Proteomics. Tissue-based map of the human proteome. Science 347, 1260419.

van Beuningen, S.F.B., Will, L., Harterink, M., Chazeau, A., van Battum, E.Y., Frias, C.P., Franker, M.A.M., Katrukha, E.A., Stucchi, R., Vocking, K., et al. (2015). TRIM46 Controls Neuronal Polarity and Axon Specification by Driving the Formation of Parallel Microtubule Arrays. Neuron 88, 1208–1226.

Vershinin, M., Carter, B.C., Razafsky, D.S., King, S.J., and Gross, S.P. (2007). Multiple-motor based transport and its regulation by Tau. Proc. Natl. Acad. Sci. U. S. A. 104, 87–92.

Winckler, B., Forscher, P., and Mellman, I. (1999). A diffusion barrier maintains distribution of membrane proteins in polarized neurons. Nature 397, 698–701.

Witte, H., Neukirchen, D., and Bradke, F. (2008). Microtubule stabilization specifies initial neuronal polarization. J Cell Biol 180, 619–632.

Woźniak, M.J., Bola, B., Brownhill, K., Yang, Y.-

3

C., Levakova, V., and Allan, V.J. (2009). Role of kinesin-1 and cytoplasmic dynein in endoplasmic reticulum movement in VERO cells. J Cell Sci 122, 1979–1989.

Zhang, X., Zhu, J., Yang, G.-Y., Wang, Q.-J., Qian, L., Chen, Y.-M., Chen, F., Tao, Y., Hu, H.-S., Wang, T., et al. (2007). Dishevelled promotes axon differentiation by regulating atypical protein kinase C. Nat. Cell Biol. 9, 743–754.

Zhang, Y., Chen, K., Sloan, S.A., Bennett, M.L., Scholze, A.R., O'Keeffe, S., Phatnani, H.P., Guarnieri, P., Caneda, C., Ruderisch, N., et al. (2014). An RNA-sequencing transcriptome and splicing database of glia, neurons, and vascular cells of the cerebral cortex. J. Neurosci. Off. J. Soc. Neurosci. 34, 11929–11947.

3

SUPPLEMENTAL INFORMATION INVENTORY

Supplemental Figures S1-S6

Figure S1, related to Figure 1

Figure S2, related to Figure 2

Figure S3, related to Figure 3

Figure S4, related to Figure 3

Figure S5, related to Figure 3

Figure S6, related to Figure 4, 5

3

Figure S1, related to Figure 1. Characterization of the MAP7, MAP7D2 and MAP7D3 antibodies in neurons and cultured cells.

(A) corresponds to figure 1B. Representative images of DIV21 neurons co-stained for MAP7 (red) and TRIM46 (green). Square box is magnified below. Scale bars: 50 µm (A: upper row), 20 µm (A: bottom row)

(B) Line scans indicate normalized intensity of MAP7 and TRIM46 from soma to axon.

(C) Polarity index of MAP7 and TRIM46 in DIV21 hippocampal neurons (n=15 neurons).

(D) DIV10 neurons were transfected with mCherry-MAP7, mCherry-MAP7D1, mCherry-MAP7D2 or mCherry-MAP7D3 for 2 days, and stained for MAP7D2 (green). Arrowheads correspond to the proximal axon where MAP7D2 antibody recognizes mCherry-MAP7D2.

(E) DIV10 neurons were transfected with mCherry-MAP7, mCherry-MAP7D1, mCherry-MAP7D2 or mCherry-MAP7D3 for 2 days, and stained for MAP7D3 (green). Arrowheads correspond to the proximal axon where MAP7D3 antibody recognizes mCherry-MAP7D3.

(F and G) MAP7D3 WT or KO Hela cells were stained for MAP7D3 (green) or MAP7D2 (green) respectively. DAPI (blue) was used as nucleus marker. The MAP7D2 antibody recognizes centrosomes in Hela cells.
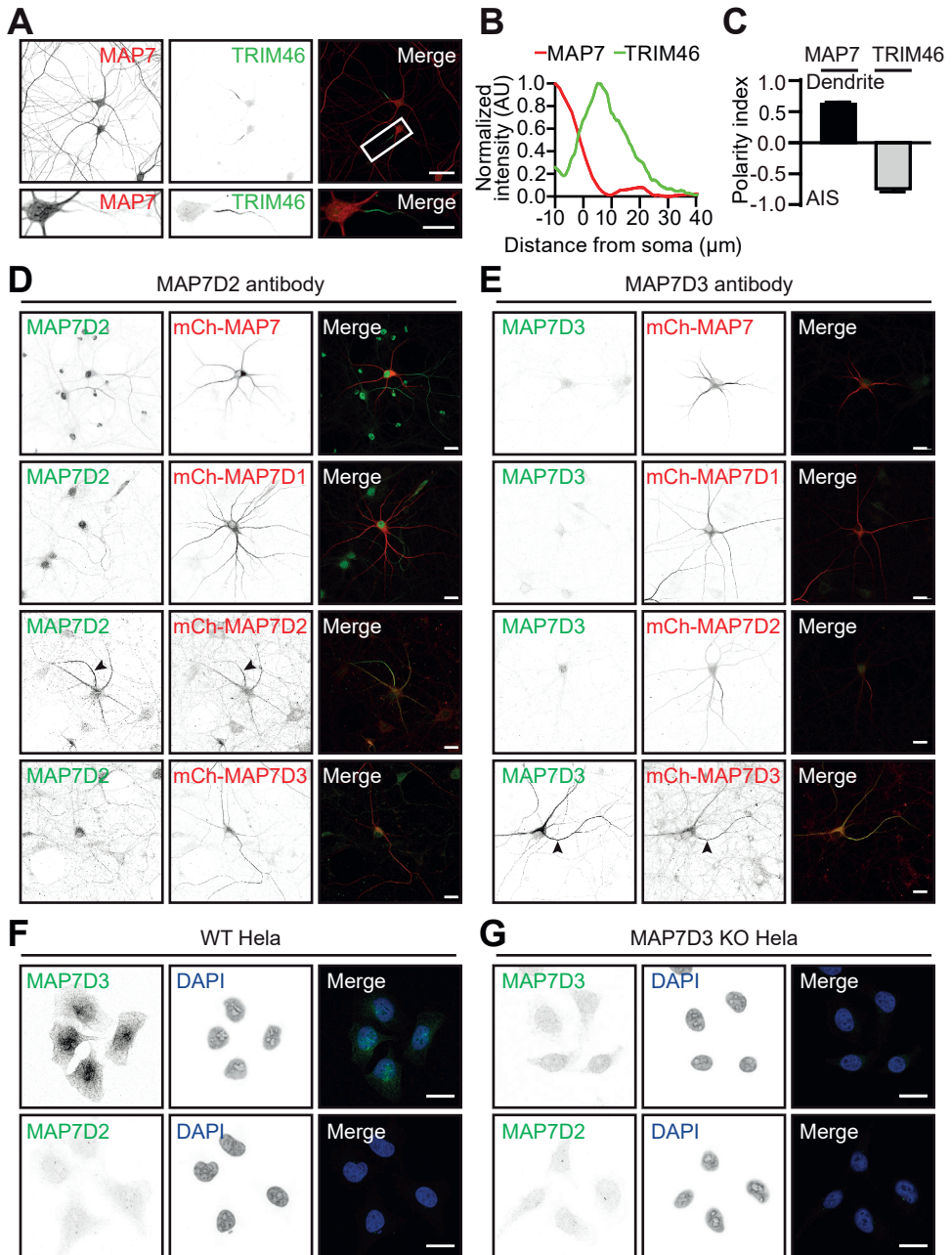
Scale bars: 20 µm

3

Figure S2, related to Figure 2. MAP7 proteins associate with microtubules by their N-terminus and are largely immobile in neurons.

(A) corresponds to figure 2A and 2C. Representative images of GFP tagged C-terminus of MAP7D1 or MAP7D2 in DIV9 neurons, co-stained for TRIM46 for axons.

(B-E) correspond to figure 2A-F. Representative images of truncations and chimeras of MAP7D1 and MAP7D2 which are able to bind to microtubules in COS7 cells. Microtubule association is marked by antibody against acetylated-tubulin.

(F) corresponds to figure 2F. COS7 cells expressed with GFP tagged or HA tagged MAP7D2(151-387) fragments in first row. The second and third row are representative images of DIV9 neuron expressing GFP tagged or HA tagged MAP7D2(151-387) fragments, and co-stained for AnkG for axon.

(G and H) FRAP images of mCherry-MAP7, mCherry-MAP7D1 and mCherry-MAP7D2 in neurons. Averaged normalized intensity of FRAP graph of mCherry-MAP7 (n=9), mCherry-MAP7D1 (n=9) and mCherry-MAP7D2 (n=7). Error bars represents SEM.

N means numbers of FRAP regions.

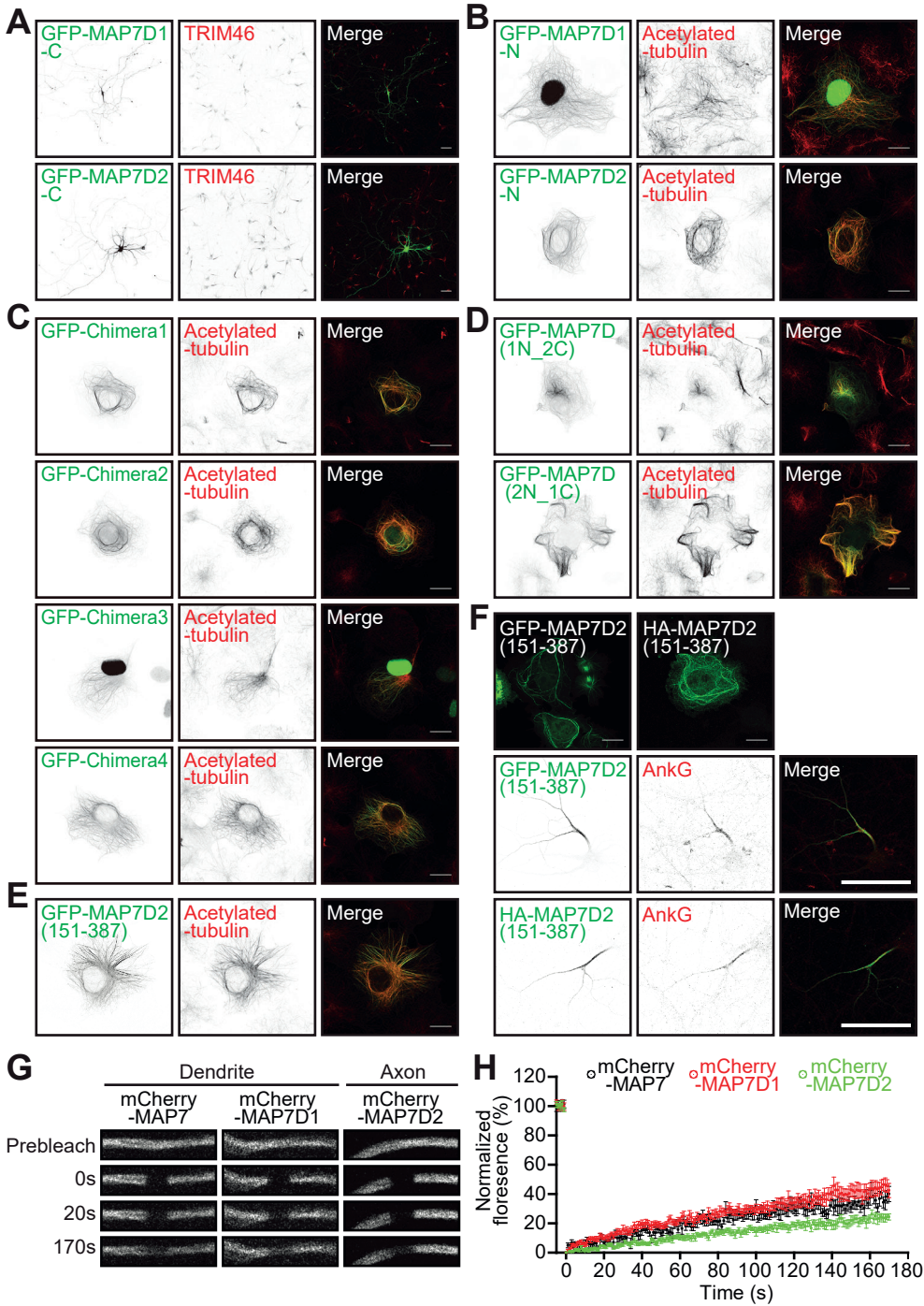Scale bars: 20 μm (A-D, F); 50 μm (E)

3

Figure S3, related to Figure 3. MAP7D2 does not interact with TRIM46, and is not essential for AIS assembly.

(A) Representative images of COS7 cells expressing mCherry-MAP7D2 and GFP-TRIM46 or GFP-TRIM46 ΔCOS. DAPI (blue) was used as nucleus marker. COS domain is essential for TRIM46 binding to microtubules.

(B) DIV11 neurons were transfected with control or MAP7D2 shRNAs together with a β-gal (red) fill for 3 days and co-stained for TRIM46 and AnkG. Asterisks pinpoint transfected neurons in each condition.

(C) Bar graph shows the normalized intensity of AnkG in control (n=30 neurons), or MAP7D2 KD (sh1 (n=33) and sh3 (n=33)) compared to neighbouring non-transfected neurons.

(D) Bar graph shows the normalized intensity of TRIM46 in control (n=57 neuron), or MAP7D2 KD (sh1 (n=60) and sh3 (n=62)) compared to neighbouring non-transfected neurons.

(E) Representative images of DIV11 neurons transfected with control or MAP7D2 shRNAs together with a β-gal fill (red) for 3 days and co-stained for AnkG (green).

(F) Bar graph shows the average AIS diameters measured by AnkG staining in control (n=41), or MAP7D2 KD (sh1 (n=46) and sh3 (n=47)).

$P<0.05$ *; $P<0.01$ **; $P<0.001$ ***. Unpaired t-test. Error bars represents SEM.

Scale bars: 20 µm (A); 10 µm (B, E)

3
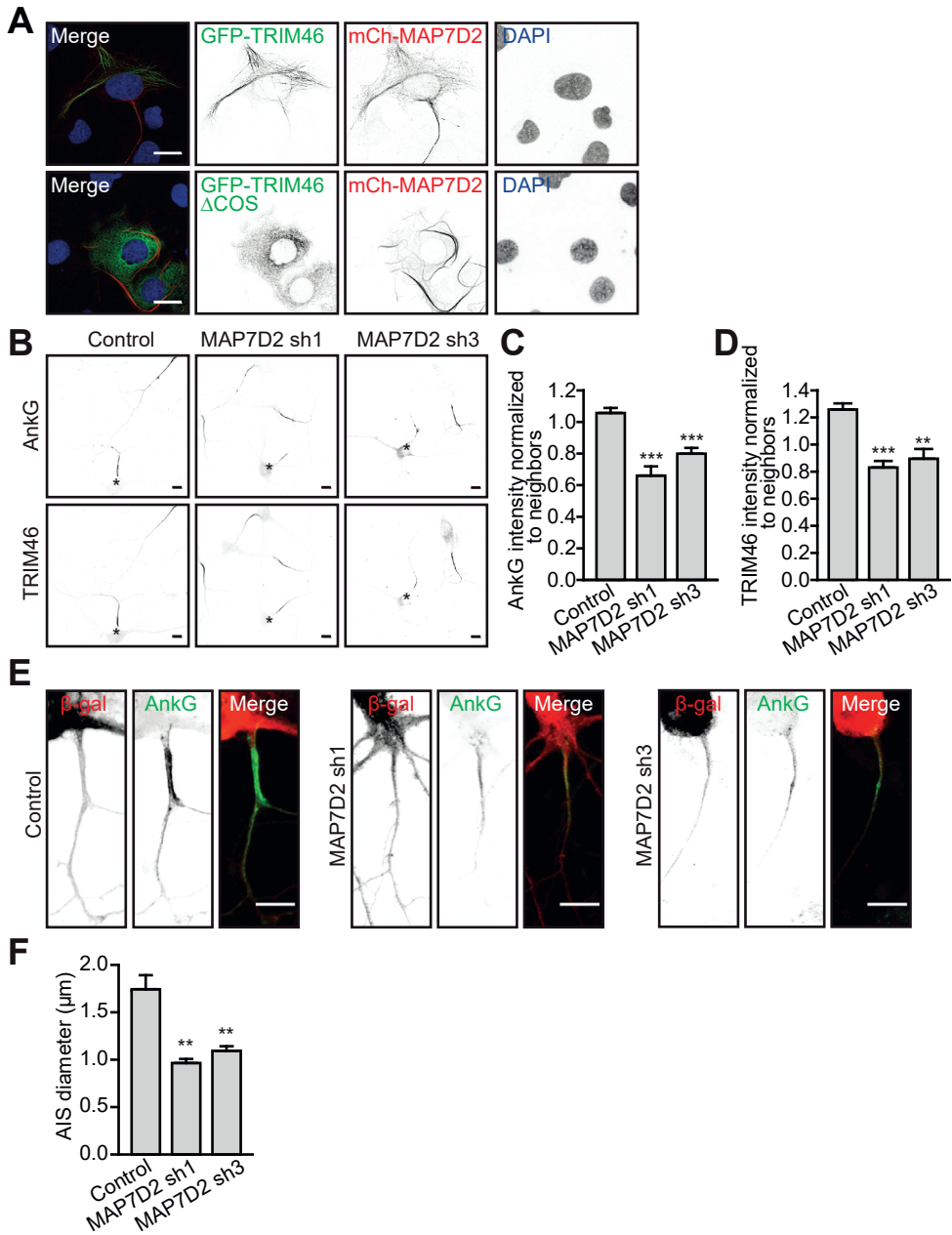
Figure S4, related to Figure 3. MAP7D2 knockdown does not lead to changes in MAP7 nor does it lead to expression of MAP7D3.

(A) DIV11 neurons were transfected with control or MAP7D2 shRNAs together with a mCherry-α-tubulin fill for 3 days and stained for MAP7D3 (green). Arrowheads correspond to the proximal axon.

(B) Bar graph shows the average intensity of MAP7D3 in the proximal axon under Control (n=8), or MAP7D2 KD (sh1 (n=8) and sh3 (n=7)), which is probably background fluorescence.

(C) DIV11 neurons were transfected with control or MAP7D2 shRNAs together with a β-gal (red) fill for 3 days and stained for MAP7 (green). Arrow heads correspond to the soma of transfected neuron.

 (D) Bar graph shows the average intensity of MAP7 in soma under Control (n=12), or MAP7D2 KD (sh1 (n=12) and sh3 (n=15)).

$P<0.05$ *; $P<0.01$ **; $P<0.001$ ***. Unpaired t-test. Error bars represents SEM.

Scale bars: 20 μm

3

A

Control | MAP7D3 | mCh-α-tubulin | Merge

MAP7D2 sh1 | MAP7D3 | mCh-α-tubulin | Merge

MAP7D2 sh3 | MAP7D3 | mCh-α-tubulin | Merge

B

Axon MAP7D3 intensity (AU): Control, MAP7D2 sh1, MAP7D2 sh3

C

Control | MAP7 | β-gal | Merge

MAP7D2 sh1 | MAP7 | β-gal | Merge

MAP7D2 sh3 | MAP7 | β-gal | Merge

D

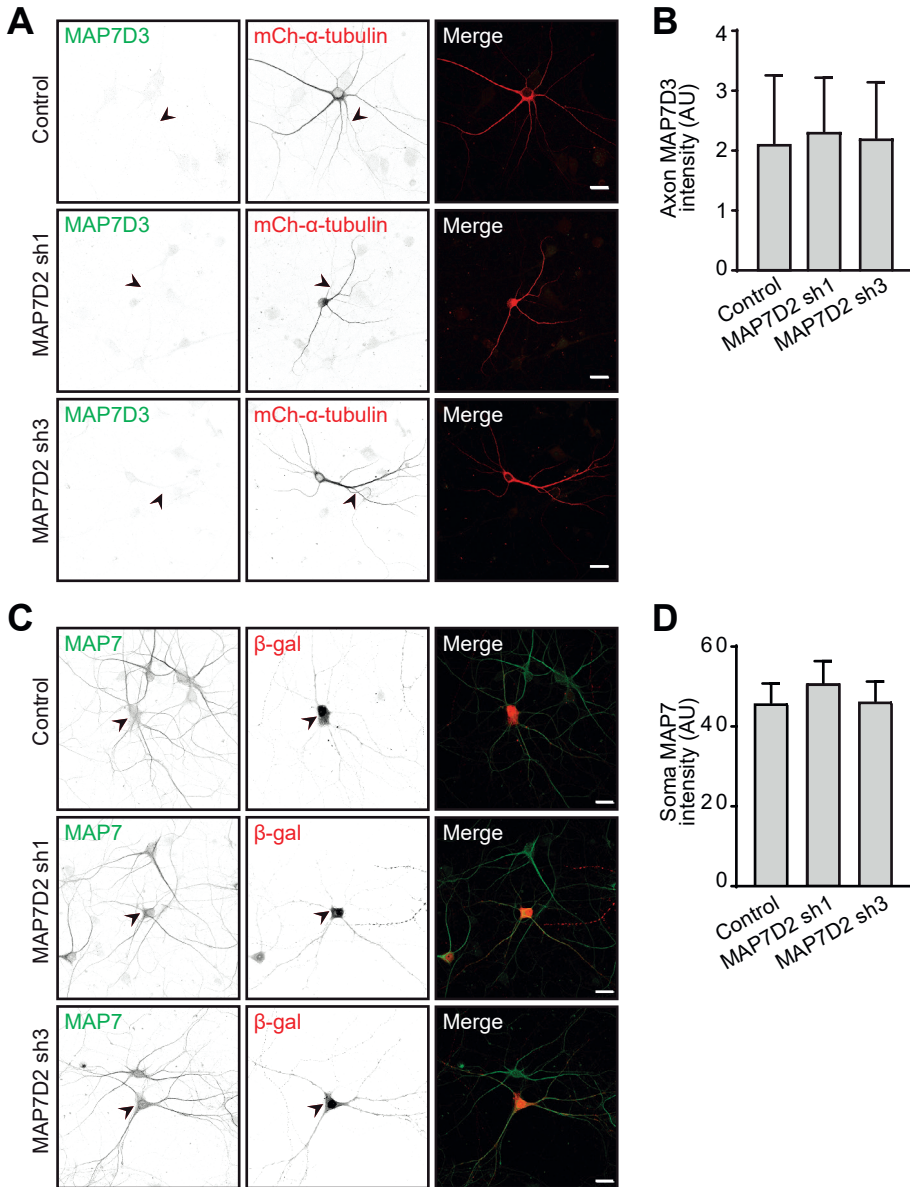Soma MAP7 intensity (AU): Control, MAP7D2 sh1, MAP7D2 sh3

3

Figure S5, related to Figure 3. MAP7D2 is important for axon formation and mouse cortical neuron migration.

(A) DIV3 neurons were transfected with control or MAP7D2 shRNAs together with a mCherry (red) fill, treated with 20 nM Taxol for 48 hours, and stained for TRIM46 (green). Arrow heads mark the axons. Scale bars: 20 μm

(B) Bar graph shows the numbers of TRIM46 positive neurites per neuron in control before (n=27) and after (n=59) Taxol treatment or MAP7D2 KD (sh1 (n=57) or sh3 (n=27)) after Taxol treatment.

(C) Percentage of DIV3 neurons electroporated with control, MAP7D2 sh1 and 3 constructs and quantified neurites positive for Tau or TRIM46, n>500 neurons for each condition.

(D) Quantifications of overexpression effect of Control (GFP empty) (n=63), GFP-MAP7D(2N_1C) (n=60) or GFP-MAP7D2 (n=57) on axon formation, TRIM46 antibody was used for marking the axon.

(E) Quantifications of overexpression effect of Control (GFP empty) (n=16), GFP-MAP7D(2N_1C) (n=12) or GFP-MAP7D2 (n=15) on axon branching, a β-galactosidase fill was used for tracing the axon morphology.

(F and G) Representative images of mouse cortex after 4 days of ex vivo electroporated with GFP and control or MAP7D2 shRNA. DAPI is in blue. Pail surface at the top and ventricle at the bottom are outlined in yellow. CP, cortical plate; IZ, intermediate zone; SVZ, subventricular zone; VA, ventricular zone. Right panels represent GFP only channel. Scale bars: 100 μm

(H) Quantifications of the normalized neuronal distribution along the radial axis from ventricle to the pail surface under control (N=5 embryos, n=8 slices), mCherry-MAP7D2 (N=3 embryos, n=7 slices), MAP7D2 shRNA (N=7 embryos, n=13 slices) and MAP7D2 shRNA plus mCherry-MAP7D2 (N=4 embryos, n=7 slices) for rescue.

$P < 0.05$ *; $P < 0.01$ **; $P < 0.001$ ***. Unpaired t-test. Error bars represents SEM.
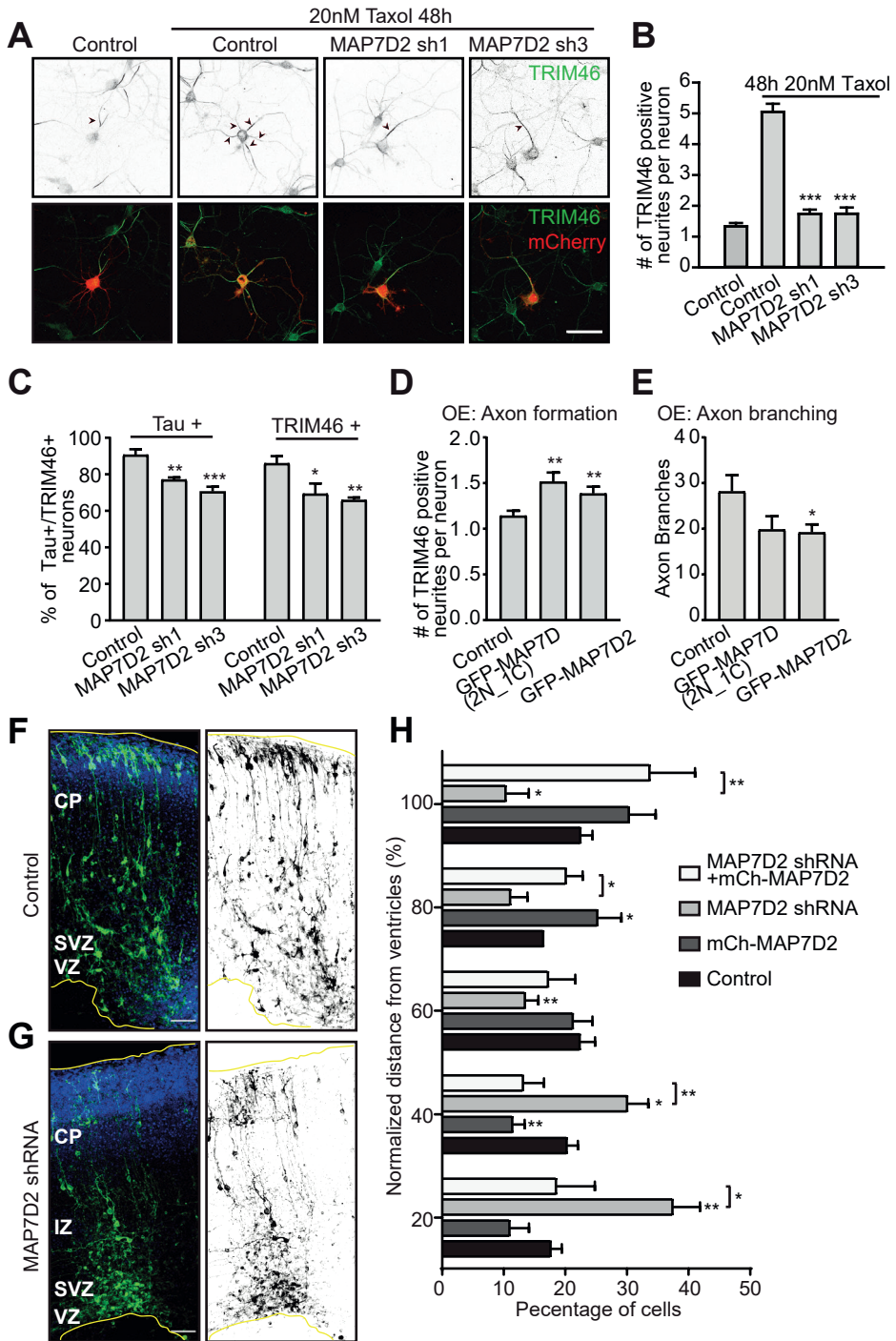
Figure S6, related to Figure 4, 5. MAP7D2 is important for recruitment of Kinesin-1 on microtubules, and affects mitochondria transport at distal axon.

(A) Representative images of COS7 cells co-transfected with KIF5C-MDC-GFP and mCherry-MAP7D2 or HA-MAP7D2-N in red. Cell borders are outlined in yellow. HA-MAP7D2-N lacks the C-terminal kinesin-1 binding domain.

(B) Representative images of neurons co-transfected with Rigor-KIF5A-GFP and Control or MAP7D2 shRNAs, and co-stained with TRIM46 for axon. Arrow heads indicate AIS.

(C) Polarity index of Rigor KIF5A-GFP in Control (n=17), MAP7D2 sh1 (n=15) and sh3 (n=20).

(D) DIV1 neurons were transfected with control or MAP7D2 shRNAs together with a GFP fill and mito-dsRed respectively for 3 days, and Representative images at the upper two panels shows mito-dsRed and GFP fill in the distal axon, kymographs at the bottom showing live cell imaging of mitochondria. Scale bars: 10 μm

(E) Quantifications for mitochondria anterograde movement along distal axon within 5 minutes under control (n=36), MAP7D2 sh1 (n=35) and MAP7D2 sh3 (n=36).

$P<0.05$ *; $P<0.01$ **; $P<0.001$ ***. Unpaired t-test. Error bars represents SEM.

Scale bars: 20 μm
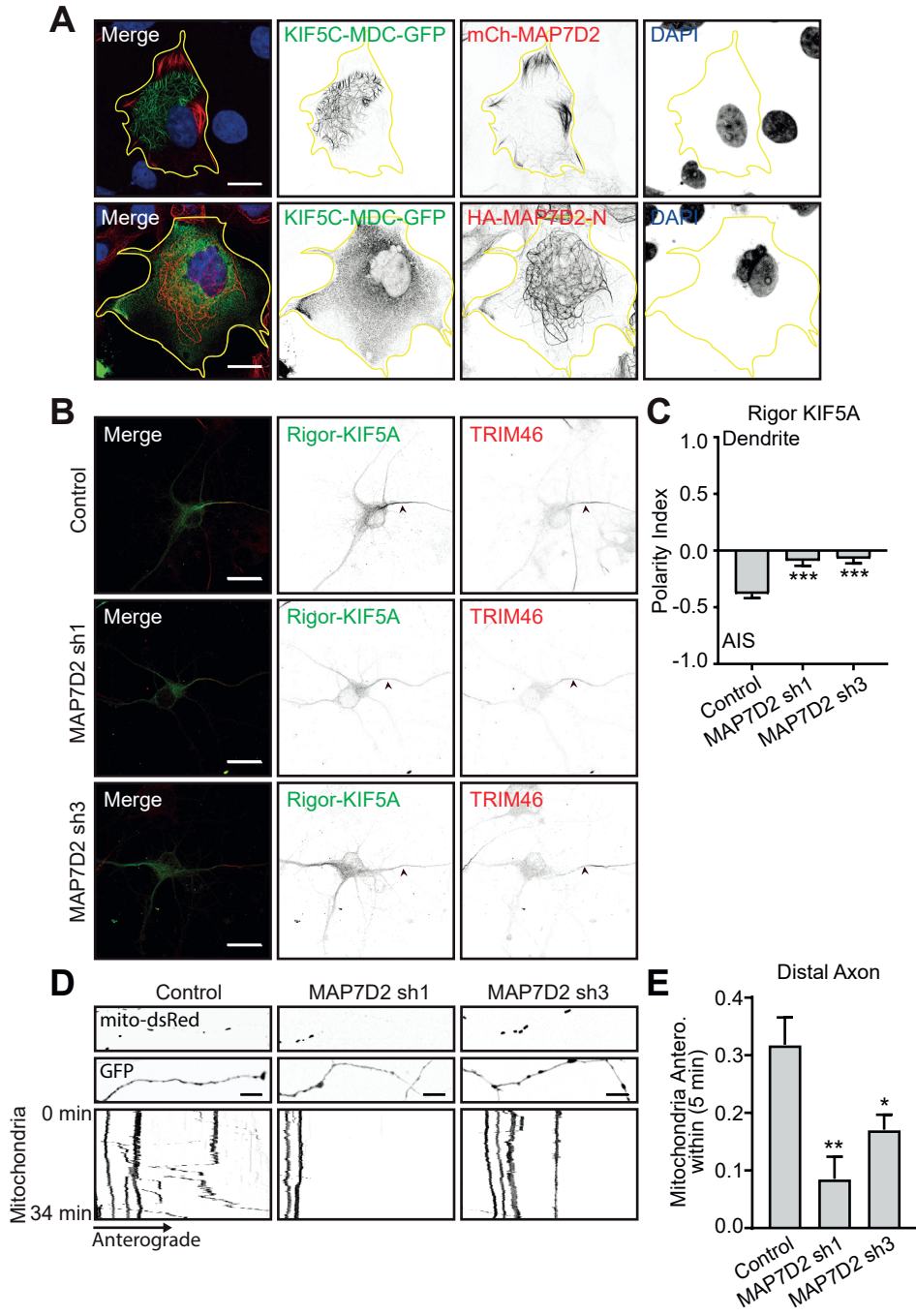
Chapter 4
The E3 ligase TRIM family members MID1 and MID2 associate with microtubules and control neurodevelopment

Xingxiu Pan[1], **Yujie Cao[1]**, Martin Harterink[1], and Casper C. Hoogenraad[1]

[1]Cell Biology, Department of Biology, Faculty of Science, Utrecht University, 3584 Utrecht, the Netherlands

This chapter is a collection of preliminary data.

ABSTRACT

The TRIM E3 ligase family member, TRIM46 has been identified as a microtubule-associated protein (MAP) which localizes to the axon initial segment (AIS) of the axon. TRIM46 is important for organizing parallel microtubule bundles in a plus-end out manner and is required for axon specification and neuronal polarization. The COS motif of TRIM46 is essential for microtubule binding. There are 10 TRIM proteins containing a COS motif that can be grouped in three TRIM subfamilies (CI, CII, CIII). However, it is not clear whether all COS domain containing TRIM family members are able to bind to microtubules and play a role in neuronal development. Here, we generated constructs for all 10 COS motif containing TRIMs, and observed that CI subfamily, MID1, MID2, TRIM46, TRIM36 are able to bind microtubules. Since the genes coding for MID1 and MID2 in humans are associated with intellectual disability, we further investigated the role of MID1/MID2 in developing neurons. We observed that both MID1 and MID2 are important for axonal development. Moreover, MID2 plays a role in dendrite development and controls dynamics and organization of dendritic microtubules.

4

INTRODUCTION

Ubiquitination and E3 ligases

The ubiquitin-proteasome system (UPS) is an important machinery to degrade proteins using three kinds of enzymes, a E1 ubiquitin-activating enzyme, a E2 ubiquitin-conjugating enzymes and a E3 ubiquitin ligase. In addition to targeting proteins for proteasomal degradation, ubiquitination plays key roles in re-localizing cellular factors and regulating protein activity.

During UPS mediated protein degradation, the substrate is covalently decorated with ubiquitin peptides through an enzymatic cascade where the E3 ligase confers for substrate specificity. TRIM family proteins (Hatakeyama, 2017), with more than 80 mammalian homologues, belong to the RING type E3 ubiquitin ligase family, which play various roles in apoptosis, protein quality control, autophagy, pathogenesis and oncogenesis. Many studies have shown that TRIM loss of function is associated with cancer, developmental disorders as well as disease in immune systems.

COS motif TRIM family proteins

TRIM family proteins share a conserved N-terminal RBCC (one Ringer finger/one or two B boxes/one coiled coil) domain, while their C-terminus contains diverse domains that control their subcellular distribution and function, such as COS domains, fibronectin type III repeats (FNIII), PRY domains, SPRY domains, acid-rich regions (ACID) and etc. By using bioinformatics, the COS motif containing TRIM proteins are classified into 3 subfamilies, CI (MID1, MID2, TRIM67, TRIM9, TRIM 36, TRIM46), CII (TRIM54, TRIM55, TRIM63), CIII (TRIM42) (Short and Cox, 2006). The COS motif was reported to direct TRIMs to microtubules potentially linking E3 ubiquitin ligase activity to microtubule cytoskeleton.

CI family TRIMs

TRIM46 specifically localizes to the newly specified axons and is enriched in the initial part of the axon. It forms uniformly oriented microtubule bundles with their plus-end out and is required for axon specification and neuronal polarity. Heterologous overexpression of TRIM46 in cells induces closely spaced microtubule bundles linked by electron dense cross-bridges, which resembles the axon specific microtubule fascicles (van Beuningen et al., 2015). Recently, by using newly developed correlative light and electron microscopy approach, it was revealed that TRIM46 localizes to the electron dense cross-bridges and depletion of TRIM46 causes loss of microtubule fasciculations in the axon of mature neurons (Harterink et al., 2019). In addition, by in vitro reconstitution assays, it was reported that TRIM46 bundles parallel microtubules and specifically promotes growth of parallel-oriented microtubules (Fréal et al., 2019). Interestingly, the role of TRIM46 in axonal microtubule organization is probably independent of its E3 ligase activity, since putative substrates and enzymatic activity for TRIM46 have not been reported and no interaction with E2 ubiquitin-conjugating enzymes was found (Deshaies and Joazeiro, 2009; Napolitano et al., 2011).

4

TRIM36, the closest paralog of TRIM46, is also a microtubule-associate protein, which plays a role in in acrosome exocytosis (Kitamura et al., 2003). Two studies done in Xenopus (Cuykendall and Houston, 2009; Yoshigai et al., 2009) demonstrated that TRIM36 has a role in somite arrangement during embryogenesis. TRIM36 regulates cortical rotation and dorsal axis formation potentially through controlling protein stability required for microtubule polymerization and proper positioning of dorsal Wnt signal during early development. Recently, it has been shown that TRIM36 is upregulated in prostate cancer and to be a novel androgen-responsive gene (Liang et al., 2018), which dramatically enhances the efficacy of anti-androgen drugs against prostate cancer (Liang 2018). TRIM36 can associate with kinetochore protein CENP-H, and overexpression of TRIM36 delays cell cycle progression and suppresses cell proliferation of NIH3T3 cells (Miyajima et al., 2009) and prostate cancer cells (Kimura et al., 2018; Liang et al., 2018). Moreover, homozygous missense mutation c.1522C > A (p.Pro508Thr) in the TRIM36 gene correlates with Anencephaly, characterized by lack of brain tissues and cranium (Singh 2017), suggesting a role for TRIM36 during early brain development (Singh et al., 2017). However, whether and how TRIM36 functions in the development of the central nervous system remains largely unknown.

MID1 gene mutations are associated with the X-linked form of Opitz G/BBB syndrome (OS) (De Falco et al., 2003), a disorder that is characterized by defects along body midline, such as hypertelorism, hypospadias, cleft lip and/or palate and is sometimes accompanying cardiac and neurological defects. OS disease related mutations are found along the MID1 gene. Since mutations do not correlate with specific clinical symptoms, it is hard to uncover molecular mechanisms that underly the OS disease onset (Cox et al., 2000). MID1 can bind to microtubules through the COS domain and MID1 patient mutations in the C-terminus show a reduced affinity for microtubules (Short and Cox, 2006). However, the mechanisms of how MID1 mutants affect microtubule network and lead to disease is unknown. Previous studies revealed that MID1 can bind to alpha4, the regulatory subunit of protein phosphatase 2A (PP2A), and guide PP2A for proteasomal degradation (Trockenbacher et al., 2001). The MID1-PP2A complex has been shown to play important roles on regulating Tau-phosphorylation and A-ß generation related to Alzheimer's disease (Hettich et al., 2014; Kickstein et al., 2010), promoting allergen and rhinovirus-induced asthma (Collison et al., 2013) and regulating axon development in mouse cortical neuron both in vitro and in vivo (Lu et al., 2013). However, the mechanisms of how MID1 regulates neuronal development is yet to be determined.

MID2 is a close paralog of MID1. They share 80% similarity in amino acid sequence and MID2 is supposed to bind to microtubules as well. It was shown to promote cytokinesis by targeting the intercellular bridge microtubule stabilizing protein Astrin for proteasomal degradation (Gholkar et al., 2016). The MID2 R347Q mutation in COS motif abolishes its microtubule binding affinity and is associated with X-linked intellectual disability (Geetha et al., 2014). But mechanisms of how MID2 contributes to the microtubule cytoskeleton in developing neurons is unknown. The coiled-coil region of MID1 mediates homo-dimerization as well as heterodimerization with MID2 (Short et al., 2002). Although it is not clear whether

MID1 / MID2 hetero-oligomers exist under physiological conditions, it is essential to study these two proteins together.

TRIM9, a brain specific E3 ligase, is mainly expressed in neurons in the cerebral cortex and hippocampus as well as the Purkinje cells of the cerebellum (Berti et al., 2002). Its expression level is reduced in the affected brain areas in Parkinson's disease and dementia with Lewy bodies (Tanji et al., 2010). Studies in invertebrates and mammals have revealed that TRIM9 plays a role in regulating netrin-dependent axon guidance, through the interaction with vasodilator-stimulated phosphoprotein (VASP), and the Netrin receptor Deleted in Colorectal Cancer (DCC) (Aiken and Buscaglia, 2016; Menon et al., 2015; Plooster et al., 2017). TRIM9 also plays a role in innate immune system, and is essential for resolving neuroinflammation to promote recovery and repair after brain injury, through regulating β-TrCP activity that turns off the NF-κB signaling pathway (Shi et al., 2014; Zeng et al., 2019).

TRIM67 is the least studied vertebrate Class I TRIM. Two studies show that TRIM67 is expressed in the mouse and human brains and to regulate neuritogenesis in a mouse neuroblastoma cell line (Yaguchi et al., 2012). It interacts with its paralog TRIM9 and the netrin receptor DCC, and is required for proper brain development, cognitive ability, and social behavior in mice (Boyer et al., 2018).

Class II family TRIMs or muscle-specific RING finger (MURF) family proteins

CII family proteins TRIM54/MURF3, TRIM55/MURF2, TRIM63/MURF1 are highly conserved paralogues. They localize to the sarcomere. They form homo- or hetero-oligomers using their coiled coil domains and regulate muscle protein turnover though their E3 ligase activity (Centner et al., 2001). CII family proteins were identified as muscle atrophy-related genes and function redundantly in ubiquitin dependent protein degradation in striated muscles. TRIM54 and TRIM63 double knockout (DKO) mice display hypertrophic cardiomyopathy and skeletal muscle myopathy (Fielitz et al., 2007), characterized by abnormal accumulation of myosin, which is reminiscent of myosin storage myopathy (MSM) in humans. TRIM55 or TRIM63 single KO mice display normal muscles, whereas DKO mice develop sever cardiac and mild skeletal hypertrophy (Witt et al., 2008). The muscle hypertrophy is likely associated with enhanced muscle protein synthesis in DKO mice.

TRIM54 and TRIM55 were shown to localize to the glutamylated microtubules during myogenesis both in vitro and in vivo (Perera et al., 2011; Spencer et al., 2000). Glutamylated microtubules are accumulating during myogenesis and are likely making the stable microtubule arrays required for active transport of proteins for building sarcomeres (Pizon et al., 2005). These observations suggest that CII TRIM subfamily members likely bind to and stabilize microtubules in striated muscle cells.

Class III subfamily protein

TRIM42 is the only member of the Class II family. However, no studies have addressed the function of this protein. In this study, we generated constructs for the

4

Figure 1 Classification of COS domain Tripartite Motif (TRIM) Family Proteins
(A)Schematic domain structure of TRIM CI (MID1, MID2, TRIM36, TRIM46, TRIM9 and TRIM67), CII (TRIM54, TRIM55 and TRIM63), CIII (TRIM42) subfamily proteins. Abbreviations: R, RING-finger domain; B1, B-box domain 1; B2, B-box domain 2; CC, coiled-coil domain; COS, cos box; FN3, fibronectin type III repeat; PRY, PRY domain; SPRY, SPRY domain.
(B)Alignment of COS motif amino acid sequences for TRIMs from human, rat and mouse.
(C)Phylogenetic tree analysis for the COS motif of human TRIM proteins . Bold characters are TIRMs that can bind microtubules.
(D)Representative images of COS7 cells transfected with GFP-MID1, MID2-GFP, TRIM36-GFP and TRIM46-GFP, stained for α-tubulin (red).
(E)Representative images of COS7 cells transfected with GFP-TRIM54, TRIM55-HA, TRIM63-HA and TRIM9-HA, stained for α-tubulin (red).
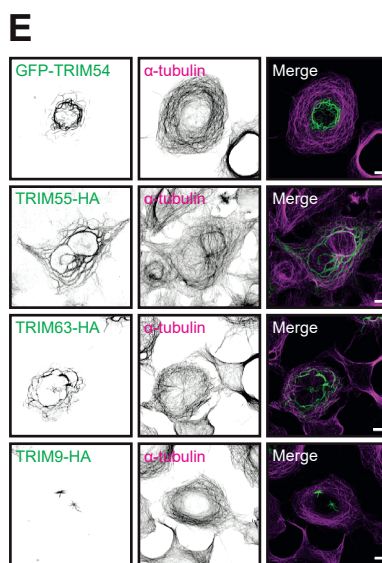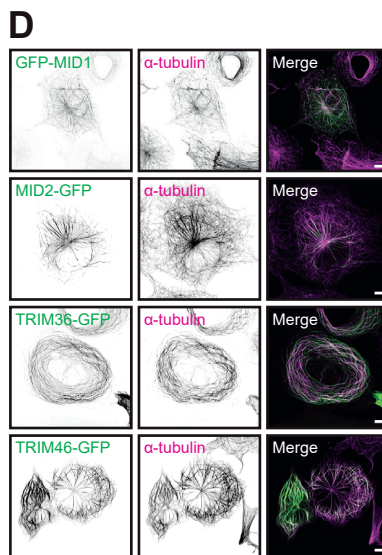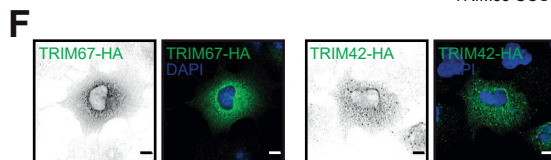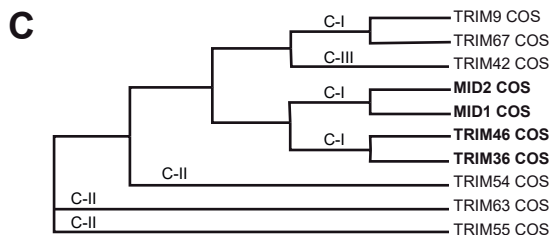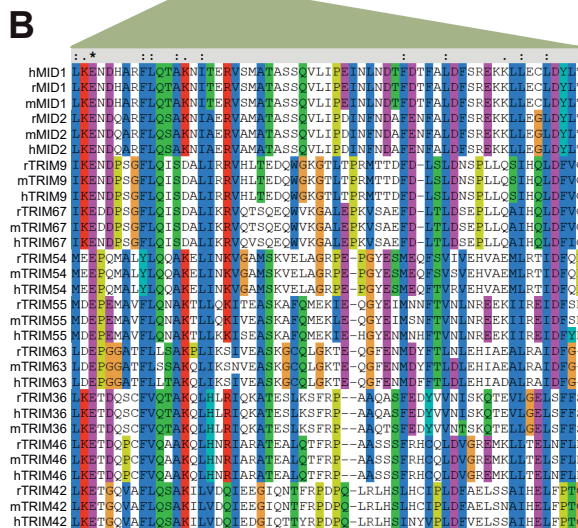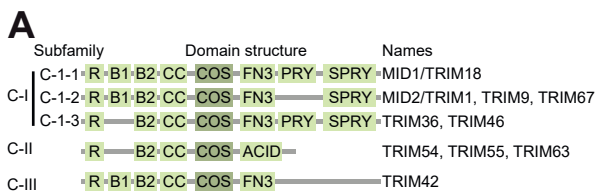(F)Representative images of COS7 cells transfected with TRIM67-HA and TRIM42-HA, Nucleus is marked with DAPI (blue). Scale bars: 10 μm (D, E, F)

10 COS motif containing TRIMs, and observed that the CI subfamily, MID1, MID2, TRIM46, TRIM36 are able to bind microtubules. we used live cell imaging and fixed super resolution imaging techniques to determine the microtubule binding properties of MID1 and MID2. We show that MID1 prefers to bind to single dynamic microtubules, whereas MID2 densely coats microtubules and makes microtubule immobile. Both MID1/MID2 are important for axonal development. Moreover, MID2 depletion impaired dendritic development and reduced the dynamics of plus-end out microtubules in dendrites. Our study reveals important roles of MID1 and MID2 in neuronal development, which might provide new insights in understanding MID1 and MID2 related diseases.

RESULTS

Not all COS motif containing TRIMs bind to microtubules

The unique COS motif in TRIM proteins was reported to be essential for microtubule binding. By using bioinformatics (Short and Cox, 2006), the COS motif containing TRIM proteins were classified into 3 subfamilies, CI (MID1, MID2, TRIM67, TRIM9, TRIM36, TRIM46), CII (TRIM54, TRIM55, TRIM63), CIII (TRIM42) (Figure 1A,1B). To validate if all the COS motif TRIMs were able to bind to microtubules, we cloned these genes and expressed them in COS7 cells. We found that MID1, MID2, TRIM36, and TRIM46 (all from the CI subfamily) are able to bind to microtubules (Figure D), while the rest either form filaments (TRIM9, TRIM54, TRIM55, TRIM63) around the nucleus (Figure 1E) or show a cytoplasmic localization (TRIM67, TIRM42) (Figure 1F). TRIM9, TRIM54, TRIM55 and TRIM63 form filaments which do not overlap with alpha-tubulin antibody staining (Figure 1E). To exclude the possibilities that the lack of colocalization was caused by antibody penetration problems, we expressed RFP tagged alpha-tubulin together with TRIM9 or TRIM55 in COS7 cells. Again, no colocalization was observed. Moreover, depolymerization of microtubules using nocodazole did not affect the filaments and no colocalization was observed between filaments and newly formed microtubules after washing out nocodazole (Figure 2A, 2B). These results suggest that TRIM9 and CII subfamily members are not microtubule binding proteins. In

A Subfamily / Domain structure / Names

C-I
C-1-1 R·B1·B2·CC·COS·FN3·PRY·SPRY MID1/TRIM18
C-1-2 R·B1·B2·CC·COS·FN3——SPRY MID2/TRIM1, TRIM9, TRIM67
C-1-3 R——B2·CC·COS·FN3·PRY·SPRY TRIM36, TRIM46

C-II R——B2·CC·COS·ACID—— TRIM54, TRIM55, TRIM63

C-III R·B1·B2·CC·COS·FN3———— TRIM42

B

C

D

E

F

4

111

addition, we found no colocalization between TRIM54 and the ER marker Sec61 or intermediate filament marker Vimentin (Figure 3A-C). Finally, a phylogenetic tree analysis based on the COS motifs shows that proteins that are able to bind microtubules tend to cluster together (Figure 1C). Taken together, these data suggest that not all COS motif TRIM family proteins are able to bind to microtubules.

MID1 and MID2 associate with microtubules

To further test the effect of MID1 and MID2 on microtubules, we performed nocodazole experiments to see if MID1/MID2 are able to protect microtubule from depolymerization. Consistently, both MID1 and MID2 colocalize with microtubules before drug treatment. Upon nocodazole treatment, MID1 becomes cytosolic, whereas MID2 becomes punctate. Moreover, MID1 and MID2 relocate to newly formed microtubules within 30 min after nocodazole wash out (Figure 2C, 2D). These data suggest that MID1 and MID2 bind to microtubules but cannot protect microtubules from depolymerization by nocodazole.

Microtubule heterogeneity is generated by different kinds of post-translational modifications (PTMs), which can affect microtubule stability. In addition, PTMs can also affect MAP attachment to microtubules. To determine which subset of microtubules MID1 and MID2 prefer, we expressed MID1 and MID2 in COS7 cells and stained for tyrosinated tubulin for dynamic microtubules and acetylated tubulin for stable microtubules. We found that MID1 overlaps more with tyrosinated microtubules (Figure 4A,B), while surprisingly MID2 shows no overlap with either tyrosinated or acetylated microtubules (Figure 4C,D). Since MID2 strongly bundles microtubules, and may block the antibodies from reaching the microtubule epitope. To validate this, we expressed an mCherry tagged alpha-tubulin together with MID2 in COS7 cells, and then stained again for alpha-tubulin. We found that MID2 colocalizes with mCherry-tubulin (Figure 4E,F). Furthermore, we successfully observed MID2 associated microtubules colocalize with acetylated tubulin after methanol fixation (Figure 4G,H). Since the thinner microtubule bundles, which MID2 decorated in the low MID2 expressing cells are both tyrosinated and acetylated, this suggests that MID2 has no preference for these PTMs. Taken together, these data suggest that MID1 binds to dynamic microtubules while MID2 has no preference for dynamic or stable microtubule.

MID2 colocalizes with CAMSAP3 in COS7 cells

To further study the effect of MID2 on microtubules, we performed live cell imaging on MID2 expressing COS7 cells. We found that MID2 decorated microtubules are immobile (data not shown), as if MID2 anchors microtubules to other cellular structures. From the literature, microtubule minus-end binding protein CAMSPAP3 can anchor microtubules to apical cortices of epithelial cells, also forms similar immobile stretches (Toya et al., 2016). To test if MID2 behaves similar to CAMSAP3, we co-expressed them in COS7 cells, surprisingly we observed colocalization between MID2 and CAMSPAP3 on microtubule bundles (Figure 5A,B). We also observed MID2 is co-transported with CAMSAP3 in low expressing cells (Figure 5C,D). On the other hand, MID1 does not colocalize with CAMSAP3 (Figure 5E,F), instead MID1 binds to dynamic microtubules which is consistent with
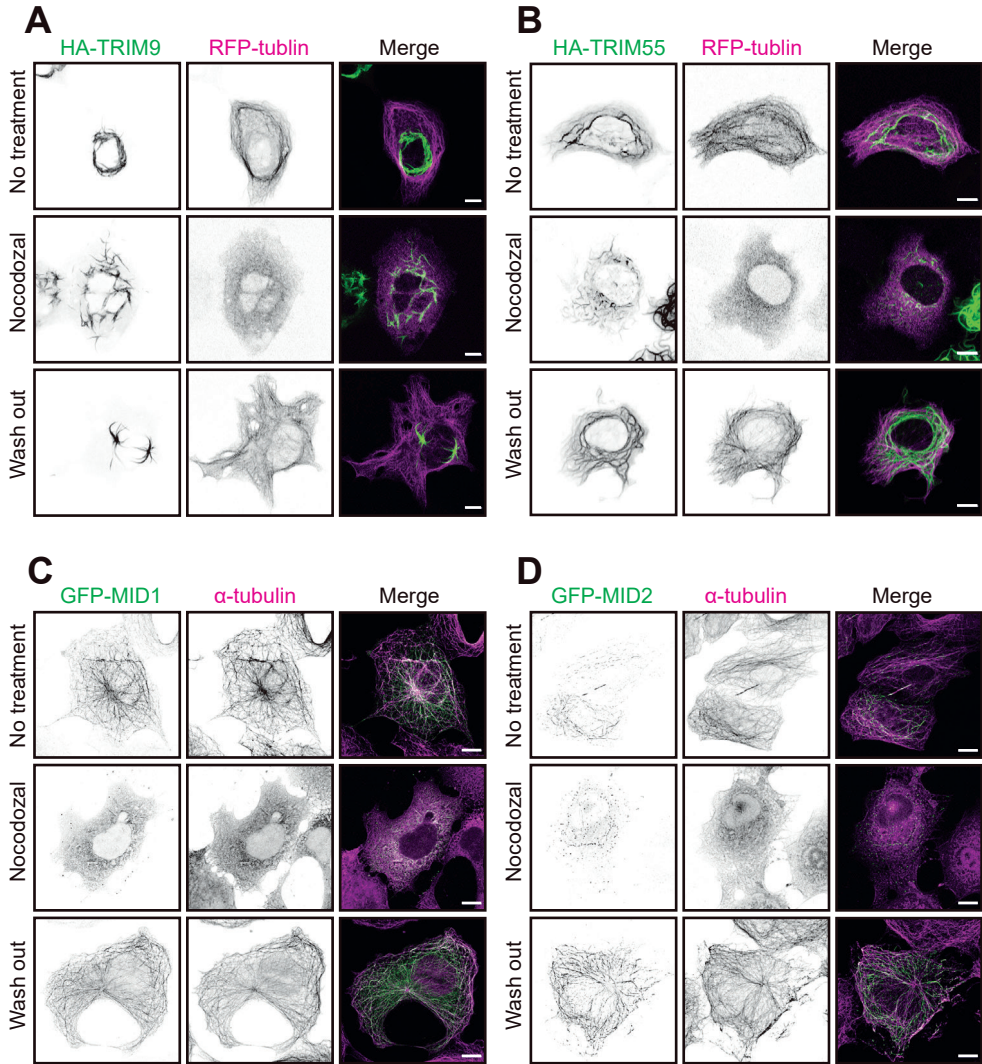
Figure 2 MID1 and MID2 bind microtubules.

(A,B) COS7 cells were transfected with HA-TRIM9 or HA-TRIM55 together with RFP-tubulin (red) for 24 hours, the first rows are control without drug treatment, the second rows are treated with Nocodozal and the third rows are nocodazole wash out condition. Scale bars: 10 µm.

(C,D) COS7 cells were transfected with GFP tagged MID1 or MID2, after 24 hours cells were fixed and stained for α-tubulin (red)., the first rows are control without drug treatment, the second rows are treated with nocodazole and the third rows are nocodazole wash out condition. Scale bars: 10 µm.

our findings that MID1 prefers tyrosinated microtubules. Taken together, these data indicate that MID2 prefers to bind CAMSAP3 decorated microtubules, while MID1 binds to dynamic microtubules.

MID1 is enriched in axons, MID2 mainly forms puncta and stretches in somatodendritic compartments and the proximal axon

MID1 and MID2 are both associated with mental retardation, indicating roles in neuronal development and/or functioning. Thus, we looked at the expression patterns in rat hippocampal neurons. Exogenous expression of MID1 and MID2 in neurons shows that MID1 is enriched in axons while MID2 mainly forms puncta in the soma, dendrites and the proximal axon (Figure 6A-D).

To determine the dynamics of MID1 and MID2 in neurons, we performed fluorescence recovery after photobleaching (FRAP) experiments using GFP-tagged proteins. We found that MID1 quickly recovers to 90% 50s after bleaching, while MID2 recovers much slower than MID1 (Figure 6E-H). Together these data indicate that MID1 dynamically localizes to the axon, while MID2 stretches and puncta are less dynamic in neurons.

MID1 and MID2 are both important for axon development

Since MID1 is enriched in axons, we tested whether MID1 is involved in axon development. We found that developing DIV4 neurons depleted of MID1 by either shRNA #3 or #4 show similar phenotypes; reduced axon branching and total length, increased average length and primary axon length compared to control neurons (Figure 7A,B). The decreased axonal branching and total length upon MID1 depletion is against a previous study done in mouse cortical neurons, which showed increased total axon length and axonal branching upon knockdown of MID1. Therefore, we made a similar shRNA to what was used in that study and tested it in rat hippocampal neurons. We observed similar phenotypes as for our shRNA #3 and #4 for reduced axon branching, but not for the total length. Moreover we were able to rescue the axon branching phenotype by re-expression of MID1 (Figure 7C,D). Taken together, these results suggest that MID1 promotes axon branching in rat hippocampal neurons. We observed similar axonal branching phenotypes with MID2 shRNA #1, #3 and #4, although the total axonal length was increased (Figure 7E,F). Together these data indicate that both MID1 and MID2 are important for axon development.

MID2 is important for dendrite development and plus-end out microtubule dynamics in dendrites

Since MID2 is enriched in the somatodendritic compartment, we determined the effect of MID2 depletion on dendritic development. We depleted neurons from DIV11 to DIV14 and analyzed their dendritic morphology (Figure 8A). Upon MID2 depletion, we observed less primary dendrites and less complexity of dendritic arbors as revealed by Sholl analysis. The phenotype of fewer primary dendrites can be fully rescued by re-expressing full length mCherry-MID2, and the complexity of dendritic arborization can be partially rescued (Figure 8B,C). We next determined
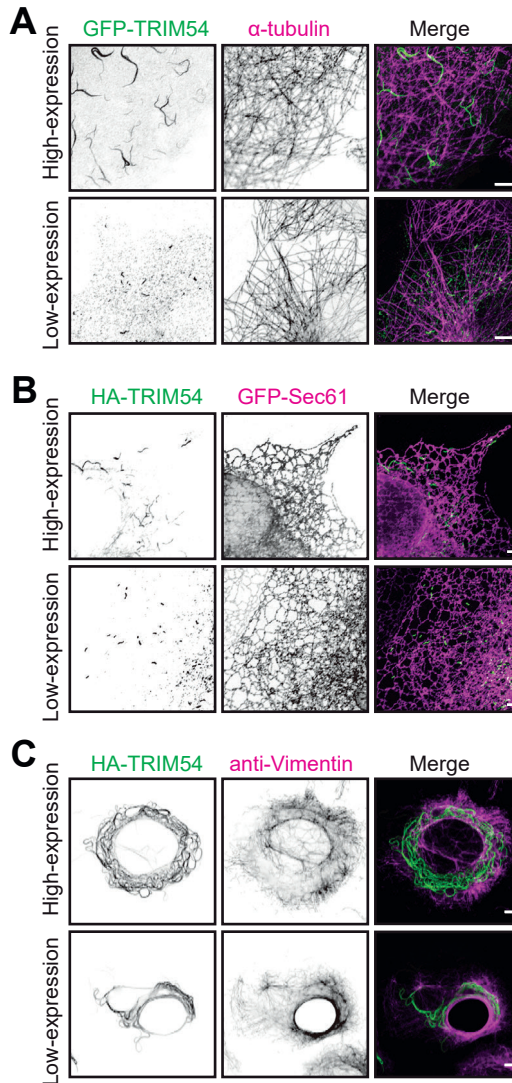
Figure 3 CIII family TRIM54 does not associate with microtubules, endoplasmic reticulum or intermediate filaments.

(A) COS7 cells were transfected with GFP tagged TRIM54, fixed and stained for α-tubulin (magenta) after 24 hours, the upper panels are high expressing cells, and the bottom panels are low expressing cells. Scale bars: 5 μm.

(B) COS7 cells were transfected with HA tagged TRIM54 and GFP tagged Sec61 (magenta), the upper panels are high expressing cells, and the bottom panels are expressing cells. Scale bars: 2 μm.

(C) COS7 cells were transfected with HA tagged TRIM54, after 24 hours cells were fixed and stained for Vimentin (magenta), the upper panels are expressing cells, and the bottom panels are low expressing cells. Scale bars: 5 μm.

Figure 4 MID1 prefers dynamic microtubules while MID2 prefers stable microtubules.

(A) COS7 cells were transfected with GFP tagged MID1, fixed and stained for Tyr-tubulin (magenta) and Acetyl-tubulin (blue) after 24 hours. Scale bars: 2 μm.

(B) Intensity profiles of each channel along the white line with arrow head are shown.

(C) COS7 cells were transfected with GFP tagged MID2, after 24 hours cells were fixed and stained for Tyr-tubulin (magenta) and Acetyl-tubulin (blue). Bottom panel is an enlargement of the boxed area. Scale bars: 2 μm.

(D) Intensity profiles of each channel along the white line with arrow head are shown.

(E) COS7 cells were transfected with GFP tagged MID2 together with mCherry-tubulin (magenta), fixed and stained for α-tubulin (blue) after 24 hours. Scale bars: 2 μm.

(F) Intensity profiles of each channel along the white line with arrow head are shown.

(G,H) COS7 cells were transfected with GFP tagged MID2, fixed and stained for Acetyl-tubulin (red) after 24 hours. Scale bars: 5 μm.

microtubule dynamics and orientation in neurons, which is critical for shaping dendrites. Neurons were transfected with either control or MID2 shRNA together with the microtubule plus-end marker GFP-MT+TIP at DIV9 and imaged at DIV12 (Figure 8D). We observed around 30% GFP-MT+TIP comets are minus-end out (retrograde) oriented microtubules and about 70% +TIP comets are plus-end out (anterograde) in dendrites of control neurons, while depletion of MID2 leads to a reduction in anterograde GFP-MT+TIP comets. This phenotype was rescued by mCherry-MID2 (Figure 8E). Moreover, we found no effect of MID2 on microtubule dynamics and organizations in axons, where over 90% +TIP comets are plus-end out in both control and MID2 depletion neurons (Figure 8C). These results suggest that MID2 specifically affects dynamics of plus-end out microtubules in dendrites and is important for dendritic development.

DISCUSSION

Homotypic and heterotypic interactions have been observed among TRIM proteins (Hatakeyama, 2017). For instance, MID1 can form homo-oligomers or hetero-oligomers with MID2 and TRIM27, while MID2 can also form homo-oligomers or hetero-oligomers with MID1, TRIM27, TRIM29, TRIM32, TRIM42 and TRIM54. We have unpublished data showing that TRIM46 can form hereto-oligomers with TRIM42 via the RING domain and with TRIM67 via C-terminal FN3/PRY/SPRY domain. Therefore, hetero-oligomerization of TRIM proteins may contribute to substrate recognition by switching their binding partners, and to a role in the regulation of enzymes through molecular interaction or dominant-negative effects. Future studies are required to study TRIM proteins systematically and the effect of oligomerization.

In this study, we systematically assessed all COS motif containing TRIMs (CI,CII,CIII TRIMs), which are supposed to bind to microtubules (Short and Cox, 2006). However, we observed that only TRIM46, TRIM36, MID1 and MID2 from the CI subfamily are able to bind microtubules, suggesting that the presence of a COS motif is not enough to target TRIMs to microtubules. Other structures may contribute together with the COS motif to bind to microtubules. More studies
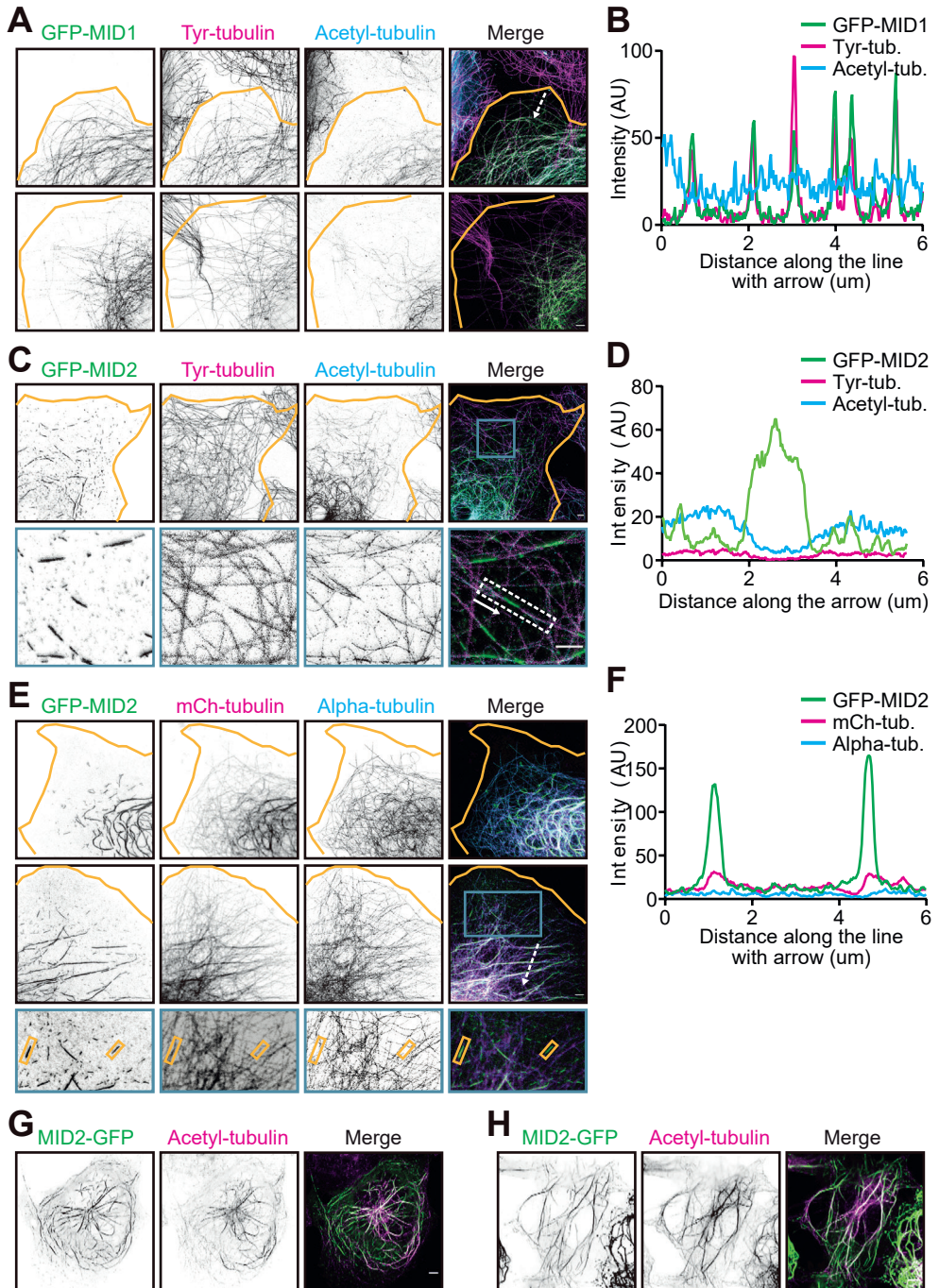
are needed to characterize minimum common microtubule binding domain in TRIMs. Our studies are based on exogeneous expression of plasmids, which could potentially induce artifacts. Using antibodies or CRISPR Knock-In strategies to study COS motif containing TRIMs will be required in the future.

In this study, we mainly focused on the MID1 and MID2 proteins. We found that MID1 binds single dynamic microtubules, while MID2 can bundle microtubules. MID2 decorated microtubule stretches are static, and colocalizes with CAMSAP3. Although MID1 and MID2 share 80% similarity in protein sequences, they bind to different subset of microtubules and the way they affect microtubules might be different. Furthermore, we found that MID1 localizes predominantly to the axons, while MID2 distributes mainly to the soma, to dendrites and to the proximal axon in cultured rat hippocampal neurons. The depletion of both MID1 and MID2 affect axonal development. We observed MID1 depletion reduced the axon branching and total length. The phenotype is against a previous study performed with mouse cortical neurons, which showed that MID1 depletion leads to increased axon branching and total length (Lu et al., 2013). We found consistent results for axonal branching in rat neurons using similar shRNA, but not for the total length. The defects in axon branching can be rescued by re-expressing full length mCherry-MID1. These data suggest that the function of MID1 for axon development is different from other species, or this difference might be the result of a difference in neuron culturing, such as differences in coating methods. Moreover, MID2 depletion decreased axon branching and increased total axon length, but the phenotype cannot be rescued by expressing mCherry-MID2. Considering that MID2 is absent from distal axon and mainly enriched in soma, the effect of MID2 on axon morphology is likely a secondary effect.

In this study, we investigate the role of MID2 in dendritic development. We observed that depletion of MID2 dramatically changes the dendritic arborization. MID2 depletion specifically affects the plus-end out microtubule dynamics in dendrites. Recent work has shown that most of the plus-end out microtubules are dynamic and spatially segregated to the outer dendrites, while minus-end out microtubules are stable and tend to distribute to the inner dendrites (Tas et al., 2017). Additionally, our results show that MID2 stretches in dendrites are immobile. It is tempting to speculate that MID2 bundles and anchors the newly generated plus-end out microtubules to other cellular structures in the outer dendrite, or that it serves as potential rescue points for a subpopulation of dendritic microtubules. Our study on MID2 provides new insights in the understanding of MID2 related X-linked intellectual disability. Future work is needed to characterize which cellular structure could anchor MID2 decorated microtubules.
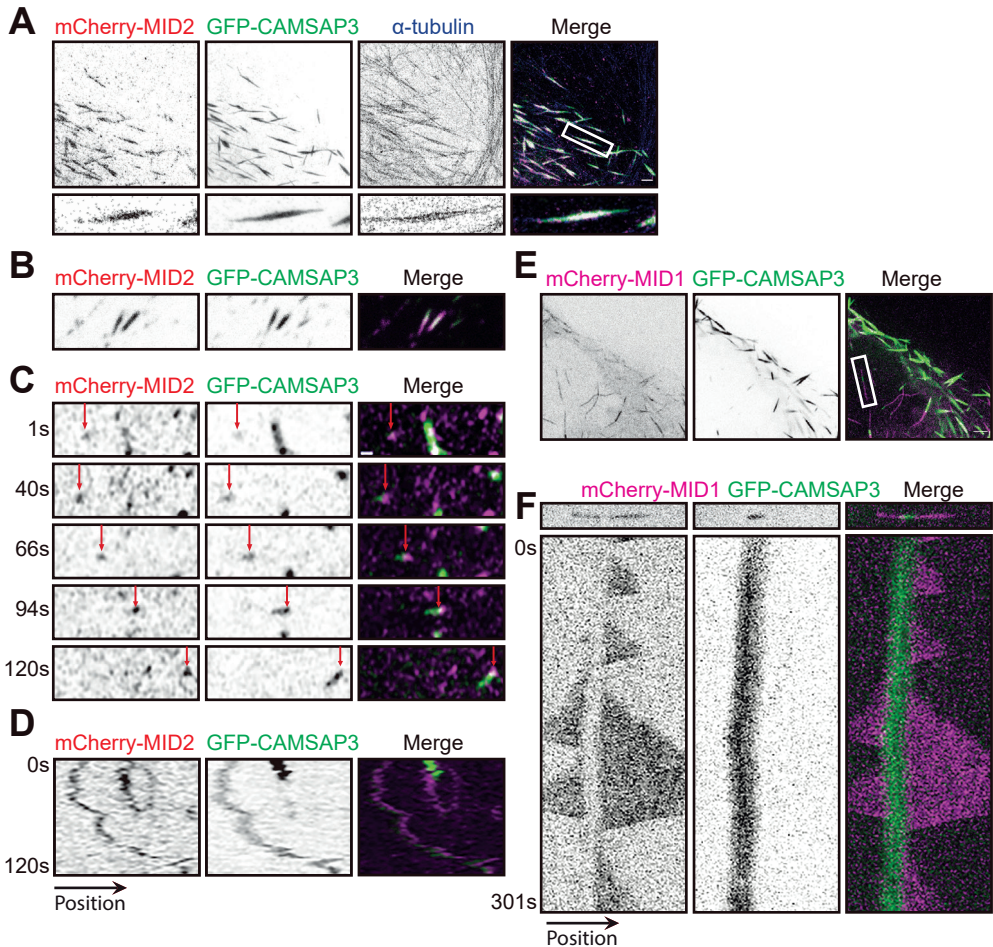
Figure 5 MID2 colocalizes with CAMSAP3, while MID1 decorates dynamic microtubules.

(A) COS7 cells were transfected with mCherry tagged MID2 together with GFP-CAMSAP3 (green), after 24 hours cells were fixed and stained for α-tubulin (blue). Bottom panel is an enlargement of the boxed area. Scale bars: 2 μm.

(B,C) COS7 cells were transfected with mCherry tagged MID2 together with GFP-CAMSAP3 (green), (B) representative images of MID2 stretches colocalizes with CAMSAP3. (C) Puncta MID2 and CAMSAP3 in different time points. Scale bars: 2 μm.

(D) Kymographs of mCherry-MID2 and GFP-CAMSAP3 in (C).

(E) Static images of COS7 cells transfected with mCherry tagged MID1 together with GFP-CAMSAP3 (green).

(F) Upper panels are enlargement of boxed area in (E), bottom panels are kymographs of mCherry-MID1 and GFP-CAMSAP3 within 5 min.

4

Figure 6 MID1 is enriched in axons while MID2 mainly forms puncta in the soma, dendrites and proximal axon.

(A-D) DIV11 neurons transfected with GFP tagged MID1 (A) or MID2 (C) together with mCherry-tubulin as fill. Middle yellow panels are zooms in of the boxed area in dendrites, the bottom panels are enlargement of the green boxed area of axons. (B) Bar graph shows the polarity index of MID1. (D) Bar graph shows the density of MID2 puncta along axons and dendrites. Scale bars: 20 μm.

(E, F) Representative FRAP images of axonal GFP-MID1 (E) or dendritic GFP-MID2 puncta (F).

(G, H) Averaged normalized intensity of the FRAP region for GFP-MID1 (E) in axons (n=5) and GFP-MID2 in dendrites (n=7). Error bars represents SEM.

A GFP-MID1 mCh-tubulin Merge

Dendrite

Axon

B

Polarity Index — Dendrite / Axon — MID1

C GFP-MID2 mCh-tubulin Merge

Dendrite

Axon

D

# of MID2 punctas/µm — Axon / Dendrite

E MID1 Axon

Prebleach, 0s, 6s, 21s, 51s, 171s

G MID1 FRAP Axon

Normalized fluorescence (%) vs Time (s)

F MID2 Dendrite

Prebleach, 0s, 6s, 21s, 51s, 171s

H MID2 puncta FRAP Denridte

Normalized fluorescence (%) vs Time (s)

4
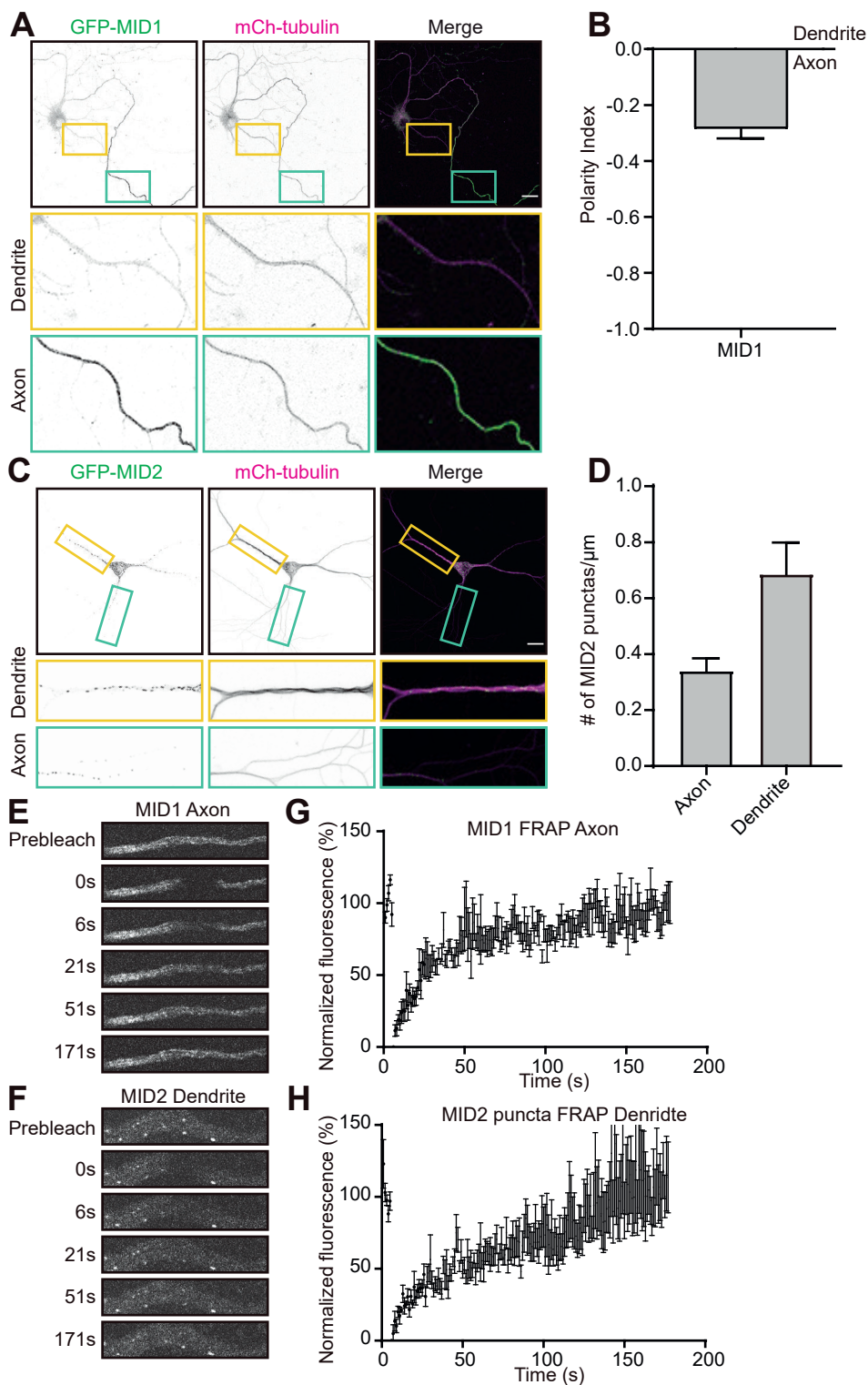
Figure 7 MID1 and MID2 are important for axon development.

(A) Representative images of DIV4 neurons transfected with control or MID1 shRNAs together with GFP fill. Scale bars: 50 μm.

(B) Quantifications of the numbers of axon branches, total axon length, average length and primary axon length of indicated conditions. Control (n=19), MID1 sh2 (n=14), MID1 sh3 (n=14), MID1 sh4 (n=20).

(C) Representative images of DIV4 neurons transfected with GFP as fill together with control, MID1 sh5 or sh5 in the presence of MID1 as rescue. Scale bars: 50 μm.

(D) Quantifications of the numbers of axon branches, total axon length, average length and primary axon length of indicated conditions. Control (n=28), MID1 sh5 (n=26) and MID1 sh5 in the presence of mCherry-MID1 (n=15) as rescue.

(E) Representative images of DIV4 neurons transfected with control or MID2 shRNAs together with GFP fill. Scale bars: 50 μm.

(F) Quantifications of the numbers of axon branches, total axon length, average length and primary axon length of indicated conditions. Control (n=15), MID2 sh1 (n=16), MID2 sh2 (n=15), MID2 sh3 (n=15), MID2 sh4 (n=13).

$P<0.05$ *; $P<0.01$ **; $P<0.001$ ***. Unpaired t-test. Error bars represents SEM.

4
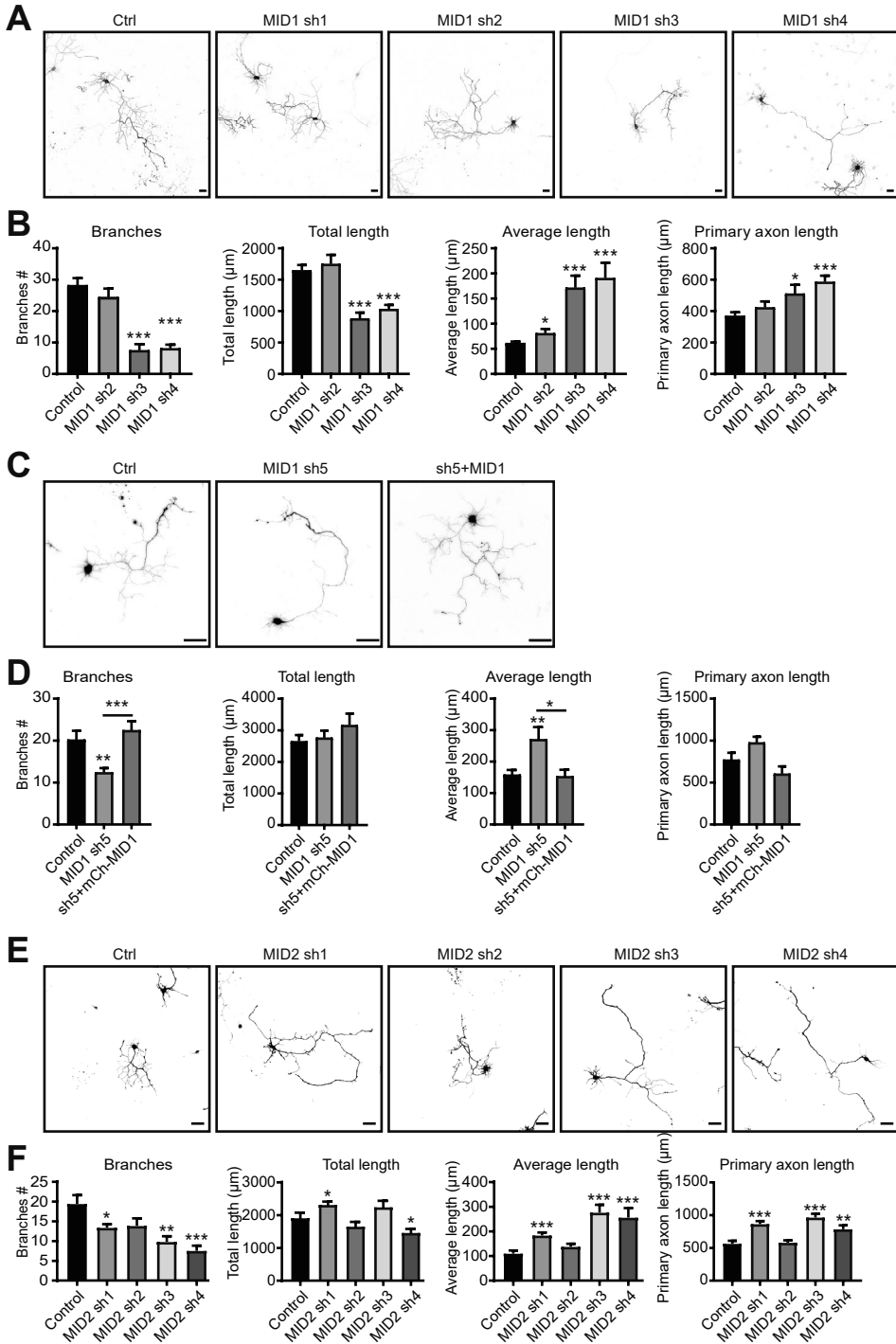
Figure 8 MID2 depletion impaired the complexity of dendritic arborization and plus-end out microtubule dynamics in dendrites

(A) Representative images of DIV14 neurons transfected with control or MID2 shRNA together with GFP fill. Dendritic morphology is filled with line in magenta. Scale bars: 50 μm.

(B) Quantifications of the numbers of primary dendrites of indicated conditions. Control (n=14), MID2 shRNA(n=14), MID2 shRNA plus mCherry-MID2 (n=14).

(C) Sholl analysis of dendritic branching at DIV14 in indicated conditions. Control (n=14), MID2 shRNA(n=14), MID2 shRNA plus mCherry-MID2 (n=14).

(D) Representative kymographs of DIV12 neurons transfected with control, MID2 shRNA or MID2 shRNA plus mCherry-MID2 together with GFP-MT+TIP. Right panels are drawing of the anterograde comets (green) and retrograde comets (red) in dendrites.

(E) Quantifications of the numbers of total, anterograde and retrograde comets of indicated conditions in dendrites. Right graph shows the ratio of anterograde comets in dendrites. Control (n=10), MID2 shRNA (n=15), MID2 shRNA+mCherry-MID2 (n=10).

(F) Quantifications of the numbers of total, anterograde and retrograde comets of indicated conditions in axons. Right graph shows the ratio of anterograde comets in axons. Control (n=9), MID2 shRNA (n=7).

$P<0.05$ *; $P<0.01$ **; $P<0.001$ ***. Unpaired t-test. Error bars represents SEM.
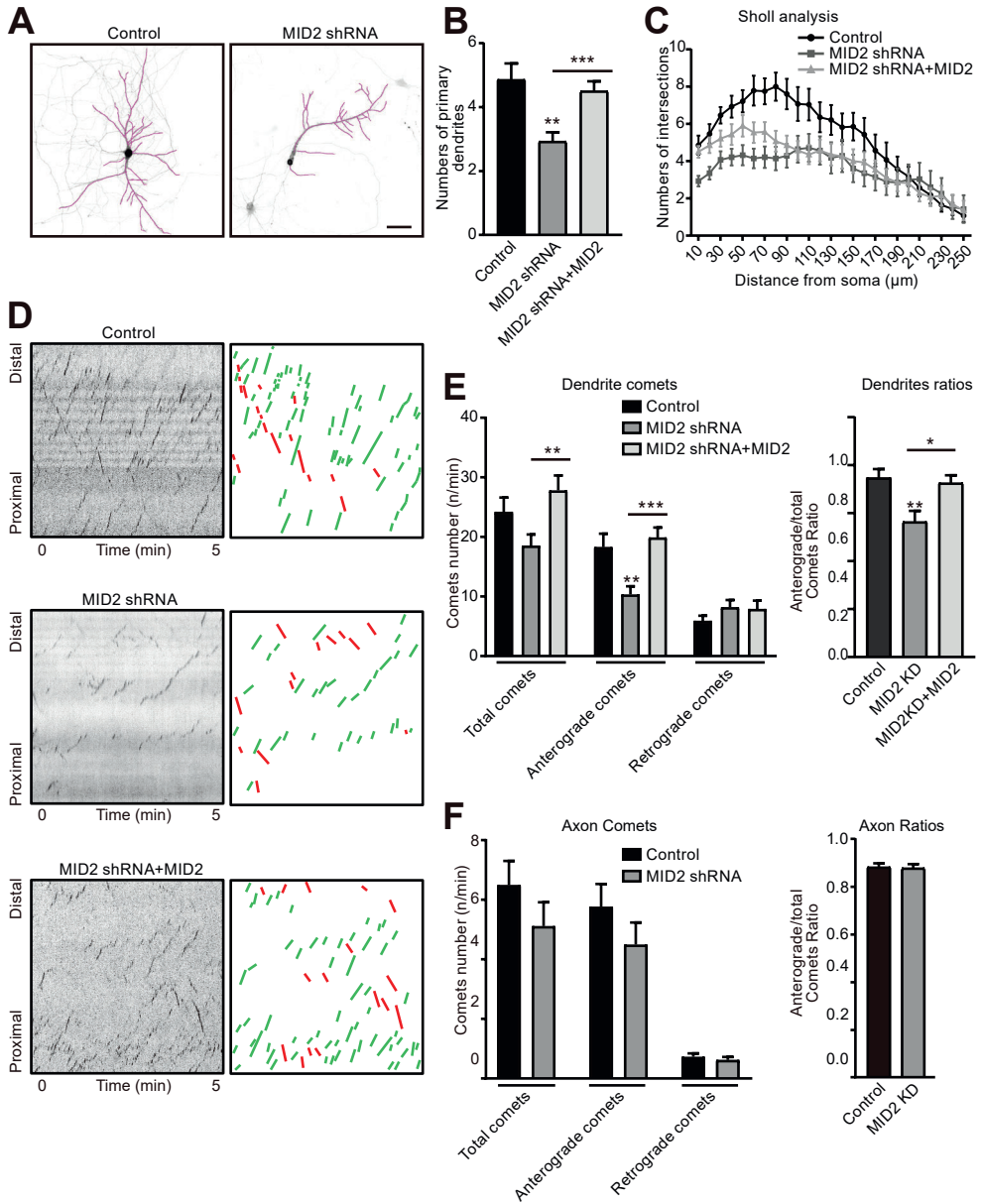
4

MATERIALS AND METHODS

Animals

All animal experiments were performed in compliance with the guidelines for the welfare of experimental animals issued by the Federal Government of the Netherlands, and were approved by the Animal Ethical Review Committee (DEC) of Utrecht University.

Antibody and reagents

The following antibodies were used for the immunofluorescence staining: mouse anti-mCherry (Clonetech, 632543); rabbit anti-GFP (Abcam, ab290), rat anti-HA (Roche, 1-867-423), mouse anti-alpha-tubulin (Sigma-Aldrich,T5168), mouse anti-acetylated-tubulin (Sigma-Aldrich, T7451), rat anti-tyrosinated-tubulin (Abcam, ab6160), mouse anti-Vimentin (Sigma-Aldrich); Alexa Fluor 405-, Alexa Fluor 488-, Alexa Fluor 568-, Alexa Fluor 647-conjugated secondary antibodies (Life Technologies).

Other reagents used in this study include: Nocodazole (Sigma-Aldrich, M1404); Lipofectamine2000 (Thermofiser, 11668019), Vectashield mounting medium (Vectorlabs, H-1000).

DNA and shRNA constructs

All TRIM CI, CII, CIII family protein constructs with GFP or HA at the N-terminus were cloned into GW1, all TRIM protein constructs with GFP and HA at C-terminus were cloned into pβactin-GFP vector or GW2-HA vector respectively, except for mCherry-MID1 and MID2 which has been cloned into a Bio-mCherry-C1 vector. Human MID1 constructs were cloned based on gift from Dr. Susann Schweiger. Human MID2 was from Dr. Mike Boxem's cDNA library which lost 60 bp at the beginning, was repaired in this paper using gimbson assembly. TRIM36 and TRIM46 were described before (van Beuningen et al., 2015). Human TRIM9 isoform 2, TRIM54 isoform 2 and TRIM55 isoform 6 was cloned based on cDNA library from Dr. Mike Boxem. Mouse TRIM67 was generated from p3x-FLAG-TRIM67 construct which was gift from Dr. Shigetsugu Hatakeyama. Mouse TRIM63 was cloned based on gift from Dr. AJ Marian. Human TRIM42 was cloned based on cDNA from Image clone 40146505 (Dharmacon), GFP-MT+TIP, RFP-tubulin, mCherry-tubulin (Yau et al., 2014), GFP-Sec61β (Lindhout et al., 2019) and GFP-CAMSAP3 (Jiang et al., 2014) construct was already described before.

The following shRNAs were used for knockdown experiments:
Rat MID1 shRNA #1 (5'-GCAGATTGCAAACTGTAAA-3'),
Rat MID1 shRNA #2 (5'-CCCTCCCACAATTAGAGAA-3'),
Rat MID1 shRNA #3 (5'-GCCAAGTTGACAGAGGAAT-3'),
Rat MID1 shRNA #4 (5'- GGAATGTGATCTTCTCATT-3'),
Rat MID1 shRNA #5 (5'-GACCTGTG TTACTTGCGAA-3');
Rat MID2 shRNA #1 (5'-GGTTATGAAACTGA GAAAG-3'),
Rat MID2 shRNA #2 (5'-TGTCCTACATGCAGGTATG-3'),
Rat MID2 shRNA #3 (5'-TGAGCGAATTGCATGTCAG-3'),

Rat MID2 shRNA #4 (5'- GTGTCAAGAGAGCATGTAA-3').

Heterologous cell and Hippocampal neuron cultures

African Green Monkey SV40-transformed kidney fibroblast (COS7) cells were cultured in a 10 cm plate with 10 ml 50% DMEM/ 50% Ham's F10 medium containing 10% FBS (Gibco) and 1% Penicillin/streptomycin in incubator with 37°Cand 5% CO2.

Hippocampus were dissected out from embryonic 18 rat brain and dissociated with Trypsin in 37°C water bath. 100K/well neurons were plated in glass coverslips pre-coated with Poly-L-lysine (37.5 µg/ml, Sigma) and Laminin (1.25µg/ml, Sigma). Neurobasal medium (Invitrogen) containing 2% B27 (Invitrogen), 0.5 mM glutamine (Invitrogen), 15.6 µM glutamate (Sigma) and 1% penicillin/streptomycin (Invitrogen) were used for neuron culture.

Transfections and immunofluorescence

COS7 cells were diluted in a ratio 1:3 24 hours before transfection. MaxPEI were used for COS7 cell transfection based on manufacture's protocol and incubated for 24 hours to 36 hours before immunofluorescence experiments.

For neurons, Lipofectamin 2000 (Invitrogen) was used for transfection via manufacture's protocol. Briefly, 1.8 µg DNA and 3.3 µl Lipofectamin 2000 reagent were mixed in 200µl Neurobasal medium for 30 minutes. The neuronal growth medium was transferred to a new 12 well plate, and the original plate was filled with fresh Neurobasal medium supplemented with 0.5 mM glutamine. The DNA mix was added into neurons for 45 minutes, washed the coverslips with pre-warmed Neurobasal medium and placed them to the new plate with growth medium. Neurons were imaged after 1 day (all the overexpression experiments) or 3 days (all knockdown experiments) transfection.

For immunofluorescence experiments, neurons were fixed with 4% PFA (paraformaldehyde) for 10-15 minutes, washed 3 times with PBS (phosphate buffer saline), and incubated with primary antibodies in GDB buffer (0.2% BSA, 0.8 M NaCl, 0.5% Triton X-100, 30 mM phosphate buffer) overnight at 4°C. Neurons were then washed with PBS for 3 times, incubated with secondary antibodies in GDB buffer for 45 minutes at room temperature, followed by washing 3 times with PBS and mounting with Vectashield mounting medium (Vector Laboratories). COS7 cells was fixed with cold Methanol for 10 minutes in -20°C. For STED super-resolution imaging, COS7 cells was fixed with extraction protocol.

Fixed cell Imaging

After immunofluorescence staining, neurons were imaged using a Nikon Eclipse 80i upright microscope or a Zeiss LSM700 confocal laser scanning microscope. A Plan Fluor 40x NA 1.30 oil objective was used for upright microscope. For the confocal microscope, a Plan Apochromat 20x NA 0.8 dry objective, 40x NA 1.3 oil and 63x NA 1.4 oil objectives were used.

4

Gated STED (gSTED) imaging of acetylated and tyrosinated microtubules was performed with a Leica TCS SP8 STED 3X microscope using a HC PL APO 100x/1.4 oil STED WHITE objective.

Live cell imaging and Photo bleaching experiments

All the live imaging was performed on a Nikon Eclipse TE2000E inverted microscope equipped with Evolve 512 EMCCD camera (Roper Scientific), spinning disk confocal (Roper Scientific), incubate chamber (Tokai Hit) and MetaMorph 7.7.5 software (Molecular Device) was used for all the live imaging experiments. Neurons were maintained in 37°C /5% CO_2 and imaged with 1 frame/s for 5 minutes using a Plan Apo VC 100x NA 1.4 oil objective for the MID1 and MID2 imaging. For FRAP experiments movies were taken for 3 minutes at 1 frame/s and indicated areas were bleached at 10 seconds.

Data analysis and statistics

Image processing and analysis were performed using ImageJ, Matlab, and Adobe Photoshop. Sigma Plot and GraphPad were used for graphs and statistics. Unpaired t-test was performed for statistics and $p < 0.05$ was considered significant. Phylogenetic analysis Conserved COS motif within CI-CIII TRIM family proteins was defined by using Pfam. ClustalX and Mega5 were used for alignment and phylogenetic tree analysis based on conserved domains.

Protein localizations in neurons.

To study protein localization in cells, tracings were made along arrows by using segmented lines in ImageJ and intensity profiles was made according to the position of maximum intensity.

Analysis of polarity index.

MID1 was expressed in DIV9 neurons, and fixed at DIV10. Average intensity of around 50 μm in axon or dendrite were measured. Polarity index was calculated with the formula: $PI = (I_d - I_a)/(I_d + I_a)$. I_d corresponds to mean dendrite intensity, while I_a is the mean axon intensity. $PI > 0$ or $PI < 0$ indicates the polarization biased toward dendrite or axon.

Analysis of MID2 puncta.

To analyse the distributions of MID2 in neurons. The puncta were counted along the dendrite and axons (around 50 μm). The average number of puncta per micron was present at last.

Analysis of FRAP experiments.

For the FRAP analysis, the mean intensities of bleached area were correct by subtracting background with the same ROI region frame by frame and calculated as I(t)= I_(bleached region) (t) – I_background (t). The normalization of recovery R_ norm (t) was calculated according to the formula:

R_norm (t)=(I(t)-I(0))/(<I(Δt)>-I(0))

I (0) corresponds to the mean intensity of regions directly after bleaching, $<I(\Delta t)>$-intensity averaged over 5 frames before bleaching. To correct bleaching due to imaging, the non-bleached region next to the bleached region was account and calculated:

$$R(t) = R\_norm \; (t) \times (<I\_control \; (\Delta t) - I\_background \; (t)>)/(I\_control \; (t) - I\_background \; (t))$$

I_control corresponds to the mean intensity of the non-bleached region and time interval Δt denotes 5 initial frames before bleaching. The curves were made by averaging each frame the recovery rate.

Quantification of axon morphology.

To quantify the axon branches, total axon length, average axon length, primary axon length of each neuron, an ImageJ plugin, NeuronJ (Meijering et al., 2004) was used for tracing the morphology of axon.

AUTHOR CONTRIBUTIONS

X.P. performed the experiments, analyzed results and wrote the manuscript; Y.C. performed live cell imaging and super resolution imaging experiments; M.H. gave advice and correct the manuscript; C.C.H. designed experiments, supervised the research and correct the manuscript.

ACKNOWLEDGEMENTS

4

REFERENCES

Aiken, J., and Buscaglia, G. (2016). TRIM9 Mediates Netrin-1-Induced Neuronal Morphogenesis in the Developing and Adult Hippocampus. J. Neurosci. 36, 9513–9515.

Berti, C., Messali, S., Ballabio, A., Reymond, A., and Meroni, G. (2002). TRIM9 is specifically expressed in the embryonic and adult nervous system. Mech. Dev. 113, 159–162.

Boyer, N.P., Monkiewicz, C., Menon, S., Moy, S.S., and Gupton, S.L. (2018). Mammalian TRIM67 Functions in Brain Development and Behavior. ENeuro 5.

Centner, T., Yano, J., Kimura, E., McElhinny, A.S., Pelin, K., Witt, C.C., Bang, M.L., Trombitas, K., Granzier, H., Gregorio, C.C., et al. (2001). Identification of muscle specific ring finger proteins as potential regulators of the titin kinase domain. J. Mol. Biol. 306, 717–726.

Collison, A., Hatchwell, L., Verrills, N., Wark, P.A.B., de Siqueira, A.P., Tooze, M., Carpenter, H., Don, A.S., Morris, J.C., Zimmermann, N., et al. (2013). The E3 ubiquitin ligase midline 1 promotes allergen and rhinovirus-induced asthma by inhibiting protein phosphatase 2A activity. Nat. Med. 19, 232–237.

Cox, T.C., Allen, L.R., Cox, L.L., Hopwood, B., Goodwin, B., Haan, E., and Suthers, G.K. (2000). New mutations in MID1 provide support for loss of function as the cause of X-linked Opitz syndrome. Hum. Mol. Genet. 9, 2553–2562.

Cuykendall, T.N., and Houston, D.W. (2009). Vegetally localized Xenopus trim36 regulates cortical rotation and dorsal axis formation. Dev. Camb. Engl. 136, 3057–3065.

De Falco, F., Cainarca, S., Andolfi, G., Ferrentino, R., Berti, C., Rodríguez Criado, G., Rittinger, O., Dennis, N., Odent, S., Rastogi, A., et al. (2003). X-linked Opitz syndrome: novel mutations in the MID1 gene and redefinition of the clinical spectrum. Am. J. Med. Genet. A. 120A, 222–228.

Deshaies, R.J., and Joazeiro, C.A.P. (2009). RING Domain E3 Ubiquitin Ligases. Annu. Rev. Biochem. 78, 399–434.

Fielitz, J., Kim, M.-S., Shelton, J.M., Latif, S., Spencer, J.A., Glass, D.J., Richardson, J.A., Bassel-Duby, R., and Olson, E.N. (2007). Myosin accumulation and striated muscle myopathy result from the loss of muscle RING finger 1 and 3. J. Clin. Invest. 117, 2486–2495.

Fréal, A., Rai, D., Tas, R.P., Pan, X., Katrukha, E.A., van de Willige, D., Stucchi, R., Aher, A., Yang, C., Altelaar, A.F.M., et al. (2019). Feedback-Driven Assembly of the Axon Initial Segment. Neuron 104, 305-321.e8.

Geetha, T.S., Michealraj, K.A., Kabra, M., Kaur, G., Juyal, R.C., and Thelma, B.K. (2014). Targeted Deep Resequencing Identifies MID2 Mutation for X-Linked Intellectual Disability with Varied Disease Severity in a Large Kindred from India. Hum. Mutat. 35, 41–44.

Gholkar, A.A., Senese, S., Lo, Y.-C., Vides, E., Contreras, E., Hodara, E., Capri, J., Whitelegge, J.P., and Torres, J.Z. (2016). The Mid2 X-linked Intellectual Disability Ubiquitin Ligase Associates with Astrin and Regulates Astrin Levels to Promote Cell Division. Cell Rep. 14, 180–188.

Harterink, M., Vocking, K., Pan, X., Jerez, E.M.S., Slenders, L., Fréal, A., Tas, R.P., Wetering, W.J. van de, Timmer, K., Motshagen, J., et al. (2019). TRIM46 organizes microtubule fasciculation in the axon initial segment. J. Neurosci. 3105–3118.

Hatakeyama, S. (2017). TRIM Family Proteins: Roles in Autophagy, Immunity, and Carcinogenesis. Trends Biochem. Sci. 42, 297–311.

Hettich, M.M., Matthes, F., Ryan, D.P., Griesche, N., Schröder, S., Dorn, S., Krauß, S., and Ehninger, D. (2014). The Anti-Diabetic Drug Metformin Reduces BACE1 Protein Level by Interfering with the MID1 Complex. PLOS ONE 9, e102420.

Jiang, K., Hua, S., Mohan, R., Grigoriev, I., Yau, K.W., Liu, Q., Katrukha, E.A., Altelaar, A.F.M., Heck, A.J.R., Hoogenraad, C.C., et al. (2014). Microtubule Minus-End Stabilization by Polymerization-Driven CAMSAP Deposition. Dev. Cell 28, 295–309.

Kickstein, E., Krauss, S., Thornhill, P., Rutschow, D., Zeller, R., Sharkey, J., Williamson, R., Fuchs, M., Köhler, A., Glossmann, H., et al. (2010). Biguanide metformin

acts on tau phosphorylation via mTOR/ protein phosphatase 2A (PP2A) signaling. Proc. Natl. Acad. Sci. 107, 21830–21835.

Kimura, N., Yamada, Y., Takayama, K.-I., Fujimura, T., Takahashi, S., Kume, H., and Inoue, S. (2018). Androgen-responsive tripartite motif 36 enhances tumor-suppressive effect by regulating apoptosis-related pathway in prostate cancer. Cancer Sci. 109, 3840–3852.

Kitamura, K., Tanaka, H., and Nishimune, Y. (2003). Haprin, a Novel Haploid Germ Cell-specific RING Finger Protein Involved in the Acrosome Reaction. J. Biol. Chem. 278, 44417–44423.

Liang, C., Wang, S., Qin, C., Bao, M., Cheng, G., Liu, B., Shao, P., Lv, Q., Song, N., Hua, L., et al. (2018). TRIM36, a novel androgen-responsive gene, enhances anti-androgen efficacy against prostate cancer by inhibiting MAPK/ERK signaling pathways. Cell Death Dis. 9, 155.

Lindhout, F.W., Cao, Y., Kevenaar, J.T., Bodzęta, A., Stucchi, R., Boumpoutsari, M.M., Katrukha, E.A., Altelaar, M., MacGillavry, H.D., and Hoogenraad, C.C. (2019). VAP-SCRN1 interaction regulates dynamic endoplasmic reticulum remodeling and presynaptic function. EMBO J. 38, e101345.

Lu, T., Chen, R., Cox, T.C., Moldrich, R.X., Kurniawan, N., Tan, G., Perry, J.K., Ashworth, A., Bartlett, P.F., Xu, L., et al. (2013). X-linked microtubule-associated protein, Mid1, regulates axon development. Proc. Natl. Acad. Sci. 110, 19131–19136.

Menon, S., Boyer, N.P., Winkle, C.C., McClain, L.M., Hanlin, C.C., Pandey, D., Rothenfußer, S., Taylor, A.M., and Gupton, S.L. (2015). The E3 Ubiquitin Ligase TRIM9 Is a Filopodia Off Switch Required for Netrin-Dependent Axon Guidance. Dev. Cell 35, 698–712.

Miyajima, N., Maruyama, S., Nonomura, K., and Hatakeyama, S. (2009). TRIM36 interacts with the kinetochore protein CENP-H and delays cell cycle progression. Biochem. Biophys. Res. Commun. 381, 383–387.

Napolitano, L.M., Jaffray, E.G., Hay, R.T., and Meroni, G. (2011). Functional interactions between ubiquitin E2 enzymes and TRIM proteins. Biochem. J. 434, 309–319.

Perera, S., Holt, M.R., Mankoo, B.S., and Gautel, M. (2011). Developmental regulation of

MURF ubiquitin ligases and autophagy proteins nbr1, p62/SQSTM1 and LC3 during cardiac myofibril assembly and turnover. Dev. Biol. 351, 46–61.

Pizon, V., Gerbal, F., Diaz, C.C., and Karsenti, E. (2005). Microtubule-dependent transport and organization of sarcomeric myosin during skeletal muscle differentiation. EMBO J. 24, 3781–3792.

Plooster, M., Menon, S., Winkle, C.C., Urbina, F.L., Monkiewicz, C., Phend, K.D., Weinberg, R.J., and Gupton, S.L. (2017). TRIM9-dependent ubiquitination of DCC constrains kinase signaling, exocytosis, and axon branching. Mol. Biol. Cell 28, 2374–2385.

Shi, M., Cho, H., Inn, K.-S., Yang, A., Zhao, Z., Liang, Q., Versteeg, G.A., Amini-Bavil-Olyaee, S., Wong, L.-Y., Zlokovic, B.V., et al. (2014). Negative regulation of NF-κB activity by brain-specific TRIpartite Motif protein 9. Nat. Commun. 5, 4820.

Short, K.M., and Cox, T.C. (2006). Subclassification of the RBCC/TRIM superfamily reveals a novel motif necessary for microtubule binding. J. Biol. Chem. 281, 8970–8980.

Short, K.M., Hopwood, B., Yi, Z., and Cox, T.C. (2002). MID1 and MID2 homo- and heterodimerise to tether the rapamycin-sensitive PP2A regulatory subunit, Alpha 4, to microtubules: implications for the clinical variability of X-linked Opitz GBBB syndrome and other developmental disorders. BMC Cell Biol. 3, 1.

Singh, N., Kumble Bhat, V., Tiwari, A., Kodaganur, S.G., Tontanahal, S.J., Sarda, A., Malini, K.V., and Kumar, A. (2017). A homozygous mutation in TRIM36 causes autosomal recessive anencephaly in an Indian family. Hum. Mol. Genet. 26, 1104–1114.

Spencer, J.A., Eliazer, S., Ilaria, R.L., Jr, Richardson, J.A., and Olson, E.N. (2000). Regulation of Microtubule Dynamics and Myogenic Differentiation by Murf, a Striated Muscle Ring-Finger Protein. J. Cell Biol. 150, 771.

Tanji, K., Kamitani, T., Mori, F., Kakita, A., Takahashi, H., and Wakabayashi, K. (2010). TRIM9, a novel brain-specific E3 ubiquitin ligase, is repressed in the brain of Parkinson's disease and dementia with Lewy bodies. Neurobiol. Dis. 38, 210–218.

4

Tas, R.P., Chazeau, A., Cloin, B.M.C., Lambers, M.L.A., Hoogenraad, C.C., and Kapitein, L.C. (2017). Differentiation between Oppositely Oriented Microtubules Controls Polarized Neuronal Transport. Neuron 96, 1264-1271.e5.

Toya, M., Kobayashi, S., Kawasaki, M., Shioi, G., Kaneko, M., Ishiuchi, T., Misaki, K., Meng, W., and Takeichi, M. (2016). CAMSAP3 orients the apical-to-basal polarity of microtubule arrays in epithelial cells. Proc. Natl. Acad. Sci. 113, 332–337.

Trockenbacher, A., Suckow, V., Foerster, J., Winter, J., Krauß, S., Ropers, H.-H., Schneider, R., and Schweiger, S. (2001). MID1 , mutated in Opitz syndrome, encodes an ubiquitin ligase that targets phosphatase 2A for degradation. Nat. Genet. 29, 287–294.

van Beuningen, S.F.B., Will, L., Harterink, M., Chazeau, A., van Battum, E.Y., Frias, C.P., Franker, M.A.M., Katrukha, E.A., Stucchi, R., Vocking, K., et al. (2015). TRIM46 Controls Neuronal Polarity and Axon Specification by Driving the Formation of Parallel Microtubule Arrays. Neuron 88, 1208–1226.

Witt, C.C., Witt, S.H., Lerche, S., Labeit, D., Back, W., and Labeit, S. (2008). Cooperative control of striated muscle mass and metabolism by MuRF1 and MuRF2. EMBO J. 27, 350–360.

Yaguchi, H., Okumura, F., Takahashi, H., Kano, T., Kameda, H., Uchigashima, M., Tanaka, S., Watanabe, M., Sasaki, H., and Hatakeyama, S. (2012). TRIM67 protein negatively regulates Ras activity through degradation of 80K-H and induces neuritogenesis. J. Biol. Chem. 287, 12050–12059.

Yau, K.W., van Beuningen, S.F.B., Cunha-Ferreira, I., Cloin, B.M.C., van Battum, E.Y., Will, L., Schätzle, P., Tas, R.P., van Krugten, J., Katrukha, E.A., et al. (2014). Microtubule Minus-End Binding Protein CAMSAP2 Controls Axon Specification and Dendrite Development. Neuron 82, 1058–1073.

Yoshigai, E., Kawamura, S., Kuhara, S., and Tashiro, K. (2009). Trim36/Haprin plays a critical role in the arrangement of somites during Xenopus embryogenesis. Biochem. Biophys. Res. Commun. 378, 428–432.

Zeng, J., Wang, Y., Luo, Z., Chang, L.-C.,

Yoo, J.S., Yan, H., Choi, Y., Xie, X., Deverman, B.E., Gradinaru, V., et al. (2019). TRIM9-Mediated Resolution of Neuroinflammation Confers Neuroprotection upon Ischemic Stroke in Mice. Cell Rep. 27, 549-560.e6.

4

Chapter 5
VAP–SCRN1 interaction regulates dynamic endoplasmic reticulum remodeling and presynaptic function

Feline W Lindhout[1], **Yujie Cao**[1,†], Josta T Kevenaar[1,†], Anna Bodzezta[1,†], Riccardo Stucchi[1,2], Maria M Boumpoutsari[1], Eugene A Katrukha[1], Maarten Altelaar[2], Harold D MacGillavry[1], and Casper C Hoogenraad[1,3,*]

[1]Department of Biology, Cell Biology, Utrecht University, Utrecht, The Netherlands

[2]Biomolecular Mass Spectrometry and Proteomics, Bijvoet Center for Biomolecular Research and Utrecht Institute for Pharmaceutical Sciences, Utrecht University, Utrecht, The Netherlands

[3]Department of Neuroscience, Genentech, Inc., South San Francisco, CA, USA

[*]Corresponding author. E-mail: c.hoogenraad@uu.nl

[†]These authors contributed equally to this work

ABSTRACT

In neurons, the continuous and dynamic endoplasmic reticulum (ER) network extends throughout the axon, and its dysfunction causes various axonopathies. However, it remains largely unknown how ER integrity and remodeling modulate presynaptic function in mammalian neurons. Here, we demonstrated that ER membrane receptors VAPA and VAPB are involved in modulating the synaptic vesicle (SV) cycle. VAP interacts with secernin-1 (SCRN1) at the ER membrane via a single FFAT-like motif. Similar to VAP, loss of SCRN1 or SCRN1-VAP interactions resulted in impaired SV cycling. Consistently, SCRN1 or VAP depletion was accompanied by decreased action potential-evoked Ca^{2+} responses. Additionally, we found that VAP-SCRN1 interactions play an important role in maintaining ER continuity and dynamics, as well as presynaptic Ca^{2+} homeostasis. Based on these findings, we propose a model where the ER-localized VAP-SCRN1 interactions provide a novel control mechanism to tune ER remodeling and thereby modulate Ca^{2+} dynamics and SV cycling at presynaptic sites. These data provide new insights into the molecular mechanisms controlling ER structure and dynamics, and highlight the relevance of ER function for SV cycling.

5

INTRODUCTION

The continuous and dynamic ER network is one of the most abundant organelles in cells. In neurons, somatodendritic domains contain both rough and smooth ER, whereas axons exclusively exhibit smooth ER. The smooth ER lacks ribosomes and is not involved in translation; instead, it is important for Ca^{2+} homeostasis, lipid synthesis and delivery, and signaling. The relevance of axonal ER in particular is highlighted by various human axonopathies caused by mutations in different generic ER proteins. More specifically, dysfunction of ER-shaping proteins such as atlastin-1, reticulon-2, receptor expression-enhancing protein 1 (REEP1), and receptor expression-enhancing protein 2 (REEP2) leads to hereditary spastic paraplegia (HSP), whereas mutations in ER receptor VAMP-associated protein B (VAPB) cause amyotrophic lateral sclerosis (ALS; Hazan et al, 1999; Zhao et al, 2001; Nishimura et al, 2004; Zuchner et al, 2006; Montenegro et al, 2012; Esteves et al, 2014; Yalcin et al, 2017). Together, these pathologies hint for an increased sensitivity for proper ER structure and function in axons.

Recent ultrastructural three-dimensional analysis revealed that the ER in axons is comprised of a conserved and unique organization (Wu et al, 2017; Yalcin et al, 2017; Terasaki, 2018). The axonal ER structure consists of narrow ER tubules, which occasionally form cisternae at tubular branch points with comparably small lumen (Wu et al, 2017; Yalcin et al, 2017; Terasaki, 2018). This distinctive ER network extends throughout all axon branches with a relative constant density of only 1–2 narrow tubules per diameter, while remaining continuous with the rest of the ER network (Wu et al, 2017; Yalcin et al, 2017; Terasaki, 2018). At presynaptic terminals, the ER forms a local tubular network opposing the active zone. This presynaptic ER structure often wraps around mitochondria and is in close proximity to the plasma membrane, and it regularly forms tight membrane contact sites with these structures (Wu et al, 2017; Yalcin et al, 2017). Moreover, fast dynamics of axonal ER was observed in Drosophila neurons using fluorescent recovery after photo-bleaching (FRAP) analysis, suggesting that the neuronal ER network likely undergoes dynamic remodeling (Wang et al, 2016; Yalcin et al, 2017). However, the precise role of the dynamic ER network in axons and at presynaptic sites remains poorly understood.

Emerging evidence implies that the presynaptic ER is engaged in modulating the tightly controlled Ca^{2+}-induced SV cycle (Summerville et al, 2016; De Gregorio et al, 2017; de Juan-Sanz et al, 2017). In Drosophila neurons, it was reported that homologues of the HSP-associated ER-shaping proteins atlastin-1 and reticulon-1 are implicated in controlling neurotransmitter release at neuromuscular junctions, as loss of these proteins resulted in a marked decrease in SV cycling (Summerville et al, 2016; De Gregorio et al, 2017). In mammalian neurons, recent reports showed that presynaptic Ca^{2+} levels in the ER are locally elevated during evoked neuronal transmission, suggesting that the presynaptic ER buffers Ca^{2+} to modulate SV cycling (de Juan-Sanz et al, 2017).

Moreover, the ER transmembrane protein VAP was originally identified as regulator

5

of synaptic transmission in Aplysia californica, where it was specifically expressed in neuronal tissue (Skehel et al, 1995). Conversely, mammalian VAPA and VAPB are ubiquitously expressed in different cell types and its intracellular localization is restricted to ER membranes. VAPs act as key players in facilitating tight membrane contact sites between the ER and other intracellular membranes, which represent functional interactions through which Ca^{2+} exchange and lipid transfer occur (Muallem et al, 2017; Wu et al, 2018). VAP contains a C-terminal transmembrane domain which is inserted into the ER membrane, and a cytoplasmic N-terminal tail with a coiled-coil domain and a major sperm protein (MSP) domain. The MSP domain exhibits a FFAT(-like) binding site, which is unique for VAP proteins. Many VAP-associated proteins (> 100) with such a FFAT(-like) motif have been described (Murphy & Levine, 2016). This includes the cytoplasmic protein SCRN1, which contains a N-terminal C69 domain and a C-terminal coiled-coil domain and was predicted to have FFAT(-like) motifs (Murphy & Levine, 2016). The large number of FFAT-containing proteins typically localize to distinct subcellular structures, which has led to the general idea that VAP may act as a key ER receptor.

In this study, we demonstrated that ER membrane protein VAP and cytoplasmic VAP-associated protein SCRN1 are important for Ca^{2+}-driven SV cycling. We found that VAP interacts with SCRN1 at the ER membrane through a single FFAT-like motif. Decreasing these ER-localized VAP-SCRN1 interactions was accompanied by a number of phenotypes, including discontinuous ER tubules, impaired ER dynamics, elevated basal presynaptic Ca^{2+} levels, and decreased SV cycling. Together, these data point toward a model where ER remodeling, mediated by VAP-SCRN1 interactions is engaged in modulating Ca^{2+} dynamics and SV cycling at presynaptic sites.

Results

ER proteins VAPA and VAPB are involved in regulating SV cycling

To determine whether the ER proteins VAPA and VAPB could be involved in modulating presynaptic function, we first mapped their subcellular localization in primary rat hippocampal neurons. Similar as reported previously in Drosophila neurons, we found that endogenous VAPA and VAPB appeared as punctae present along ER structures in axons which often co-localized with presynaptic marker synaptotagmin (Syt; Pennetta et al, 2002). At somatodendritic regions, endogenous VAPA and VAPB revealed a more diffuse patchy staining pattern that co-localized with expressed ER membrane protein Sec61β (Fig 1A). Exogenous HA-VAPA and HA-VAPB were observed at ER structures throughout neurons and also partially co-localized with presynaptic boutons (Fig S1A). Thus, VAP is abundantly present at ER structures throughout the cell including at presynaptic sites. To test whether VAP could be engaged in regulating synaptic functions, we next investigated whether VAPA and VAPB are engaged in modulating the SV cycle. This was addressed using the Syt antibody uptake assay, which provides a quantifiable read-out of exo- and endocytosis efficiency at presynaptic sites (Fig 1B). Live neurons were incubated with antibodies recognizing the luminal side of SV membrane protein Syt, while neurons were briefly stimulated by bicuculline. Subsequently, neurons were fixed

and the fluorescence intensity of internalized Syt at individual presynaptic boutons was measured. VAP was depleted from neurons by expressing shRNAs targeting VAPA and VAPB, which we have validated in the previous studies (Teuling et al, 2007; Kuijpers et al, 2013). Co-depletion of VAPA and VAPB showed a marked decrease (~ 50%) in Syt internalization compared to control cells (Fig 1C and D). In addition, VAPA and VAPB knockdown resulted in a slight decrease in bouton size and bouton density (Figs 1C, and S1B and C). In summary, we observed that loss of function of ER proteins VAPA and VAPB was accompanied by decreased SV cycling and defects in bouton maintenance.

VAPA and VAPB associate with brain-enriched SCRN1 proteins

VAPs function as ER receptors for a large number of VAP-associated proteins containing a FFAT or FFAT-like motif (Murphy & Levine, 2016). To gain more insight into the underlying mechanism of VAP at presynaptic sites, we sought to identify the VAP interactor(s) that could be involved in controlling this function. In a recent study, many new VAP-associated proteins were identified by pull-down and mass spectrometry analysis, including the cytoplasmic protein SCRN1 (Murphy & Levine, 2016). Western blot analysis of lysates from different rat tissues using two different antibodies revealed that SCRN1 is abundantly enriched in brain tissues (Figs 1E and S1D). This is consistent with the reported enriched expression of SCRN1 in the brain as described in various online expression databases (Protein Atlas, Expression Atlas, Alan Brain Atlas). We confirmed the association between VAP and SCRN1 with various biochemical assays. First, we conducted a pull-down experiment on lysates of HEK293T cells co-expressing biotinylated GFP (BioGFP) or GFP-SCRN1 (BioGFP-SCRN1) and Myc-VAPA or Myc-VAPB. Both Myc-VAPA and Myc-VAPB efficiently co-precipitated with BioGFP-SCRN1 (Fig 1F and G). Next, we examined the SCRN1 interactome using a more unbiased approach and performed BioGFP-SCRN1 pull-downs followed by mass spectrometry analysis using HEK293T cell lysates and adult rat brain extracts. The associations between SCRN1 and the VAPs were identified in both HEK293T lysates and brain extracts (Figs 1H and S1E). Of all potential SCRN1-interacting proteins, both VAPA and VAPB showed the highest peptide-spectrum match (PSM) values in both datasets. Together, these biochemical data indicated that VAPs are associated with SCRN1.

VAP-associated protein SCRN1 is involved in modulating SV cycling

We next tested whether SCRN1 was present at presynaptic sites and if this protein could be engaged in modulating SV cycling. Similar to VAP, immunostaining for endogenous SCRN1 revealed a punctate pattern throughout the neuron and regularly co-localized with presynaptic marker Syt (Fig 1I). Exogenous GFP-SCRN1 showed a diffuse cytoplasmic signal, which also co-localized with presynaptic boutons (Fig S1F). To conduct loss-of-function experiments, we next generated and validated three shRNA targeting SCRN1 and continued our depletion experiments with a single shRNA (Fig S1G–J). We tested the role of SCRN1 in SV cycling by conducting the Syt uptake assay in neurons depleted from SCRN1. SCRN1 knockdown also showed a marked decrease (~ 40%) in relative Syt internalization compared to control cells, thereby phenocopying the effect of VAP knockdown (Fig 1J and K). The presynaptic phenotype in SCRN1 knockdown neurons was

Figure 1.VAP and VAP-associated protein SCRN1 modulate SV cycling

(A) Endogenous localization of VAPA or VAPB and Syt in hippocampal neurons (DIV16) expressing GFP-Sec61β. Zooms represent (1) an axonal structure with presynaptic boutons (arrowheads), and (2) a dendritic structure. Scale bars: 10 μm (full size) and 5 μm (zoom).

(B) Schematic illustration of the Syt antibody uptake assay: live neurons were stimulated with bicuculline and incubated with primary Syt antibodies, and next neurons were fixed and stained with secondary antibodies.

(C) Representative image of Syt antibody uptake at axons of hippocampal neurons (DIV18) co-expressing RFP and pSuper empty vector or VAPA/B shRNAs. Yellow and gray arrowheads mark presynaptic boutons with and without internalized Syt, respectively. Zooms represent typical boutons. Scale bars: 5 μm (full size) and 2 μm (zoom).

(D) Quantifications of fluorescence intensity of internalized endogenous Syt at single presynaptic boutons of hippocampal neurons (DIV18) co-expressing RFP and pSuper empty vector or VAPA/B shRNAs. N = 2, n = 288–541 boutons.

(E) Western blot of endogenous SCRN1 expression in indicated adult rat neuronal and non-neuronal tissues. Cereb., cerebellum. Hippoc., hippocampus. Spin., spinal.

(F) Pull-down assay of HEK293T cells co-expressing Myc-VAPA with BioGFP or BioGFP-SCRN1.

(G) Pull-down assay of HEK293T cells co-expressing Myc-VAPB with BioGFP or BioGFP-SCRN1.

(H) Scaled representation of SCRN1-associated proteins identified with pull-down assay followed by mass spectrometry analysis of purified BioGFP or BioGFP-SCRN1 from HEK293T cell lysates with adult rat brain extracts. All candidates showed > 10 enrichment of PSM compared to control.

(I) Endogenous localization of SCRN1 and Syt in cortical neurons (DIV18) expressing GFP. Zoom represents an axon structure with presynaptic boutons (arrowheads). Scale bars: 10 μm (full size) and 5 μm (zoom).

(J) Representative image of Syt antibody uptake at axons of hippocampal neurons (DIV18) co-expressing RFP and pSuper empty vector, SCRN1 shRNA, or SCRN1 shRNA with GFP-SCRN1. Yellow and gray arrowheads mark presynaptic boutons with and without internalized Syt, respectively. Zooms represent typical boutons. Scale bars: 5 μm (full size) and 2 μm (zoom).

(K) Quantifications of fluorescence intensity of internalized endogenous Syt at single presynaptic boutons of hippocampal neurons (DIV18) co-expressing RFP and pSuper empty vector, SCRN1 shRNA alone, or SCRN1 shRNA with GFP-SCRN1. N = 2, n = 201–300 boutons.

Data information: Data represent mean ± SEM; ***$P < 0.001$, by Mann–Whitney U-test.

5

---

rescued by expressing wild-type GFP-SCRN1 (Fig 1J and K). Together, these results illustrate that SCRN1 depletion, similarly to VAP depletion, results in impaired SV cycling.

SCRN1 does not exhibit autolytic protease activity

To better understand the molecular function of VAP-associated protein SCRN1, we next tested whether its conserved proteolytic domain could be involved. Like all SCRN family members, SCRN1 contains a C69 protease domain and therefore belongs to the N-terminal nucleophile (Ntn) aminohydrolases superfamily (Pei & Grishin, 2003). Proteolytic activity in this superfamily relies on autolytic cleavage
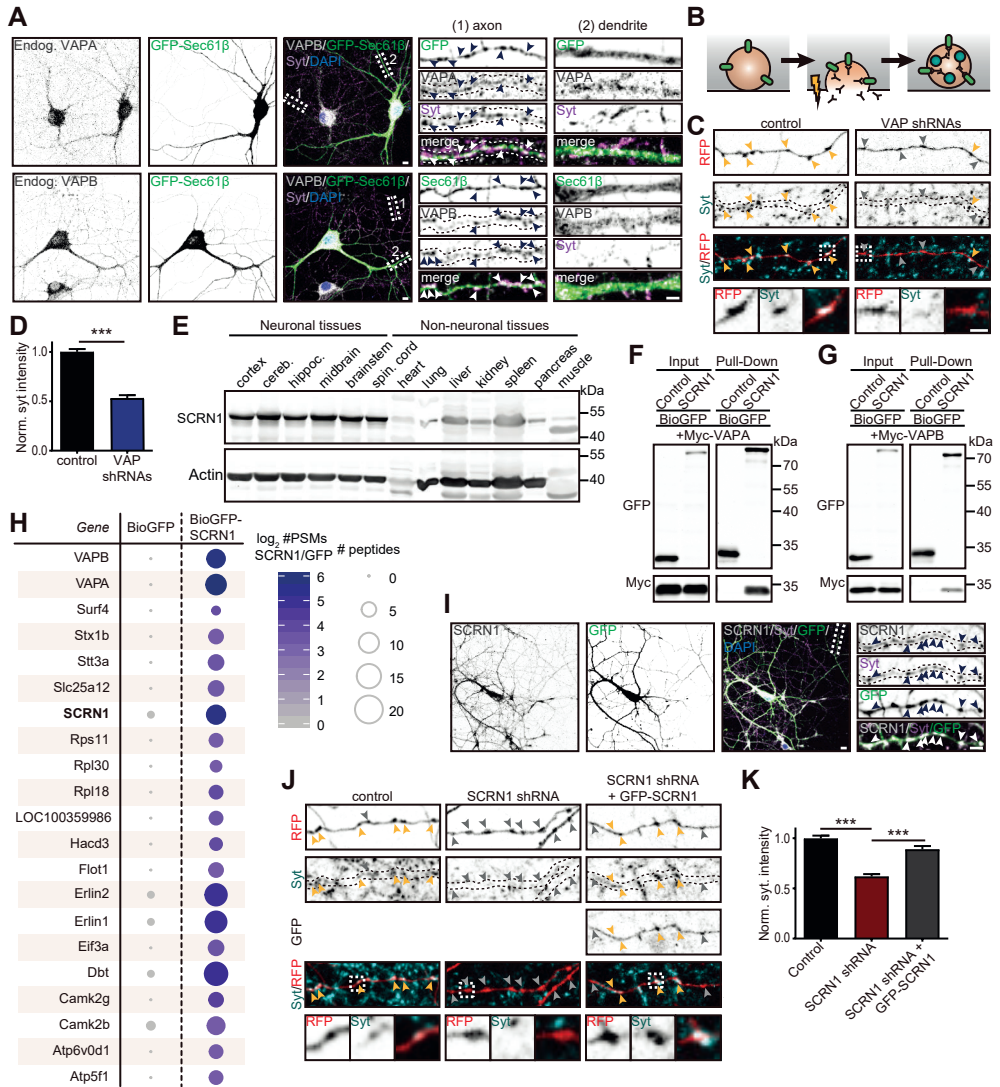
of the auto-inhibitory N-terminal of the precursor protein by the mature protein (Fig S2A). This cleavage occurs right before the catalytic site of the protein, which is a cysteine residue in the SCRN family. Sequence alignment of the SCRN proteins revealed that the position of the predicted catalytic cysteine including the flanking residues is shared in SCRN2 and SCRN3, but not in SCRN1 (Fig S2B). We analyzed N-terminal SCRN cleavage by conducting Western blotting of lysates from HEK293T cells expressing wild-type GFP-SCRN1, GFP-SCRN2, or GFP-SCRN3 (Fig S2C). In lysates of GFP-SCRN2 and GFP-SCRN3 expressing cells, we identified a low molecular weight band corresponding to the predicted size of GFP fused to the N-terminal cleavage product. Conversely, this cleavage product was not observed in lysates of GFP-SCRN1 expressing cells. Moreover, mutant SCRN1, SCRN2, and SCRN3 constructs in which the predicted catalytic cysteine was replaced by a non-catalytic alanine residue also did not show a cleavage product (Fig S2C). These data suggest that SCRN1, unlike its family members SCRN2 and SCRN3, does not exhibit autolytic protease activity.

SCRN1 is recruited to VAP at the ER membrane

To further examine the function of VAP-associated protein SCRN1, we next assessed whether the subcellular localization of SCRN1 could be controlled by VAP. This was addressed by conducting co-expression experiments of GFP-SCRN1 and HA-VAPA or HA-VAPB in cultured neurons and COS7 cells. In COS7 cells, the ER structures are relatively less compact and easier to visualize than in neurons. GFP-SCRN1 expression alone in neurons or COS7 cells showed a diffuse cytoplasmic distribution, which only partly coincided with ER structures (Fig 2A and B). In neurons, co-expression of GFP-SCRN1 with either HA-VAPA or HA-VAPB resulted in the formation of dense VAP/SCRN1-positive clusters at neurites (Fig 2C). COS7 cells co-expressing GFP-SCRN1 and HA-VAPA or HA-VAPB showed marked differences in SCRN1 localization, as it induced abundant SCRN1 recruitment to VAP at the ER membrane (Fig 2D). This observation suggests that enhancing the number of VAPs at the ER membrane allows for increased SCRN1 binding, presumably because it decreases the competition with other FFAT(-like)-containing proteins for the VAP-binding pockets (Fig 2E). Next, we assessed whether the observed recruitment to VAP at ER structures is shared within the SCRN family. Contrarily, we observed no change in GFP-SCRN2 or GFP-SCRN3 localization when co-expressed with HA-VAPB in COS7 cells (Fig 2F). Together, these data indicate that SCRN1, and not SCRN2 and SCRN3, is recruited to VAP at the ER membrane.

SCRN1 interacts with VAP through a single FFAT-like motif

Next, we sought to determine the specific domains responsible for the interaction between VAP and SCRN1. We found that the C-terminal coiled-coil region of SCRN1 and the N-terminal major sperm protein (MSP) domain of VAPB are the minimal binding domains required for this interaction, as shown by co-expression experiments in COS7 cells and pull-down analysis of HEK293T lysates (Figs S2D–I, 3A and E, and S3B). The MSP domain of VAP contains a FFAT(-like) motif binding site, and FFAT(-like) motifs are found in the majority of the VAP-interacting
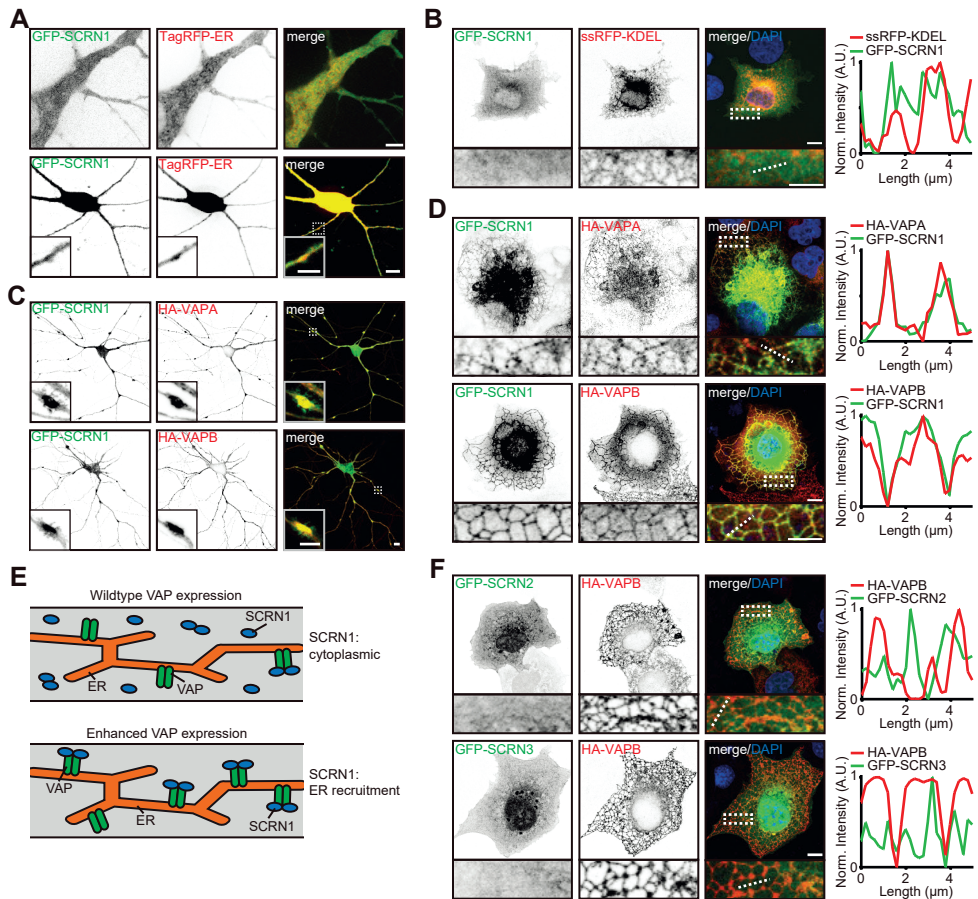
Figure 2. SCRN1 is recruited to VAP at the ER membrane

(A) Localization of GFP-SCRN1 and TagRFP-ER in hippocampal neurons (DIV16–18). Scale bars: 10 μm (bottom panel, full size) and 5 μm (top panel; bottom panel, zoom).

(B) Localization of GFP-SCRN1 and ssRFP-KDEL in COS7 cells with normalized intensity plot of indicated line (dotted). Scale bars: 10 μm (full size) and 5 μm (zoom).

(C) Hippocampal neurons (DIV16) co-expressing GFP-SCRN1 with HA-VAPA or HA-VAPB. Scale bars: 10 μm (full size) and 5 μm (zoom).

(D) COS7 cells co-expressing GFP-SCRN1 with HA-VAPA or HA-VAPB with normalized intensity plot of indicated line (dotted). Scale bars: 10 μm (full size) and 5 μm (zoom).

(E) Schematic illustration of SCRN1 recruitment to ER membranes upon increasing VAP levels.

(F) COS7 cells co-expressing HA-VAPB with GFP-SCRN2 or GFP-SCRN3 with normalized intensity plot of indicated line (dotted). Scale bars: 10 μm (full size) and 5 μm (zoom).

5

Figure 3.VAP-SCRN1 interaction at the ER is mediated by a single FFAT-like motif

(A) Schematic overview of SCRN1 and VAP constructs (asterisks represent mutations). Indicated is if expressed VAP/SCRN1 proteins co-localize in both hippocampal neurons and COS cells, and co-precipitate in pull-down assays.

(B) COS7 cells co-expressing GFP-SCRN1 with HA-VAPB-K87D/M89D. Normalized intensity plot represents indicated line (dotted). Scale bars: 10 μm (full size) and 5 μm (zoom).

(C) COS7 cells co-expressing HA-VAPB with GFP-SCRN1-Y40A, GFP-SCRN1-F144A, GFP-SCRN1-F153A, or GFP-SCRN1-F402A. Normalized intensity plot represents indicated line (dotted).Scale bars: 10 μm (full size) and 5 μm (zoom).

(D) Hippocampal neurons (DIV16) co-expressing HA-VAPB with GFP-SCRN1-Y40A, GFP-SCRN1-F144A, GFP-SCRN1-F153A, or GFP-SCRN1-F402A. Scale bars: 10 μm (full size) and 5 μm (zoom).

(E) Quantifications of SCRN1 recruitment to VAPB-positive structures in COS7 cells (%). Left graph: co-expression of GFP-SCRN1 with HA-VAPB or HA-VAPB-K87D/M89D (N = 2–3, n = 44–46). Right graph: co-expression of HA-VAPB with GFP or GFP-SCRN1-FL, GFP-SCRN1-N, GFP-SCRN1-C, GFP-SCRN1-Y40A, GFP-SCRN1-F144A, GFP-SCRN1-F153A, or GFP-SCRN1-F402A (N = 2–3, n = 41–64).

(F) Pull-down assay of HEK293T cells co-expressing Myc-VAPB with GFP, GFP-SCRN1-WT, GFP-SCRN1-Y40A, GFP-SCRN1-F144A, GFP-SCRN1-F153A, or GFP-SCRN1-F402A.

(G) Sequence alignment of the C-terminal human SCRN1, SCRN2, and SCRN3. Amino acid position 3 (asterisk) in FFAT-like motif (orange) of SCRN1 is not shared in SCRN2 and SCRN3.

Data information: ***P < 0.001, by chi-square test with post hoc analysis including Bonferroni correction.

---

proteins (Loewen et al, 2003; Murphy & Levine, 2016). Indeed, we found that the FFAT binding motif in VAP is responsible for the interaction with SCRN1. The VAP mutant VAP-K87D/M89D, in which FFAT binding is disrupted, was no longer able to recruit GFP-SCRN1 (Fig 3A, B and E; Kaiser et al, 2005). Next, we searched for FFAT(-like) motifs in SCRN1 using a previously reported algorithm and identified four potential FFAT-like motifs (Fig S3A; Murphy & Levine, 2016). We generated SCRN1 constructs with single-point mutations for each single FFAT-like motif (Fig 3A). VAP association was disrupted when mutating the most C-terminal FFAT-like motif in SCRN1 (GFP-SCRN1-F402A), but not the other motifs, as shown by pull-down assays and co-expression experiments (Figs 3C–F, and S3B–D). Sequence alignment of the SCRN family members revealed that this newly identified FFAT-like motif in SCRN1 is not shared with the other two SCRN family members, which is consistent with our observation that exogenous VAP is unable to recruit GFP-SCRN2 and GFP-SCRN3 (Figs 2F and 3G). Together, these data show that the MSP domains of VAPA and VAPB interact with a single FFAT-like motif in the C-terminal region of SCRN1.

SCRN1 and VAP are required for proper ER morphology

Previously, it was shown that VAP interactions with FFAT-containing proteins are engaged in maintaining ER morphology (Kaiser et al, 2005). Next, we aimed to investigate whether its interaction with SCRN1 at the ER membrane could be

A

	Co-localiz.	Co-IP
SCRN1		
SCRN1	+	+
SCRN1-N	–	–
SCRN1-C	+	+
SCRN1-Y40A	+	+
SCRN1-F144A	+	+
SCRN1-F153A	+	+
SCRN1-F402A	–	–
VAPA/B		
VAPA	+	+
VAPB	+	+
VAPB-K87D/M89D	–	–

G

FFAT-like motif

```
SCRN1: ILTSSEPLDPAEVGDLFYDCVDTEIKFFK---------
SCRN2: LLAGEWAPPLWELGSLFQAFVKRESQAYA---------
SCRN3: LLQNKHL-DVEKIVNLFEQCTKDEIQIYQSNLSVKVSS
```

F

Input / Pull-Down

GFP / Myc

kDa: 70, 55, 40, 35, 25

E

No SCRN1 recruitment / SCRN1 recruitment

SCRN1 recruitment to HA-VAPB (% cells)

WT, K87D/M89D

GFP, FL, N, C, Y40A, F144A, F153A, F402A — GFP-SCRN1
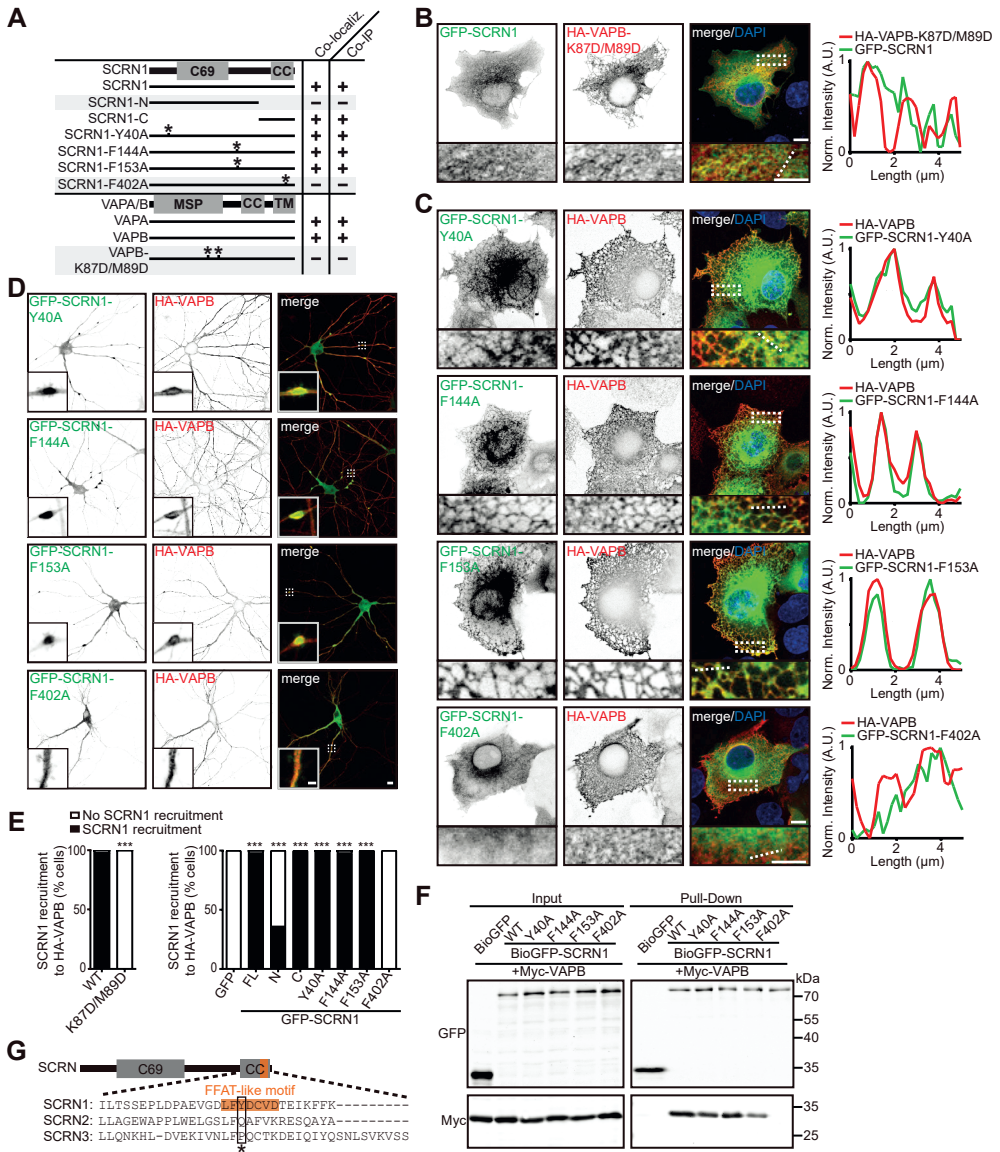
***

5

Figure 4.VAP and SCRN1 control ER continuity and remodeling

(A) Summary of observed phenotypes on SCRN1 recruitment and ER morphology in cells co-expressing indicated SCRN1 and VAP constructs (asterisks represent mutations).

(B) Live hippocampal neurons (DIV17–18) co-expressing TagRFP-ER with GFP, GFP-SCRN1, GFP-SCRN1-F402A, SCRN1 shRNA, or VAPA/B shRNAs. Scale bars: 5 μm (full size) and 2 μm (zoom).

(C) Time-lapse of TagRFP-ER dynamics in hippocampal neurons (DIV16–18) co-expressing GFP, GFP-SCRN1, GFP-SCRN1-F402A, SCRN1 shRNA, or VAPA/B shRNAs. Intact and stable ER structures (dark arrowheads), intact and dynamic ER structures (light arrowheads), and impaired non-dynamic ER structures (arrows) are indicated. Scale bars: 5 μm (full size) and 2 μm (zoom).

(D) Schematic illustration of the effect of VAP-SCRN1 interactions on ER structure and dynamics.

(E) ER nanostructures visualized with GFP-Sec61β in axons of hippocampal neurons (DIV18) immunostained for α-tubulin and co-expressed with pSuper empty vector, SCRN1 shRNA, or VAPA/B shRNAs, and subjected to expansion microscopy. Scale bars: 2 μm (full size) and 500 nm (zoom).

(F) FRAP experiment of TagRFP-ER in hippocampal neurons (DIV17–18) co-expressing GFP, GFP-SCRN1, and GFP-SCRN1-F402A. Scale bar: 2 μm.

(G) Average normalized fluorescent TagRFP-ER recovery after photo-bleaching in hippocampal neurons (DIV17–18) co-expressing GFP, GFP-SCRN1, and GFP-SCRN1-F402A. N = 2, n = 9 neurons.

(H) Normalized fluorescent TagRFP-ER recovery after photo-bleaching at T = 60 s in hippocampal neurons (DIV17–18) co-expressing GFP, GFP-SCRN1, and GFP-SCRN1-F402A. N = 2, n = 9 neurons.

(I) Average normalized fluorescent TagRFP-ER recovery after photo-bleaching in hippocampal neurons (DIV18) co-expressing pSuper empty vector, SCRN1 shRNA, and VAPA/B shRNAs. N = 4, n = 6–12 neurons.

(J) Normalized fluorescent TagRFP-ER recovery after photo-bleaching at T = 60 s in hippocampal neurons (DIV18) co-expressing pSuper empty vector, SCRN1 shRNA, and VAPA/B shRNAs. N = 4, n = 6–12 neurons.

Data information: Data represent mean ± SEM; n.s.: not significant; *P < 0.05; **P < 0.01, by Mann–Whitney U-test.

---

important for this function. Similar to previously reported results, we found that COS7 cells expressing VAP-K87D/M89D, VAP mutant lacking proper FFAT binding, showed a robust phenotype that was characterized by non-reticular VAP structures throughout the cytosol (Figs 3B, 4A, and S4A; Kaiser et al, 2005). Likewise, similar aberrant VAP-positive structures were found in COS7 cells expressing wild-type HA-VAP and GFP-SCRN1-F402A or GFP-SCRN1-N, both lacking a functional FFAT-like motif (Figs 3C, S3C, 4A, and EV4A and B). These observed phenotypes were also detected with ER luminal marker TagRFP-ER, indicating that the non-reticular VAP signals represent affected underlying ER structures (Fig S4C and D). Similarly, both in VAP and in SCRN1 knockdown neurons, as well as in neurons expressing GFP-SCRN1-F402A, ER morphology was severely disrupted (Fig 4B). Notably, in these neurons we observed dense ER patches surrounded by less dense or absent ER structures. On the other hand, neurons overexpressing wild-type SCRN1 also showed dense ER patches; however, these did seem properly connected
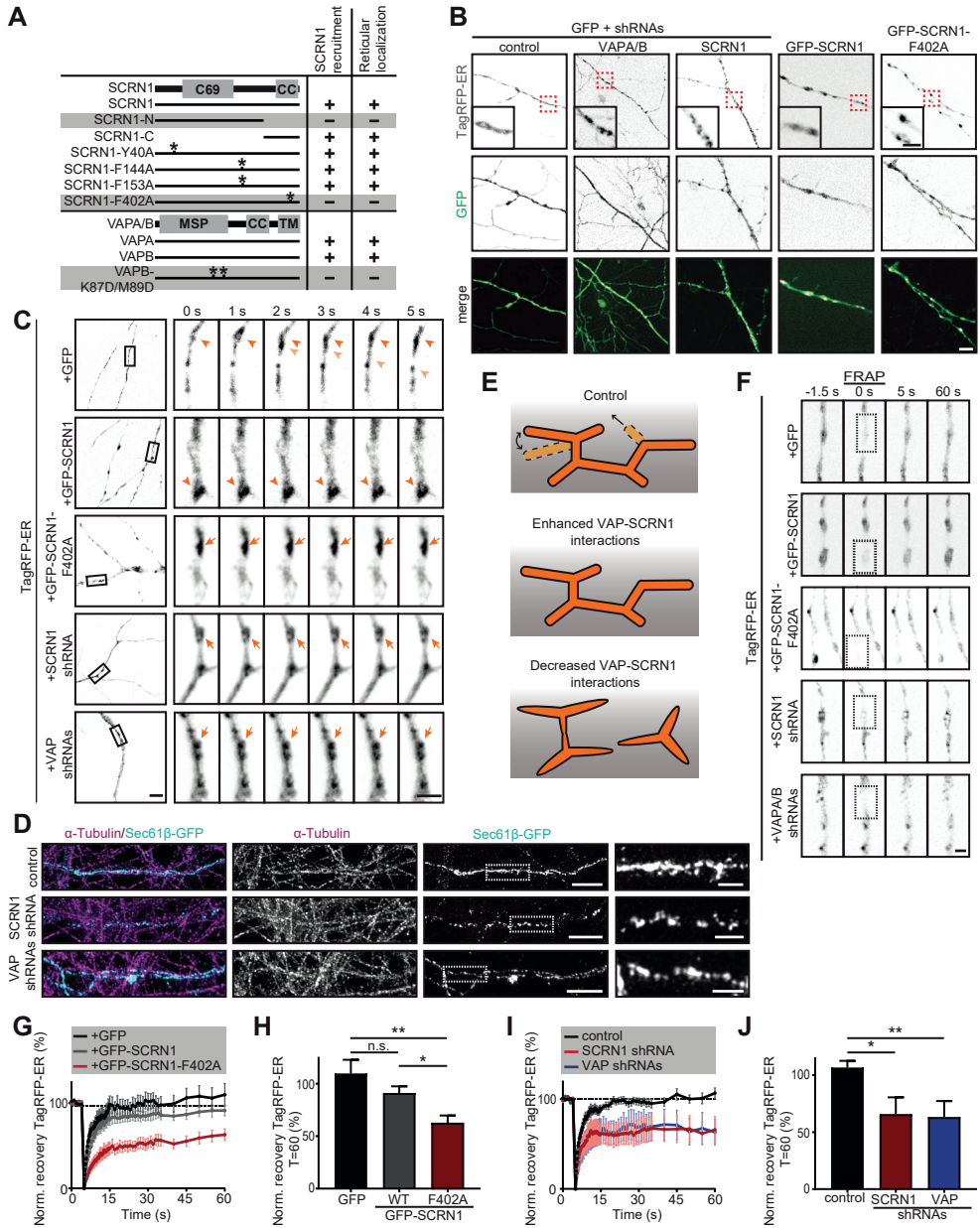
to the rest of the ER structure. Thus, structural disruptions in ER morphology were consistently observed when the VAP-SCRN1 interactions were abrogated (Fig 4A). As such, expression of SCRN1-F402A showed the same phenotype on ER morphology as SCRN1 depletion, suggesting that SCRN1-F402A may act as a dominant-negative. As SCRN1-F402A is cytoplasmic, it could recruit and capture endogenous SCRN1 to the cytoplasmic pool, thereby preventing it from binding to VAP and execute its function at the ER. Indeed, oligomerization is a common feature of the Ntn aminohydrolases superfamily, and pull-down assays showed that both SCRN1 and SCRN1-F402A were associated with other SCRN1 proteins (Fig S4E and F). These results confirm that SCRN1 undergoes oligomerization and that SCRN1-F402A could act as a dominant-negative. Together, these data indicate that both SCRN1 and VAP are required for proper ER morphology, which is mediated by VAP-SCRN1 interactions at the ER membrane.

SCRN1 and VAP are engaged in maintaining ER continuity and dynamics

The ER structure undergoes constant remodeling while remaining continuous for proper functioning. Thus, next we sought to determine the effect of VAP and SCRN1 on both ER continuity and dynamics. We used live-cell imaging to map ER dynamics in cells expressing luminal ER marker TagRFP-ER. We observed fast remodeling of ER structures in both neurons and COS7 cells, ranging from ER tubule growth events and structural ER "wiggling" events (Figs 4C and D, and S4G). The dense ER patches observed when expressing wild-type SCRN1 represented stabilized ER structures (Figs 4C and D, and S4G; Movies S1 and S2). On the other hand, decreasing SCRN1 or VAP levels, or expressing dominant-negative SCRN1-F402A mutant, resulted in overall impaired dynamics of the dense ER patches that seemed partially discontinuous with the remaining ER structures (Figs 4C and D, and S4G; Movie S3). To gain more detailed insights into the role of VAP-SCRN1 interactions on ER morphology, we next sought to visualize ER nanostructures in neurons using the recently developed expansion microscopy (ExM) technique (Tillberg et al, 2016). This ExM approach allows for a ~ 4.5-fold physical sample magnification by isotropic chemical expansion and has been validated to preserve the nanoscale organization within different biological specimens (reviewed in Wassie et al, 2019). Here, we successfully resolved the dense neuronal ER structures, which enabled us to distinguish individual ER tubules and sheets in neurons expressing ER membrane marker GFP-Sec61β (Movie S4; Figs 4E, and S4H and I). Consistent with reported EM studies, we observed that the axonal ER network was comprised of 1 or 2 ER tubules per diameter and regularly formed tubular structures (Fig 4D; Terasaki, 2018; Wu et al, 2017; Yalcin et al, 2017). VAP or SCRN1 knockdown neurons showed marked differences on ER nanostructures. More specifically, these neurons showed severe discontinuity of ER tubules in axons, and overall less dense and irregular ER structures in axons, dendrites, and soma (Figs 4E, and S4H and I). To quantitatively validate the role of VAP-SCRN1 interactions on ER continuity and dynamics, we conducted FRAP experiments on the previously observed characteristic dense ER patches in TagRFP-ER expressing neurons. Consistent with previous indications, photo-bleached TagRFP-ER co-expressed with either GFP or GFP-SCRN1 showed full recovery within 60 s of the ER patches (Fig 4F–H). This suggests rapid and complete redistribution of luminal ER content consistent

with an intact ER structure. In contrast, the recovery of TagRFP-ER at ER patches was markedly reduced by ~ 45% in neurons expressing either GFP-SCRN-F402A, SCRN1 shRNA, or VAPA/B shRNAs, which implies incomplete redistribution of the luminal ER marker due to discontinuity (Fig 4F, I, and J). Together, these data indicate that loss of VAP and SCRN1 results in discontinuous ER structures and impaired ER dynamics in neurons, which is mediated by VAP-SCRN1 interactions.

SCRN1-VAP interaction controls SV cycling

Next, we aimed to test whether the VAP-SCRN1 interactions at the ER membrane may be engaged in regulating the SV cycle, as we previously observed that VAP or SCRN1 depletion resulted in decreased SV cycling (Fig 1B–D, J and K). To test this, we conducted the Syt uptake assay in neurons depleted from SCRN1 and expressing SCRN1-F402A, thereby abolishing VAP-SCRN1 interactions. Unlike wild-type SCRN1 expression, exogenous mutant SCRN1-F402A was unable to rescue the effect of SCRN1 knockdown on SV cycling (Figs 5A and B). These data imply that the VAP-SCRN1 interactions, which we identified as regulators of ER remodeling, are engaged in modulating SV cycling at presynaptic sites.

VAP and SCRN1 are engaged in regulating evoked presynaptic Ca^{2+} responses

Neurotransmitter release is induced by a local cytoplasmic Ca^{2+} influx upon neuronal stimulation. Thus, to further investigate the phenotype of VAP and SCRN1 on SV cycling, we next assessed whether they are engaged in regulating evoked Ca^{2+} influx. To test this, we measured Ca^{2+} dynamics at single boutons with the genetically encoded Ca^{2+} indicator GCaMP6f and triggered trains of action potentials (50 APs, 20 Hz) using electric field stimulation (Fig 5C). Presynaptic boutons were identified as GCaMP6f-positive swellings along axons, which were shown to co-localize with the presynaptic active zone marker RIM1a-mCherry (Fig 5C). Loss of VAP or SCRN1 both resulted in a marked ~ 25% decreased peak amplitude of evoked Ca^{2+} transients (Fig 5D–F). These results indicate that both the ER receptor VAP and the VAP-interacting protein SCRN1 are involved in modulating presynaptic Ca^{2+} influx and thereby could affect SV cycling.

VAP-SCRN1 interactions modulate Ca^{2+} homeostasis at presynaptic sites

To better understand the effects of VAP and SCRN1 on evoked Ca^{2+} influx, we next sought to determine whether these proteins could interfere with ER-mediated Ca^{2+} homeostasis. Maintaining basal Ca^{2+} levels is one of the key functions of smooth ER, which is the only type of ER that is present in axons. Thus, we hypothesized that the observed structural ER defects with abolished VAP-SCRN1 interactions could perturb ER-mediated Ca^{2+} homeostasis and thereby affect Ca^{2+}-mediated SV cycling. We compared relative basal Ca^{2+} levels at presynaptic sites in neurons expressing Ca^{2+} indicators GCaMP6f or R-GECO1, as well as mRFP or GFP to identify transfected cells and presynaptic boutons. Relative basal Ca^{2+} levels were obtained by determining the ratio (F0/Fmax) of fluorescent GCaMP6f or R-GECO1 signals before (F0) and after (Fmax) ionomycin treatment. Ionomycin is an ionophore which induces Ca^{2+} permeability at membranes, thereby enables effectively saturating Ca^{2+} indicators to determine Fmax. In VAP knockdown

Figure 5.VAP and SCRN1 control Ca2+ homeostasis and presynaptic release

(A) Representative image of Syt antibody uptake at axons of hippocampal neurons (DIV18) co-expressing RFP and pSuper empty vector, SCRN1 shRNA, or SCRN1 shRNA with GFP-SCRN1-F402A. Yellow and gray arrowheads mark presynaptic boutons with and without internalized Syt, respectively. Zooms represent typical boutons. Scale bars: 5 μm (full size) and 2 μm (zoom).

(B) Quantifications of fluorescence intensity of internalized endogenous Syt at individual presynaptic boutons of hippocampal neurons (DIV18) co-expressing RFP and pSuper empty vector, SCRN1 shRNA, or SCRN1 shRNA with GFP-SCRN1-F402A. N = 2, n = 201–300 boutons.

(C) Representative time-lapse of cytosolic GCaMP6f upon electric field stimulation (50 APs, 20 Hz) in axons of hippocampal neurons (DIV21) co-expressed with RIM1a-mCherry to visualize presynaptic sites (arrowheads). Scale bar: 5 μm.

(D) Time-lapses of cytosolic GCaMP6f upon electric field stimulation (50 APs, 20 Hz) in axons of hippocampal neurons (DIV21) co-expressing pSuper control, SCRN1 shRNA, or VAPA/B shRNAs. Scale bar: 5 μm.

(E) Average normalized response of GCaMP6f fluorescent intensity at presynaptic boutons upon stimulation (50 APs, 20 Hz) in hippocampal neurons (DIV21) co-expressing pSuper empty vector, SCRN1 shRNA, or VAPA/B shRNAs. N = 5–6, n = 15–27.

(F) Average normalized peak response of GCaMP6f at presynaptic boutons upon stimulation (50 APs, 20 Hz) in hippocampal neurons (DIV21) co-expressing pSuper empty vector, SCRN1 shRNA, or VAPA/B shRNAs. N = 5–6, n = 15–27.

(G) Representative time-lapse of cytosolic GCaMP6f before (F0) and after (Fmax) ionomycin treatment at axons of hippocampal neurons (DIV18) co-expressed with mRFP and pSuper empty vector or VAPA/B shRNAs. Arrowheads mark presynaptic boutons. Scale bar: 5 μm.

(H) Basal GCaMP6f fluorescence (F) normalized to the maximum GCaMP6f fluorescence (Fmax) after ionomycin treatment at presynaptic boutons of hippocampal neurons (DIV18) co-expressing mRFP with pSuper empty vector or VAPA/B shRNAs. N = 2, n = 47–50.

(I) Average basal GCaMP6f fluorescence (F0) normalized to the max GCaMP6f fluorescence intensity (Fmax) after ionomycin treatment at presynaptic boutons of hippocampal neurons (DIV18) co-expressing mRFP with pSuper empty vector or VAPA/B shRNAs. N = 2, n = 47–50.

(J) Representative time-lapse of cytosolic R-GECO1 before (F0) and after (Fmax) ionomycin treatment at axons of hippocampal neurons (DIV18) co-expressing GFP, GFP-SCRN1, or GFP-SCRN1-F402A. Arrowheads mark presynaptic boutons. Scale bar: 5 μm.

(K) Basal R-GECO1 fluorescence (F) normalized to the maximum R-GECO1 fluorescence (Fmax) after ionomycin treatment at presynaptic boutons of hippocampal neurons (DIV18) co-expressing GFP, GFP-SCRN1, or GFP-SCRN1-F402A. N = 3, n = 70–89.

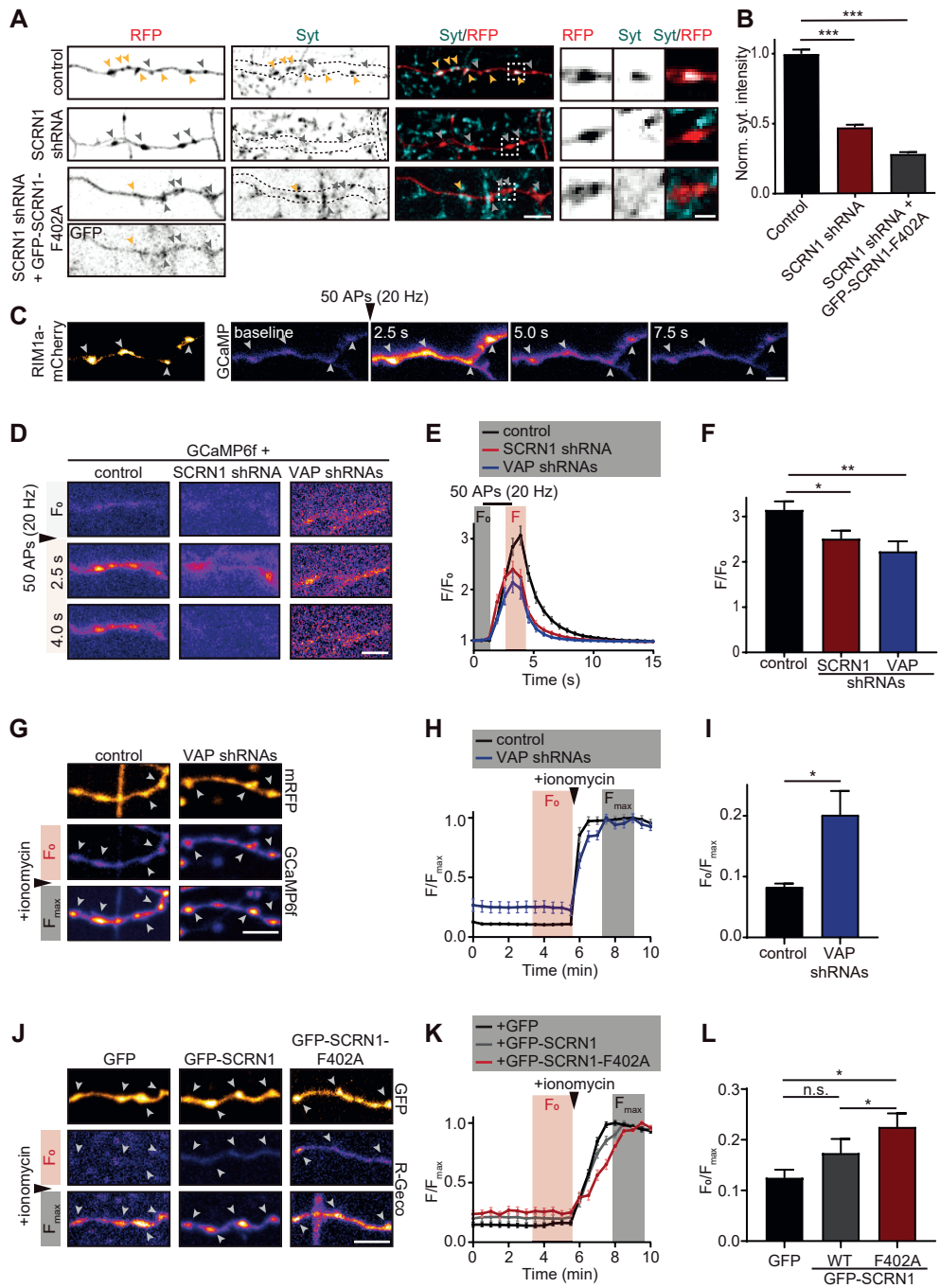(L) Average basal R-GECO1 fluorescence (F0) normalized to the maximum R-GECO1 fluorescence intensity (Fmax) after ionomycin treatment at presynaptic boutons of hippocampal neurons (DIV18) co-expressing GFP, GFP-SCRN1, or GFP-SCRN1-F402A. N = 3, n = 70–89.

Data information: Data represent mean ± SEM; n.s.: not significant; *P < 0.05; **P < 0.01; ***P < 0.001, by Mann–Whitney U-test.

neurons, relative basal Ca^{2+} levels at single boutons were markedly elevated ($\sim$ 2.5-fold) compared to control (Fig 5G–I). This is in line with the observed decreased evoked Ca^{2+} influx, as higher basal Ca^{2+} levels will result in a lower extracellular-cytoplasmic Ca^{2+} concentration gradient. Consistently, presynaptic Ca^{2+} levels were significantly increased ($\sim$ 2-fold) with dominant-negative SCRN1-F402A expression, but not with SCRN1 wild-type expression, indicating that the observed effect is mediated by VAP-SCRN1 interactions (Fig 5J–L). Together, these data imply that ER-localized VAP-SCRN1 interactions are engaged in modulating basal Ca^{2+} levels at presynaptic sites.

Discussion

The dynamic and continuous ER network extends throughout the axon, and evidence for its role in controlling presynaptic neurotransmitter release begins to emerge (Summerville et al, 2016; De Gregorio et al, 2017; de Juan-Sanz et al, 2017). In this study, we identified novel control mechanisms for ER remodeling, presynaptic Ca^{2+} homeostasis, and Ca^{2+}-induced SV cycling, which are mediated by ER receptor VAP together with VAP-interacting protein SCRN1. Together, these data point toward a model where VAP-SCRN1 interactions tune ER integrity and dynamics, and thereby could modulate basal Ca^{2+} levels and subsequently SV cycling at presynaptic sites.

SCRN1 is a VAP-interacting protein

Here, we demonstrated that loss of ER membrane receptor VAP results in discontinuous ER structures, impaired ER dynamics, and decreased SV cycling. This is in line with previous studies which already hinted for a role of VAP in maintaining ER morphology and regulating synaptic function (Skehel et al, 1995; Kaiser et al, 2005; Gomez-Suaga et al, 2019). To gain further mechanistic insights into the VAP-mediated phenotypes, we sought to identify a VAP-associated protein involved in this function. Hence, we selected SCRN1 as a potential candidate for several reasons. First, SCRN1 was abundantly expressed in brain tissue, as indicated by various expression databases (Protein Atlas, Expression Atlas, Alan Brain Atlas) and confirmed by our Western blot analysis of different rat tissues. Second, in non-neuronal cells, SCRN1 was found to play a role in regulating Ca^{2+}-controlled exocytosis, which is also a key process of the SV cycle (Way et al, 2002; Lin et al, 2015). We confirmed the interaction between VAP and SCRN1, and identified a single FFAT-like motif responsible for the interaction. Consistent with our hypothesis, we found that either SCRN1 depletion or dominant-negative SCRN1-F402A expression phenocopied the effect of VAP depletion on both ER remodeling and SV cycling. The dominant-negative effect was consistently more potent than the shRNA knockdown effect, similar to what is often observed when comparing dominant-negative and shRNA silencing expression constructs of proteins. Here, the difference could be explained by incomplete depletion of endogenous SCRN1 during the SCRN1 shRNA silencing period, whereas on the other hand dominant-negative SCRN1-F402A actively recruits and captures endogenous SCRN1 proteins and thereby impairs its function. Nevertheless, we cannot exclude that additional functions of SCRN1-F402A might be at play. Together, our data indicate that

SCRN1-VAP interactions are engaged in controlling the VAP-associated phenotypes, and further investigations are required to examine whether additional VAP-interacting proteins could also be involved in modulating SV cycling.

VAP-SCRN1 interactions control ER continuity and dynamics

The ER network is composed of a well-maintained interconnected structure that undergoes continuous remodeling for proper functioning. Here, we identified the VAP-SCRN1 interactions as critical regulators for maintaining ER structure and dynamics. Considering that VAPs are best known to act as major ER receptors by facilitating tight membrane contact sites between the ER and other organelles, it is tempting to speculate that these membrane contact sites might be engaged in controlling VAP-mediated functions on ER integrity and dynamics (Muallem et al, 2017; Wu et al, 2018). One plausible mechanism could be that these membrane contact sites may act as "anchor points" which locally stabilize the ER network. These VAP-facilitated membrane contact sites are abundantly present throughout the cell and can thus stabilize local spots within the large interconnected and highly dynamic ER network. As such, this hypothesis follows the assumption that proper ER integrity relies on a defined balance between ER dynamics and stability. In line with this, it was previously shown that depleting either ER-forming protein atlastin or ER-stabilizing protein reticulon resulted in ER tubule fragmentation, which could remarkably be rescued by depleting both proteins simultaneously (Wang et al, 2016). Alternatively, VAP-mediated membrane contact sites could control ER remodeling by enabling fast lipid delivery. We showed that ER remodeling in neurons is a fast process and that ER tubule growth events can occur in a few seconds. This fast ER remodeling requires the continuous and rapid rearrangement of lipids. This may be accomplished via fast lipid transfer at membrane contact sites between ER and other organelles, rather than via the relatively slower lipid synthesis and redistribution at the ER membrane. Note worthily, considering that VAPs are implicated in a wide range of functions, various other possible direct or indirect VAP-mediated mechanisms to control ER remodeling might be at play.

Maintaining axonal ER structures is important to preserve presynaptic function

In recent EM studies, it was reported that ER structures in axons show specific adaptations, characterized by small ER lumen and low density of 1–2 tubules per axon diameter. These adaptations likely allow the axonal ER to extend throughout all axon branches while remaining continuous with the remaining ER network, which is typically more dense and branched. In this study, we found that VAP and SCRN1 depletion affected ER structures throughout the cell, though axonal ER structures seemed most severely disrupted. Interestingly, mutations in generic structural ER proteins such as atlastin-1, reticulon-2, REEP1, and REEP2 are causative for the axonopathy HSP (Hazan et al, 1999; Zhao et al, 2001; Nishimura et al, 2004; Zuchner et al, 2006; Montenegro et al, 2012; Esteves et al, 2014; Yalcin et al, 2017). Together, these findings indicate that the delicate ER network in axons is more sensitive to maintenance defects. Therefore, ubiquitous ER disruptions may result in more profound phenotypes on particularly axonal functions. Here, we demonstrated that the observed ER abrogations with decreased VAP-SCRN1

5

interactions were accompanied with impaired SV cycling at presynaptic sites. Consistent with this, recent studies in Drosophila neurons showed that loss of ER-shaping protein atlastin or reticulon also resulted in impaired ER structures as well as decreased neurotransmitter release (Summerville et al, 2016; De Gregorio et al, 2017). Together, these findings imply that ER structure and function are engaged in modulating SV cycling. Notably, investigating the direct relation between these phenotypes is challenging, as it is not feasible to specifically isolate the local function of ER at presynaptic sites since all ER membranes and lumen in the cell are continuous. Nevertheless, considering that the neuronal ER network remains fully continuous despite its complex cellular morphology may actually highlight the functional relevance of this continuity for its role at presynaptic sites. Toward this end, it would be interesting to direct future work on investigating whether the continuity of the neuronal ER network is important for the reported ER-mediated functions at presynaptic sites.

VAP-SCRN1 interactions modulate presynaptic Ca^{2+} dynamics and SV cycling

In this study, we reported that the ER defects observed with VAP or SCRN1 depletion are accompanied with reduced presynaptic Ca^{2+} influx and SV cycling. Considering that axonal ER structures are exclusively comprised of smooth ER, we hypothesized that defects in maintaining Ca^{2+} homeostasis, which is a key function of smooth ER, could provide a mechanistic link between the observed phenotypes on ER integrity and SV cycling. Previous reports already hinted for a correlation between ER-mediated Ca^{2+} homeostasis and neurotransmitter release. In a recent study, a feedback loop between ER Ca^{2+} concentration, presynaptic Ca^{2+} influx, and SV exocytosis was identified in dissociated rodent neurons (de Juan-Sanz et al, 2017). Additionally, in Drosophila HSP models, both impaired ER integrity and affected SV cycling were rescued upon Ca^{2+} bath application (Summerville et al, 2016). In this report, we found that loss of VAP-SCRN1 interactions in neurons results in elevated basal Ca^{2+} levels at presynaptic sites. This implies that the cytoplasmic-extracellular Ca^{2+} concentration gradient is reduced, which could explain the reduction in evoked Ca^{2+} response and subsequent decreased SV cycling. Consistently, previous reports in non-neuronal cells showed that VAP-mediated membrane contact sites regulate Ca^{2+} homeostasis and that SCRN1 controls Ca^{2+}-dependent processes (Way et al, 2002; Lin et al, 2015; Paillusson et al, 2017). It remains poorly understood how prolonged increase in basal Ca^{2+} levels leads to reduced SV cycling. We speculate that chronic elevation of basal Ca^{2+} levels could result in compensatory responses that may lead to downscaled synaptic strength. This could be accomplished at different levels, e.g., by decreasing bouton size, lower number of synapses and SVs, and downregulation of proteins involved in the SV cycle machinery. Consistent with this idea, we observed less and smaller boutons in VAP knockdown neurons. In addition to the Ca^{2+}-mediated effects, the smooth ER in axons could also modulate SV cycling by controlling lipid homeostasis. The presynaptic membrane is comprised of a unique presynaptic lipid composition that is required for proper overall presynaptic function (Lauwers et al, 2016). Possibly, this presynaptic lipid composition could be facilitated and maintained by enabling lipid delivery at VAP-mediated membrane contact sites. Taken together, it would be interesting to direct future research in exploring the

possible roles of VAP-SCRN1 interactions in controlling Ca^{2+} homeostasis and presynaptic lipid composition, and on how this could modulate the tightly spatiotemporal controlled SV cycle.

Molecular function of VAP-interacting protein SCRN1

It remains unclear how the SCRN1 interaction with VAP at the ER membrane may control the observed phenotypes on ER integrity. The C69 protease domain of SCRN1 did not show proteolytic activity, whereas this was observed for family members SCRN2 and SCRN3. Thus, it is unlikely that the observed VAP-mediated functions involve enzymatic activity of SCRN1. However, we did observe oligomerization of SCRN1, which may hint for a scaffolding function of SCRN1. Possibly, as scaffolding protein, SCRN1 could promote stabilization of VAP interactions at membrane contact sites. Consistent with this, we observed increased stabilization of ER structures upon wild-type SCRN1 expression. This highlights the importance of controlling the endogenous levels of SCRN1 at the ER membrane in order to balance between ER dynamics and stability. This is supported by the observation that endogenous SCRN1 proteins were not robustly localized at ER structures, whereas SCRN1 proteins were fully recruited to VAP at the ER membrane upon elevating VAP and SCRN1 levels. Similarly, it was previously shown that many other proteins containing a FFAT(-like) motif also did not fully coincide with ER structures (Murphy & Levine, 2016). Together, these findings imply that SCRN1, as well as many other FFAT(-like) proteins, undergoes continuous cycles of competitive binding and unbinding to the limited available VAP-binding pockets. As such, we propose that controlling endogenous intracellular SCRN1 levels, and thus competition with other VAP interactors, could be a novel mechanism to tune ER dynamics and subsequently presynaptic function. Moreover, unlike the ubiquitously expressed VAPs, SCRN1 expression is highly enriched in brain tissue. Therefore, SCRN1 may be engaged in controlling VAP-mediated functions in brain tissue specifically.

In summary, we propose that VAP-SCRN1 interactions act as a novel control mechanism for dynamic ER remodeling, and consequently Ca^{2+} homeostasis and SV cycling. Future work is required to better understand the molecular function of VAP-SCRN1 interactions in mediating ER integrity and Ca^{2+}-driven SV cycling. Finally, investigating additional ER-mediated control mechanisms that are engaged in modulating presynaptic function is required to obtain more insights into the precise function of the dynamic and continuous neuronal ER network in controlling SV cycling.

5

Materials and Methods

Animals

All animal experiments were approved by the Animal Ethical Review Committee (DEC) of Utrecht University and performed in accordance with the guidelines for the welfare of experimental animals issued by the Dutch law and following European regulations (Guideline 86/609/EEC).

Primary rat neuron culture and transfection

Dissociated hippocampal and cortical neuron cultures were prepared from embryonic day 18 rat pups of mixed gender. Cells were plated on 18-mm glass coverslips coated with poly-l-lysine (37.5 mg/ml) and laminin (1.25 mg/ml) in a 12-well plate at a density of 100k/well for hippocampal neurons and 50k/well for cortical neurons. Cultures were maintained in Neurobasal medium (NB) supplemented with 2% B27, 0.5 mM glutamine, 16.6 μM glutamate, and 1% penicillin/streptomycin at 37°C in 5% CO_2.

Neuron cultures were transfected using a mixture of 3.3 μl lipofectamine 2000 (Invitrogen), 1.5–3.0 μg DNA, and 200 μl NB per coverslip. For knockdown experiments, a total of 1.5 μg DNA of shRNA construct(s) was used per coverslip. The transfection mixture was added to the coverslips, which were placed in fresh NB supplemented with 0.5 mM glutamine, and incubated for 45–90 min. Next, coverslips were washed once in prewarmed NB and transferred back to their original medium. Cells were maintained for 4 days (for knockdown experiments) or 24–48 h (for other experiments) prior to fixation or live-cell imaging.

Cell line culture and transfection

COS7 and HEK293T cells were cultured on plastic at 37°C in 5% CO_2 in DMEM/Ham's F10 (50%/50%) medium supplemented with 10% FCS and 1% penicillin/streptomycin. COS7 and HEK293T cells were plated on, respectively, 18-mm glass coverslips or plastic 1 day prior to transfection with MaxPEI (Polysciences). In brief, MaxPEI/DNA (3:1 ratio) was mixed in fresh serum-free DMEM or Ham's F10 medium, incubated for 20 min, and added to the cell culture. After 24 h, cells were either processed for biochemistry, fixed, or used for live-cell imaging.

DNA plasmids

The following plasmids are described previously: Myc-VAPA, Myc-VAPB, HA-VAPA (with E178G mutation), HA-VAPB, HA-VAPB-K87D/M89D, GFP-VAPB-TM, GFP-VAPB-MSP-CC, and VAPB-MSP-GFP (with E6I single nucleotide polymorphism and K139R mutation; Teuling et al, 2007); pGFPC1-Sec61β (Hradsky et al, 2011); HA-BirA (de Boer et al, 2003); BioGFP (Jaworski et al, 2009); GW1-RFP and pGW1-GFP (Hoogenraad et al, 2005); pSuper vector (Brummelkamp et al, 2002); ssRFP-KDEL (Addgene plasmid #62236, gift from Dr. Erik Snapp; Snapp et al, 2006), TagRFP-ER (Schatzle et al, 2018), HA-Erlin1, and HA-Erlin2 (gift from Dr. Richard J.H. Wojcikiewicz; Pearce et al, 2007, 2009); GCaMP6f (Addgene plasmid #58514, gift from Prof. Adam E. Cohen; Venkatachalam & Cohen, 2014);

5

and R-GECO1 (Addgene plasmid #45494, gift from Prof. Robert E. Campbell; Wu et al, 2013).

The cDNAs of SCRN1a (AAH_40492.1), SCRN2 (AAH_10408.2), and SCRN3 (AAI_19685.1) were obtained from a human cDNA library kindly provided by Dr. Mike Boxem. All wild-type SCRN1, SCRN1-N (1–293), SCRN1-C (293–414), SCRN2, and SCRN3 constructs were generated using PCR-based cloning strategies and inserted into β-actin (for HA-SCRN1) or GW1 (for all other constructs) vectors. Constructs with single-point mutations were generated using site-directed mutagenesis. SCRN1 FFAT-like mutant constructs were obtained for each predicted FFAT-like motif identified by a previously reported algorithm (Murphy & Levine, 2016). More specifically, SCRN1-Y40A, SCRN1-F144A, SCRN1-F153A, and SCRN1-F402A were generated by replacing the conserved hydrophobic phenylalanine or tyrosine residue for an alanine residue. Proteolytic dead mutant constructs SCRN1-C9A, SCRN2-C12A, and SCRN3-C6A were generated by replacing the predicted proteolytic cysteine residue, as identified by the online MEROPS database, by a non-catalytic alanine residue. The RIM1a-mCherry construct was obtained by exchanging the HA-tag of the previously reported pAJ14063-pFUGW-RIM1aWT-HA construct (de Jong et al, 2018). The following shRNAs inserted in pSuper vectors were used in this study: VAPA shRNA #1 (5′-GCATGCAGAGTGCTGTTTC-3′; Teuling et al, 2007), VAPA shRNA #2 (5′-GGAAACTGATGGAAGAGTG-3′; Teuling et al, 2007), and VAPB shRNA #1 (5′-GGTGATGGAAGAGTGC-3′; Teuling et al, 2007); and SCRN1 shRNA #1 (5′-GATCCTTCCAGGTCCATAT-3′), SCRN1 shRNA #2 (5′-GCACTTACATCTCAATTGA-3′), and SCRN1 shRNA #3 (5′-CAGGCTTGGTTTAGAACGA-3′).

Antibodies

The following primary antibodies were used for this study: rabbit anti-VAPA (homemade #1006-04; Teuling et al, 2007) and anti-VAPB (homemade #1006-00; Teuling et al, 2007); mouse anti-synaptotagmin (SySy, 105311, clone 604.2); rabbit anti-SCRN1 (SySy, 289003; used in Fig 1E), rabbit anti-SCRN1 (Abcam, ab105355; used in Fig S1D), and rabbit anti-SCRN1 (Sigma, HPA024517, RRID:AB_2184811; used for all other experiments; validation SCRN1 antibodies in Fig S1G–J); guinea pig anti-vGlut (Millipore, ab5095); rat anti-HA (Roche, 1867423; used for immunostainings); mouse anti-HA (BioLegend, mms-101p, clone 16B12; used for immunoblots); mouse anti-actin (Chemicon, MAB1501R, clone C4); rabbit anti-GFP (Abcam, ab290); mouse anti-Myc (Santa Cruz, SC40, clone 9E10); and mouse α-Tubulin (Sigma, T5168, clone B-5-1-2, RRID:AB_477579). The following secondary antibodies were used for this study: anti-rabbit Alexa 488 (Life Technologies, A11034), anti-rabbit Alexa 568 (Life Technologies, A11036), anti-rat Alexa 568 (Life Technologies, A11077), anti-guinea pig Alexa 568 (Life Technologies, A11075), anti-mouse Alexa 647 (Life Technologies, A21236), anti-mouse anti-HRP (Dako, P0260), anti-rabbit anti-HRP (Dako, P0399), anti-mouse IRDye 680LT (Li-Cor, 926-68020), and anti-rabbit IRDye 800CW (Li-Cor, 926-32211).

5

Tissue extracts, cell extracts, and immunoblotting

To generate tissue extracts for Western blot and mass spectrometry analysis, different brain regions (cerebellum, cortex, hippocampus, midbrain, brainstem, and spinal cord) or whole brains were dissected from adult female rats. Samples were homogenized in ice-cold homogenization buffer (150 mM NaCl, 50 mM Tris, 0.1% SDS, 0.2% NP-40, pH 7.8) supplemented with 1× complete protease inhibitor cocktail (Roche), sonicated, and centrifuged (15 min, 900 g, 4°C). Protein concentrations of supernatant were measured using a BCA protein assay (Pierce). Next, 20 µg protein per sample was resuspended in SDS sample buffer and boiled for 5 min at 95°C. To generate cell extracts for Western blot analysis, transfected HEK293T cells were washed and harvested in ice-cold PBS. Cells were centrifuged (5 min, 300 g, 4°C), and the pellet was resuspended in ice-cold lysis buffer (100 mM Tris, 150 mM NaCl, 1% Triton, pH 7.5) supplemented with 1× complete protease inhibitor cocktail (Roche). Cell lysates were centrifuged (5 min, 20,000 g, 4°C), and supernatant was resuspended in SDS sample buffer and boiled for 10 min at 100°C. Samples were resolved on SDS–page gels and transferred to nitrocellulose membranes (Bio-Rad) or polyvinylidene difluoride membranes (Millipore). Membranes were blocked for 30 min with PBS-T (PBS with 0.05% Tween) with 2% BSA. Next, membranes were sequentially incubated with primary and secondary antibodies diluted in PBS-T with 2% BSA, and washed three times with PBS-T after each antibody incubation step. Proteins resolved on the membranes were visualized using Odyssey Infrared Imaging (Li-Cor Biosciences) or enhanced chemiluminescence.

Pull-down assays and mass spectrometry analysis

For biotin–streptavidin pull-down assays, HEK293T cells were co-transfected with BirA, BioGFP(-fusion) plasmids (used as bait), and an additional plasmid (used as prey). After ~ 24 h, cells were washed once with ice-cold PBS, harvested in ice-cold PBS supplemented with 0.5× complete protease inhibitor cocktail (Roche), and centrifuged (5 min, 300 g, 4°C). Cell pellets were resuspended in ice-cold lysis buffer (100 mM Tris, 150 mM NaCl, 1% Triton, pH 7.5) supplemented with 1× complete protease inhibitor cocktail, incubated for 10 min on ice, and centrifuged (5 min, 20,000 g, 4°C). Supernatant was used for the binding assay and for generating input samples by boiling for 5 min at 100°C in SDS sample buffer. Beads were pretreated before the binding assay. For regular pull-down assays with cell culture extracts, magnetic Dynabeads M-280 Streptavidin (Thermo Fisher Scientific) were prewashed once with normal washing buffer (20 mM Tris HCl, 150 mM KCl, 0.5% Triton, pH 7.5), incubated for 30 min at room temperature with blocking buffer (20 mM Tris, 150 mM KCl, 0.2 µg/µl CEA, pH 7.5), and washed twice with normal washing buffer. Binding of HEK293T cell lysates and beads was performed for 1 h at 4°C. Beads were subsequently washed five times using normal washing buffer and boiled for 5 min at 100°C in lysis buffer with SDS sample buffer to elute proteins and generate pull-down samples. Alternatively, for pull-down assays with whole brain extracts for mass spectrometry analysis, beads were prewashed twice with low salt buffer (100 mM KCl, 0.1% Triton X-100, 20 mM Tris, pH 7.6), twice with high salt buffer (500 mM KCl, 0.1% Triton X-100, 20 mM Tris, pH 7.6), and twice

again in low salt buffer. Binding of HEK293T cell lysates and beads was performed for 1 h at 4°C in presence of whole rat brain extract (prepared as described above), and beads were subsequently washed five times using normal washing buffer. Mass spectrometry analysis of samples was conducted as described before (Cunha-Ferreira et al, 2018). All the mass spectrometry proteomics data have been deposited to the Pride database (http://www.ebi.ac.uk/pride) with the dataset identifier PXD014534.

Immunofluorescence staining

Cells were fixed for 10 min in 4% formaldehyde and 4% sucrose (neurons) or in 4% formaldehyde (COS7 cells) at room temperature and washed three times with PBS. Fixed neurons were sequentially incubated with primary and secondary antibodies diluted in GDB (0.2% BSA, 0.8 M NaCl, 0.5% Triton X-100, 30 mM phosphate buffer, pH 7.4). Fixed COS7 cells were first permeabilized for 10 min in PBS with 0.1% Triton-X, blocked for 30 min in PBS with 2% BSA, and sequentially incubated with primary and secondary antibodies diluted in PBS with 2% BSA. Cells were washed three times with PBS after each antibody incubation step.

Expansion microscopy sample preparation

Expansion microscopy was performed according to proExM protocol (Tillberg et al, 2016). Briefly, immunostained cells on 18-mm glass coverslips were incubated overnight in PBS with 0.1 mg/ml Acryloyl-X (Thermo Fisher, A20770) and 0.002% of 0.1 μm yellow–green Fluorospheres (Thermo Fisher, F8803). These bright fluorescent microspheres adhered to cell surfaces, thereby this cell boundary marker simplified the localization of cells in the expanded samples. Cells were washed three times with PBS and transferred to a gelation chamber (13 mm diameter, 120 μl volume) made of silicone molds (Sigma-Aldrich, GBL664107) on a parafilm-covered glass slide. The chamber was prefilled with monomer solution (PBS, 2 M NaCl, 8.625% (w/w) sodium acrylate, 2.5% (w/w) acrylamide, and 0.15% (w/w) N,N′-methylenebisacrylamide) supplemented with 0.4% (w/w) tetramethylethylenediamine (TEMED) accelerator and 0.2% (w/w) ammonium persulfate (APS) initiator. The gelation proceeded for 1 h at 37°C in a humidified incubator. Gels were further immersed into 2 ml of 8 units/ml proteinase-K in digestion buffer (pH 8.0, 50 mM Tris, 1 mM EDTA, 0.5% Triton X-100, 0.08 M guanidine HCl) solution for 4 h at 37°C for digestion. Gels were transferred to 50 ml deionized water for overnight expansion, and water was refreshed once to ensure the expansion reached plateau. Plasma-cleaned #1.5 coverslips for gel imaging were incubated in 0.1% poly-l-lysine to reduce gel's drift during acquisition. Gels were mounted using custom-printed imaging chambers (https://www.tinkercad.com/things/7qqYCygcbNU). Expansion factor was calculated as a ratio of a gel's diameter to the diameter of gelation chamber and was in the range of 4.0–4.1.

Confocal microscopy

Confocal microscopy of fixed samples on glass coverslips was performed with a LSM 700 confocal laser-scanning microscope (Zeiss) equipped with a Plan-Apochromat 63x NA 1.40 oil DIC, EC Plan-Neofluar 40x NA1.30 Oil DIC, and a Plan-Apochromat 20x NA 0.8 objective. Each confocal image represents a maximum intensity projection of a z-series covering the region of interest. For

5

fluorescence intensity measurements, settings were kept the same for all conditions. Confocal microscopy of fixed samples on expanded gels was performed with a Leica TCS SP8 STED 3X microscope using a HC PL APO 63×/1.20 W CORR CS2 water immersion objective. Images were acquired with lateral pixel size in the range of 70–80 nm and axial of 180 nm using internal HyD detector. If necessary, a drift correction of Z-stack was performed in Huygens Professional version 17.04 (Scientific Volume Imaging, The Netherlands) using cross-correlation between adjacent slices. All images were deconvolved in the same program, using the CMLE algorithm, with SNR:7 and 20 iterations. Movies of 3D reconstructions of z-stacks were performed in Blender version 2.79b (Blender Institute, Amsterdam).

Syt uptake assay

Hippocampal neurons were pretreated with 50 μM bicuculline (Sigma, 14340) in their original NB medium for 10 min at 37°C in 5% CO2. Next, neurons were directly incubated for 10 min with Syt antibodies targeting the luminal side of the synaptic vesicle protein, which were diluted (1:200) in the same original NB medium supplemented with 50 μM bicuculline at 37°C in 5% CO2. Next, cells were fixed, stained with secondary antibodies, and subjected to image quantifications and analysis.

Image quantification and analysis

Quantifications of fluorescent Syt intensity at presynaptic boutons

Presynaptic boutons were identified by swellings along the axon using expressed RFP as fill, similar as described previously (Bamji et al, 2003; Leal-Ortiz et al, 2008; Spangler et al, 2013). Fluorescent intensity of internalized Syt at each bouton was measured using a circular region of interest with a fixed size of ø 1.39 μm/ø 7 pix.

SCRN1 knockdown quantifications

SCRN1 knockdown efficiency was analyzed in cortical neurons (DIV4) co-transfected with RFP and a single SCRN1 shRNA. The average fluorescence intensity was measured of the somatic region without nucleus.

Quantifications of SCRN1 recruitment and ER morphology

For analyzing SCRN1 recruitment to ER in COS7 cells, the number of cells showing obvious enriched SCRN1 localization at ER structures was scored. For analyzing reticular ER structures in COS7 cells, the number of cells containing less than ~ 30% detectable ER tubules in cytoplasm was scored as "non-reticular ER localization".

Live-cell imaging

Live-cell imaging (other than electric field stimulation experiments) was conducted on an inverted microscope Nikon Eclipse Ti-E (Nikon), equipped with a Plan Apo VC 100x NA 1.40 oil objective (Nikon), Plan Apo VC 60x N.A. 1.40 oil objective (Nikon), a Plan Apo VC 40x NA 1.40 oil objective (Nikon), a Yokogawa CSU-X1-A1 spinning disk confocal unit (Roper Scientific), a Photometrics Evolve 512 EMCCD camera (Roper Scientific), and an incubation chamber (Tokai Hit) mounted

on a motorized XYZ stage (Applied Scientific Instrumentation), all controlled by MetaMorph (Molecular Devices) software. Cells were imaged in their original medium. During acquisition, the objective was kept at 37°C and the imaging chamber was kept at 37°C in 5% CO2.

Relative basal Ca^{2+} levels' measurements

Hippocampal neurons were transfected with Ca^{2+} indicators GCaMP6f or R-GECO1, and mRFP or GFP to identify transfected neurons and presynaptic boutons. Field of views with axonal structures for all conditions were selected based on similar expression levels, while remaining blind for the expression levels of Ca^{2+} indicators. Duo-color time-lapses were acquired of 21 frames with 30-s time interval, with a Z-stack of three planes with 0.5-μm interval for each frame, and cells were treated with 1–10 μM ionomycin (Santa Cruz, SC3592) prior to frame 13. Fluorescent intensities of GCaMPf or R-GECO1 at single boutons were measured for the maximum intensity projections of each frame using a fixed ROI. Fluorescent values were corrected for background fluorescence and normalized to the maximum fluorescent intensity within seven frames after ionomycin treatment (F/Fmax). Relative basal Ca^{2+} levels were determined by the F0/Fmax ratio, where baseline values (F0) were obtained by averaging the fluorescent intensities of the five frames prior to ionomycin treatment.

Fluorescent recovery after photo-bleaching

Fluorescent recovery after photo-bleaching experiments were conducted on the characteristic dense ER clusters in TagRFP-ER expressing hippocampal neurons showing this phenotype, or in regular dense ER structures for control conditions, using the ILas system (Roper Scientific; Fig 4E). Fluorescence recovery of TagRFP-ER in bleached regions can be interpreted as the result from two processes: (i) diffusion of TagRFP-ER within existing ER tubules (Yalcin et al, 2017) and (ii) local ER remodeling within the photo-bleached region. The FRAP area size and imaging settings were kept the same for all conditions. For analysis, fluorescence intensity of the bleached region was corrected for background noise and for overall bleaching occurring during acquisition. Next, the post-bleaching fluorescent recovery values were normalized to the baseline fluorescence, which was defined by the average fluorescent intensity of five initial frames prior to onset of photo-bleaching.

5

Electric field stimulation and real-time Ca^{2+} dynamics

All experiments were carried out in modified Tyrode's solution (pH 7.4, 25 mM HEPES, 119 mM NaCl, 2.4 mM KCl, 2 mM CaCl2, 2 mM $MgCl^2$, 30 mM glucose). Objective was prewarmed to 37°C with objective heater (Tokai Hit). Hippocampal neurons were placed in a stimulation chamber (World Precision Instruments) and stimulated (50 Aps, 20 Hz) by electric field stimulation (platinum electrodes, 10 mm spacing, 1 ms pulses of 50 mA, alternating polarity) applied by constant current stimulus isolator (WPI A 385, World Precision Instruments) in the presence of 10 μM 6-cyano-7 nitroquinoxaline-2,3-dione and 50 μM D,L-2-amino-5-phosphonovaleric acid (CNQX/AP5; Tocris Bioscience). Imaging was performed on an inverted Nikon Eclipse TE2000 microscope equipped with mercury lamp

(Nikon). Fluorescence emission was detected using a 40× oil-immersion objective [Nikon Apo, numerical aperture (NA) 1.3] and ET-GFP filter (GCaMP) or ET-mCherry (mCherry), together with a EMCCD camera (Evolve 512, Photometrics) controlled by MetaMorph 7.7 software (Molecular Devices). Images were acquired every 650 ms with exposure times between 50 and 100 ms in 1×1 binning mode. Quantitative analyses of GCaMP experiments were performed with custom macros in Igor Pro (WaveMetrics) using an automated detection algorithm as described previously (Wienisch & Klingauf, 2006).

Statistical analysis

Statistical details are included in corresponding figure legends. P-values are annotated as follows: *$P < 0.05$, **$P < 0.01$, and ***$P < 0.001$. Data processing and statistical analysis were conducted in Prism GraphPad (version 7.0) software.

Acknowledgements

Author contributions

FWL designed, conducted, and interpreted experiments, and wrote the article. YC performed biochemical experiments and cloned constructs. JTK initiated the study, cloned constructs, and performed initial experiments together with MMB. AB conducted the electric field stimulation experiments, RS performed the mass spectrometry experiments and was supported by MA, and EAK provided the expansion microscopy data. HDM gave advice throughout the project and edited the article. CCH supervised the research, coordinated the study, and edited the article.

Conflict of interest

CCH is an employee of Genentech, Inc., a member of the Roche group. The authors declare that they have no additional conflict of interest.

REFERENCES

Bamji SX, Shimazu K, Kimes N, Huelsken J, Birchmeier W, Lu B, Reichardt LF(2003) Role of beta-catenin in synaptic vesicle localization andpresynaptic assembly. Neuron 40: 719 – 731

de Boer E, Rodriguez P, Bonte E, Krijgsveld J, Katsantoni E, Heck A, Grosveld F,Strouboulis J (2003) Efficient biotinylation and single-step purification of tagged transcription factors in mammalian cells and transgenic mice. Proc Natl Acad Sci USA 100: 7480 – 7485

Brummelkamp TR, Bernards R, Agami R (2002) A system for stable expression of short interfering RNAs in mammalian cells. Science 296: 550 – 553

Cunha-Ferreira I, Chazeau A, Buijs RR, Stucchi R, Will L, Pan X, Adolfs Y, vander Meer C, Wolthuis JC, Kahn OI et al (2018) The HAUS complex is a keyregulator of non-centrosomal microtubule organization during neuronal development. Cell Rep 24: 791 – 800

De Gregorio C, Delgado R, Ibacache A, Sierralta J, Couve A (2017) Drosophila atlastin in motor neurons is required for locomotion and presynaptic function. J Cell Sci 130: 3507 – 3516

Esteves T, Durr A, Mundwiller E, Loureiro JL, Boutry M, Gonzalez MA, GauthierJ, El-Hachimi KH, Depienne C, Muriel MP et al (2014) Loss of association of REEP2 with membranes leads to hereditary spastic paraplegia. Am JHum Genet 94: 268 – 277

Gomez-Suaga P, Perez-Nievas BG, Glennon EB, Lau DHW, Paillusson S, Morotz GM, Cali T, Pizzo P, Noble W, Miller CCJ (2019) The VAPB-PTPIP51 endoplasmic reticulum-mitochondria tethering proteins are present in neuronal synapses and regulate synaptic activity. Acta Neuropathol Commun 7: 35

Hazan J, Fonknechten N, Mavel D, Paternotte C, Samson D, Artiguenave F, Davoine CS, Cruaud C, Durr A, Wincker P et al (1999) Spastin, a new AAA protein, is altered in the most frequent form of autosomal dominant spastic paraplegia. Nat Genet 23: 296 – 303

Hoogenraad CC, Milstein AD, Ethell IM, Henkemeyer M, Sheng M (2005) GRIP1 controls dendrite morphogenesis by regulating EphB receptor trafficking. Nat Neurosci 8: 906 – 915

Hradsky J, Raghuram V, Reddy PP, Navarro G, Hupe M, Casado V, McCormick PJ, Sharma Y, Kreutz MR, Mikhaylova M (2011) Post-translational membrane insertion of tail-anchored transmembrane EF-hand Ca2+sensor calneurons requires the TRC40/Asna1 protein chaperone. J Biol Chem 286: 36762 – 36776

Jaworski J, Kapitein LC, Gouveia SM, Dortland BR, Wulf PS, Grigoriev I, CameraP, Spangler SA, Di Stefano P, Demmers J et al (2009) Dynamic microtubules regulate dendritic spine morphology and synaptic plasticity. Neuron 61: 85 – 100

de Jong APH, Roggero CM, Ho MR, Wong MY, Brautigam CA, Rizo J, Kaeser PS (2018) RIM C2B domains target presynaptic active zone functions to PIP2-containing membranes. Neuron 98: 335 – 349.e7

de Juan-Sanz J, Holt GT, Schreiter ER, de Juan F, Kim DS, Ryan TA (2017) Axonal endoplasmic reticulum Ca(2+) content controls release probability in CNS nerve terminals. Neuron 93: 867 – 881.e6

Kaiser SE, Brickner JH, Reilein AR, Fenn TD, Walter P, Brunger AT (2005) Structural basis of FFAT motif-mediated ER targeting. Structure 13: 1035 – 1045

Kuijpers M, van Dis V, Haasdijk ED, Harterink M, Vocking K, Post JA, ScheperW, Hoogenraad CC, Jaarsma D (2013) Amyotrophic lateral sclerosis (ALS)-associated VAPB-P56S inclusions represent an ER quality control compartment. Acta Neuropathol Commun 1: 24

Lauwers E, Goodchild R, Verstreken P (2016) Membrane lipids in presynaptic function and disease. Neuron 90: 11 – 25

Leal-Ortiz S, Waites CL, Terry-Lorenzo R, Zamorano P, Gundelfinger ED, Garner CC (2008) Piccolo modulation of Synapsin1a dynamics regulates synaptic vesicle exocytosis. J Cell Biol 181: 831 –846

Lin S, Jiang T, Yu Y, Tang H, Lu S, Peng Z, Fan J (2015) Secernin-1 contributes to colon cancer progression through enhancing matrix metalloproteinase-2/9 exocytosis. Dis Markers 2015: 230703

5

Loewen CJ, Roy A, Levine TP (2003) A conserved ER targeting motif in three families of lipid binding proteins and in Opi1p binds VAP. EMBO J 22:2025 – 2035

Montenegro G, Rebelo AP, Connell J, Allison R, Babalini C, D'Aloia M, MontieriP, Schule R, Ishiura H, Price J et al (2012) Mutations in the ER-shaping protein reticulon 2 cause the axon-degenerative disorder hereditary spastic paraplegia type 12. J Clin Invest 122: 538 – 544

Muallem S, Chung WY, Jha A, Ahuja M (2017) Lipids at membrane contact sites: cell signaling and ion transport. EMBO Rep 18: 1893 – 1904

Murphy SE, Levine TP (2016) VAP, a versatile access point for then doplasmic reticulum: review and analysis of FFAT-like motifs in the VAPome. Biochim Biophys Acta 1861: 952 – 961

Nishimura AL, Mitne-Neto M, Silva HC, Richieri-Costa A, Middleton S,Cascio D, Kok F, Oliveira JR, Gillingwater T, Webb J et al (2004) A mutation in the vesicle-trafficking protein VAPB causes late-onset spinal muscular atrophy and amyotrophic lateral sclerosis. Am J Hum Genet 75:822 – 831

Paillusson S, Gomez-Suaga P, Stoica R, Little D, Gissen P, Devine MJ, Noble W, Hanger DP, Miller CCJ (2017) alpha-Synuclein binds to the ER-mitochondria tethering protein VAPB to disrupt Ca(2+) homeostasis and mitochondrial ATP production. Acta Neuropathol 134: 129 – 149

Pearce MM, Wang Y, Kelley GG, Wojcikiewicz RJ (2007) SPFH2 mediates the endoplasmic reticulum-associated degradation of inositol 1,4,5-trisphosphate receptors and other substrates in mammalian cells. J BiolChem 282: 20104 – 20115

Pearce MM, Wormer DB, Wilkens S, Wojcikiewicz RJ (2009) An endoplasmic reticulum (ER) membrane complex composed of SPFH1 and SPFH2 mediates the ER-associated degradation of inositol 1,4,5-trisphosphatereceptors. J Biol Chem 284: 10433 – 10445

Pei J, Grishin NV (2003) Peptidase family U34 belongs to the superfamily of N-terminal nucleophile hydrolases. Protein Sci 12: 1131 – 1135

Pennetta G, Hiesinger PR, Fabian-Fine R, Meinertzhagen IA, Bellen HJ (2002) Drosophila VAP-33A directs bouton formation at neuromuscular junctions in a dosage-dependent manner. Neuron 35: 291 – 306

Schatzle P, Esteves da Silva M, Tas RP, Katrukha EA, Hu HY, Wierenga CJ, Kapitein LC, Hoogenraad CC (2018) Activity-dependent actin remodeling at the base of dendritic spines promotes microtubule entry. Curr Biol 28:2081 – 2093.e6

Skehel PA, Martin KC, Kandel ER, Bartsch D (1995) A VAMP-binding protein from Aplysia required for neurotransmitter release. Science 269:1580 – 1583

Snapp EL, Sharma A, Lippincott-Schwartz J, Hegde RS (2006) Monitoring chaperone engagement of substrates in the endoplasmic reticulum of live cells. Proc Natl Acad Sci USA 103: 6536 – 6541

Spangler SA, Schmitz SK, Kevenaar JT, de Graaff E, de Wit H, Demmers J, Toonen RF, Hoogenraad CC (2013) Liprin-alpha2 promotes the presynaptic recruitment and turnover of RIM1/CASK to facilitate synaptic transmission. J Cell Biol 201: 915 – 928

Summerville JB, Faust JF, Fan E, Pendin D, Daga A, Formella J, Stern M, McNew JA (2016) The effects of ER morphology on synaptic structure and function in Drosophila melanogaster. J Cell Sci 129: 1635 – 1648

Terasaki M (2018) Axonal endoplasmic reticulum is very narrow. J Cell Sci131: jcs210450

Teuling E, Ahmed S, Haasdijk E, Demmers J, Steinmetz MO, Akhmanova A, Jaarsma D, Hoogenraad CC (2007) Motor neuron disease-associated mutant vesicle-associated membrane protein-associated protein (VAP) B recruits wild-type VAPs into endoplasmic reticulum-derived tubular aggregates. J Neurosci 27: 9801 – 9815

Tillberg PW, Chen F, Piatkevich KD, Zhao Y, Yu CC, English BP, Gao L, Martorell A, Suk HJ, Yoshida F et al (2016) Protein-retention expansion microscopy of cells and tissues labeled using standard fluorescent proteins and antibodies. Nat Biotechnol 34: 987 – 992

Venkatachalam V, Cohen AE (2014) Imaging GFP-based reporters in neurons with multiwavelength optogenetic control. Biophys J 107: 1554 – 1563

Wang S, Tukachinsky H, Romano FB, Rapoport

5

TA (2016) Cooperation of the ER-shaping proteins atlastin, lunapark, and reticulons to generate a tubular membrane network. Elife 5: e18605

Wassie AT, Zhao Y, Boyden ES (2019) Expansion microscopy: principles and uses in biological research. Nat Methods 16: 33 – 41

Way G, Morrice N, Smythe C, O'Sullivan AJ (2002) Purification and identification of secernin, a novel cytosolic protein that regulates exocytosis in mast cells. Mol Biol Cell 13: 3344 – 3354

Wienisch M, Klingauf J (2006) Vesicular proteins exocytosed and subsequently retrieved by compensatory endocytosis are nonidentical. Nat Neurosci 9:1019 – 1027

Wu J, Liu L, Matsuda T, Zhao Y, Rebane A, Drobizhev M, Chang YF, Araki S, Arai Y, March K et al (2013) Improved orange and red Ca(2)+/ indicators and photophysical considerations for optogenetic applications. ACS Chem Neurosci 4: 963 – 972

Wu Y, Whiteus C, Xu CS, Hayworth KJ, Weinberg RJ, Hess HF, De Camilli P (2017) Contacts between the endoplasmic reticulum and other membranes in neurons. Proc Natl Acad Sci USA 114: E4859 – E4867

Wu H, Carvalho P, Voeltz GK (2018) Here, there, and everywhere: the importance of ER membrane contact sites. Science 361: eaan 5835

Yalcin B, Zhao L, Stofanko M, O'Sullivan NC, Kang ZH, Roost A, Thomas MR, Zaessinger S, Blard O, Patto AL et al (2017) Modeling of axonal endoplasmic reticulum network by spastic paraplegia proteins. Elife 6: e23882

Zhao X, Alvarado D, Rainier S, Lemons R, Hedera P, Weber CH, Tukel T, Apak M, Heiman-Patters on T, Ming L et al (2001) Mutations in a newly identified GTPase gene cause autosomal dominant hereditary spastic paraplegia. Nat Genet 29: 326 – 331

Zuchner S, Wang G, Tran-Viet KN, Nance MA, Gaskell PC, Vance JM, Ashley-Koch AE, Pericak-Vance MA (2006) Mutations in the novel mitochondrial protein REEP1 cause hereditary spastic paraplegia type 31. Am J Hum Genet 79: 365 – 369

5

5

SUPPLEMENTAL INFORMATION INVENTORY

Supplemental Figures S1-S4

Figure S1-S2, related to Figure 1

Figure S3, related to Figure 3

Figure S4, related to Figure 4

5

Figure S1. VAPs modulate bouton maintenance and are associated with brain-enriched SCRN1 proteins

(A) Localization of exogenous HA-VAPA or HA-VAPB in neurons (DIV18) co-expressing GFP-Sec61β and immunostained for bassoon. Zooms represent (1) an axonal structure with bassoon-positive presynaptic boutons (arrowheads), and (2) a dendritic structure. Scale bars: 10 μm (full size) and 5 μm (zoom).

(B) Quantifications of bouton density in hippocampal neurons (DIV18) co-expressing RFP and pSuper empty vector or VAPA/B shRNAs. N = 2, n = 80 boutons.

(C) Quantifications of bouton size in hippocampal neurons (DIV18) co-expressing RFP and pSuper empty vector or VAPA/B shRNAs. N = 2, n = 380–400 boutons.

(D) Western blot of endogenous SCRN1 expression in indicated adult rat neuronal and non-neuronal tissues. Cereb., cerebellum. Hippoc., hippocampus. Spin., spinal.

(E) Scaled representation of SCRN1-associated proteins identified with pull-down assay followed by mass spectrometry analysis of purified BioGFP or BioGFP-SCRN1 from HEK293T cell lysates. Selected candidates all showed > 10 enrichment of PSM compared to control.

(F) Localization of exogenous GFP-SCRN1 in hippocampal neurons (DIV18) immunostained for vGlut. Zoom represents an axon structure with presynaptic sites (arrowheads). Scale bars: 10 μm (full size) and 5 μm (zoom).

(G) COS7 cells expressing BioGFP-SCRN1, BioGFP-SCRN2, or BioGFP-SCRN3 and immunostained for SCRN1. Scale bar: 10 μm.

(H) Western blot of lysates from HEK293T cells expressing BioGFP-SCRN1, BioGFP-SCRN2, or BioGFP-SCRN2 and immunostained for indicated antibodies. Arrowheads represent (1) BioGFP-SCRN1 expression, (2) endogenous SCRN1 expression, (3) full-length BioGFP-SCRN proteins, and (4) N-terminal cleaved Bio GFP-SCRN2 and Bio GFP-SCRN3. Actin was used as loading control.

(I) Cortical neurons (DIV4) co-expressing RFP with pSuper empty vector (control) or SCRN1 shRNA #1. Scale bar: 10 μm.

(J) Quantifications of fluorescence intensity of endogenous SCRN1 in cortical neurons (DIV4) co-expressing RFP with pSuper empty vector (control) or SCRN1 shRNA #1, #2, or #3. N = 2, n = 13–14 cells.

Data information: Data represent mean ± SEM; **P < 0.01; ***P < 0.001, by Mann–Whitney U-test.
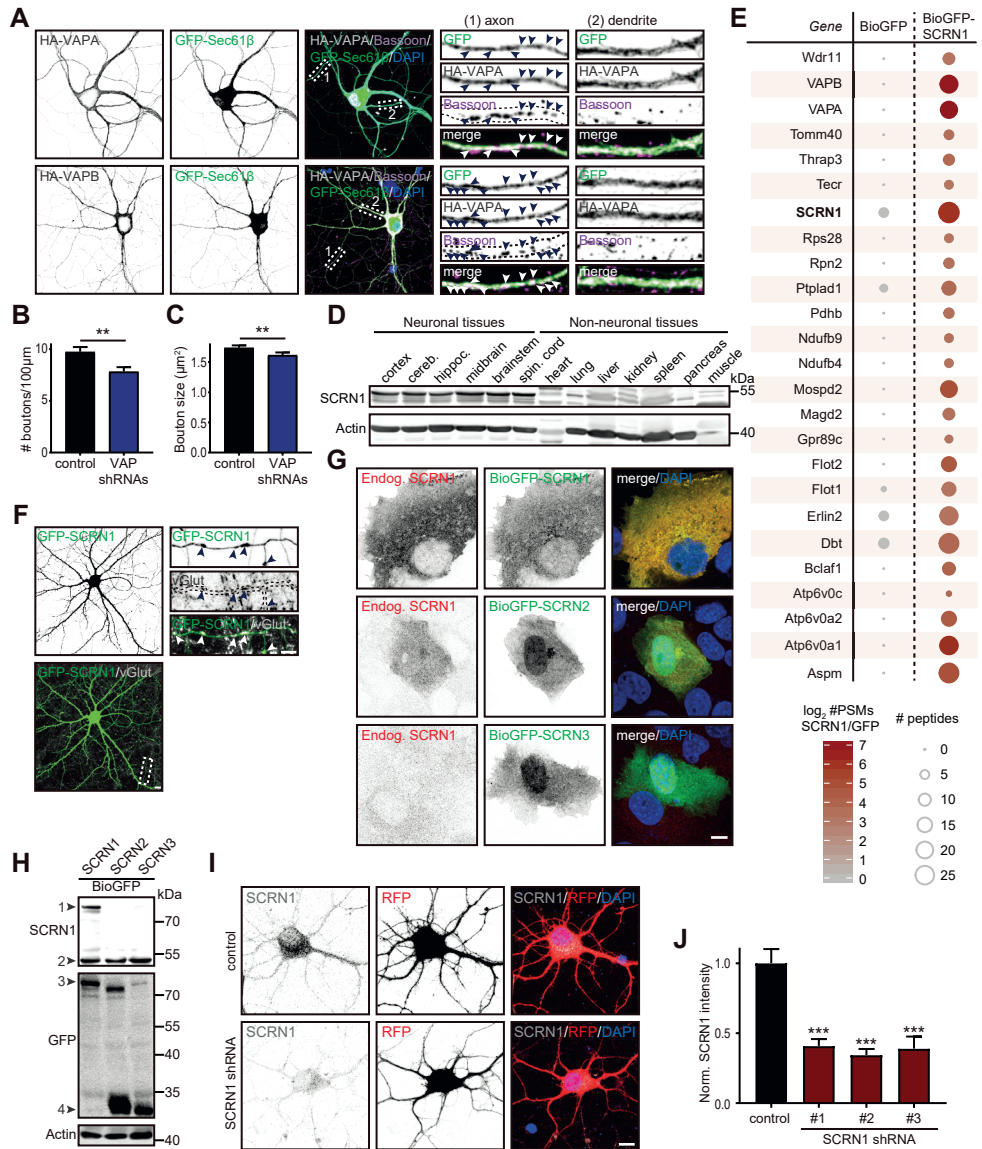
Figure S2.SCRN1 does not exhibit proteolytic activity and its C-terminal is recruited to VAP MSP domain

(A) Schematic illustration of autolytic protease activation of C69 family members.

(B) Sequence alignment of predicted proteolytic sites of SCRN family members according to the MEROPS database.

(C) Western blot of lysates from HEK293T cells expressing BioGFP-SCRN1-WT, BioGFP-SCRN1-C9A, BioGFP-SCRN2-WT, BioGFP-SCRN2-C12A, BioGFP-SCRN3-WT, or BioGFP-SCRN3-C6A. Arrowheads represent (1) full-length BioGFP-SCRN proteins and (2) N-terminal cleaved BioGFP-SCRN2 and BioGFP-SCRN3.

(D) Pull-down assay of HEK293T cells co-expressing Myc-VAPA with BioGFP, BioGFP-SCRN1-WT, BioGFP-SCRN1-C9A, BioGFP-SCRN1-N, or BioGFP-SCRN1-C.

(E) Pull-down assay of HEK293T cells co-expressing Myc-VAPB with BioGFP, BioGFP-SCRN1-WT, BioGFP-SCRN1-C9A, BioGFP-SCRN1-N, or BioGFP-SCRN1-C.

(F) Hippocampal neurons (DIV16) co-expressing HA-VAPB with GFP-SCRN1-N or GFP-SCRN1-C. Scale bars: 10 μm (full size) and 2 μm (zoom).

(G) COS7 cells co-expressing GFP-SCRN1-C with HA-VAPA or HA-VAPB. Scale bars: 10 μm (full size) and 5 μm (zoom).

(H) COS7 cells co-expressing HA-SCRN1 with GFP-VAPB-TM, GFP-VAPB-MSP-CC, or GFP-VAPB-MSP. Scale bars: 10 μm (full size) and 5 μm (zoom).

(I) COS7 cells co-expressing GFP-SCRN1-N with HA-VAPA or HA-VAPB. Scale bars: 10 μm (full size) and 5 μm (zoom).
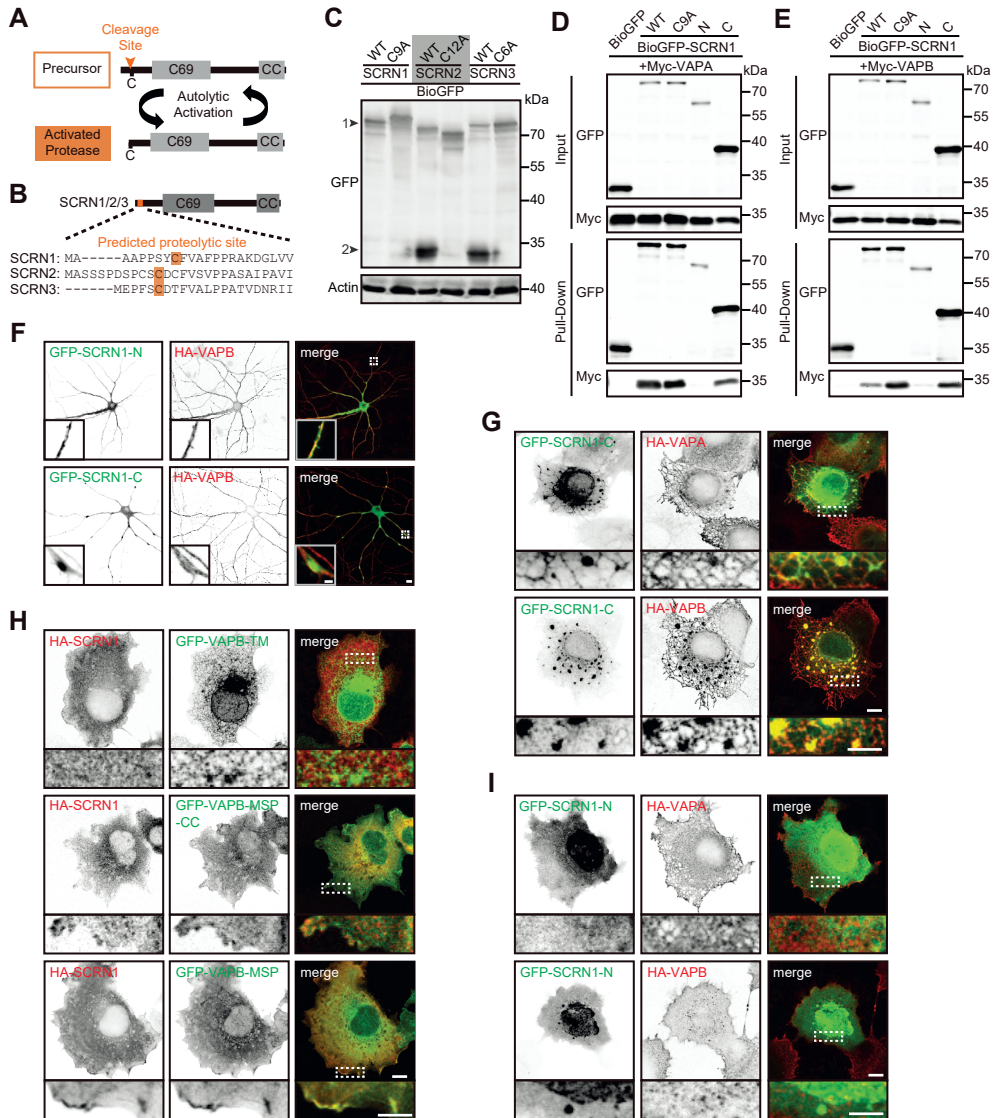
Figure S3.VAP-SCRN1 interaction at the ER is mediated by a single FFAT-like motif

(A) Schematic representation of the four potential FFAT-like motifs in SCRN1. Amino acid position number 2 (orange) of the FFAT-like motifs was mutated to alanine residues.

(B) Quantifications of SCRN1 recruitment to VAPA-positive structures in COS7 cells (%) co-expressing HA-VAPA with GFP or GFP-SCRN1, GFP-SCRN1-N, GFP-SCRN1-C, GFP-SCRN1-Y40A, GFP-SCRN1-F144A, GFP-SCRN1-F153A, or GFP-SCRN1-F402A. N = 2–3, n = 39–59.

(C) COS7 cells co-expressing HA-VAPA with GFP-SCRN1-Y40A, GFP-SCRN1-F144A, GFP-SCRN1-F153A, or GFP-SCRN1-F402A. Scale bars: 10 μm (full size) and 5 μm (zoom).

(D) Hippocampal neurons (DIV16) co-expressing HA-VAPA with GFP-SCRN1-Y40A, GFP-SCRN1-F144A, GFP-SCRN1-F153A, or GFP-SCRN1-F402A. Scale bars: 10 μm (full size) and 5 μm (zoom).

Data information: ***P < 0.001, by chi-square test with post hoc analysis including Bonferroni correction.

5

Figure S4.SCRN1 oligomerizes and regulates ER remodeling together with VAP

(A) Quantifications of reticular localization of expressed VAPB in COS7 cells (%). Cells with non-reticular ER structures contained < 30% detectable ER tubules in cytoplasm. Gray bars represent non-reticular localization accompanied with impaired VAP-SCRN1 interaction. Left: co-expression GFP-SCRN1 with HA-VAPB or HA-VAPB-K87D/M89D (N = 2–3, n = 44–46). Right: co-expression of HA-VAPB with GFP or GFP-SCRN1, GFP-SCRN1-N, GFP-SCRN1-C, GFP-SCRN1-Y40A, GFP-SCRN1-F144A, GFP-SCRN1-F153A, or GFP-SCRN1-F402A (N = 2–3, n = 41–64).

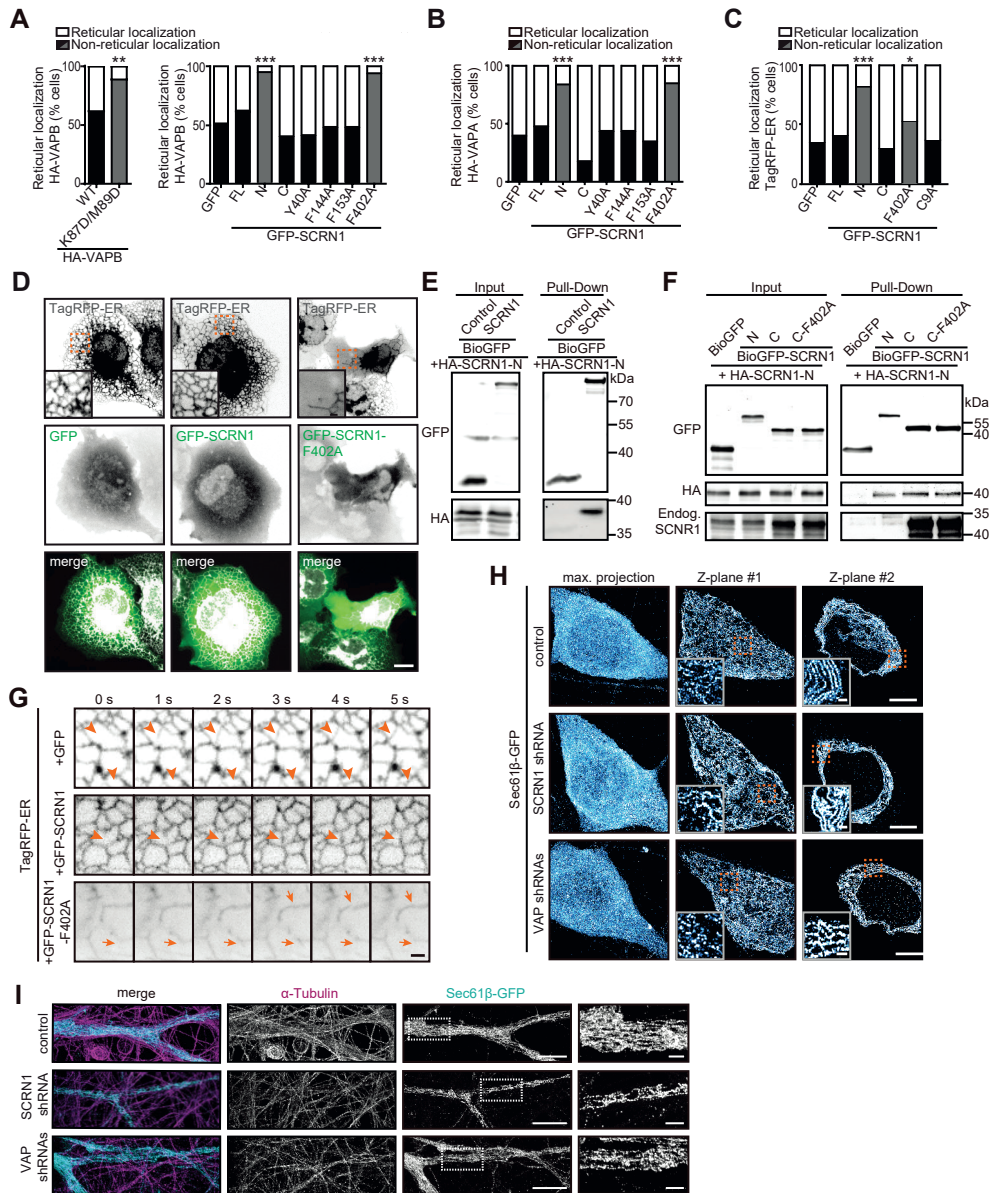(B) Quantifications of reticular localization in COS7 cells (%) co-expressing HA-VAPA with GFP or GFP-SCRN1, GFP-SCRN1-N, GFP-SCRN1-C, GFP-SCRN1-Y40A, GFP-SCRN1-F144A, GFP-SCRN1-F153A, or GFP-SCRN1-F402A. Cells with non-reticular ER structures contained < 30% detectable ER tubules in cytoplasm. Gray bars represent non-reticular localization accompanied with impaired VAP-SCRN1 interaction. N = 2–3, n = 39–62 cells.

(C) Quantifications of reticular localization of TagRFP-ER co-expressed with GFP, GFP-SCRN1, GFP-SCRN1-N, GFP-SCRN1-C, GFP-SCRN1-F402A, or GFP-SCRN1-C9A in COS7 cells. Gray bars represent non-reticular localization accompanied with impaired VAP-SCRN1 interaction. Cells with non-reticular ER structures contained < 30% detectable ER tubules in cytoplasm. N = 2–4, n = 58–120.

(D) Live COS7 cells co-expressing TagRFP-ER with GFP, GFP-SCRN1, or GFP-SCRN1-F402A. Scale bars: 10 μm (full size) and 2 μm (zoom).

(E) Pull-down assay of HEK293T cells co-expressing HA-SCRN1-N with BioGFP and BioGFP-SCRN1.

(F) Pull-down assay of HEK293T cells co-expressing HA-SCRN1-N with BioGFP, BioGFP-SCRN1-N, BioGFP-SCRN1-C, and BioGFP-SCRN1-F402A.

(G) Time-lapse of COS7 cells co-expressing TagRFP-ER and GFP, GFP-SCRN1, or GFP-SCRN1-F402A. Arrowheads mark ER tubule remodeling event, and arrows mark ER remodeling artifacts. Scale bar: 2 μm.

(H) ER nanostructures in somatic structures of hippocampal neurons (DIV18) co-expressing GFP-Sec61β with pSuper empty vector, SCRN1 shRNA, or VAPA/B shRNAs, and subjected to expansion microscopy. Left panels show maximum intensity projections of all Z-planes. Individual ER tubules and perinuclear sheets are shown in zooms of Z-plane #1 and Z-plane #2, respectively. Scale bars: 5 μm (full size) and 500 nm (zoom).

(I) ER nanostructures visualized with GFP-Sec61β in dendrites of hippocampal neurons (DIV18) immunostained for α-tubulin and co-expressed with pSuper empty vector, SCRN1 shRNA, or VAPA/B shRNAs, and subjected to expansion microscopy. Scale bars: 5 μm (full size) and 1 μm (zoom).

Data information: *$P < 0.05$; **$P < 0.01$; ***$P < 0.001$, by chi-square test (A–C) with post hoc analysis including Bonferroni correction (A, B).
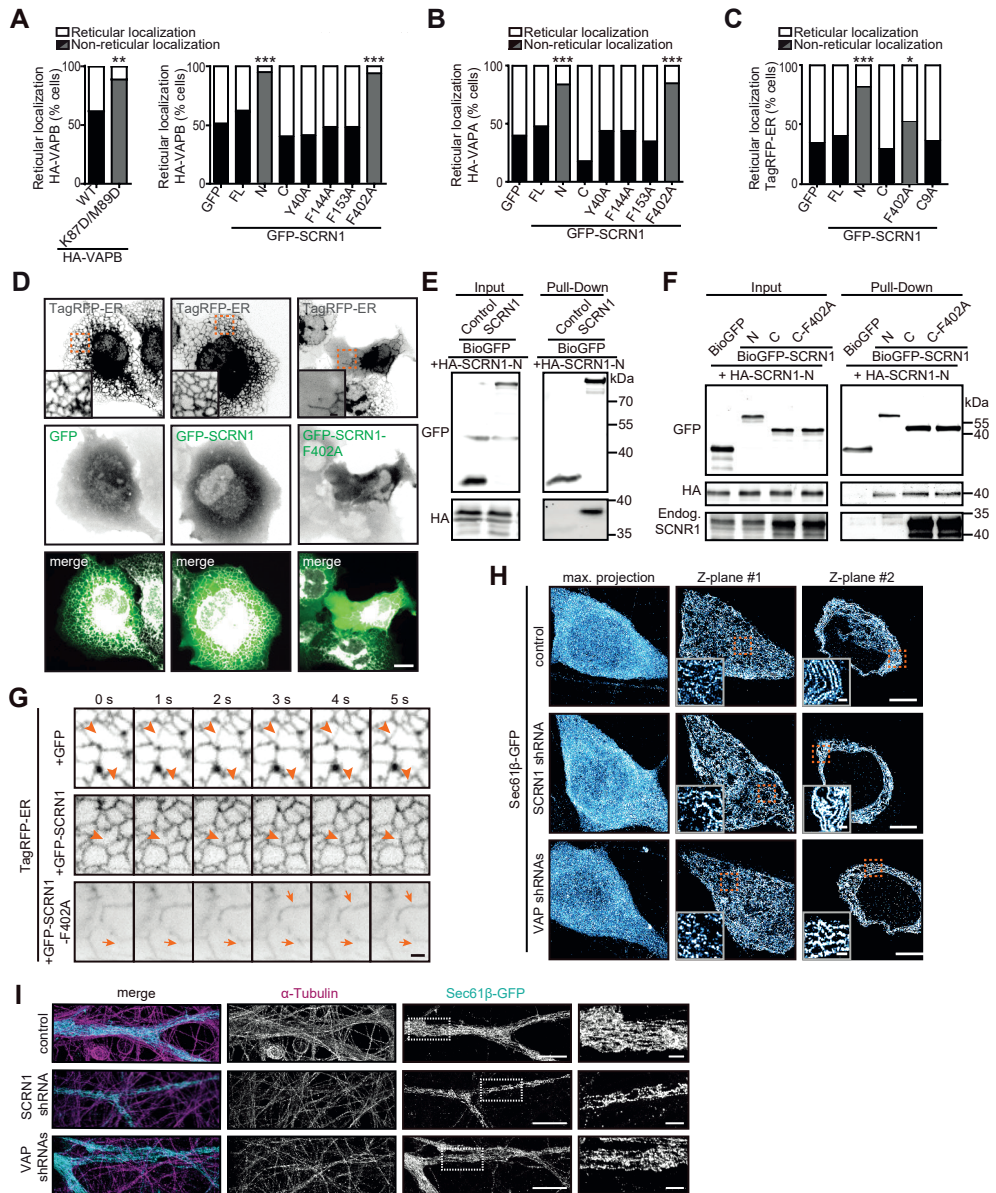
Chapter 6
General Discussion

Yujie Cao[1]

[1]Cell Biology, Department of Biology, Faculty of Science, Utrecht University, 3584 CH Utrecht, The Netherlands.

Neuronal microtubule organization and motor-driven transport are crucial for neuronal development and functioning (Kapitein and Hoogenraad, 2015). Structural microtubule-associated proteins (MAPs) are highly involved in the organization of microtubule arrays and intracellular transport in neurons, and mutations in structural MAPs are linked to various neurodevelopmental disorders, psychiatric conditions and neurodegenerative diseases (Tortosa et al., 2016). Although some structural MAPs have been exhaustively investigated and characterized, the majority of structural MAPs are not well studied, and several important questions remain unsolved (Bodakuntla et al., 2019). For example: Is there competition or cooperation between different MAPs for microtubule binding? How are local MAPs concentrations regulated? What is the influence of microtubule modifications on the binding of certain MAPs?

In this thesis, we found that different MAPs could cooperate and control microtubule organization and neurodevelopment. In Chapter 2, our results show that KIFC3 interacts and colocalizes with CAMSAP2 on dendritic microtubules. The cooperation between KIFC3 and CAMSAP2 is critical for the stabilization of dendritic microtubules. In Chapter 3, it is found that MAP7D2 interacts with Kinesin1 and promotes Kinesin1-driven transport in the proximal axon. The interaction and cooperation are important for neuronal polarization and migration. Several mechanisms may regulate local MAP concentration. First, it might be regulated by other MAPs. CAMSAP2 is known to recognize and bind to the microtubule minus-ends. KIFC3 is a microtubule minus-end directed motors, but overexpressed KIFC3 does not show specific binding on microtubule minus-ends in cell lines. In Chapter 2, we found that the endogenous KIFC3 colocalizes with the endogenous CAMSAP2 at microtubule minus-ends in neurons. And the minus-end binding of KIFC3 could be regulated by the interaction with CAMSAP2. In Chapter 3, we found another way to regulate the microtubule binding of MAPs. Certain MAPs contain more than one microtubule binding domain, which can have different microtubule binding affinity and/or microtubule preference. There are two microtubule binding domains in MAP7D2, the coil-coiled domain and the P-domain (a region full of potential phosphorylation sites). The coil-coiled domain does not show specific microtubule binding, but the P-domain could recognize the stable microtubules. The mechanism might be the same for other MAPs that have multiple microtubule binding domains. The direct relationship between MAPs and microtubule modification is not clear yet, but we do find that the microtubule binding of certain MAPs correlates to the modification. KIFC3 in Chapter 2 and MAP7D2 in Chapter 3 specifically bind to acetylated microtubules (relatively stable), while MID1 in Chapter 4 prefers tyrosinated microtubules (relatively dynamic). However, the details for this preferential binding are still largely remain unclear. This thesis aims to expand our understanding of the structural MAPs and their contribution to neuronal polarization.

6

The Axonal Microtubule Cytoskeleton

In axons all microtubules show a uniform and highly bundled plus-end out orientation (Heidemann et al., 1981; Kapitein and Hoogenraad, 2015; Yau et al., 2016). The parallel microtubule bundling and characteristic stabilization of these microtubules is crucial for axon formation (van Beuningen and Hoogenraad, 2016). While most axonal microtubules are relatively stable, recent studies show mature neurons also contain a small portion of dynamic microtubules (Kapitein and Hoogenraad, 2015; Yau et al., 2016). In the past decade, various MAPs that are involved in the regulation of axonal microtubules have been identified and characterized. In the axon, the best-studied structural MAP is Tau, mutations of which are associated with various neurological diseases, such as frontotemporal dementia and Alzheimer's disease (AD) (Del Carmen Alonso, 2010; Gao et al., 2018; Ghetti et al., 2015; Irwin et al., 2013; Tolnay and Probst, 1999). Tau is highly enriched in the distal axon and is commonly used as an axonal marker. For a long time, Tau was believed to stabilize microtubules in the axon, however more recent data argue against a microtubule stabilizing function for Tau (Qiang et al., 2018). Most research focuses on the phosphorylated Tau, which cannot bind to microtubules, and its roles in AD. However, the precise effect of Tau on microtubule organization remains unclear and still needs further investigation. Tau could be more important for the microtubule organization in distal axon and is absent from axon initial segment (AIS) in mature neuron. In the AIS, microtubules are bundled together with a very regular spacing and electron-dense cross-bridges can be observed between microtubules by using electron microscopy (Harterink et al., 2019; Palay et al., 1968). The microtubule fascicles extend into the proximal axon, but are not found in the distal axon (Leterrier et al., 2017). TRIM46 (Tripartite Motif Containing 46) and MTCL1 (Microtubule Crosslinking Factor 1) are the potential microtubule crosslinkers responsible for those fascicles (Satake et al., 2017). The microtubule plus-end binding EB1 and EB3 are also found enriched in the AIS. There, instead of microtubule plus-end tracking, EB1 and EB3 bind to the lattice of microtubules and participate in the maintenance of the AIS by binding to the scaffold protein Ankyring-G (AnkG) (Leterrier et al., 2011). In Chapter 4, we studied MID1, a paralogue of TRIM46, which is also involved in microtubule stabilization in the axon, but the mechanism remains largely unclear. The region between soma and AIS is known as axon hillock or pre-axonal exclusion zone (PAEZ) (Farias et al., 2015). The microtubule minus-end binding protein CAMSAP2 (Calmodulin-Regulated Spectrin-Associated Protein 2) is enriched in PAEZ and it might stabilize the minus-ends of axonal microtubules (van Beuningen et al., 2015; Yau et al., 2014). CAMSAP3 (Calmodulin-Regulated Spectrin-Associated Protein 3) is more enriched in the proximal and distal axon, prefers dynamic microtubules and is suggested to be important to maintain microtubule dynamics in the axon (Pongrakhananon et al., 2018). Another complex involved in microtubule minus-ends stabilization is HAUS/Augmin, which is found to regulate microtubule nucleation in the axon by interacting with the γ-tubulin ring complex (γ-TuRC) (Cunha-Ferreira et al., 2018; Sanchez-Huertas et al., 2016). The newly formed microtubules by HAUS are at relatively shallow angles (Petry et al., 2013; Petry et al., 2011), and the ordered arrangement of microtubule array ensures the uniform polarity in axon.

6

New Insights into Dendritic Microtubule Organization

Dendritic microtubules are highly organized in neurons. Unlike axons, in which microtubules have a uniform organization, dendrites have microtubules with a mixed polarity: half plus-ends out and half minus-ends out (Baas et al., 1988; Yau et al., 2016). Recently, it was found that the microtubules with the same orientation preferentially bundle together in dendrites (Figure 1A), although the microtubule crosslinkers responsible for this specific architecture remain elusive (Tas et al., 2017). The bundled microtubules with uniform polarity can promote persistent Kinesin motility (Balabanian et al., 2017; Conway et al., 2014; Tas and Kapitein, 2018). In addition, the orientation of dendritic microtubules highly correlates to their post-translation modifications (PTMs), which therefore might explain the predominantly axonal transport by Kinesin1, that prefer the stable microtubules (minus-ends out in dendrite and plus-ends out in axon) and the accumulation of Kinesin3, that prefer the dynamic (plus-ends out in dendrite) microtubules, at dendrite tips (Tas et al., 2017). Hereby, this specialized organization could be crucial for selective and efficient transport in neurons (Tas and Kapitein, 2018). In Chapter 2 we found that CAMSAP2 and KIFC3 can specifically crosslink minus-end out microtubules in dendrites, and therefore locally control the bundling and/or stabilization of microtubules (Cao et al., 2020). Plus-end out microtubules in dendrites are also grouped together (Figure 1A), but the microtubule crosslinkers targeting those microtubules remain unclear (Tas et al., 2017). A potential candidate could be MAP2, which is known to be involved in microtubule spacing, although there is no direct evidence showing MAP2 specificity for subsets of microtubules. Another structural MAP, MAP4, as a microtubule crosslinker could also be good candidates for future studies (Mogessie et al., 2015). The microtubule binding (MTB) domain of MAP4 is very similar to MAP2 and Tau, and a neuron specific isoform of MAP4 was found recently (Chen et al., 1992; Dehmelt and Halpain, 2005; Mogessie et al., 2015). The neuron specific MAP4 might also be involved in microtubule crosslinking and spacing in neurons. In Chapter 4, we found that another TRIM46 paralog, MID2, binds to microtubules in dendrites and specifically regulates plus-ends out microtubules. Our preliminary results show that MID2 protect microtubules from catastrophe and new microtubules could regrow from MID2 puncta in COS7 cells (data not shown), thus MID2 may serve as rescue point to maintain microtubule dynamics (Figure 1C).

Kinesin14 Family Proteins Function as Microtubule Crosslinkers

Kinesin superfamily proteins are molecular motors and their motor domain allows them to bind to and move along microtubules (Hirokawa et al., 2009). Kinesins are well known for their functions in intracellular transport, including the transport of membranous organelles, protein complexes and mRNAs. Unlike most Kinesins, which have their motor domain at the N-terminus and move toward the plus-end of the microtubules, the motor domain of Kinesin14 family proteins are C-terminal and they move towards the microtubule minus-ends (Hirokawa et al., 2009; Lipka et al., 2016). In rodents and human, there are 3 members in the Kinesin14 family, KIFC1, KIFC2 and KIFC3. Based on their microtubule minus-end directed motility, Kinesin14 proteins are important for intracellular transport in cell lines and neurons.
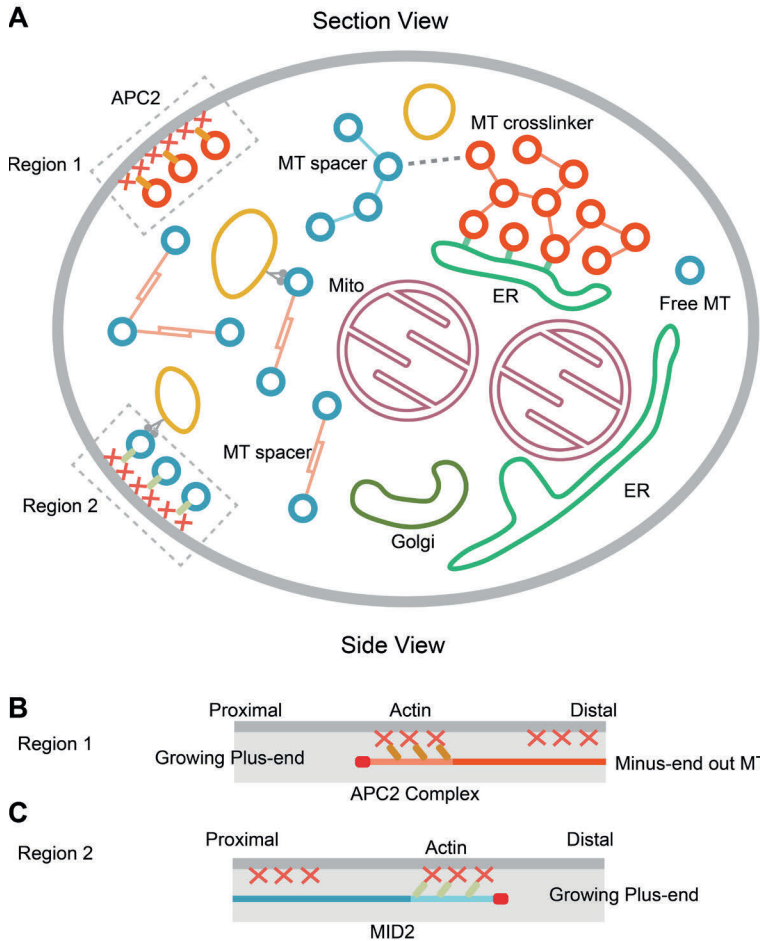
Figure 1, The microtubule organization in dendrite.
Grey cycle and grey lines indicate cell membrane, red circles indicate minus-end out microtubules and blue circles indicate plus-end out microtubules. Red crossings on the cell membrane indicate actin. Lines between microtubules represent microtubule crosslinking proteins. (A) Section view of dendrite: The minus-end out microtubules (red circles) are highly bundled and stabilized. The minus-end out microtubules could also be stabilized by ER. The plus-end out microtubules (blue circles) are loosely bundled by different microtubule crosslinkers (lines in different colors between blue circles). (B)-(C): Dark blue and dark orange lines indicate stable (long-lived) microtubules and light blue, and light orange lines indicate dynamic (short-lived) microtubules. Red dots represent microtubule plus-ends. (B): The longitudinal enlargement of Region1 in (A). APC2 (brown dots) crosslink minus-end out microtubules, which localizes to the outer edge of the dendrite, and promote the microtubule dynamics. (C): The longitudinal enlargement of Region2 in (A). MID2 (brownish-green dots) crosslink plus-end out microtubules near the outer edge of dendrite and promote the maintenance of the microtubule dynamics.

6

For example, KIFC1 is required for the motility and fission of early endocytic vesicles (Nath et al., 2007) and ciliary membrane protein transport (Lee et al., 2018). KIFC2 is enriched in dendrites and important for multivesicular body-like organelle transport (Hirokawa, 1997; Saito et al., 1997). KIFC3 is involved in the transport of annexin XIIIb–associated membranes in epithelial cells (Noda et al., 2001). Apart from intracellular transport, Kinesin14 proteins are also involved in the maintenance of various cellular structures. For example, KIFC1 (She et al., 2017) and KIFC3 (Xu et al., 2002) regulate the positioning and structural integrity of the Golgi apparatus by anchoring it to microtubules. KIFC3 is also involved in peroxisome positioning (Dietrich et al., 2013).

Kinesin14 proteins are known to directly regulate microtubule organization. Besides its motor domain, KIFC1 has an extra microtubule binding MTB domain (the first coiled-coil domain) in the N-terminal tail, which allows KIFC1 to bundle or slide microtubules. KIFC1 and its function on microtubule organization is well studied in mitosis (Vitre et al., 2020), where KIFC1 can crosslink and slide microtubules during the spindle formation (Cai et al., 2009; Mountain et al., 1999). Recent data also shows that KIFC1 crosslinks and stabilizes axonal microtubule in neurons (Muralidharan and Baas, 2019). The additional MTB domain in the N-terminus is not found in KIFC2 and KIFC3. Recently, KIFC3 was shown to form a tetrameric complex in vitro (Hata et al., 2019), which potentially explains how KIFC3 bundles and slides microtubules. Another potential explanation is that KIFC3 binds to other MAPs, which would provide extra microtubule-binding sites. In Chapter 2, we discovered that KIFC3 interacts with CAMSAP2 and that the KIFC3-CAMSAP2 complex is important for the stabilization of minus-end out microtubules in dendrites. New findings on dendritic microtubule organization show that most minus-ends out microtubules are stable in dendrites (Tas et al., 2017). As both KIFC3 and CAMSAP2 preferentially localize at stable microtubules, this could explain why the KIFC3-CAMSAP2 complex mainly targets the minus-ends out microtubules in dendrites (Jiang et al., 2014; Tas et al., 2017). Therefore, the microtubule preference could be the reason for the minus-ends out microtubules targeting by the KIFC3-CAMSAP2 complex. Our results suggest that the KIFC3-CAMSAP2 complex bundles but does not slide microtubules in dendrites. While the motor function of KIFC3 is crucial for the microtubule bundling and stabilization, it is still not clear how this motor domain is involved in microtubule organization. Here, we speculate that the KIFC3-CAMSAP2 complex promotes minus-end out microtubules bundling and stabilization in dendrites and the force generated by the KIFC3 motor is important for microtubule crosslinking. Recently, KIFC2 was found to control apical dendrite branching (Szczurkowska et al., 2020), but KIFC2 did not show any direct effect on microtubule organization. Further investigation could focus more on the direct regulation of KIFC2 on cytoskeleton.

Microtubule Minus-end Regulation in Neurons

The microtubule minus-end is less studied than the plus-end in neurons. Microtubule minus-ends are relatively stable, though it also shows dynamics in vivo and in vitro (Feng et al., 2019). The γ-TuRC is predominantly present at centrosomes and thought to promote microtubule nucleation and to cap the minus-ends (Kollman

6

et al., 2011). During neuronal maturation, the centrosome becomes inactive and the HAUS complex starts to promote non-centrosomal microtubule nucleation by interacting with γ-TuRC (Cunha-Ferreira et al., 2018; Sanchez-Huertas et al., 2016).

The CAMSAP (Calmodulin-Regulated Spectrin-Associated Protein) family proteins are known to regulate microtubule minus-end dynamics in neurons. All CAMSAPs proteins contain a calponin homology (CH) domain, 4 predicted coiled-coil domains and a characteristic domain for CAMSAP family proteins, the calmodulin-regulated spectrin-associated (CKK) domain (Figure 2A) (Baines et al., 2009). The CKK domain of CAMSAPs can specifically recognize and bind to microtubule minus-ends (Atherton et al., 2019). Besides, CAMSAP2 and CAMSAP3 have an extra MTB domain, which is not found in CAMSAP1. Both CAMSAP2 and CAMSAP3 can decorate and stabilize microtubule lattice, and their binding also inhibits the growth of microtubule minus-ends (Jiang et al., 2014). In neurons, CAMSAP2 promotes the stabilization of dendritic microtubules, and CAMSAP3 is important to maintain a dynamic microtubule pool within the axon (Figure 2D) (Pongrakhananon et al., 2018; Yau et al., 2014). Microtubule minus-ends decorated by CAMSAP2 and CAMSAP3 are generally thought to be stable and to not show dynamics in cells (Cao et al., 2020; Tanaka et al., 2012). Unlike CAMSAP2 and CAMSAP3, that decorate and stabilize microtubule lattice, CAMSAP1 binds to microtubule minus-ends and tracks growing minus-ends in cell lines and in vitro (Figure 2B) (Hendershott and Vale, 2014; Jiang et al., 2014). In Drosophila, there is only one CAMSAP family protein, Patronin. Similar to CAMSAP1, Patronin was shown to track and move with the growing microtubule minus-ends in dendrites (Feng et al., 2019; Hendershott and Vale, 2014). The difference on minus-ends tracking properties among CAMSAPs could be explained by the MTB domain, found in CAMSAP2/3. The CKK domain tracks microtubule minus-ends but shows weaker microtubule binding, while the MTB domain shows stronger microtubule binding but cannot track minus-ends (Jiang et al., 2014). CAMSAP2/3 could recognize and bind microtubule minus-end by their CKK domain and MTB domain. MTB domain of CAMSAP2/3 further promotes their microtubule binding affinity, thus inhibits the minus-ends tracking by CKK domain. CAMSAP1 does not have the MTB domain, therefore it can only recognize and track minus-ends by its CKK domain. Interestingly, in neurons CAMSAP1 is expressed in both dendrites and the axon and knock down (KD) of CAMSAP1 was shown to induce multiple axons in vitro and migration defects in vivo (Zhou et al., 2020b). CAMSAP1 might protect microtubule minus-ends from depolymerization, maintain the stability of microtubule seeds and control the neuron polarity (Zhou et al., 2020b). However, it is not clear if this phenotype is due to a direct effect of CAMSAP1 on microtubules, as KD of CAMSAP1 did not affect the microtubule organization in cell lines (Jiang et al., 2014). And it is also unclear if CAMSAP1 could track growing microtubule minus-ends in live neurons. Additional studies should focus on the role of CAMSAP1 at neuronal microtubule minus-ends to elucidate its effect on the microtubule cytoskeleton in neurons.

WDR47 (WD Repeat Domain 47) interacts with all 3 CAMSAP proteins and it is found to cooperate with CAMSAP3 to regulate microtubule organization in the axon (Chen et al., 2020). In younger neurons, WDR47 facilitates the neurite localization

6

Figure 2: CAMSAP family proteins regulate microtubule minus-ends.

(A), The secondary structure of CAMSAP1, CAMSAP2 and CAMSAP3. All CAMSAP family proteins contain a calponin homology (CH) domain, 4 predicted coiled-coil (CC) domains and a calmodulin-regulated spectrin-associated (CKK) domain. CAMSAP2 and CAMSAP3 have an extra MTB domain and a Katanin binding helix, which is indicated in purple.

(B), CAMSAP1 tracks microtubule minus-ends and promotes persistent growth of minus-ends with EB1/3 complex. WDR47 might enhance the microtubule minus-end binding of CAMSAP1. MARK2 could phosphorylate CAMSAP1 and weaken the microtubule binding affinity of CAMSAP1. Without CAMSAP1, the microtubule "seed" might be depolymerized by Kinesin13 family proteins.
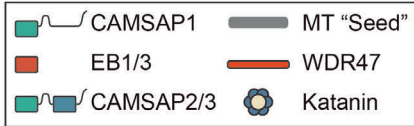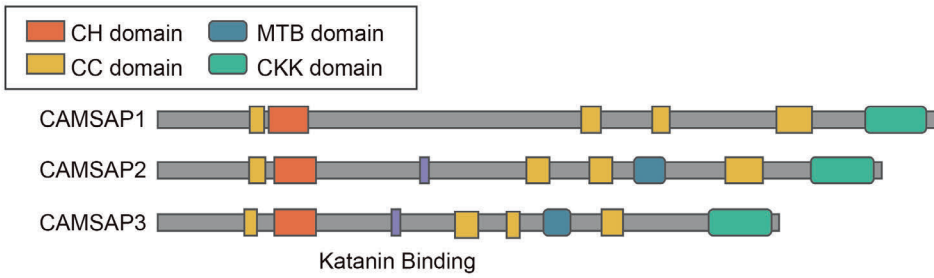
(C), CAMSAP2 and CAMSAP3 stabilize microtubule minus-ends and inhibit the growth of minus-ends. WDR47 promotes the minus-ends binding of CAMSAP2 and CAMSAP3. Together with WDR47, CAMSAP2 and CAMSAP3 form long stretches in neurons and promote the elongation of microtubule minus-ends. Katanin binds to microtubule minus-ends, cuts the microtubule, and shortens CAMSAP2/3 stretches.

(D), In neurons, CAMSAP2 prefers long-lived microtubules, forms long stretches, and stabilizes microtubule minus-ends. CAMSAP3 binds to short-lived microtubules and promotes microtubule dynamics. CAMSAP1 might bind to the growing minus-ends.

of CAMSAP3, which suggests that the long CAMSAP2 and CAMSAP3 stretches in mature neurons might also be regulated by WDR47 (Pongrakhananon et al., 2018; Yau et al., 2014) (Figure 2C). It is likely that WDR47 regulates the functioning of CAMSAP1 in neurons, however this has thus far not been demonstrated. The microtubule-severing enzyme, Katanin, can interact with CAMSAP2 and CAMSAP3 to cut the microtubules and shorten CAMSAP2/3 stretches (Jiang et al., 2018). Perhaps, WDR47 might counter Katanin cutting microtubules by competitive binding, but the mechanism remains elusive. Katanin binding domain was not found in CAMSAP1 (Figure 2A), and it is also known that Patronin protects microtubule minus-ends against Kinesin13-induced depolymerization (Goodwin and Vale, 2010). Therefore, it would be interesting to investigate if the microtubule regulation of CAMSAP1 is also Kinesin13 related (Figure 2B).

Another interesting candidate is Ninein, that is concentrated at the subdistal appendages of the centriole (Martin and Akhmanova, 2018). Ninein could anchor microtubule minus-ends to centrosome, and is also involved in non-centrosomal microtubule organization (Delgehyr et al., 2005; Goldspink et al., 2017; Moss et al., 2007; Wang et al., 2015). In epithelial cells, Ninein is found to relocalize from centrosome to non-centrosomal sites (Moss et al., 2007). In neurons, similar relocalization was observed and it is due to alternative splicing mediated by RNA-binding proteins, Rbfox (Ohama and Hayashi, 2009; Zhang et al., 2014). C-terminal segment of Ninein associates with the centriole, and alternative splicing induces a frameshift and truncates the C terminus of Ninein, thus Ninein translocates from centrosome to non-centrosomal loci in neurons (Zhang et al., 2014). It would be interesting to investigate if Ninein regulates the minus-ends of centrosomal and/or non-centrosomal microtubules in neurons. More studies are needed to further reveal the role of microtubule minus-end binding proteins and microtubule minus-ends organization in neuronal polarity.

6

A

CH domain
CC domain
MTB domain
CKK domain

CAMSAP1

CAMSAP2

CAMSAP3

Katanin Binding

CAMSAP1
EB1/3
CAMSAP2/3
MT "Seed"
WDR47
Katanin

B **CAMSAP1 Tracks Growing MT-end**

MT-end depolymerization
-end   +end

MARK2/Kinesin13 ⇵ WDR47

-end
+end

MT-end Persistent Growth
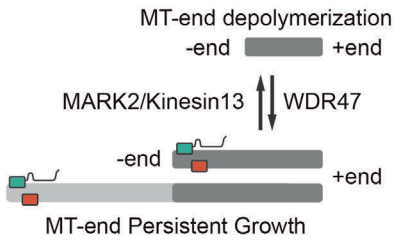
C **CAMSAP2/3 Maintain MT "Seed"**

MT-end elongation

Old CAMSAP2/3
Stretches Maintained

-end   +end

WDR47   Katanin

WDR47

CAMSAP2/3
Stretches Shortened

MT Cutting
Katanin

-end   +end   -end   +end
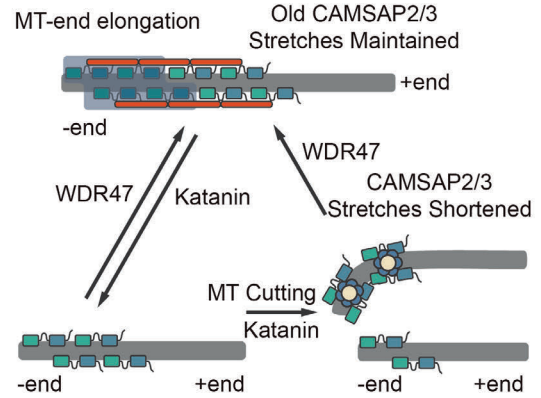
D **CAMSAPs Regulate Neuronal MTs**

?

CAMSAP1
CAMSAP2
CAMSAP3
EB1/3
Long-lived MTs
Short-lived MTs

6
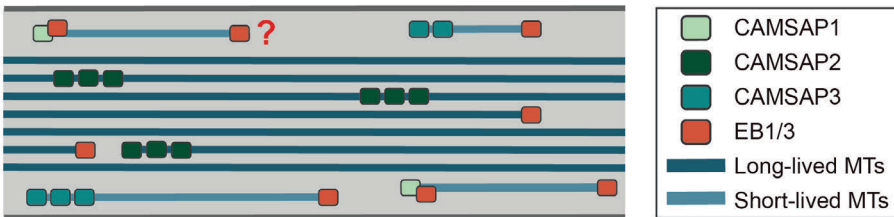
MAP7 Family Proteins Regulates Kinesin1 Transports

The MAP7 protein family consists of 4 members in mammals, MAP7, MAP7D1, MAP7D2 and MAP7D3 (Hooikaas et al., 2019). They are all expressed in the nervous system, except MAP7D3 (Pan et al., 2019). In Chapter 3, we investigate all MAP7 members in neurons. MAP7 proteins are characterized by their coiled-coil domain (also called MAP7 domain) at the C- terminus (Figure 3A), which is known to bind to the Kinesin1 family proteins (Metzger et al., 2012). There is no evidence showing that MAP7 family members could directly regulate microtubule organization in neurons. Instead, they are known to promote Kinesin1-related transport (Barlan et al., 2013). Recent studies show that the N-terminus of MAP7 proteins (Figure 3A) is also conserved (Hooikaas et al., 2019; Pan et al., 2019; Tymanskyj et al., 2018). There are two domains at the N-terminus, a coiled-coil domain and a P-domain (a region full of potential phosphorylation sites), and they both can bind microtubules independently (Masson and Kreis, 1995; Tymanskyj et al., 2018). Unlike the coiled-coil domain, which binds all microtubules, the P-domain seems to be more important for the selective microtubule binding in neurons (Figure 3B). In DRG neurons, MAP7 is enriched at axon branchpoints and prefers stable microtubules (Tymanskyj and Ma, 2019) but it loses its microtubule-binding specificity when the P-domain is removed (Tymanskyj et al., 2018). In primary cultured hippocampal neurons, we found that MAP7 is more enriched in the proximal dendrites. As microtubules in the proximal dendrite are relatively more stable (Yau et al., 2016), this nicely coincides with the fact that MAP7 prefers stable microtubules. Moreover, we found that MAP7D2 specifically localizes to the AIS where it promotes Kinesin1 cargo transport into axon. And it is the P-domain of MAP7D2 that determines its AIS localization.

Here, we propose that the coiled-coil domain of MAP7 proteins is important for their microtubule binding affinity, that the P-domain is required to recognize a specific subset of microtubules and that the MAP7 domain is important for Kinesin1 binding (Figure 3B). P-domains from different MAP7 family proteins might recognize microtubules with different PTMs, parallel/antiparallel microtubules or bundled microtubules with different spacing, thus specifically bind to dendritic or axonal microtubules. For example, the P-domain of MAP7D2 might prefer stable and/or parallel microtubules in the axon, so that it could recognize axonal microtubules. Based on the binding to microtubules and Kinesin1 proteins, there might be 4 different models for MAP7 functioning. Model 1: The MAP has strong microtubule binding affinity and transiently binds Kinesin1 (Figure 3C). In this case the MAP stays bound to the microtubule, where it could recruit and/or activate Kinesins

6

Figure 3: MAP7 family proteins promote Kinesin1 transport.

(A), The secondary structure of MAP7, MAP7D1 and MAP7D2. They all have coiled-coil (CC) domain, P-domain, Pro-rich region and MAP7 domain.

(B), A general model for Kinesin1 regulation by MAP7 proteins. The coiled-coil domain binds to microtubules but has no preference, while the P-domain helps to recognize and bind specific microtubules. The MAP7 domain interacts with Kinesin1 and regulates Kinesin1 movement on microtubules.

(C)-(F), 4 different models of Kinesin1 regulation.

A

MT binding | MT binding and preference | Not clear | Kinesin1 binding

MAP7D2
NM_001289778.1
CC | P-domian | Pro-rich | MAP7 — 763aa

MAP7
NM_001106270.2
CC | P-domian | Pro-rich | MAP7 — 751aa

MAP7D1
NM_001109438.1
CC | P-domian | Pro-rich | MAP7 — 817aa

B

MAP7 family proteins

Kinesin1 binding

Kinesin1 proteins

Bind certain subset of MTs

MT binding with no preference

C

Model I:Strong MT binding and weak kinesin binding

Promote Kinesin1 transport

D

Model II:Weak MT binding and strong kinesin binding

"Hopping" with Kinesin1

E

Model III:Strong MT binding and strong kinesin binding

Anchor Kinesin1 and slide MTs

F

Model IV:Weak MT binding and weak kinesin binding

Locally and transiently promote Kinesin1 transport

Inhibited Kinesin1

Activate Kinesin1

Inhibited Kinesin1 Dissociates from MT

Promote Kinesin1 transport

MAP7 Dissociates from Kinesin1

6

to move along the microtubule. This model explains the promotion of Kinesin1-related transport by MAP7D2 in the axon (Pan et al., 2019). Model 2: The MAP shows weak microtubule binding and strong Kinesin1 binding (Figure 3D). The MAP localizes to the microtubules where it recruits and/or activates Kinesin. While Kinesin starts to move, due to the force generated by the motor the MAP dissociates from the microtubule, which leads to the MAP moving together with the Kinesin along the microtubule. Dissociation or slowing down of the motor might lead to reassociation of the MAP with microtubules. Such co-transport was observed for MAP7D3 with Kinesin1 in an in vitro reconstitution assay and in a mammalian cell line (Hooikaas et al., 2019). Model 3: The MAP has strong microtubule binding and strong Kinesin binding (Figure 3E). The MAP could recruit and anchor Kinesin to the microtubule. The MAP-Kinesin complex on microtubules could inhibit Kinesin movement, crosslink microtubules, or promote microtubule sliding. The Kif5b-MAP7 dependent nuclear positioning may be explained by this model (Metzger et al., 2012). Model 4: The MAP has weak microtubule binding and weak Kinesin binding (Figure 3F). In this model, the MAP would be more cytosolic in cells, and could promote the transient and local transport of Kinesin. This latter model appears the most likely for MAP7D1 in primary cultured neurons, where our preliminary results indeed show that MAP7D1 is more cytosolic in dendrites (data not shown).

MID1 and MID2 Regulates Neuronal Microtubule Organization

TRIM46 from TRIM superfamily is known to control neuronal polarity and axon specification by microtubule bundling and stabilization (van Beuningen et al., 2015). The TRIM superfamily, also called RBCC superfamily, is characterized by a RING finger domain, a B-box domain, and a coiled-coil domain at the N-terminus (Figure 4) and belongs to the E3 ubiquitin ligases superfamily (Hatakeyama, 2017). The general function of E3 ubiquitin ligases superfamily proteins is to mediate E2 ubiquitin-conjugating enzymes (Figure 4) to recognize the substrate (Hatakeyama, 2017). Interestingly, TRIM46 does not require this E3 ligase activity to bundle and stabilize microtubules (van Beuningen et al., 2015). According to the C-terminal domains, TRIM superfamily can be further divided into 9 subfamilies. To investigate if other TRIM proteins are also involved in neuronal polarity and microtubule organization, we investigated all proteins from TRIM C-I, C-II and C-III family. We found that only MID1, MID2, TRIM46 and TRIM36 could bind to microtubules. They all belong to type C-I family, which is characterized by the C-terminal COS domain, fibronectin type III motif and B30.2-like domains (Figure 4). In humans, MID1 gene mutations are associated with the X-linked form of Opitz G/BBB syndrome (Cox et al., 2000; De Falco et al., 2003) and a MID2 mutation is associated with X-linked intellectual disability (Geetha et al., 2014), which indicates that MID1 and MID2 are indeed important for proper development of the central nervous system. Furthermore, we found that MID1 and MID2 are also important for neuronal microtubule organization.

MID1 is enriched in the axon and KD of MID1 leads to more dynamic axonal microtubules, which suggests that MID1 is involved in microtubule stabilization. Although axonal microtubules are quite stable, there is still a dynamic microtubule pool present (Baas et al., 2016). MID1 might recognize those dynamic microtubules
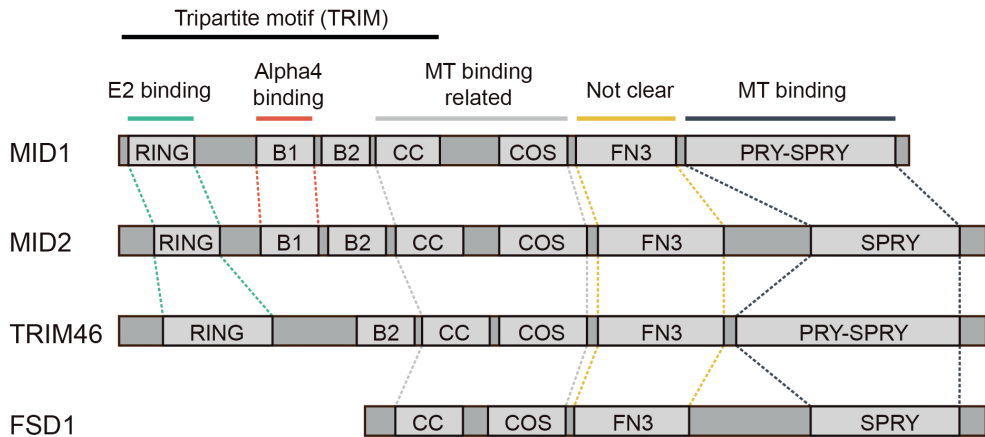
Figure 4: The secondary structure of MID1, MID2, TRIM46 and FSD1.
RING: RING finger domain, B1: Type I B-box domain, B2: Type II B-box domain, CC: coiled-coil domain, COS: COS domain, FN3: Type III fibronectin domain, SPRY: SPla and the RYanodine Receptor domain, PRY-SPRY domain: also named B30.2 domain, PRY motif extension with SPRY domain. The dashed lines indicate the homology between proteins.

and immobilize them, as MID1 prefers dynamic microtubules in COS7 cells. Unlike MID1, MID2 is more enriched in dendrites and MID2 KD leads to less dendrite branching and less anterograde comets in dendrites. This suggests that MID2 is important to maintain dendritic microtubule dynamics. However, it is unclear how MID2 would specifically recognize plus-ends out microtubules.

Much remains elusive about the functioning of MID1 and MID2, including the microtubule binding mechanism. In TRIM46, the COS domain (specialized coiled-coil domain) is important for microtubule binding (Short and Cox, 2006; van Beuningen et al., 2015). The COS domain of MID1 together with the neighboring coiled-coil domain is known to bind microtubules directly in vitro, though the binding is quite weak (Wright et al., 2016). The mutation or depletion of the COS domain abolishes the microtubule binding of MID1, MID2 and TRIM46 (Cox et al., 2000; Geetha et al., 2014; van Beuningen et al., 2015). However, we found that the overexpression of the COS domain itself in cells did not bind to microtubules (data not shown). The coiled-coil domain of TRIM5α, TRIM C-IV family member, was found to be involved in homo-oligomerization (Hatakeyama, 2017; Mische et al., 2005; Short and Cox, 2006). Thus, we believe that the COS domain together with the neighboring coiled-coil domain (Figure 4) is important for the multimerization of MID1, MID2 and TRIM46 (Short and Cox, 2006). Moreover, other studies indicate that the multimerization of MID1 and MID2 could be crucial for microtubule binding (Cainarca et al., 1999; Short and Cox, 2006). The SPRY domain of FSD1 is highly similar to the SPRY domain of MID1 and MID2, and it can bind to microtubules independently (D'Cruz et al., 2013; Tu et al., 2018). It suggests that the C-terminus of MID1 and MID2 are responsible for microtubule binding (Figure 4). However further investigations are necessary to map the exact MTB domain(s) of MID1 and MID2.

MID1 and MID2 both contain a RING finger domain, which binds to E2 ubiquitin-conjugating enzymes and is important for E3 ligase activity (Hatakeyama, 2017). MID1 and MID2 are known to be involved in the ubiquitination of protein phosphatase 2A (Du et al., 2014; Short et al., 2002), though it is still unclear if the E3 ubiquitin ligase function is needed for microtubule organization. It is possible that, like for TRIM46, the E3 ligase activity of MID1 and MID2 is not involved in microtubule organization and that the RING finger domain has an additional function. For example, the RING domain of TRIM46 is necessary for axon targeting (van Beuningen et al., 2015), and it might be the same for MID1 to localize in the axon. The enrichment of MID2 in dendrites remains unclear., Rescue experiments in MID KD neurons with expression of MID1 and MID2 truncations and chimeric constructs could be useful to further investigate this question.

Endoplasmic Reticulum Associated with Microtubules in Axon

ER (Endoplasmic Reticulum) distribution and sheet/tubule balance are highly influenced by microtubules in mammalian cells (Dabora and Sheetz, 1988; Lee and Chen, 1988; Lu et al., 2009; Terasaki et al., 1986; Waterman-Storer and Salmon, 1998). Lots of ER transmembrane proteins, such as CLIMP63 (Cytoskeleton Associated Protein 4), P180 (Ribosome Binding Protein 1), REEP1 (Receptor Accessory Protein 1), and Sec61b, are found to directly interact with microtubules. Recently, a connection between the ER and the microtubule network was also observed in neurons, and found to be important for the establishment of microtubule organization and neuronal polarity (Farias et al., 2019; Gurel et al., 2014). P180 is an ER shaping protein present in ER tubules and it is enriched in proximal axon in neurons. Similar to MAP7 family proteins, P180 binds to microtubules and Kinesin 1 proteins, stabilizes and bundles microtubules (Farias et al., 2019; Ogawa-Goto et al., 2007). In addition, its Kinesin 1 binding domain has been suggested to contribute to organelle translocation (Özkan et al., 2020). CLIMP63 is known to generate and maintain flattened ER cisternae, and it also binds to microtubules (Farah et al., 2005; Nikonov et al., 2007; Shibata et al., 2008; Vedrenne et al., 2005; Voeltz et al., 2006; Westrate et al., 2015). In neurons, CLIMP63 is present in dendrites and binds to MAP2 (Renvoise and Blackstone, 2010; Sandoz and van der Goot, 2015). P180 and CLIMP63 could act as unconventional MAPs (associated to ER membrane) to contribute to neuronal microtubule organization. Conversely, the microtubules are also involved in the stabilization and transport of ER tubules in neurons (Figure 1A). The entrance of ER tubules into dendrites apparently depends on EB comets, while the ER entrance into the axon largely depends on Kinesin1 (Farias et al., 2019). The ER is also important for the Ca^{2+} homeostasis, lipid synthesis and delivery, and signaling. In Chapter 5, we show that VAPA/B and SCRN1 colocalize at the ER tubules at presynaptic sites and modulate synaptic vesicle (SV) recycling. Furthermore, the VAPA/B-SCRN1 complex is also important to maintain proper ER morphology. It is known that VAPA/B facilitates membrane contact sites between the ER and other organelles. The membrane contacts might promote the fast lipid transfer between ER and other organelles, thus stabilize ER and control ER continuity and dynamics. Recently, microtubule nucleation was found at presynapse where it promotes SV motility and exocytosis (Qu et al., 2019). Since we found that smooth ER in the axon is important for SV recycling, it would be interesting to

investigate if the ER complex is involved in the local microtubule nucleation at the presynapse.

Future Perspective

This thesis mainly discusses MAPs and their functions in microtubule organization during neuron development. Many questions remain and require further investigations. The availability of antibodies is a limiting factor in our studies, which complicates studying our candidate proteins at the endogenous level. Furthermore, the regulation of microtubule dynamics by MAPs is a highly concentration-dependent biophysical process; overexpression of MAPs often leads to hyperstabilization and bundling of the microtubule network. Two recent technical developments might overcome these hurdles of cellular neurodevelopment research and show great promise for substantial progress in the near future.

The recently developed HITI (Homology Independent Targeted Integration) CRISPR (clustered regularly interspaced short palindromic repeats) knock-in approach enables tagging proteins endogenously in post-mitotic neurons (Suzuki et al., 2016; Willems et al., 2020). This allows investigation of the structural MAPs at physiological levels. The study of mammalian neuronal development and functioning is typically performed in rodent cultured neurons or brain slices. The results obtained with these model organisms might not fully recapitulate the human situation. Neurons derived from human induced pluripotent stem cells (hiPSCs) could be a good way to overcome this problem and make a more relevant model to study human disorders and develop potential drugs (Lancaster et al., 2013; Lindhout et al., 2020; Meijer et al., 2019; Zhao and Bhattacharyya, 2018). In addition to iPSC-induced neurons, a glia-induced-neuron system exists, in which the repression of a single RNA binding polypyrimidine-tract-binding (PTB) protein can transdifferentiate mouse (in vivo) and human (in vitro) astrocytes into functional neurons (Qian et al., 2020; Xue et al., 2013). In mouse brains, the induced neurons could target proper brain regions in vivo and repair damaged brain function (Qian et al., 2020; Zhou et al., 2020a). This provides an exciting new approach to study brain function and neuron development. For example, glia-induced-neuron can be applied to study axon initiation and dendrite development during the trans-differentiation. Compared to iPSC induced neurons, the PTB system might offer a cleaner situation with less contamination from other cells types or immature neurons during the culture (Pistollato et al., 2017). The relatively low costs and convenience also make it better and cheaper for biochemistry and mass spectrometry-based quantitative proteomic studies (Xue et al., 2013). Furthermore, PTB system could reduce the risk of tumor formation, and be a potential therapy for neurodegenerative disease, including Parkinson's disease (Li et al., 2008; Qian et al., 2020; Wang et al., 2012).

6

This thesis shows the importance of MAPs during neuronal development and functioning. Though many open questions remain, with the benefits of newly developed techniques and methods, the functions of neuronal MAPs and how they are involved in the neuronal microtubule organization and neuronal transport will likely be further revealed in the future.

Abbreviation	Definition
AD	Alzheimer's Disease
AIS	Axon Initial Segment
AnkG	Ankyring-G
CAMSAP1/2/3	Calmodulin-Regulated Spectrin-Associated Protein 1/2/3
CH domain	Calponin Homology Domain
CLIMP63	Cytoskeleton Associated Protein 4
CRISPR	Clustered Regularly Interspaced Short Palindromic Repeats)
C-terminus/terminal	Carboxyl-terminus/terminal
EB1/2/3	End Binding Family Protein 1/2/3
ER	Endoplasmic Reticulum
hiPSCs	Human-induced Pluripotent Stem Cells
HITI	Homology Independent Targeted Integration
KD	Knock Down
KIFC1/2/3	Kinesin Family Member C1/C2/C3
MAP(s)	Microtubule Associated Protein(s)
MAP7D 1/2/3	MAP7 Domain Containing 1/2/3
MID1	Midline 1
MID2	Midline 2
mRNA	Messenger Ribonucleic Acid
MTB domain	The Microtubule Binding Domain
MTCL1	Microtubule Crosslinking Factor 1
N-terminus/terminal	Amino-terminus/terminal
P180	Ribosome Binding Protein 1
PAEZ	Pre-axonal Exclusion Zone
REEP1	Receptor Accessory Protein 1
SCRN1	Secernin 1
TRIM	Tripartite Motif (RING, B-box and Coiled-coil)
TRIM46	Tripartite Motif Containing 46
VAPA/B	Vesicle-associated Membrane Protein-associated Protein A/B
WDR47	WD Repeat Domain 47
γ-TuRC	γ-tubulin Ring Complex

6

REFERENCES

Atherton, J., Luo, Y., Xiang, S., Yang, C., Rai, A., Jiang, K., Stangier, M., Vemu, A., Cook, A.D., Wang, S., et al. (2019). Structural determinants of microtubule minus end preference in CAMSAP CKK domains. Nat Commun 10, 5236.

Baas, P.W., Deitch, J.S., Black, M.M., and Banker, G.A. (1988). Polarity orientation of microtubules in hippocampal neurons: uniformity in the axon and nonuniformity in the dendrite. Proc Natl Acad Sci U S A 85, 8335-8339.

Baas, P.W., Rao, A.N., Matamoros, A.J., and Leo, L. (2016). Stability properties of neuronal microtubules. Cytoskeleton (Hoboken) 73, 442-460.

Baines, A.J., Bignone, P.A., King, M.D., Maggs, A.M., Bennett, P.M., Pinder, J.C., and Phillips, G.W. (2009). The CKK domain (DUF1781) binds microtubules and defines the CAMSAP/ssp4 family of animal proteins. Mol Biol Evol 26, 2005-2014.

Balabanian, L., Berger, C.L., and Hendricks, A.G. (2017). Acetylated Microtubules Are Preferentially Bundled Leading to Enhanced Kinesin-1 Motility. Biophys J 113, 1551-1560.

Barlan, K., Lu, W., and Gelfand, V.I. (2013). The microtubule-binding protein ensconsin is an essential cofactor of kinesin-1. Curr Biol 23, 317-322.

Bodakuntla, S., Jijumon, A.S., Villablanca, C., Gonzalez-Billault, C., and Janke, C. (2019). Microtubule-Associated Proteins: Structuring the Cytoskeleton. Trends Cell Biol 29, 804-819.

Cai, S., Weaver, L.N., Ems-McClung, S.C., and Walczak, C.E. (2009). Kinesin-14 family proteins HSET/XCTK2 control spindle length by cross-linking and sliding microtubules. Mol Biol Cell 20, 1348-1359.

Cainarca, S., Messali, S., Ballabio, A., and Meroni, G. (1999). Functional characterization of the Opitz syndrome gene product (midin): evidence for homodimerization and association with microtubules throughout the cell cycle. Hum Mol Genet 8, 1387-1396.

Cao, Y., Lipka, J., Stucchi, R., Burute, M., Pan, X., Portegies, S., Tas, R., Willems, J., Will, L., MacGillavry, H., et al. (2020).

Microtubule Minus-End Binding Protein CAMSAP2 and Kinesin-14 Motor KIFC3 Control Dendritic Microtubule Organization. Curr Biol 30, 899-908 e896.

Chen, J., Kanai, Y., Cowan, N.J., and Hirokawa, N. (1992). Projection domains of MAP2 and tau determine spacings between microtubules in dendrites and axons. Nature 360, 674-677.

Chen, Y., Zheng, J., Li, X., Zhu, L., Shao, Z., Yan, X., and Zhu, X. (2020). Wdr47 Controls Neuronal Polarization through the Camsap Family Microtubule Minus-End-Binding Proteins. Cell Rep 31, 107526.

Conway, L., Gramlich, M.W., Ali Tabei, S.M., and Ross, J.L. (2014). Microtubule orientation and spacing within bundles is critical for long-range kinesin-1 motility. Cytoskeleton (Hoboken) 71, 595-610.

Cox, T.C., Allen, L.R., Cox, L.L., Hopwood, B., Goodwin, B., Haan, E., and Suthers, G.K. (2000). New mutations in MID1 provide support for loss of function as the cause of X-linked Opitz syndrome. Hum Mol Genet 9, 2553-2562.

Cunha-Ferreira, I., Chazeau, A., Buijs, R.R., Stucchi, R., Will, L., Pan, X., Adolfs, Y., van der Meer, C., Wolthuis, J.C., Kahn, O.I., et al. (2018). The HAUS Complex Is a Key Regulator of Non-centrosomal Microtubule Organization during Neuronal Development. Cell Rep 24, 791-800.

D'Cruz, A.A., Babon, J.J., Norton, R.S., Nicola, N.A., and Nicholson, S.E. (2013). Structure and function of the SPRY/B30.2 domain proteins involved in innate immunity. Protein Sci 22, 1-10.

Dabora, S.L., and Sheetz, M.P. (1988). The microtubule-dependent formation of a tubulovesicular network with characteristics of the ER from cultured cell extracts. Cell 54, 27-35.

De Falco, F., Cainarca, S., Andolfi, G., Ferrentino, R., Berti, C., Rodriguez Criado, G., Rittinger, O., Dennis, N., Odent, S., Rastogi, A., et al. (2003). X-linked Opitz syndrome: novel mutations in the MID1 gene and redefinition of the clinical spectrum. Am J Med Genet A 120A, 222-228.

6

Dehmelt, L., and Halpain, S. (2005). The MAP2/Tau family of microtubule-associated proteins. Genome Biol 6, 204.

Del Carmen Alonso, A. (2010). Tau, neurodegeneration and Alzheimer's disease. Curr Alzheimer Res 7, 653-655.

Delgehyr, N., Sillibourne, J., and Bornens, M. (2005). Microtubule nucleation and anchoring at the centrosome are independent processes linked by ninein function. J Cell Sci 118, 1565-1575.

Dietrich, D., Seiler, F., Essmann, F., and Dodt, G. (2013). Identification of the kinesin KifC3 as a new player for positioning of peroxisomes and other organelles in mammalian cells. Biochim Biophys Acta 1833, 3013-3024.

Du, H., Wu, K., Didoronkute, A., Levy, M.V., Todi, N., Shchelokova, A., and Massiah, M.A. (2014). MID1 catalyzes the ubiquitination of protein phosphatase 2A and mutations within its Bbox1 domain disrupt polyubiquitination of alpha4 but not of PP2Ac. PLoS One 9, e107428.

Farah, C.A., Liazoghli, D., Perreault, S., Desjardins, M., Guimont, A., Anton, A., Lauzon, M., Kreibich, G., Paiement, J., and Leclerc, N. (2005). Interaction of microtubule-associated protein-2 and p63: a new link between microtubules and rough endoplasmic reticulum membranes in neurons. J Biol Chem 280, 9439-9449.

Farias, G.G., Freal, A., Tortosa, E., Stucchi, R., Pan, X., Portegies, S., Will, L., Altelaar, M., and Hoogenraad, C.C. (2019). Feedback-Driven Mechanisms between Microtubules and the Endoplasmic Reticulum Instruct Neuronal Polarity. Neuron 102, 184-201 e188.

Farias, G.G., Guardia, C.M., Britt, D.J., Guo, X., and Bonifacino, J.S. (2015). Sorting of Dendritic and Axonal Vesicles at the Pre-axonal Exclusion Zone. Cell Rep 13, 1221-1232.

Feng, C., Thyagarajan, P., Shorey, M., Seebold, D.Y., Weiner, A.T., Albertson, R.M., Rao, K.S., Sagasti, A., Goetschius, D.J., and Rolls, M.M. (2019). Patronin-mediated minus end growth is required for dendritic microtubule polarity. J Cell Biol 218, 2309-2328.

Ferro, L.S., Eshun-Wilson, L., Gölcük, M., Fernandes, J., Huijben, T., Gerber, E., Jack, A., Costa, K., Gür, M., Fang, Q., et al. (2020). The mechanism of motor inhibition by microtubule-associated proteins. bioRxiv, 2020.2010.2022.351346.

Gao, Y., Tan, L., Yu, J.T., and Tan, L. (2018). Tau in Alzheimer's Disease: Mechanisms and Therapeutic Strategies. Curr Alzheimer Res 15, 283-300.

Geetha, T.S., Michealraj, K.A., Kabra, M., Kaur, G., Juyal, R.C., and Thelma, B.K. (2014). Targeted deep resequencing identifies MID2 mutation for X-linked intellectual disability with varied disease severity in a large kindred from India. Hum Mutat 35, 41-44.

Ghetti, B., Oblak, A.L., Boeve, B.F., Johnson, K.A., Dickerson, B.C., and Goedert, M. (2015). Invited review: Frontotemporal dementia caused by microtubule-associated protein tau gene (MAPT) mutations: a chameleon for neuropathology and neuroimaging. Neuropathol Appl Neurobiol 41, 24-46.

Goldspink, D.A., Rookyard, C., Tyrrell, B.J., Gadsby, J., Perkins, J., Lund, E.K., Galjart, N., Thomas, P., Wileman, T., and Mogensen, M.M. (2017). Ninein is essential for apico-basal microtubule formation and CLIP-170 facilitates its redeployment to non-centrosomal microtubule organizing centres. Open Biol 7.

Goodwin, S.S., and Vale, R.D. (2010). Patronin regulates the microtubule network by protecting microtubule minus ends. Cell 143, 263-274.

Gurel, P.S., Hatch, A.L., and Higgs, H.N. (2014). Connecting the cytoskeleton to the endoplasmic reticulum and Golgi. Curr Biol 24, R660-R672

Harterink, M., Vocking, K., Pan, X., Soriano Jerez, E.M., Slenders, L., Freal, A., Tas, R.P., van de Wetering, W.J., Timmer, K., Motshagen, J., et al. (2019). TRIM46 Organizes Microtubule Fasciculation in the Axon Initial Segment. J Neurosci 39, 4864-4873.

Hata, S., Pastor Peidro, A., Panic, M., Liu, P., Atorino, E., Funaya, C., Jakle, U., Pereira, G., and Schiebel, E. (2019). The balance between KIFC3 and EG5 tetrameric kinesins controls the onset of mitotic spindle assembly. Nat Cell Biol 21, 1138-1151.

Hatakeyama, S. (2017). TRIM Family Proteins: Roles in Autophagy, Immunity, and Carcinogenesis. Trends Biochem Sci 42,

6

297-311.

Heidemann, S.R., Landers, J.M., and Hamborg, M.A. (1981). Polarity orientation of axonal microtubules. J Cell Biol 91, 661-665.

Hendershott, M.C., and Vale, R.D. (2014). Regulation of microtubule minus-end dynamics by CAMSAPs and Patronin. Proc Natl Acad Sci U S A 111, 5860-5865.

Hirokawa, N. (1997). The mechanisms of fast and slow transport in neurons: identification and characterization of the new kinesin superfamily motors. Curr Opin Neurobiol 7, 605-614.

Hirokawa, N., Noda, Y., Tanaka, Y., and Niwa, S. (2009). Kinesin superfamily motor proteins and intracellular transport. Nat Rev Mol Cell Biol 10, 682-696.

Hooikaas, P.J., Martin, M., Muhlethaler, T., Kuijntjes, G.J., Peeters, C.A.E., Katrukha, E.A., Ferrari, L., Stucchi, R., Verhagen, D.G.F., van Riel, W.E., et al. (2019). MAP7 family proteins regulate kinesin-1 recruitment and activation. J Cell Biol 218, 1298-1318.

Irwin, D.J., Lee, V.M., and Trojanowski, J.Q. (2013). Parkinson's disease dementia: convergence of alpha-synuclein, tau and amyloid-beta pathologies. Nat Rev Neurosci 14, 626-636.

Jiang, K., Faltova, L., Hua, S., Capitani, G., Prota, A.E., Landgraf, C., Volkmer, R., Kammerer, R.A., Steinmetz, M.O., and Akhmanova, A. (2018). Structural Basis of Formation of the Microtubule Minus-End-Regulating CAMSAP-Katanin Complex. Structure 26, 375-382 e374.

Jiang, K., Hua, S., Mohan, R., Grigoriev, I., Yau, K.W., Liu, Q., Katrukha, E.A., Altelaar, A.F., Heck, A.J., Hoogenraad, C.C., et al. (2014). Microtubule minus-end stabilization by polymerization-driven CAMSAP deposition. Dev Cell 28, 295-309.

Kapitein, L.C., and Hoogenraad, C.C. (2015). Building the Neuronal Microtubule Cytoskeleton. Neuron 87, 492-506.

Kollman, J.M., Merdes, A., Mourey, L., and Agard, D.A. (2011). Microtubule nucleation by gamma-tubulin complexes. Nat Rev Mol Cell Biol 12, 709-721.

Lancaster, M.A., Renner, M., Martin, C.A., Wenzel, D., Bicknell, L.S., Hurles, M.E., Homfray, T., Penninger, J.M., Jackson, A.P., and Knoblich, J.A. (2013).

Cerebral organoids model human brain development and microcephaly. Nature 501, 373-379.

Lee, C., and Chen, L.B. (1988). Dynamic behavior of endoplasmic reticulum in living cells. Cell 54, 37-46.

Lee, S.H., Joo, K., Jung, E.J., Hong, H., Seo, J., and Kim, J. (2018). Export of membrane proteins from the Golgi complex to the primary cilium requires the kinesin motor, KIFC1. FASEB J 32, 957-968.

Leterrier, C., Dubey, P., and Roy, S. (2017). The nano-architecture of the axonal cytoskeleton. Nat Rev Neurosci 18, 713-726.

Leterrier, C., Vacher, H., Fache, M.P., d'Ortoli, S.A., Castets, F., Autillo-Touati, A., and Dargent, B. (2011). End-binding proteins EB3 and EB1 link microtubules to ankyrin G in the axon initial segment. Proc Natl Acad Sci U S A 108, 8826-8831.

Li, J.Y., Christophersen, N.S., Hall, V., Soulet, D., and Brundin, P. (2008). Critical issues of clinical human embryonic stem cell therapy for brain repair. Trends Neurosci 31, 146-153.

Lindhout, F.W., Kooistra, R., Portegies, S., Herstel, L.J., Stucchi, R., Snoek, B.L., Altelaar, A.M., MacGillavry, H.D., Wierenga, C.J., and Hoogenraad, C.C. (2020). Quantitative mapping of transcriptome and proteome dynamics during polarization of human iPSC-derived neurons. Elife 9.

Lipka, J., Kapitein, L.C., Jaworski, J., and Hoogenraad, C.C. (2016). Microtubule-binding protein doublecortin-like kinase 1 (DCLK1) guides kinesin-3-mediated cargo transport to dendrites. EMBO J 35, 302-318.

Lu, L., Ladinsky, M.S., and Kirchhausen, T. (2009). Cisternal organization of the endoplasmic reticulum during mitosis. Mol Biol Cell 20, 3471-3480.

Martin, M., and Akhmanova, A. (2018). Coming into Focus: Mechanisms of Microtubule Minus-End Organization. Trends Cell Biol 28, 574-588.

Masson, D., and Kreis, T.E. (1995). Binding of E-MAP-115 to microtubules is regulated by cell cycle-dependent phosphorylation. J Cell Biol 131, 1015-1024.

Meijer, M., Rehbach, K., Brunner, J.W., Classen, J.A., Lammertse, H.C.A., van Linge, L.A., Schut, D., Krutenko, T., Hebisch,

6

M., Cornelisse, L.N., et al. (2019). A Single-Cell Model for Synaptic Transmission and Plasticity in Human iPSC-Derived Neurons. Cell Rep 27, 2199-2211 e2196.

Metzger, T., Gache, V., Xu, M., Cadot, B., Folker, E.S., Richardson, B.E., Gomes, E.R., and Baylies, M.K. (2012). MAP and kinesin-dependent nuclear positioning is required for skeletal muscle function. Nature 484, 120-124.

Mische, C.C., Javanbakht, H., Song, B., Diaz-Griffero, F., Stremlau, M., Strack, B., Si, Z., and Sodroski, J. (2005). Retroviral restriction factor TRIM5alpha is a trimer. J Virol 79, 14446-14450.Mogessie, B., Roth, D., Rahil, Z., and Straube, A. (2015). A novel isoform of MAP4 organises the paraxial microtubule array required for muscle cell differentiation. Elife 4, e05697.

Monroy, B.Y., Sawyer, D.L., Ackermann, B.E., Borden, M.M., Tan, T.C., and Ori-McKenney, K.M. (2018). Competition between microtubule-associated proteins directs motor transport. Nat Commun 9, 1487.

Moss, D.K., Bellett, G., Carter, J.M., Liovic, M., Keynton, J., Prescott, A.R., Lane, E.B., and Mogensen, M.M. (2007). Ninein is released from the centrosome and moves bi-directionally along microtubules. J Cell Sci 120, 3064-3074.

Mountain, V., Simerly, C., Howard, L., Ando, A., Schatten, G., and Compton, D.A. (1999). The kinesin-related protein, HSET, opposes the activity of Eg5 and cross-links microtubules in the mammalian mitotic spindle. J Cell Biol 147, 351-366.

Muralidharan, H., and Baas, P.W. (2019). Mitotic Motor KIFC1 Is an Organizer of Microtubules in the Axon. J Neurosci 39, 3792-3811.

Nath, S., Bananis, E., Sarkar, S., Stockert, R.J., Sperry, A.O., Murray, J.W., and Wolkoff, A.W. (2007). Kif5B and Kifc1 interact and are required for motility and fission of early endocytic vesicles in mouse liver. Mol Biol Cell 18, 1839-1849.

Nikonov, A.V., Hauri, H.P., Lauring, B., and Kreibich, G. (2007). Climp-63-mediated binding of microtubules to the ER affects the lateral mobility of translocon complexes. J Cell Sci 120, 2248-2258.

Noda, Y., Okada, Y., Saito, N., Setou, M., Xu, Y., Zhang, Z., and Hirokawa, N. (2001). KIFC3, a microtubule minus end-directed motor for the apical transport of annexin XIIIb-associated Triton-insoluble membranes. J Cell Biol 155, 77-88.

Ogawa-Goto, K., Tanaka, K., Ueno, T., Tanaka, K., Kurata, T., Sata, T., and Irie, S. (2007). p180 Is Involved in the Interaction between the Endoplasmic Reticulum and Microtubules through a Novel Microtubule-binding and Bundling Domain. Molecular Biology of the Cell 18, 3741-3751.

Ohama, Y., and Hayashi, K. (2009). Relocalization of a microtubule-anchoring protein, ninein, from the centrosome to dendrites during differentiation of mouse neurons. Histochem Cell Biol 132, 515-524.

Özkan, N., Koppers, M., van Soest, I., van Harten, A., Liv, N., Klumperman, J., Hoogenraad, C.C., and Farías, G.G. (2020). ER – lysosome contacts at a pre-axonal region regulate axonal lysosome availability. bioRxiv, 2020.2006.2016.153734.

Palay, S.L., Sotelo, C., Peters, A., and Orkand, P.M. (1968). The axon hillock and the initial segment. J Cell Biol 38, 193-201.

Pan, X., Cao, Y., Stucchi, R., Hooikaas, P.J., Portegies, S., Will, L., Martin, M., Akhmanova, A., Harterink, M., and Hoogenraad, C.C. (2019). MAP7D2 Localizes to the Proximal Axon and Locally Promotes Kinesin-1-Mediated Cargo Transport into the Axon. Cell Rep 26, 1988-1999 e1986.

Petry, S., Groen, A.C., Ishihara, K., Mitchison, T.J., and Vale, R.D. (2013). Branching microtubule nucleation in Xenopus egg extracts mediated by augmin and TPX2. Cell 152, 768-777.

Petry, S., Pugieux, C., Nedelec, F.J., and Vale, R.D. (2011). Augmin promotes meiotic spindle formation and bipolarity in Xenopus egg extracts. Proc Natl Acad Sci U S A 108, 14473-14478.

Pistollato, F., Canovas-Jorda, D., Zagoura, D., and Price, A. (2017). Protocol for the Differentiation of Human Induced Pluripotent Stem Cells into Mixed Cultures of Neurons and Glia for Neurotoxicity Testing. J Vis Exp.

Pongrakhananon, V., Saito, H., Hiver, S., Abe, T., Shioi, G., Meng, W., and Takeichi, M. (2018). CAMSAP3 maintains neuronal polarity through regulation of microtubule stability. Proc Natl Acad Sci U S A 115, 9750-9755.

6

Qian, H., Kang, X., Hu, J., Zhang, D., Liang, Z., Meng, F., Zhang, X., Xue, Y., Maimon, R., Dowdy, S.F., et al. (2020). Reversing a model of Parkinson's disease with in situ converted nigral neurons. Nature 582, 550-556.

Qiang, L., Sun, X., Austin, T.O., Muralidharan, H., Jean, D.C., Liu, M., Yu, W., and Baas, P.W. (2018). Tau Does Not Stabilize Axonal Microtubules but Rather Enables Them to Have Long Labile Domains. Curr Biol 28, 2181-2189 e2184.

Qu, X., Kumar, A., Blockus, H., Waites, C., and Bartolini, F. (2019). Activity-Dependent Nucleation of Dynamic Microtubules at Presynaptic Boutons Controls Neurotransmission. Curr Biol 29, 4231-4240 e4235.

Renvoise, B., and Blackstone, C. (2010). Emerging themes of ER organization in the development and maintenance of axons. Curr Opin Neurobiol 20, 531-537.

Saito, N., Okada, Y., Noda, Y., Kinoshita, Y., Kondo, S., and Hirokawa, N. (1997). KIFC2 is a novel neuron-specific C-terminal type kinesin superfamily motor for dendritic transport of multivesicular body-like organelles. Neuron 18, 425-438.

Sanchez-Huertas, C., Freixo, F., Viais, R., Lacasa, C., Soriano, E., and Luders, J. (2016). Non-centrosomal nucleation mediated by augmin organizes microtubules in post-mitotic neurons and controls axonal microtubule polarity. Nat Commun 7, 12187.

Sandoz, P.A., and van der Goot, F.G. (2015). How many lives does CLIMP-63 have? Biochem Soc Trans 43, 222-228.

Satake, T., Yamashita, K., Hayashi, K., Miyatake, S., Tamura-Nakano, M., Doi, H., Furuta, Y., Shioi, G., Miura, E., Takeo, Y.H., et al. (2017). MTCL1 plays an essential role in maintaining Purkinje neuron axon initial segment. EMBO J 36, 1227-1242.

She, Z.Y., Pan, M.Y., Tan, F.Q., and Yang, W.X. (2017). Minus end-directed kinesin-14 KIFC1 regulates the positioning and architecture of the Golgi apparatus. Oncotarget 8, 36469-36483.

Shibata, Y., Voss, C., Rist, J.M., Hu, J., Rapoport, T.A., Prinz, W.A., and Voeltz, G.K. (2008). The reticulon and DP1/Yop1p proteins form immobile oligomers in the tubular endoplasmic reticulum. J Biol Chem 283, 18892-18904.

Short, K.M., and Cox, T.C. (2006). Subclassification of the RBCC/TRIM superfamily reveals a novel motif necessary for microtubule binding. J Biol Chem 281, 8970-8980.

Short, K.M., Hopwood, B., Yi, Z., and Cox, T.C. (2002). MID1 and MID2 homo- and heterodimerise to tether the rapamycin-sensitive PP2A regulatory subunit, alpha 4, to microtubules: implications for the clinical variability of X-linked Opitz GBBB syndrome and other developmental disorders. BMC Cell Biol 3, 1.

Suzuki, K., Tsunekawa, Y., Hernandez-Benitez, R., Wu, J., Zhu, J., Kim, E.J., Hatanaka, F., Yamamoto, M., Araoka, T., Li, Z., et al. (2016). In vivo genome editing via CRISPR/Cas9 mediated homology-independent targeted integration. Nature 540, 144-149.

Szczurkowska, J., Lee, S.I., Guo, A., Cwetsch, A.W., Khan, T., Rao, S., Walz, G., Huber, T.B., Cancedda, L., Pautot, S., et al. (2020). A Localized Scaffold for cGMP Increase Is Required for Apical Dendrite Development. Cell Rep 31, 107519.

Tanaka, N., Meng, W., Nagae, S., and Takeichi, M. (2012). Nezha/CAMSAP3 and CAMSAP2 cooperate in epithelial-specific organization of noncentrosomal microtubules. Proc Natl Acad Sci U S A 109, 20029-20034.

Tas, R.P., Chazeau, A., Cloin, B.M.C., Lambers, M.L.A., Hoogenraad, C.C., and Kapitein, L.C. (2017). Differentiation between Oppositely Oriented Microtubules Controls Polarized Neuronal Transport. Neuron 96, 1264-1271 e1265.

Tas, R.P., and Kapitein, L.C. (2018). Exploring cytoskeletal diversity in neurons. Science 361, 231-232.

Terasaki, M., Chen, L.B., and Fujiwara, K. (1986). Microtubules and the endoplasmic reticulum are highly interdependent structures. J Cell Biol 103, 1557-1568.

Tolnay, M., and Probst, A. (1999). REVIEW: tau protein pathology in Alzheimer's disease and related disorders. Neuropathol Appl Neurobiol 25, 171-187.

Tortosa, E., Kapitein, L.C., and Hoogenraad, C.C. (2016). Microtubule Organization and Microtubule-Associated Proteins (MAPs). In Dendrites: Development and Disease, K. Emoto, R. Wong, E. Huang, and C. Hoogenraad, eds.

6

(Tokyo: Springer Japan), pp. 31-75.

Tu, H.Q., Qin, X.H., Liu, Z.B., Song, Z.Q., Hu, H.B., Zhang, Y.C., Chang, Y., Wu, M., Huang, Y., Bai, Y.F., et al. (2018). Microtubule asters anchored by FSD1 control axoneme assembly and ciliogenesis. Nat Commun 9, 5277.

Tymanskyj, S.R., and Ma, L. (2019). MAP7 Prevents Axonal Branch Retraction by Creating a Stable Microtubule Boundary to Rescue Polymerization. J Neurosci 39, 7118-7131.

Tymanskyj, S.R., Yang, B.H., Verhey, K.J., and Ma, L. (2018). MAP7 regulates axon morphogenesis by recruiting kinesin-1 to microtubules and modulating organelle transport. Elife 7.

van Beuningen, S.F., and Hoogenraad, C.C. (2016). Neuronal polarity: remodeling microtubule organization. Curr Opin Neurobiol 39, 1-7.

van Beuningen, S.F.B., Will, L., Harterink, M., Chazeau, A., van Battum, E.Y., Frias, C.P., Franker, M.A.M., Katrukha, E.A., Stucchi, R., Vocking, K., et al. (2015). TRIM46 Controls Neuronal Polarity and Axon Specification by Driving the Formation of Parallel Microtubule Arrays. Neuron 88, 1208-1226.

Vedrenne, C., Klopfenstein, D.R., and Hauri, H.P. (2005). Phosphorylation controls CLIMP-63-mediated anchoring of the endoplasmic reticulum to microtubules. Mol Biol Cell 16, 1928-1937.

Vitre, B., Taulet, N., Guesdon, A., Douanier, A., Dosdane, A., Cisneros, M., Maurin, J., Hettinger, S., Anguille, C., Taschner, M., et al. (2020). IFT proteins interact with HSET to promote supernumerary centrosome clustering in mitosis. EMBO Rep 21, e49234.

Voeltz, G.K., Prinz, W.A., Shibata, Y., Rist, J.M., and Rapoport, T.A. (2006). A class of membrane proteins shaping the tubular endoplasmic reticulum. Cell 124, 573-586.

Wang, S., Wu, D., Quintin, S., Green, R.A., Cheerambathur, D.K., Ochoa, S.D., Desai, A., and Oegema, K. (2015). NOCA-1 functions with gamma-tubulin and in parallel to Patronin to assemble non-centrosomal microtubule arrays in C. elegans. Elife 4, e08649.

Wang, Y., Yang, D., Song, L., Li, T., Yang, J., Zhang, X., and Le, W. (2012). Mifepristone-inducible caspase-1 expression in mouse embryonic stem cells eliminates tumor formation but spares differentiated cells in vitro and in vivo. Stem Cells 30, 169-179.

Waterman-Storer, C.M., and Salmon, E.D. (1998). Endoplasmic reticulum membrane tubules are distributed by microtubules in living cells using three distinct mechanisms. Curr Biol 8, 798-806.

Waterman-Storer, C.M., and Salmon, E.D. (1998). Endoplasmic reticulum membrane tubules are distributed by microtubules in living cells using three distinct mechanisms. Curr Biol 8, 798-806.

Westrate, L.M., Lee, J.E., Prinz, W.A., and Voeltz, G.K. (2015). Form follows function: the importance of endoplasmic reticulum shape. Annu Rev Biochem 84, 791-811.

Willems, J., de Jong, A.P.H., Scheefhals, N., Mertens, E., Catsburg, L.A.E., Poorthuis, R.B., de Winter, F., Verhaagen, J., Meye, F.J., and MacGillavry, H.D. (2020). ORANGE: A CRISPR/Cas9-based genome editing toolbox for epitope tagging of endogenous proteins in neurons. PLoS Biol 18, e3000665.

Wright, K.M., Du, H., Dagnachew, M., and Massiah, M.A. (2016). Solution structure of the microtubule-targeting COS domain of MID1. FEBS J 283, 3089-3102.

Xu, Y., Takeda, S., Nakata, T., Noda, Y., Tanaka, Y., and Hirokawa, N. (2002). Role of KIFC3 motor protein in Golgi positioning and integration. J Cell Biol 158, 293-303.

Xue, Y., Ouyang, K., Huang, J., Zhou, Y., Ouyang, H., Li, H., Wang, G., Wu, Q., Wei, C., Bi, Y., et al. (2013). Direct conversion of fibroblasts to neurons by reprogramming PTB-regulated microRNA circuits. Cell 152, 82-96.

Yau, K.W., Schatzle, P., Tortosa, E., Pages, S., Holtmaat, A., Kapitein, L.C., and Hoogenraad, C.C. (2016). Dendrites In Vitro and In Vivo Contain Microtubules of Opposite Polarity and Axon Formation Correlates with Uniform Plus-End-Out Microtubule Orientation. J Neurosci 36, 1071-1085.

Yau, K.W., van Beuningen, S.F., Cunha-Ferreira, I., Cloin, B.M., van Battum, E.Y., Will, L., Schatzle, P., Tas, R.P., van Krugten, J., Katrukha, E.A., et al. (2014). Microtubule minus-end binding protein CAMSAP2 controls axon specification and dendrite

development. Neuron 82, 1058-1073.

Zhang, Y., Chen, K., Sloan, S.A., Bennett, M.L., Scholze, A.R., O'Keeffe, S., Phatnani, H.P., Guarnieri, P., Caneda, C., Ruderisch, N., et al. (2014). An RNA-sequencing transcriptome and splicing database of glia, neurons, and vascular cells of the cerebral cortex. J Neurosci 34, 11929-11947.

Zhao, X., and Bhattacharyya, A. (2018). Human Models Are Needed for Studying Human Neurodevelopmental Disorders. Am J Hum Genet 103, 829-857.

Zhou, H., Su, J., Hu, X., Zhou, C., Li, H., Chen, Z., Xiao, Q., Wang, B., Wu, W., Sun, Y., et al. (2020a). Glia-to-Neuron Conversion by CRISPR-CasRx Alleviates Symptoms of Neurological Disease in Mice. Cell 181, 590-603 e516.

Zhou, Z., Xu, H., Li, Y., Yang, M., Zhang, R., Shiraishi, A., Kiyonari, H., Liang, X., Huang, X., Wang, Y., et al. (2020b). CAMSAP1 breaks the homeostatic microtubule network to instruct neuronal polarity. Proc Natl Acad Sci U S A 117, 22193-22203.

6

Appendix

Curriculum vitae
List of publications
English summary
Nederlandse samenvatting
Acknowledgements

Curriculum vitae

Biography

Yujie Cao was born in Yantai (China) on November 12, 1988. After graduated from Yantai No.3 high school, he continued study biology at Shandong University in 2007. After obtaining his bachelor's diploma in 2011, Yujie Cao stayed at Shandong University and continued his study in developmental biology in Zhigang Xu's lab. During his masters, he studied the development and maintenance of the hair cell in mouse inner ear. In 2014, he joined Casper Hoogenraad's lab in Utrecht University (Netherlands). He studied the microtubule associated proteins and microtubule organization in neurons under the daily supervision of Dr. Martin Harterink. The study he performed during this period is present here in this thesis.

Education

2014-2021   PhD
Utrecht University, the Netherlands
Department: Cell Biology
Major: Cell Biology and Molecular Neuroscience
Promotor: Prof. Casper Hoogenraad

2011-2014   Master
Shandong University, China
Department: School of Life Science
Major: Development Biology
Promotor: Prof. Xu Zhigang

2007-2011   Bachelor
Shandong University, China
Department: School of Life Science
Major: Biological Sciences

Research   PhD period:
1, The organization and dynamics of microtubule cytoskeleton during neurodevelopment and synaptic plasticity.
2, Kinesin-driven regulation of intracellular transport underlies neuronal development and function.
3, Endoplasmic reticulum structure in synaptic function.

Master period:
The development and maintenance of stereocilia in auditory hair cells.

Teaching

2018	Supervised Research Internship of Natasja Deshayes, MSc student from Biomedical Science and Molecular Neuroscience Program (University of Amsterdam)
2018	Teaching Assistant Molecular Research Courses of BSc Biology Program, Utrecht University
2018-2019	Assisted Workshop of "Neural Circuit Development and Plasticity" Summer School Organized by Cell Biology Department, Utrecht University (annual)-Spinning Disc Confocal Introduction (2018, 2019)
2018-2020	Teaching Assistant Molecular Genetics Research Techniques Courses (MGOT) of BSc Biology Program, Utrecht University (annual)

Conference

2019	NWO life sciences congress: Life2019 (Netherlands)-Presented a poster
2019	Science for Life conference 2019 (Netherlands)
2019	EMBO Workshop Emerging Concepts of the Neuronal Cytoskeleton (Chile) -Presented a poster
2017	NWO Dutch Biophysics (Netherlands)
2017	Cell Biology of the Neruon Polarity, Plasticity and Regeneration (Greece)
2016	EMBO EMBL Symposium: Microtubules: From Atoms to Complex (Germany)

Awards

2012	Kwang-Hua Scholarship, Shandong University
2007	Second-Class Student Scholarship, Shandong University
2007	Excellent Student Cadre of Life Science Department

&

List of Publications

Microtubule Minus-End Binding Protein CAMSAP2 and Kinesin-14 Motor KIFC3 Control Dendritic Microtubule Organization.
<u>Cao, Y.</u>, Lipka, J., Stucchi, R., Burute, M., Pan, X., Portegies, S., Tas, R., Willems, J., Will, L., MacGillavry, H., et al. Curr Biol 30, 899-908 e896 (2020).

The E3 ligase TRIM family members MID1 and MID2 associate with microtubules and control neurodevelopment.
Xingxiu Pan, <u>Yujie Cao</u>, Martin Harterink and Casper C. Hoogenraad. *In preparation* (2020).

WDR47 protects neuronal microtubule minus ends from katanin-mediated severing.
Robin Rouanne Buijs, Jessica J. A. Hummel, Mithila Burute, Xingxiu Pan, <u>Yujie Cao</u>, Riccardo Stucchi, Maarten Altelaar, Anna Akhmanova, Lukas C. Kapitein, Casper C. Hoogenraad. Cell Rep *under revision* (2021).

MAP7D2 Localizes to the Proximal Axon and Locally Promotes Kinesin-1-Mediated Cargo Transport into the Axon.
Pan, X., <u>Cao, Y.</u>, Stucchi, R., Hooikaas, P.J., Portegies, S., Will, L., Martin, M., Akhmanova, A., Harterink, M.[#], and Hoogenraad, CC[#]. Cell Rep 26, 1988-1999 e1986 (2019).

VAP-SCRN1 interaction regulates dynamic endoplasmic reticulum remodeling and presynaptic function.
Lindhout, F.W., <u>Cao, Y.*</u>, Kevenaar, J.T.*, Bodzeta, A.*, Stucchi, R., Boumpoutsari, M.M., Katrukha, E.A., Altelaar, M., MacGillavry, H.D., and Hoogenraad, CC. EMBO J 38, e101345 (2019).

Three-Step Model for Polarized Sorting of KIF17 into Dendrites.
Franker, M.A., Esteves da Silva, M., Tas, R.P., Tortosa, E., <u>Cao, Y.</u>, Frias, C.P., Janssen, A.F.J., Wulf, P.S., Kapitein, L.C., and Hoogenraad, CC. Curr Biol 26, 1705-1712 (2016).

Sorting nexin 9 (SNX9) is not essential for development and auditory function in mice.
Liu, C., Zhai, X., Du, H., <u>Cao, Y.</u>, Cao, H., Wang, Y., Yu, X., Gao, J., and Xu, Z. Oncotarget 7, 68921-68932 (2016).

FCHSD1 and FCHSD2 are expressed in hair cell stereocilia and cuticular plate and regulate actin polymerization in vitro.
Cao, H., Yin, X., <u>Cao, Y.</u>, Jin, Y., Wang, S., Kong, Y., Chen, Y., Gao, J., Heller, S., and Xu, Z. PLoS One 8, e56516 (2013).

*These authors contributed equally.
[#]Co-corresponding authors.

English Summary

The human brain is the most complicated organ, that processes the information from the sensory organs, forms memories and controls motor functions. Neurons are the fundamental units of the brain. These highly specialized cells are connected via synapses. There are 100 billion neurons in the human brain that form the enormous complexity. To understand how the brain works, it is essential to study the fundamental units, the neurons. Neurons are highly polarized cells and critically rely on their cytoskeletal filaments to acquire and maintain their specialized morphology and functions. Microtubules are the major cytoskeletal components of neurons and they are important for neurodevelopment from differentiation, migration and development to synapses connection. They serve as tracks for long distance transport, support neuronal morphology, and control local signaling events. In neurons, microtubules are organized into a specialized architecture. Neurons express abundant microtubule-associated proteins (MAPs). It is becoming clear that MAPs are critical for the establishment and maintenance of the microtubule architecture. To date, our understanding on MAPs and their function is still quite limited, and it is what we aim to explore in this thesis.

In Chapter 2, we describe a novel mechanism that regulates the dendritic microtubule organization by KIFC3 and CAMSAP2. Calmodulin-Regulated Spectrin-Associated Proteins (CAMSAPs) are known for microtubule minus-ends stabilization. KIFC3 from Kinesin14 family is a microtubule minus-end directed motor protein. The regulation of microtubule minus-ends and the functions of minus-end directed motors are relatively less studied in neurons. We found that in neurons, KIFC3 and CAMSAP2 colocalize at the microtubule minus-ends and anchor them to other microtubules in dendrites. Apart from that, it was found that the KIFC3/CAMSAP2 complex could specifically crosslink and stabilize minus-ends out microtubules in dendrites. Our findings help to understand the establishment and the spatial arrangement of dendritic microtubules. Furthermore, our data also provide new insights into the stabilization of microtubule minus-ends in neurons.

Chapter 3 investigates the regulation of MAPs on motor activity. Kinesin1 is well known for intracellular transport in neuronal axon. Our results show that MAP7 family protein, MAP7D2, specifically concentrated at the proximal axon and locally promotes Kinesin1-mediated cargo transport. Here, we propose the model that Kinesin1-driven transport could be locally regulated by MAP7D2, and the MAP-Kinesin collaboration is important for neurodevelopment and polarization.

In Chapter 4, we look into the TRIM E3 ligase family proteins. TRIM46 is a new identified MAP, that localizes to the axon initial segment, crosslinks microtubules and is required for neuronal polarity and axon specification. It is still not clear how TRIM46 binds to the microtubules, but the COS domain of TRIM46 is essential for its microtubule binding and neuronal functions. There are 10 TRIMs from 3 TRIM subfamilies (CI, CII and CIII) that contains the COS domain. Our results show that only MID1, MID2 TRIM46 and TRIM36 from the TRIM-CI subfamily could bind to microtubules. Furthermore, we found MID1 and MID2 are important for neurodevelopment.

&

Recently, the Endoplasmic Reticulum (ER) is found to be involved in the establishment of microtubule organization and neuronal polarity. In Chapter 5, we investigate SCRN1 and VAPA/B and their functions in the ER tubules at presynaptic sites. Our data show that the SCRN1/VAP complex is important for proper ER morphology, maintenance of ER continuity and dynamics, preservation of Ca^{2+} homeostasis and synaptic vesicle cycling. It is unclear if the ER complex at the presynapse is involved in microtubule nucleation and/or organization, but it would be interesting for future study.

In this thesis, we shed light on multiple functions and regulations of MAPs during neuronal development. We addressed the emerging concept that MAPs crosslink microtubules and contribute to the specific microtubule organization in neurons. Furthermore, we explored the MAPs and their regulation on motor activity. Our insights may support future research in the field of neuronal microtubule organization and MAPs to unravel the role of those proteins in neurodevelopment and brain functions.

&

Nederlandse Samenvatting

Het humane brein is het meest complexe orgaan dat informatie van de sensorische organen verwerkt, herinneringen vormt en de motorische functies bestuurt. Neuronen zijn de fundamentele eenheden van de hersenen. Deze zeer gespecialiseerde cellen staan met elkaar in verbinding via synapsen. Er zijn 100 miljard neuronen in het humane brein die samen de enorme complexiteit vormen. Om te kunnen begrijpen hoe het brein werkt, is het essentieel de fundamentele eenheden te bestuderen: de neuronen. Neuronen zijn zeer gepolariseerde cellen en zijn voor een groot gedeelte afhankelijk van de filamenten van het cytoskelet om hun gespecialiseerde morfologie en functies te verkrijgen en te behouden. Microtubuli zijn de belangrijkste componenten van het neuronale cytoskelet en ze zijn essentieel voor de ontwikkeling van neuronen, van differentiatie, migratie en ontwikkeling tot aan de connectie van synapsen. Ze dienen als sporen voor transport over lange afstanden, ondersteunen neuronale morfologie en besturen lokale signaaloverdracht. In neuronen vormen microtubuli een gespecialiseerde architectuur en komen microtubule-associated proteins (MAPs) in overmaat tot expressie. Het wordt duidelijk dat MAP's cruciaal zijn voor het opzetten en onderhouden van deze microtubuli structuur. Tot op heden is ons begrip van MAP's en hun functie nog vrij beperkt, en dat is wat we willen onderzoeken in dit proefschrift.

In Hoofdstuk 2 beschrijven we een nieuw mechanisme dat de organisatie van dendritische microtubuli reguleert door KIFC3 en CAMSAP2. Calmoduline-gereguleerde spectrine-geassocieerde eiwitten (CAMSAP's) staan bekend om hun stabilisatie van de minus-uiteinden van microtubuli. KIFC3 van de Kinesin14-familie is een motoreiwit dat altijd richting de minus-kant van microtubuli beweegt. De regulatie van microtubulus minus-uiteinden en de functies van minus-eind gerichte motoren zijn relatief weinig bestudeerd in neuronen. We ontdekten dat in neuronen, KIFC3 en CAMSAP2 colokaliseren bij de microtubuli minus-uiteinden en dat ze deze verankeren aan andere microtubuli in dendrieten. Verder werd gevonden dat het KIFC3/CAMSAP2-complex in dendrieten een subgroep van microtubuli kan crosslinken en stabiliseren, namelijk specifiek de microtubuli die hun minus-uiteinden naar buiten hebben gericht. Onze bevindingen dragen bij aan het begrijpen van het ontstaan van dendritische microtubuli en hun ruimtelijke ordening. Bovendien bieden onze gegevens ook nieuwe inzichten in de stabilisatie van microtubulus minus-uiteinden in neuronen.

Hoofdstuk 3 onderzoekt de regulatie van MAPs op motorische activiteit. Kinesin1 staat bekend om zijn rol in intracellulair transport in neuronale axonen. Onze resultaten laten zien dat MAP7-familie-eiwit MAP7D2 specifiek geconcentreerd is in het proximale axon en daar lokaal het door Kinesin1 gemedieerd transport bevordert. Hier stellen we het model voor dat Kinesin1-aangedreven transport lokaal kan worden gereguleerd door MAP7D2, en dat MAP-Kinesin-samenwerking belangrijk is voor neuronale ontwikkeling en polarisatie.

In Hoofdstuk 4 onderzoeken we de eiwitten van de TRIM E3-ligase-familie. TRIM46 is een nieuw geïdentificeerd MAP. Het is gelokaliseerd bij het axon initieel segment (AIS), het crosslinkt microtubuli en is van belang voor neuronale polariteit en axon-specificatie. Het is nog steeds niet duidelijk hoe TRIM46 zich bindt aan de

&

microtubuli, maar het COS-domein van TRIM46 is essentieel voor deze binding en zijn neuronale functies. Er zijn 10 TRIM's uit 3 TRIM-subfamilies (CI, CII en CIII) die het COS-domein bevatten. Onze resultaten laten zien dat alleen MID1, MID2, TRIM46 en TRIM36 uit de TRIM-CI-subfamilie konden binden aan de microtubuli. Verder vonden we dat MID1 en MID2 belangrijk zijn voor de ontwikkeling van neuronen.

Onlangs is gebleken dat het Endoplasmatisch Reticulum (ER) betrokken is bij de organisatie van microtubuli en neuronale polariteit. In Hoofdstuk 5 onderzoeken we de eiwitten SCRN1 en VAPA/B en hun functies in de ER-tubuli op presynaptische locaties. Onze bevindingen tonen aan dat het SCRN1/VAP-complex belangrijk is voor een goede ER-morfologie, de handhaving van ER-continuïteit en dynamiek, het behoud van Ca2 + homeostase en de kringloop van synaptische blaasjes. Het is onduidelijk of het ER-complex bij de presynaps betrokken is bij de nucleatie en/of organisatie van microtubuli, maar het zou interessant zijn voor toekomstig onderzoek.

In dit proefschrift belichten we meerdere functies en regulaties van MAP's tijdens de neuronale ontwikkeling. We hebben het opkomende concept behandeld, namelijk dat MAP's microtubuli crosslinken en bijdragen aan de specifieke microtubuli-organisatie in neuronen. Verder hebben we de MAP's en hun regulering van motor activiteit onderzocht. Onze inzichten kunnen toekomstig onderzoek op het gebied van de organisatie van neuronale microtubuli en MAP's ondersteunen om de rol van die eiwitten in neuronale ontwikkeling en hersenfuncties te ontrafelen.

&

Acknowledgements

A good story always has a dramatic beginning. I guess it is the same for my story here. Things started several years ago when I almost finished my master. I was not sure what to do next. By chance, I knew a seminar in Beijing, which is about study abroad in Europe. Luckily, I registered it just few days before the deadline. I met a lady from UU there, and she introduced Utrecht University and a list of research groups to me. Unfortunately, I did not find one that attracted me. She thought for a while and said, 'Maybe. I still know another lab but not on the list.' That is how I know Casper Hoogenraad lab. Few months after that, I made the application, took the flight, and arrived here, which was also the first time for me to go abroad. Till now, I still remember my original intention to start my PhD here, 'to do some cool imaging stuff.' I am glad I did it. Now, it is the time to finish my PhD.

First and foremost, I would like to thank my promotor, Casper. Thank you for offering me the opportunity to work here, and for your guidance and great support on my research. You are always full of enthusiasm, passion, and creativity, and I get tons of great ideas and knowledge from you. You have extraordinary memory, and always remember all the constructs (years ago) and where to find them. You are always optimistic, even for those negative results I get. Your encouragement inspired me and helped me to overcome all the difficulties encountered in the research. I also enjoyed a lot the monthly meeting with you. There are not only the scientific discussions, but also lots of anecdotes and funny stories. From you, I know better about science and better about life. Oh, just a kindly reminder, I still need your signature on my diploma. Hope to see you soon in San Francisco!

A big thank you to my daily supervisor and co-promotor, Martin. I am so lucky to have you as my daily supervisor. You are the person who spend the most time on this thesis (except me). You always try your best to help me with my projects, my presentations, and my writing. Without you, I cannot have done such great work and have such good papers. Your enthusiasm and attitude toward science encouraged me to be better and better. Of course, I also learned a lot about champagne from you. (e.g., how to open it quickly and properly.) And the champagne village you told me is still on my wish list. Thank you for all your help and contributions to this thesis. Cheers to new adventures!

Thanks to all the members of my reading and defense committee: Erik Storkebaum, Madelon Maurice, Maarten Kole, Ginny Farias and Peter Burbach for reading and accepting this thesis.

Special thanks to Anna, Lukas, Corette, Esther, Ginny, Harold, Sabrina, Sander and Mike for all the nice discussions during the Monday meeting and Friday meeting. I really benefit a lot,

Thanks to the neuron culture team. Thank you all for your time and efforts to maintain our neuron culture. And special thanks to lab outing committee for organizing such great event and so many funny and cool activities every year. Thanks to Eugene and Ilya for your great support on our imaging platform.

Next, I would like to acknowledge the current and former lab members in Casper

&

group. Special thanks to Phebe and Robin. It is great to have you as my paranymphs. And many thanks for your help with the Dutch summary of this thesis. Phebe, we are so lucky to have you to manage our lab. I cannot imagine the lab without you. You are always warm, friendly, and helpful to people. It is you that organize and prepare letter chocolates, birthday cakes, gift cards, borrel and BBQ. I am also quite lucky to be in the 'November Birthday Group' with you. Robin, thanks for the proofreading and the Dutch summary of this thesis. Thank you for the input about HAUS and γ-tubulin. I learned a lot from the discussions with you, and I also like those stories you shared about your trip in Canada and China very much. Good luck for your revision, thesis, and the defense. Robbelien, (one of) the fishkeeping master in our office. Always feel comfortable and peaceful while watching those fishes, shrimps, and snails. Thank you for keeping the 'Underwater World' for us. Thanks for your help with the proofreading of this thesis. So good to have you in our office. I always learn lots of news and cool ideas from you. Good luck for your project and defense. Eitan, such great time to have tea with you. Good taste! I also like the conversation with you very much, especially the various stories about history and different cultures. Wish you have a great time in your new job. Best wishes to you and your family in Israel! Riccardo, many thanks for your great help with all mass specs. Thanks for the nice talks at the lunch table. Best wishes for your new life in Switzerland. Dieudonnée, just hope you pass(ed) the master trial of Zelda before the new one comes. It is great to have someone to talk about my hobby. Wish you great success in your new job. Feline, nice to collaborate with you on SCRN1 project. Thanks for organizing lab events and our group meeting. Best wished for you new life in UK. Fingers crossed. Jessica and Liu, thanks for the chats and discussions. Wish you great papers and good luck with your defense. Ginny, I learned a lot about KIF5 and PAEZ from you. It is so grateful that you start your own lab here. Many thanks for your feedback on this thesis. Best wishes to you and your family. Amélie, you are the person who knows AnkG (pretty sure) and wine (also pretty sure) the most in our lab. Such a pity that I did not learn more about them from you. Sybren and Lena, thank you for helping with the KIFC3 paper. Sybren, good luck with your writing and defense. Bart, you are always so gentle and humorous in the lab. Thanks for your help with all kinds of cloning and packages. Natasja, nice to work with you on MAP6 and UNC119 projects, and good job. Hope you enjoy your new job in UMC and best wishes. Gabi, thanks for all the nice chats during teatime, the cakes you brought and your help with figure making. All my best wishes. Laura, wish you great success in New Zealand. Hope to see you in the coming conferences. Olga and Elena, wish you a good life in California. Hope to see you soon there. Sam, all the special beers you shared are so good! Inês, Eliana, Marta, Phil, Mariella and Marleen, wish you great success in the future. Yuhao, wish you have a fantastic PhD life in Hamburg. Special thanks to Joanna and Josta for helping me to initiate my projects. With your help, I can quickly get used to the working environment here.

I would like to thank everybody in the labs of Anna, Lukas, Harold, Corette and Ginny: Chao, great to work with you. Congrats on your new baby. Wish you great success and papers in your new lab. Roderick, thank you for your help with KIFC3 paper and great support on super resolution imaging. You are always full of enthusiasms in the lab. Hey man, all my best wishes and good luck! Mithila, thanks

for your help with the live imaging experiments. Thanks for the discussions and chats with you. Fangrui, you are so good at cooking. I like those traditional Chinese food you shared a lot. Chiung Yi, thanks for the chats and all kinds of food and snacks you shared. Good luck with your defense. Jelmer, thank you for the knock in constructs and protocol. Dipti and Boris, always nice to talk with you and listen to the stories you shared. Nazmiye and Ha, good luck and hope you enjoy your PhD life here. Eugene, thanks for the plugin and support on the microscope. Kai and Qingyang, many thanks for all the constructs and support on pull down experiments. Jian, good luck with your thesis. Have fun in Shanghai (I am a bit jealous). PJ and York, congrats on your defense. Good luck to your new life. Wilco, thanks for the nice chats in the cell culture room and your great support on cloning. Janine, good luck with your project. Cyntha, Hugo, Funso, Joyce, Ankit, Kyle, Max, Maud, Ruddi, Ivar, Amol, Helma, Daphne, Klara, Desiree, Petra, Marijn, Manon, Anna, Carlijn, Lotte, Marvin, Jingchao, Dennis, Arthur, Anne and Hai Yin, thank you all for the nice atmosphere during work and after. Good luck in the future.

Thanks to N502 members! It is great to have you as roommates. So many great moments in our office. I enjoyed a lot with the chats and "Office Teatime" with you. René, it is always interesting to discuss the taste of tea bags with you. Wish you have more collections in your secret drawer. Nicky, wish you have more great papers to fill Champagne bottles. Sam, Mariella and Margriet, wish you all great success and a wonderful future.

To my 'short period' roommates from the South Wing: Cátia, Bas, Max and Anaël. Nice to have you around and you always make the office full of happiness and sweetness (candy jar). To my old roommates at the end of North Wing: Purvi, Rachid, Sofia and Sabrina. Thanks for the lunch time and nice talks. Wish you all great success in the future!

Thank you to all the members in the labs of Paul, Sabrina, Sander and Mike: Rachid, Sofia, Purvi, Inge, Dušan, Katerina, Sara, Vida and Ruben. Thank you for all the nice talks and discussions during our Monday meetings. Wish you all the best.

Xingxiu, thanks for you accompany all the time. Thanks for all the great moments in Barcelona and San Diego we had together. You are the reason I practice cooking skills. When I have trouble, you can always provide me with different perspectives. You let me know that there are more options and possibilities in this world. Hope you find your ideal job soon. Good luck.

最后，我希望感谢我的父母。感谢你们的无私的奉献，默默的支持，以及无条件的信任和理解。没有你们背后的付出，不会有我现在的成绩。不管在外面经历什么，你们总是庇护我最后的港湾。其实我知道你们更希望像其他的父母那样，能有子女的陪伴，然而你们却放开了手，让我能去寻找自己的理想和目标。同时也感谢我的姐姐和姐夫，一直默默的陪在爸妈身边照顾他们，我才能没有后顾之忧，安心的在外面闯荡。谢谢你们。

Anyway, there needs to be an end. Thank you all for being with me in my 'story'. My best wishes to you all.

Yujie Cao

&

&

Camelopardalis

Lynx

Auriga

NEOWISE